

Faculty of Engineering

Predictive Maximum Power Point Tracking for Proton Exchange Membrane Fuel Cell System

Fam Jye Yun

Doctor of Philosophy
2025

Predictive Maximum Power Point Tracking for Proton Exchange Membrane Fuel Cell System

Fam Jye Yun

A thesis submitted

In fulfillment of the requirements for the degree of Doctor of Philosophy

(Electrical Engineering)

Faculty of Engineering
UNIVERSITI MALAYSIA SARAWAK
2025

DECLARATION

I declare that the work in this thesis was carried out in accordance with the regulations of Universiti Malaysia Sarawak. Except where due acknowledgements have been made, the work is that of the author alone. The thesis has not been accepted for any degree and is not concurrently submitted in candidature of any other degree.



……

Signature

Name: Fam Jye Yun

Matric No.: 20020357

Faculty of Engineering

Universiti Malaysia Sarawak

Date : 17 October 2025

ACKNOWLEDGEMENT

I would like to express my deepest gratitude to all those who have contributed to the completion of my PhD thesis.

First, I would like to thank Universiti Malaysia Sarawak (UNIMAS) for providing me with the opportunity to pursue and achieve my academic goals. I am also deeply grateful to the Faculty of Engineering for its academic and technical support, as well as to the Centre for Graduate Studies for the advice and support given throughout my period of study.

I sincerely thanks to my main supervisor, Ir Dr Hazrul bin Mohamed Basri. His knowledge, insightful feedback, and unwavering support have been invaluable in shaping this research. His mentorship has profoundly influenced my academic journey and inspired me to strive for excellence. I would also like to extend my heartfelt gratitude to my co-supervisors, Professor Dr. Mohammad Omar bin Abdullah and Associate Professor Ir. Ts. Dr. Wong Shen Yuong. Professor Dr. Mohammad Omar generously shared his expertise in chemical knowledge with me and provided constructive feedback while completing my journal publication. I would like to give a special thanks to Associate Professor Ir. Ts. Dr. Wong for her care and dedication to my research. She not only contributed valuable technological insights but also provided me with financial support for my journal publication. Her graciousness and commitment were instrumental in ensuring the success of my work.

Lastly, I would like to extend my heartfelt appreciation to Yayasan Sarawak Tun Taib scholarship for their financial support. This generous scholarship has alleviated my financial burden and allowed me to focus entirely on my research without distractions.

ABSTRACT

Proton exchange membrane fuel cells (PEMFC) are devices for converting renewable energy sources of hydrogen and oxygen into electricity with several benefits, including quick startup, high power density, and the ability to operate at low temperatures. However, fluctuations in the internal parameters of PEMFC can cause variations in power output. Additionally, PEMFC generates direct current (DC), while most electrical appliances rely on alternating current (AC). This project aims to design the predictive maximum power point tracking (MPPT) and voltage control system for a PEMFC. It incorporates the model predictive control algorithm for a direct current to direct current (DC-DC) boost converter and a single-phase direct current to alternating current (DC-AC) inverter to optimize the output power and convert the electrical power from DC to AC, respectively. All simulations were conducted using MATLAB software to demonstrate the PEMFC power characteristics and output power extraction. The results show that the predictive MPPT algorithms can track the maximum power point (MPP) within $19.2ms$ with 99.88% accuracy. The new MPP can be determined within $0.5ms$ when there are fast variations of PEMFC parameters. Therefore, the newly designed predictive MPPT methods exhibit fast-tracking of the MPP locus, outstanding accuracy, and robustness to environmental changes. Furthermore, the predictive voltage control technique supplies the AC power with $12V$ amplitude and $50Hz$ frequency throughout the simulations. It ensures that the DC voltage is inverted to a stable AC voltage.

Keywords: DC-DC boost converter, MPPT, PEMFC, single-phase DC-AC inverter, voltage control

Penjejakan Titik Kuasa Maksimum Ramalan untuk Sistem Sel Bahan Bakar Membran Penukar Proton

ABSTRAK

Sel bahan bakar membran pertukaran proton (PEMFC) adalah peranti untuk menukar tenaga boleh baharu seperti hidrogen dan oksigen kepada elektrik dengan beberapa kelebihan, termasuk penghidupan cepat, ketumpatan kuasa tinggi, dan operasi pada suhu rendah. Walau bagaimanapun, perubahan parameter dalaman PEMFC boleh menyebabkan variasi output kuasa. Selain itu, PEMFC menghasilkan arus terus (DC), sedangkan kebanyakan peralatan elektrik bergantung pada arus ulang-alik (AC). Projek ini bertujuan mereka bentuk sistem penjejakan titik kuasa maksimum (MPPT) dan kawalan voltan ramalan untuk PEMFC. Ia menggabungkan algoritma kawalan ramalan model untuk penukar penggalak DC-DC dan penyongsang DC-AC satu fasa bagi mengoptimumkan kuasa output dan menukar kuasa elektrik daripada DC kepada AC. Semua simulasi dijalankan menggunakan MATLAB untuk menunjukkan ciri kuasa PEMFC dan pengekstrakan kuasa output. Hasil simulasi menunjukkan algoritma MPPT ramalan boleh menjejaki titik kuasa maksimum (MPP) dalam 19.2ms dengan ketepatan 99.88%. Titik kuasa maksimum baharu dapat ditentukan dalam 0.5ms apabila berlaku perubahan pantas parameter PEMFC. Oleh itu, kaedah MPPT ramalan ini menunjukkan penjejakan pantas terhadap MPP, ketepatan cemerlang, dan ketahanan terhadap perubahan persekitaran. Selain itu, teknik kawalan voltan ramalan membekalkan kuasa AC dengan amplitud 12V dan frekuensi 50Hz sepanjang simulasi, memastikan voltan DC ditukar kepada voltan AC stabil.

Kata kunci: *Penukar penggalak DC-DC, MPPT, PEMFC, penyongsang DC-AC fasa tunggal, kawalan voltan*

TABLE OF CONTENTS

		Page
DECLARATION		i
ACKNOWLEDGEMENT		ii
ABSTRACT		iii
ABSTRAK		iv
TABLE OF CONTENTS		v
LIST OF TABLES		xiii
LIST OF FIGURES		xv
LIST OF ABBREVIATIONS		xxiii
CHAPTER 1: INTRODUCTION		1
1.1	Study Background	1
1.2	Research Motivation	2
1.3	Research Overview	4
1.3.1	Introduction to Proton Exchange Membrane Fuel Cell (PEMFC)	4
1.3.2	MPPT of PEMFC	6
1.4	Problem Statement	9
1.5	Research Questions	11
1.6	Objectives	12

1.7 Hypothesis 13

1.8 Significance of Research 13

1.9 Research Scope 14

1.10 Thesis Outline 15

CHAPTER 2: LITERATURE REVIEW 17

2.1 Introduction 17

2.2 Fuel Cell 17

2.2.1 Proton Exchange Membrane Fuel Cell (PEMFC) 18

2.2.2 Alkaline Fuel Cell (AFC) 18

2.2.3 Direct Methanol Fuel Cell (DMFC) 19

2.2.4 Solid Oxide Fuel Cell (SOFC) 20

2.2.5 Molten Carbonate Fuel Cell (MCFC) 21

2.2.6 Phosphoric Acid Fuel Cell (PAFC) 21

2.2.7 Comparison of Fuel Cell Types 22

2.3 Mathematical Modeling of PEMFC System 25

2.3.1 Nernst Equation 25

2.3.2 Activation Overvoltage 27

2.3.3 Ohmic Overvoltage 28

2.3.4 Concentration Overvoltage 29

2.3.5 PEMFC Output Power 29

2.4 Maximum Power Point Tracking (MPPT) 30

2.4.1 Sliding Mode Control (SMC) 30

2.4.2 Twisting Algorithm-based High-Order SMC (HOSM-TA) 31

2.4.3 Backstepping Algorithm 33

2.4.4 Perturb and Observe (P&O) 37

2.4.5 Increment Conductance Method (IC) 38

2.4.6 Radial Basic Function Network (RBFN) 39

2.4.7 Fuzzy Logic Control (FLC) 41

2.4.8 Particle Swarm Optimizer (PSO) 44

2.4.9 Salp Swarm Algorithm (SSA) 47

2.4.10 Forensic-based Investigation Algorithm (FBI) 50

2.4.11 Golden Jackal Optimization Algorithm (GJOA) 53

2.4.12 Artificial Bee Colony Algorithm (ABC) 56

2.4.13 Summary of MPPT in Literature Review 57

2.5 Model Predictive Control (MPC) 64

2.5.1 MPC for DC-DC Buck Converter 66

2.5.2 MPC for DC-DC Boost Converter 68

2.5.3 MPC for DC-DC Buck-Boost Converter 73

2.5.4 MPC for Single-Phase AC-DC Converter 76

2.5.5 MPC for Three-Phase AC-DC Converter 79

2.5.6 MPC for Single-Phase DC-AC Inverter 82

2.5.7 MPC for Three-Phase DC-AC Inverter 87

2.5.8 MPC for Three-Phase AC Output Control 94

2.6 Chapter Summary 97

CHAPTER 3: RESEARCH METHODOLOGY 99

3.1 Introduction 99

3.2 Mathematical Model of PEMFC 100

3.3 Maximum Power Point Tracker 101

3.3.1 Newton–Raphson Method 102

3.3.2 First Derivative of Reversible Thermodynamic Power 103

3.3.3 First Derivative of Activation Power Loss 104

3.3.4 First Derivative of Ohmic Power Loss 104

3.3.5 First Derivative of Concentration Power Loss 105

3.3.6 Second Derivative of Reversible Thermodynamic Power 106

3.3.7 Second Derivative of Activation Power Loss 106

3.3.8 Second Derivative of Ohmic Power Loss 107

3.3.9 Second Derivative of Concentration Power Loss 107

3.3.10 Newton–Raphson Equation 108

3.4 DC-DC Power Converter 108

3.5 Predictive Maximum Power Point Tracking Method 112

3.5.1 Discrete-time Model Equation 113

3.5.2 Predictive Switching State Control Technique 114

3.5.3 Predictive Duty Cycle Control Technique 114

3.6 Cost Function 115

3.7 Switching Frequency Reduction Technique 116

3.7.1 Construction of Decision Matrix 116

3.7.2 Normalized Decision Matrix Construction 117

3.7.3 Weighted Normalized Decision-making Construction 117

3.7.4 Determining the PIS and NIS 118

3.7.5 Calculating the Distances of Each Alternative to the PIS and NIS 119

3.7.6 Calculate the Relative Closeness 119

3.7.7 Frequency Reduction by TOPSIS in MPPT Technique 120

3.8 Summary of MPPT Technique in Simulation 122

3.8.1 Process Flow of Predictive MPPT by Switching State Control Technique 122

3.8.2 Process Flow of Predictive MPPT by Duty Cycle Control Technique 123

3.8.3 Process Flow of Predictive MPPT with Switching Frequency Reduction Technique 125

3.9 Predictive Voltage Control Technique 127

3.9.1 H-Bridge Inverter 127

3.9.2 Voltage Control Algorithm 128

3.9.3 Fuel Control Algorithm 131

3.10 Chapter Summary 136

CHAPTER 4: RESULTS AND DISCUSSION 138

4.1 Introduction 138

4.2 PEMFC Characteristics in Simulation 138

4.3 Simulation with Constant PEMFC Parameters and Constant Load 140

4.3.1 Simulation with Constant PEMFC Parameters by Predictive Switching State MPPT Technique 141

4.3.2 Simulation with Constant PEMFC Parameters by Predictive Duty Cycle MPPT Technique 145

4.3.3 Simulation with Constant PEMFC Parameters by Predictive Switching State MPPT with Frequency Reduction Technique 157

4.3.4 Summary of Simulation Results with Constant PEMFC Parameters 168

4.4 Simulation with Variable PEMFC Parameters and Constant Load 181

4.4.1 Simulation with Variable PEMFC Parameters by Predictive Switching State MPPT Technique 183

4.4.2 Simulation with Variable PEMFC Parameters by Predictive Duty Cycle MPPT Technique 190

4.4.3 Simulation with Variable PEMFC Parameters by Predictive Switching State MPPT with Frequency Reduction Technique 198

4.4.4 Summary of Simulation Results with Variable PEMFC Parameters 205

4.5 Simulation with Constant PEMFC Parameters and Variable Load Resistance 211

4.5.1 Simulation with Variable Load by Predictive Switching State MPPT Technique 212

4.5.2 Simulation with Variable Load by Predictive Duty Cycle MPPT Technique 219

4.5.3 Simulation with Variable Load by Predictive Switching State MPPT with Frequency Reduction Technique 227

4.5.4 Summary of Simulation Results with Variable Load Resistance 234

4.6 Simulation with Variable AC Load 241

4.6.1 Simulation by Predictive Switching State MPPT with Voltage Control Method 242

4.6.2 Simulation by Predictive Duty Cycle MPPT with Voltage Control Method 247

4.6.3 Simulation by Predictive Switching State MPPT with Frequency Reduction and Voltage Control Method 251

4.6.4 Summary of Simulation by Predictive MPPT and Voltage Control Techniques 255

4.7 Chapter Summary 267

CHAPTER 5: CONCLUSIONS AND RECOMMENDATIONS 270

5.1 Research Outcomes 270

5.2 Research Contributions 272

5.3 Future Recommendation 273

REFERENCES 275

APPENDICES 292

LIST OF TABLES

		Page
Table 1.1	Components of Single Fuel Cell Stack	4
Table 2.1	Comparison of the Fuel Cell Types	23
Table 2.2	Summary of the MPPT Techniques	58
Table 2.3	Switching Combinations of Single-Phase Five-Level ANPC Inverter	86
Table 2.4	Switching Combinations of Three-Phase Five-Level ANPC Inverter	91
Table 3.1	Decision Matrix	117
Table 3.2	Weighted Normalised Decision Matrix	118
Table 3.3	PIS and NIS Matrix	118
Table 3.4	Euclidean Distance Matrix	119
Table 3.5	Relative Closeness Index for ON and OFF Switching State	120
Table 3.6	Possible Switching States Responding to vs	128
Table 3.7	Parameters for Predictive Voltage Control Technique	131
Table 3.8	Parameters for Predictive Fuel Control Algorithm	134
Table 4.1	PEMFC Parameters	139
Table 4.2	Comparison of Proposed Predictive MPPT Techniques under Constant PEMFC Parameters	175
Table 4.3	Comparison of Proposed MPPT Technique with Other Techniques	178
Table 4.4	Comparison of Load Power Quality under Constant PEMFC Parameters	180
Table 4.5	Comparison of Proposed Predictive MPPT Techniques under Variable PEMFC Parameters	206
Table 4.6	Comparison of Load Power Quality under Variable PEMFC Parameters	208
Table 4.7	Comparison of Proposed Predictive MPPT Techniques under Variable Load Resistance	235
Table 4.8	Comparison of Load Power Quality under Variable Load Resistance	238

Table 4.9 Comparison of PEMFC Behaviour by Predictive MPPT with Voltage Control Techniques 261

Table 4.10 Comparison of Load Power Quality by Predictive Voltage Control Technique 265

LIST OF FIGURES

		Page
Figure 1.1	PEMFC and Single Cell Stack Level (Daming, 2018)	5
Figure 1.2	Single PEMFC Configuration (Samal et al., 2018)	6
Figure 1.3	PEMFC Polarization Curve (Loo et al., 2011)	7
Figure 1.4	PEMFC Polarization Curve and Operation Point	8
Figure 1.5	PEMFC Polarization Curve with Different Operation Temperatures	9
Figure 2.1	Duty Cycle Versus Operation Region (Abdi et al., 2012)	31
Figure 2.2	MPP Curve and P-I Curve for Different PEMFC Parameters (Derbeli et al., 2018)	34
Figure 2.3	Flowchart for P&O-based MPPT Method (Barhoumi et al., 2020)	37
Figure 2.4	Flowchart for IC-based MPPT Method (Karami et al., 2014)	39
Figure 2.5	RBFN Structure (K. J. Reddy & Sudhakar, 2017)	40
Figure 2.6	Input and Output Membership of Mamdani FLC (Luta & Raji, 2019b)	42
Figure 2.7	Rules Table (Luta & Raji, 2019b)	43
Figure 2.8	Fuzzy MF Design (Aly et al., 2023; Rezk et al., 2023)	44
Figure 2.9	Flowchart of PSO MPPT Controller (Luta & Raji, 2019b)	46
Figure 2.10	Flowchart of SSA (Fathy, Abdelkareem, et al., 2021)	49
Figure 2.11	Flowchart of FBI (Fathy, Rezk, et al., 2021)	52
Figure 2.12	Flowchart of GJOA (Agwa et al., 2023)	55
Figure 2.13	DC-DC Buck Converter Circuit Topology	66
Figure 2.14	DC-DC Boost Converter Circuit Topology	69
Figure 2.15	Two-Phase Interleaved Boost Converter Circuit Topology	71
Figure 2.16	Three-Level Boost Converter Circuit Topology	72
Figure 2.17	DC-DC Buck-Boost Converter Circuit Topology	74

Figure 2.18 Non-Inverting DC-DC Buck-Boost Converter Circuit Topology 76

Figure 2.19 Single-Phase Three-Level Neutral Point Clamped Converter Circuit Topology 77

Figure 2.20 Three-Phase AC-DC Converter Circuit Topology 79

Figure 2.21 Bidirectional Switches Controlled Three-Phase AC-DC Converter Circuit Topology 81

Figure 2.22 Single-Phase DC-AC Inverter Circuit Topology 82

Figure 2.23 Single-Phase Quasi-Z Source Inverter Circuit Topology 83

Figure 2.24 Single-Phase Five-Level ANPC Inverter 85

Figure 2.25 General Model of Three-Phase DC-AC Inverter Circuit Topology 88

Figure 2.26 Switching Combination Responding to AC Voltage for Three-Phase Inverter (Rodriguez et al., 2020) 89

Figure 2.27 Three-Phase Five-Level Active NPC Inverter Circuit Topology 90

Figure 2.28 Switching Combination Responding to AC Voltage for Three-Phase Five-Level Inverter (Liu et al., 2020) 92

Figure 2.29 Three-Phase Four-Legged Inverter Circuit Topology 93

Figure 2.30 Three-Phase Direct Matrix Converter Circuit Topology 94

Figure 2.31 Three-level Four-Leg Indirect Matrix Converter 95

Figure 3.1 PEMFC System and Predictive MPPT Controller Configuration (a) Without Predictive Voltage Control Inverter, (b) With Predictive Voltage Control Inverter 100

Figure 3.2 Fully Functional Mathematical Modeling of PEMFC System 101

Figure 3.3 Newton–Raphson Approximation Concept 102

Figure 3.4 DC-DC Boost Converter 109

Figure 3.5 DC-DC Boost Converter for ON Switching State 109

Figure 3.6 DC-DC Boost Converter for OFF Switching State 110

Figure 3.7 Change in Inductor Voltage and Current 111

Figure 3.8 TOPSIS Flowchart 121

Figure 3.9 Predictive MPPT by Switching State Control Flowchart 123

Figure 3.10 Predictive MPPT by Duty Cycle Control Flowchart 124

Figure 3.11 Predictive MPPT by Switching with TOPSIS Control Flowchart 126

Figure 3.12 H-bridge Inverter with Second-order Input Filter 127

Figure 3.13 Predictive Voltage Control Technique Flowchart 130

Figure 3.14 Fuel Control Algorithm Flowchart 135

Figure 4.1 V-I and P-I Characteristics for 50W PEMFC 140

Figure 4.2 Simulation Results of PEMFC for Predictive Switching State MPPT under Constant PEMFC Parameters 141

Figure 4.3 Simulation Results of Switching State for Predictive Switching State MPPT under Constant PEMFC Parameters 143

Figure 4.4 Simulation Results of Load for Predictive Switching State MPPT under Constant PEMFC Parameters 144

Figure 4.5 Simulation Results of PEMFC for Predictive Duty Cycle MPPT with $10kHz$ Frequency under Constant PEMFC Parameters 146

Figure 4.6 Simulation Results of PEMFC for Predictive Duty Cycle MPPT with $20kHz$ Frequency under Constant PEMFC Parameters 147

Figure 4.7 Simulation Results of PEMFC for Predictive Duty Cycle MPPT with $30kHz$ Frequency under Constant PEMFC Parameters 148

Figure 4.8 Simulation Results of Duty Cycle for Predictive Duty Cycle MPPT under Constant PEMFC Parameters 150

Figure 4.9 Simulation Results of Switching State for Predictive Duty Cycle MPPT with $10kHz$ Frequency under Constant PEMFC Parameters 151

Figure 4.10 Simulation Results of Switching State for Predictive Duty Cycle MPPT with $20kHz$ Frequency under Constant PEMFC Parameters 152

Figure 4.11 Simulation Results of Switching State for Predictive Duty Cycle MPPT with $30kHz$ Frequency under Constant PEMFC Parameters 153

Figure 4.12 Simulation Results of Load for Predictive Duty Cycle MPPT with $10kHz$ Frequency under Constant PEMFC Parameters 154

Figure 4.13 Simulation Results of Load for Predictive Duty Cycle MPPT with $20kHz$ Frequency under Constant PEMFC Parameters 155

Figure 4.14 Simulation Results of Load for Predictive Duty Cycle MPPT with $30kHz$ Frequency under Constant PEMFC Parameters 156

Figure 4.15 Simulation Results of PEMFC for Predictive Switching State MPPT with 0.1 Weighting Factor of Frequency Reduction under Constant PEMFC Parameters 158

Figure 4.16 Simulation Results of PEMFC for Predictive Switching State MPPT with 0.2 Weighting Factor of Frequency Reduction under Constant PEMFC Parameters 159

Figure 4.17 Simulation Results of PEMFC for Predictive Switching State MPPT with 0.3 Weighting Factor of Frequency Reduction under Constant PEMFC Parameters 160

Figure 4.18 Simulation Results of Switching State for Predictive Switching State MPPT with 0.1 Weighting Factor of Frequency Reduction under Constant PEMFC Parameters 162

Figure 4.19 Simulation Results of Switching State for Predictive Switching State MPPT with 0.2 Weighting Factor of Frequency Reduction under Constant PEMFC Parameters 163

Figure 4.20 Simulation Results of Switching State for Predictive Switching State MPPT with 0.3 Weighting Factor of Frequency Reduction under Constant PEMFC Parameters 164

Figure 4.21 Simulation Results of Load for Predictive Switching State MPPT with 0.1 Weighting Factor of Frequency Reduction under Constant PEMFC Parameters 165

Figure 4.22 Simulation Results of Load for Predictive Switching State MPPT with 0.2 Weighting Factor of Frequency Reduction under Constant PEMFC Parameters 166

Figure 4.23 Simulation Results of Load for Predictive Switching State MPPT with 0.3 Weighting Factor of Frequency Reduction under Constant PEMFC Parameters 167

Figure 4.24 Partial Pressure of Hydrogen and Oxygen during Operation 169

Figure 4.25 Starting and Final PEMFC P-I Curve 169

Figure 4.26 Current Flow in DC-DC Boost Converter when Switch is ON 171

Figure 4.27 Current Flow in DC-DC Boost Converter when Switch is OFF 171

Figure 4.28 Simulation Results of Electrical Power Absorbed by Capacitor and Load vs PEMFC Output Power 172

Figure 4.29 Variations of Hydrogen and Oxygen Input Flow Rates 181

Figure 4.30 PEMFC P-I Polarization Curve under Different Input Flow Rates 182

Figure 4.31 Simulation Results of PEMFC Output Voltage for Predictive Switching State MPPT under Variable PEMFC Parameters 183

Figure 4.32 Simulation Results of PEMFC Output Current for Predictive Switching State MPPT under Variable PEMFC Parameters 184

Figure 4.33 Simulation Results of PEMFC Output Power for Predictive Switching State MPPT under Variable PEMFC Parameters 185

Figure 4.34 Simulation Results of Switching State for Predictive Switching State MPPT under Variable PEMFC Parameters 186

Figure 4.35 Simulation Results of Load Voltage for Predictive Switching State MPPT under Variable PEMFC Parameters 188

Figure 4.36 Simulation Results of Load Current for Predictive Switching State MPPT under Variable PEMFC Parameters 189

Figure 4.37 Simulation Results of Load Power for Predictive Switching State MPPT under Variable PEMFC Parameters 190

Figure 4.38 Simulation Results of PEMFC Output Voltage for Predictive Duty Cycle MPPT under Variable PEMFC Parameters 191

Figure 4.39 Simulation Results of PEMFC Output Current for Predictive Duty Cycle MPPT under Variable PEMFC Parameters 192

Figure 4.40 Simulation Results of PEMFC Output Power for Predictive Duty Cycle MPPT under Variable PEMFC Parameters 193

Figure 4.41 Simulation Results of Duty Cycle for Predictive Duty Cycle MPPT under Variable PEMFC Parameters 194

Figure 4.42 Simulation Results of Switching State for Predictive Duty Cycle MPPT under Variable PEMFC Parameters 195

Figure 4.43 Simulation Results of Load Voltage for Predictive Duty Cycle MPPT under Variable PEMFC Parameters 196

Figure 4.44 Simulation Results of Load Current for Predictive Duty Cycle MPPT under Variable PEMFC Parameters 197

Figure 4.45 Simulation Results of Load Power for Predictive Duty Cycle MPPT under Variable PEMFC Parameters 198

Figure 4.46 Simulation Results of PEMFC Output Voltage for Predictive Switching State MPPT with Frequency Reduction under Variable PEMFC Parameters 199

Figure 4.47 Simulation Results of PEMFC Output Current for Predictive Switching State MPPT with Frequency Reduction under Variable PEMFC Parameters 200

Figure 4.48 Simulation Results of PEMFC Output Power for Predictive Switching State MPPT with Frequency Reduction under Variable PEMFC Parameters 201

Figure 4.49 Simulation Results of Switching State for Predictive Switching State MPPT with Frequency Reduction under Variable PEMFC Parameters 202

Figure 4.50 Simulation Results of Load Voltage for Predictive Switching State MPPT with Frequency Reduction under Variable PEMFC Parameters 203

Figure 4.51 Simulation Results of Load Current for Predictive Switching State MPPT with Frequency Reduction under Variable PEMFC Parameters 204

Figure 4.52 Simulation Results of Load Power for Predictive Switching State MPPT with Frequency Reduction under Variable PEMFC Parameters 205

Figure 4.53 Variations of Load Resistance 212

Figure 4.54 Simulation Results of PEMFC Output Voltage for Predictive Switching State MPPT under Variable Load Resistance 213

Figure 4.55 Simulation Results of PEMFC Output Current for Predictive Switching State MPPT under Variable Load Resistance 214

Figure 4.56 Simulation Results of PEMFC Output Power for Predictive Switching State MPPT under Variable Load Resistance 215

Figure 4.57 Simulation Results of Switching State for Predictive Switching State MPPT under Variable Load Resistance 216

Figure 4.58 Simulation Results of Load Voltage for Predictive Switching State MPPT under Variable Load Resistance 217

Figure 4.59 Simulation Results of Load Current for Predictive Switching State MPPT under Variable Load Resistance 218

Figure 4.60 Simulation Results of Load Power for Predictive Switching State MPPT under Variable Load Resistance 219

Figure 4.61 Simulation Results of PEMFC Output Voltage for Predictive Duty Cycle MPPT under Variable Load Resistance 220

Figure 4.62 Simulation Results of PEMFC Output Current for Predictive Duty Cycle MPPT under Variable Load Resistance 221

Figure 4.63 Simulation Results of PEMFC Output Power for Predictive Duty Cycle MPPT under Variable Load Resistance 222

Figure 4.64 Simulation Results of Duty Cycle for Predictive Duty Cycle MPPT under Variable Load Resistance 223

Figure 4.65 Simulation Results of Switching State for Predictive Duty Cycle MPPT under Variable Load Resistance 224

Figure 4.66 Simulation Results of Load Voltage for Predictive Duty Cycle MPPT under Variable Load Resistance 225

Figure 4.67 Simulation Results of Load Current for Predictive Duty Cycle MPPT under Variable Load Resistance 226

Figure 4.68 Simulation Results of Load Power for Predictive Duty Cycle MPPT under Variable Load Resistance 227

Figure 4.69 Simulation Results of PEMFC Output Voltage for Predictive Switching State MPPT with Frequency Reduction under Variable Load Resistance 228

Figure 4.70 Simulation Results of PEMFC Output Current for Predictive Switching State MPPT with Frequency Reduction under Variable Load Resistance 229

Figure 4.71 Simulation Results of PEMFC Output Power for Predictive Switching State MPPT with Frequency Reduction under Variable Load Resistance 230

Figure 4.72 Simulation Results of Switching State for Predictive Switching State MPPT with Frequency Reduction under Variable Load Resistance 231

Figure 4.73 Simulation Results of Load Voltage for Predictive Switching State MPPT with Frequency Reduction under Variable Load Resistance 232

Figure 4.74 Simulation Results of Load Current for Predictive Switching State MPPT with Frequency Reduction under Variable Load Resistance 233

Figure 4.75 Simulation Results of Load Power for Predictive Switching State MPPT with Frequency Reduction under Variable Load Resistance 234

Figure 4.76 Simulation Results of PEMFC for Predictive Switching State MPPT with Voltage Control Technique 242

Figure 4.77 Simulation Results of Capacitor Behaviour for Predictive Switching State MPPT with Voltage Control Technique 244

Figure 4.78 Simulation Results of Load for Predictive Switching State MPPT with Voltage Control Technique 246

Figure 4.79 Simulation Results of PEMFC for Predictive Duty Cycle MPPT with Voltage Control Technique 247

Figure 4.80 Simulation Results of Capacitor Behaviour for Predictive Duty Cycle MPPT with Voltage Control Technique 249

Figure 4.81 Simulation Results of Load for Predictive Duty Cycle MPPT with Voltage Control Technique 250

Figure 4.82 Simulation Results of PEMFC for Predictive Switching State MPPT with Frequency Reduction and Voltage Control Technique 251

Figure 4.83 Simulation Results of Capacitor Behaviour for Predictive Switching State MPPT with Frequency Reduction and Voltage Control Technique 253

Figure 4.84 Simulation Results of Load for Predictive Switching State MPPT with Frequency Reduction and Voltage Control Technique 254

Figure 4.85 Simulation Results of Electrical Power Distributed to Capacitor and AC Power Converter 256

Figure 4.86 Simulation Results of DC-DC Boost Converter Output Power 257

Figure 4.87 Current Flow in DC-DC Boost Converter when Peak Capacitor Current Occurs 258

Figure 4.88 Simulation Results of PEMFC Output Power, Load Power Consumption, and Average Capacitor Power 259

Figure 4.89 Simulation Results of Input Flow Rate of Fuel, PEMFC Output Power, and Capacitor Voltage for 3 Seconds Simulation 260

Figure 4.90 Simulation Results of Switching State for All Predictive MPPT with Voltage Control Technique 263

LIST OF ABBREVIATIONS

AC	Alternating Current
AC-DC	Alternating Current to Direct Current
AEO	Artificial Ecosystem Optimizer
AFC	Alkaline Fuel Cell
ALO	Antlion Optimizer
CRE	Current Reference Estimation
DC	Direct Current
DC-AC	Direct Current to Alternating Current
DC-DC	Direct Current to Direct Current
DMFC	Direct Methanol Fuel Cell
FBI	Forensic-based Investigation
FC	Fuel Cell
FCS-MPC	Finite-Control-Set Model Predictive Control
FLC	Fuzzy Logic Control
FOPID	Fractional-order Proportional-integral-derivative
FiFu	Fitness Function
GBO	Gradient-based Optimization
GPC	Generalised Model Predictive Controller
GPIO	Generalized Proportional Integral Observer
GWO	Grey Wolf Optimizer
HOSM-TA	High Order SMC-based “Twisting Algorithm”
H_2	Hydrogen

IBC	Interleaved Boost Converter
IC	Incremental Conductance
IGBT	Insulated Gate Bipolar Transistor
IWO	Invasive Weed Optimizer
LSHADE	Success-History-based Adaptive Differential Evolution Algorithm with Linear Population Size Reduction
MBA	Mine-blast Algorithm
MCDM	Multiple Criteria Decision-making
MCFC	Molten Carbonate Fuel Cell
MEA	Membrane Electrode Assembly
MF	Membership Function
MOSFET	Metal-oxide-semiconductor Field-effect Transistor
MPC	Model Predictive Control
MPP	Maximum Power Point
MPPT	Maximum Power Point Tracking
NB	Negative Big
NIS	Negative-ideal Solutions
NPC	Neutral Point Clamped
NS	Negative Small
O_2	Oxygen
P&O	Perturb and Observe
PAFC	Phosphoric Acid Fuel Cell
PB	Positive Big
PEM	Proton Exchange Membrane
PEMFC	Proton Exchange Membrane Fuel Cell

P-I	Power-Current
PD	Proportional-Derivative
PI	Proportional-Integral
PID	Proportional-Integral-Derivative
PIS	Positive-ideal Solutions
PS	Positive Small
PSO	Particle Swarm Optimizer
PV	Photovoltaic
PWM	Pulse Width Modulation
RBFN	Radial Basis Function Network
RE	Renewable Energy
RL	Resistor-indictor
RLC	Resistor-indictor-capacitor
rms	root means square
SCA	Sin-cosine Algorithm
SMC	Sliding Mode Control
SOFC	Solid Oxide Fuel Cell
SSA	Salp Swarm Algorithm
THD	Total Harmonic Distortion
TIBC	Two-phase Interleaved Boost Converter
TLBC	Three-Level Boost Converter
TOPSIS	Technique for Order of Preference by Similarity to Ideal Solution
V-I	Voltage-Current
VSS	Variable Step Size
Z	Zero

ZrO_2	Zirconia

CHAPTER 1

INTRODUCTION

1.1 Study Background

Hydrogen was first generated using electricity in 1789, when van Troostwijk and Deiman applied an electrostatic generator as a direct current source. Following Volta's invention of the voltaic pile in 1800, Carlisle and Nicholson utilized this device to split water into hydrogen and oxygen (Smolinka et al., 2022). Building on this process, William Grove conceived the idea of reversing the reaction to recompose hydrogen and oxygen into water (Grove, 1839). This was achieved by separating platinum electrodes in containers of oxygen and hydrogen, each submerged in a sulfuric acid electrolyte solution, forming a single cell known as the Grove cell. Several cells were then connected in series to increase the voltage, resulting in the creation of a gas-voltaic battery. This gas-voltaic battery produced $12A$ of current at approximately $1.8V$ (Spiegel, 2008). Thus, the first Fuel Cell (FC) was successfully invented by William Grove in 1839.

FC is one of the renewable energies that is emerging to deliver clean and efficient power. FC can generate electrical power ranging from portable kilowatt to multimegawatt stationary power plants (Zhi et al., 2021). This technology applies to residential, commercial, and industrial. FC can be considered as the top of the desirable technologies for a broad spectrum of power generation applications. This is because it exhibits high efficiency, high power density, modular, noise-free operation, negligible environmental emissions, and is non-site-specific (Ahmed et al., 2023).

FC is powered by Hydrogen, which exists in abundance in our surroundings. On top of that, Hydrogen is a sustainable and clean source offering eco-friendly solutions. Thanks to the high efficiency of the fuel cell, this technology has been adapted to various domains, such as electric vehicles (Hamedani et al., 2024), portable electronics, and off-grid power plants (Ahmed et al., 2023). There are some fuel cell technologies available to be explored, such as Proton Exchange Membrane Fuel Cell (PEMFC), Solid Oxide Fuel Cell (SOFC), Alkaline Fuel Cell (AFC), Phosphoric Acid Fuel Cell (PAFC), and Molten Carbonate Fuel Cell (MCFC) (Karthikeyan et al., 2018).

Among the fuel cell technologies, PEMFC has the interesting feature of high power density, fast start-up, and low operating temperature (Singla et al., 2023). It is also known as the Polymer Electrolyte Membrane Fuel Cell and has been intensively studied. It can suit diverse applications for terrestrial vehicles and rural power plants, but fuel cells require a large investment.

1.2 Research Motivation

It is a well-known fact that Earth suffers from the depletion of fossil fuels (Karami et al., 2014; Singla et al., 2023; Sultan, Menesy, Kamel, Hasanien, et al., 2020). This has become a global challenge because global energy demand is rising (Gupta et al., 2021; Jawad et al., 2022; Yaqoob et al., 2021). In addition, the combustion of fossil fuels leads to environmental changes because it produces greenhouse gas emissions and causes high air pollution (Jawad et al., 2022; Sultan, Menesy, Kamel, Tostado-Veliz, et al., 2020; Yaqoob et al., 2021). Thus, there is an urge to look into alternative energy sources to create a proportion between the resource and demand. As a result, Renewable Energy (RE) sources have started to penetrate the modern power system. RE sources are better alternatives to

fossil fuel-based conventional power systems for environmental and economic reasons. Among the RE sources, hydrogen is the most viable source since these technologies are modular and non-site specific. Therefore, the fuel cell becomes the best choice because it has the advantages of low emissions, noise-free operation, and high output efficiency (Karthikeyan et al., 2018).

Despite the relatively high efficiency of the fuel cell, the power extracted from the fuel cell is not always optimum due to ever-changing internal variables (Karami et al., 2014). A maximum power point tracking (MPPT) algorithm is needed via the power electronics interface to ensure maximum power extraction. The proposed MPPT algorithm will modulate the Direct Current to Direct Current (DC-DC) power converter to extract the maximum power from the system and guarantee optimal usage of the resource (Karthikeyan et al., 2018). Most of the existing MPPT algorithms suffer from the drawback of being slow-tracked. Due to this, the utilization efficiency is reduced. The current methods vary in implementation complexity, sensed parameters, required number of sensors, convergence speed, and cost.

This research seeks to formulate a fully functional PEMFC based on mathematical modeling and synthesize a modified MPPT based on a predictive approach. A discretized mathematical model of the PEMFC is defined to express the future behavior of the system. This research also investigates the new predictive MPPT algorithm by using the MPC approach. The purpose of the newly designed MPPT is expected to exhibit fast convergence of the maximum power point (MPP) locus, outstanding accuracy, and robustness to environmental changes.

1.3 Research Overview

This research focuses on the MPPT of the PEMFC. Therefore, it is essential to study the PEMFC system so that the mathematical modeling of the PEMFC can be simulated. To design the new MPPT algorithm technique, power electronics such as a DC-DC converter are required. This research also involves the model predictive control to predict the future behavior of the PEMFC system. From the prediction, the model predictive control gives the best output and controls the power electronics. This predictive MPPT algorithm can lead the PEMFC to generate the highest electrical power.

1.3.1 Introduction to Proton Exchange Membrane Fuel Cell (PEMFC)

PEMFC is the most popular fuel cell type, which uses hydrogen gas as fuel. It converts hydrogen and oxygen from chemical energy into electrical energy. A PEMFC system is built up of many fuel cell stacks. Every single fuel cell stack level can be separated into eight layers (Daming, 2018).

Table 1.1: Components of Single Fuel Cell Stack

No	Components
1	Cathode cooling channel layer
2	Cathode gas supply channel layer
3	Cathode gas diffusion layer
4	Cathode catalyst layer
5	Proton exchange membrane layer
6	Anode catalyst layer
7	Anode gas diffusion layer
8	Anode gas supply channel layer

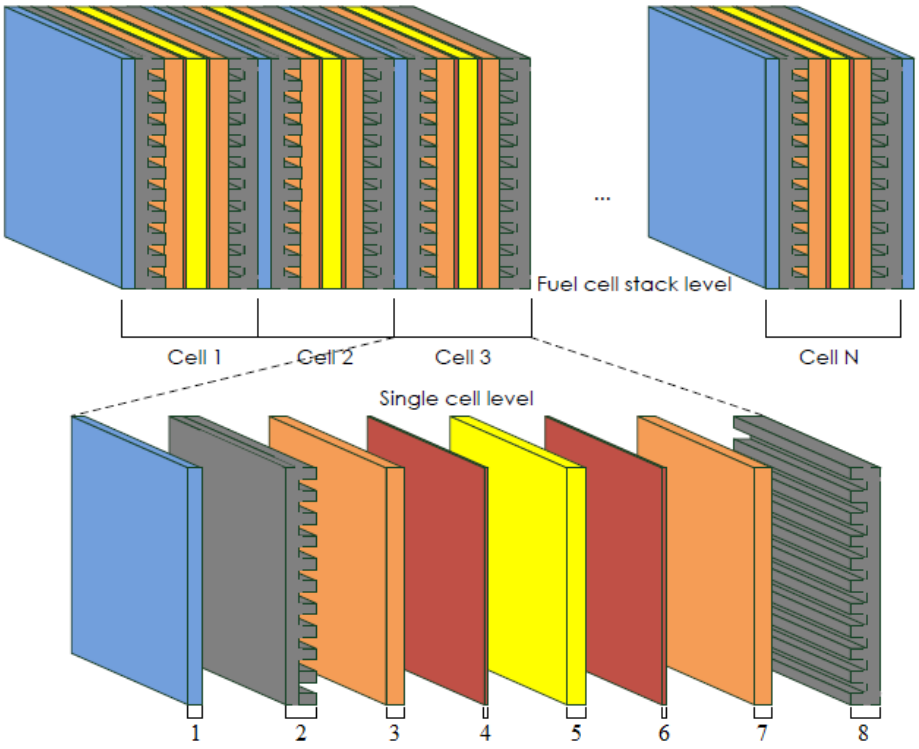


Figure 1.1: PEMFC and Single Cell Stack Level (Daming, 2018)

Since the potential difference of every single fuel cell is low, the fuel cell stacks are arranged in series to build up the voltage. The stacks of cathode-electrolyte-anode are generally known as a Membrane Electrode Assembly (MEA) (Andrew & David, 2018). Therefore, the output voltage of the PEMFC is highly dependent on the number of cells in the system.

There are positively charged electrodes called cathodes and negatively charged electrodes called anodes in each fuel cell stack. Hydrogen fuel is supplied to the anode gas supply channel layer, while oxygen is supplied to the cathode gas supply channel layers. The anode and cathode gas diffusion layers allow the hydrogen and oxygen to travel through the

porous layers, respectively. Then, the anode catalyst layers break the hydrogen into positively charged hydrogen ions and electrons. Proton Exchange Membrane (PEM) only allows the positively charged hydrogen ions to travel from the anode to the cathode. Hydrogen ions react with the oxidant at the cathode to form water. However, electrons can only travel through an external circuit to the cathode, which creates an electrical current. During the operation of PEMFC, electrical energy is generated (Afsharinejad et al., 2020). At the same time, water and waste heat are also produced. Therefore, unwanted water and waste heat must be removed continuously to prevent critical issues (Guo et al., 2022). Figure 1.2 shows the flow of reactants and the reactions inside the fuel cell.

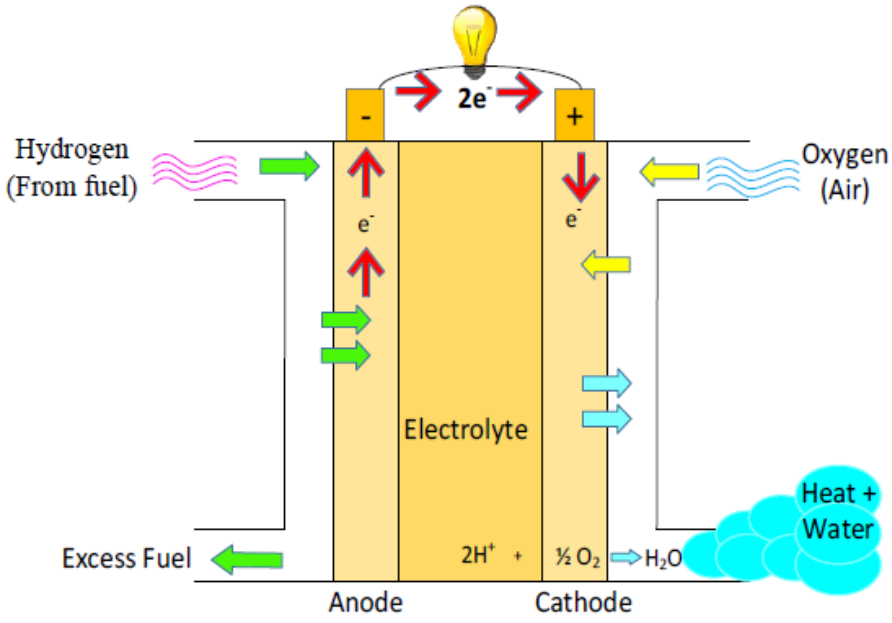


Figure 1.2: Single PEMFC Configuration (Samal et al., 2018)

1.3.2 MPPT of PEMFC

The typical output power and output voltage of a PEMFC can be expressed in the form of a non-linear function of fuel cell current or current density. From several empirical

studies, the power and voltage characteristics can be illustrated as a polarization curve consisting of three regions, namely activation, ohmic, and concentration region (Loo et al., 2011). As current is drawn from the PEMFC, the output voltage of the PEMFC changes throughout the three regions. Details of the polarization curve can be found in Figure 1.3.

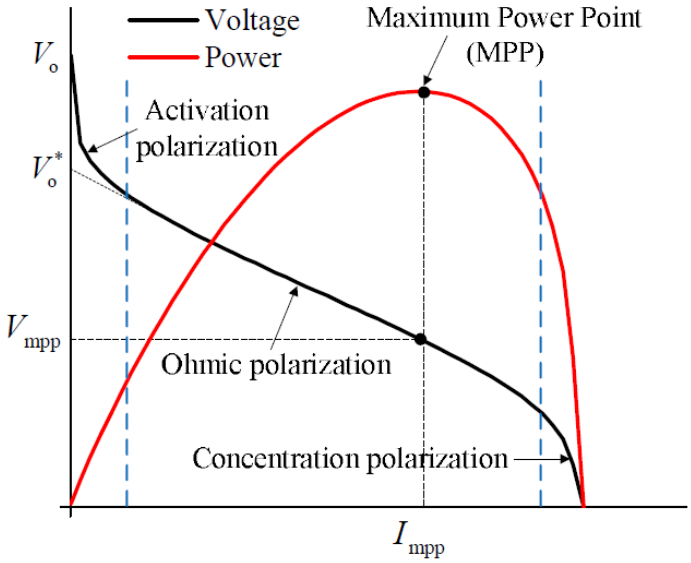


Figure 1.3: PEMFC Polarization Curve (Loo et al., 2011)

When a PEMFC is directly connected to an external load, the output voltage and output current are based on the load resistance due to Ohm's law. At the same time, the output voltage of the PEMFC also depends on the polarization curve, as shown in Figure 1.3. By fulfilling both conditions, the operation point of the system is the intersection point between the Voltage-Current (V-I) curve and the load line. Therefore, the output power of the PEMFC depends on both the internal electrochemical and the external load impedance (Soltani et al., 2013). The unique operation point known as the MPP is the point at which the system generates the maximum electrical power. Figure 1.4 shows some examples of the V-I curve, the Power-Current (P-I) curve of a PEMFC system, and the load line with different

resistance. For the fuel cell system in Figure 1.4, the power consumed by the load with resistance 0.1Ω is nearest to the MPP.

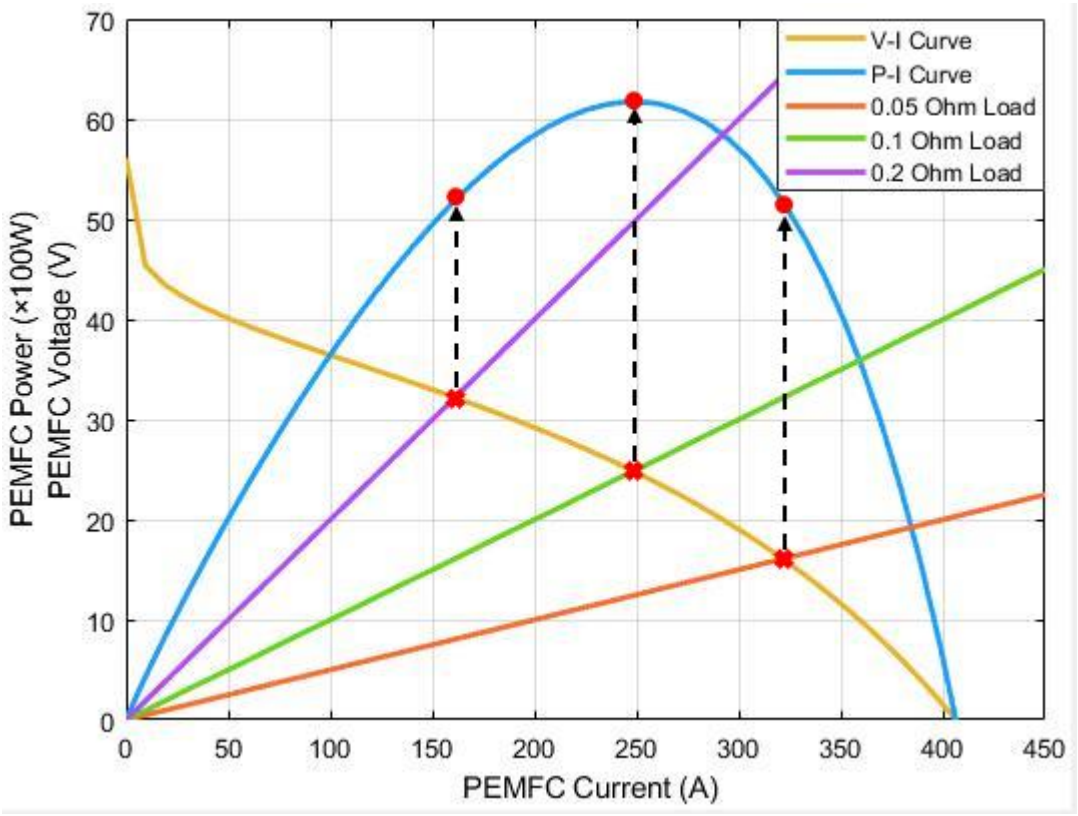


Figure 1.4: PEMFC Polarization Curve and Operation Point

The above figure illustrates the fact that the PEMFC system may not operate at MPP. Besides, some factors that appear may have an impact on the waveform of the polarization curve, such as changes in temperature, partial pressure of reactant gases, and membrane water content (Sarvi & Barati, 2010). Therefore, the MPP keeps changing at every instant depending on numerous physical and electrochemical parameters. Figure 1.5 illustrates a graphical description of the effect of temperature on the polarization curve. The indirect interpretation of this figure is that, as the temperature increases, the output voltage will increase dramatically, and the current density will marginally increase.

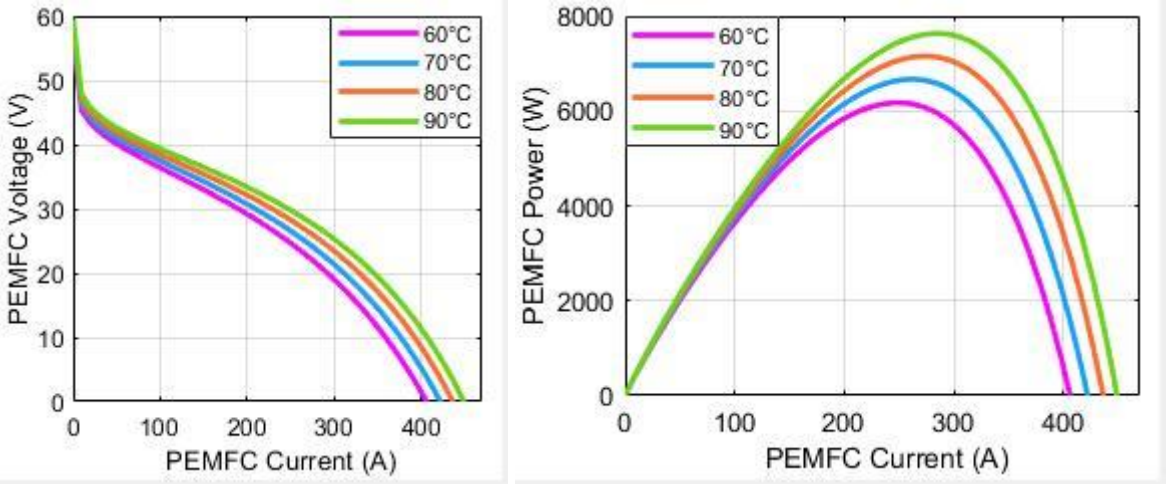


Figure 1.5: PEMFC Polarization Curve with Different Operation Temperatures

The MPPT technique is required to obtain the maximum output power from PEMFC. The MPPT control technique is an algorithm to track the maximum power point of an electrical generator. It is mainly applied to a photovoltaic (PV) system to extract the maximum capable power of the PV modules with respect to solar irradiance, temperature, or load resistance at a particular instant of time by an MPPT controller. Since there is an MPP in operating PEMFC, the MPPT technique should be applicable in the PEMFC system. There are many types of existing MPPT algorithms that are introduced in Chapter 2.

1.4 Problem Statement

There are various renewable energy sources available in Malaysia, such as solar, wind, tidal, biomass, and Hydrogen. Hydrogen is being used for fuel cell technology and can be considered the most reliable RE source. This is because hydrogen is an abundant element, comprising about 90% of all atoms, and has strong potential as an energy carrier to support decarbonization across multiple sectors (Hamedani et al., 2024). One of the current issues related to the fuel cell is the MPPT. MPPT is not widely used for fuel cells but remains an

important aspect while ensuring optimal fuel utilization and extracting maximum power (Samal et al., 2018). As the name indicates, MPPT tracks the maximum power from the power curve. The ability of FC systems to produce power is limited. Therefore, it is crucial to ensure the fuel cell is operating in the condition corresponding to the MPP (Naseri et al., 2018; Obaid et al., 2018; Rezk, 2016). By implementing the MPPT, the output power of the PEMFC can be increased to above 96% of its maximum power (Fan & Ma, 2022).

This algorithm tracks the point that corresponds to the maximum power on the power curve. The power curve can be obtained by computing the current and voltage characteristics of the fuel cell. However, the computation of this curve is not easy because it depends on many non-linear parameters that constantly change during the operation of the fuel cell. Therefore, the P-I curve is a dynamic curve with a moving MPP, which produces the maximum power. Any changes in the parameters might cause the MPP to shift from one point to another point at every sampling instant. Therefore, it is difficult to predict whether the fuel cell is working at the MPP at any instant by a modeling approach.

After tracking the MPP of the fuel cell, it requires a DC-DC power converter to maximize the output power. This process will generate electrical power with ripple. It reflects the power quality of the electrical power. If the power ripple is high, it can cause severe overheating, noise, energy losses, and system instability. Although this issue cannot be avoided, it can be minimized. Therefore, it is important to keep the power ripple as low as possible.

In addition, PEMFC is a Direct Current (DC) electrical power generator. The electrical power extracted from the PEMFC is not suitable for normal home electrical appliance. In most of the country, the standard electricity supply voltage is AC $110V/220V$

with frequency $50Hz/60Hz$. Therefore, the DC power must be inverted to standard AC power before it is supplied to any electrical appliances. A voltage source inverter is a component that converts the DC voltage to Alternative Current (AC) voltage with a particular root mean square (rms) voltage and frequency. For Direct current to Alternative Current (DC-AC) inverter, a voltage control technique becomes crucial because the control technique will directly affect the power quality (Ashraf et al., 2021). Fast dynamic response, strong disturbance rejection, offset-free tracking error, and low overall harmonic distortion should all be ensured for high-performance DC-AC inverter systems (Wang et al., 2019).

The predictive technique requires accurate mathematical modeling to predict the future behavior of the fuel cell's electrical parameters. With a Finite-Control-Set Model Predictive Control (FCS-MPC), the technique predicts the future voltage, current, and power of the PEMFC at the next sampling step. The advantage of MPC is that its control algorithm is based on the mathematical model, so it can predict and determine the next optimum alternative. Therefore, it can surpass the other advanced control methods if the mathematical model is accurate. This predictive MPPT technique is expected to ensure the output power at the MPP with fast tracking speed, high accuracy, and robustness to parameter changes. When the same technique is applied to the voltage control, the technique ensures the output voltage always approaches the standard AC voltage. With this technology, the output power of PEMFC can be directly supplied to the AC load.

1.5 Research Questions

To develop the MPPT for PEMFC, it is important to examine its performance by simulation. For a simulation, the mathematical model of PEMFC is crucial because it is the core of this research. Then, the performance of the designed MPPT technique can be

observed after it is implemented in the PEMFC. This paper investigates several questions related to this research.

i. How can the operational characteristics and behavior of the PEMFC be studied under various conditions?

ii. What MPPT techniques can be used to optimize the output power of PEMFC?

iii. What is the configuration for a PEMFC system to efficiently extract DC power and convert it into stable AC power?

iv. How does the proposed predictive MPPT and voltage control scheme perform under varying and robust operating conditions?

1.6 Objectives

This research aims to introduce a new MPPT technique that can predict the future behavior of the PEMFC electrical parameters. This MPPT technique is expected to obtain the maximum power of the PEMFC under robust conditions. The main objectives for this research are:

i. To compute a fully functional PEMFC based on a mathematical model for simulation

ii. To develop the predictive MPPT techniques for highly efficient power extraction from PEMFC

iii. To design the configuration of a PEMFC system to supply stable AC power with a predictive voltage control technique

iv. To examine the proposed control scheme under robust operating conditions

1.7 Hypothesis

To design a new MPPT technique on PEMFC, the research initially started with the pre-assumptions of:

i. The mathematical modeling is accurate and able to imitate the real operation of PEMFC

ii. The predictive MPPT control has an outstanding performance in tracking the MPP of the PEMFC

iii. The predictive voltage control is integrable with predictive MPPT control to invert the maximized DC power to AC power with a high power quality

iv. The predictive MPPT control is suitable for PEMFC and shows excellent results with fast environmental changes

1.8 Significance of Research

The research presented in this thesis makes significant contributions to the field of renewable energy. Firstly, the fully functional mathematical model of PEMFC is derived from the mathematical equation of the PEMFC. The mathematical model of PEMFC is computed in the simulation software, and it can imitate the behavior of the real PEMFC. For the simulation, the parameters inside the mathematical model can be adjusted to observe the PEMFC behavior. Therefore, the studies of any parameter changes that affect the output power of the PEMFC became easier.

Next, this research presents a new predictive MPPT technique that is specialized for PEMFC. The newly designed predictive MPPT technique should have fast convergence of the MPP locus, low output power fluctuation, and be robust to environmental factors. The proposed MPPT technique is applied to the PEMFC with simulation software. This may help to enhance the fuel cell technology by maximizing the output power of PEMFC.

Furthermore, a predictive voltage control technique is also introduced and applied to the PEMFC. As discussed in section 1.4, the purpose of implementing the predictive voltage control technique is to invert the DC electrical power into AC electrical power. The predictive voltage control technique should provide a high-quality AC voltage. This will enable the PEMFC to directly supply the electrical power to the AC electrical appliances.

1.9 Research Scope

This research introduces a new predictive MPPT and voltage control technique for the PEMFC system. The research is divided into two major parts. The first major part is to design the predictive MPPT technique for PEMFC. As discussed in section 1.3.2, the parameters of the PEMFC and the load will affect its power efficiency. Therefore, the factor that affects the PEMFC's output power is studied. For all conditions of PEMFC, the predictive MPPT technique should be able to maximize the output power. The second major part is to design the predictive voltage control system for PEMFC. The purpose of this development is to invert the DC power of PEMFC to AC power. This step is important to prove the availability of the electricity generated by the PEMFC. The proposed voltage control method should be able to provide a stable AC voltage with constant amplitude and frequency. Since a constant amplitude of AC voltage is supplied to the load, the load's power consumption is dependent on its total resistance. Therefore, a fuel control algorithm is

programmed to control the PEMFC output power. When the power electronics are integrated with the predictive algorithm, the PEMFC output power can be maximized, and it can be inverted to AC power.

In this research, the newly designed predictive MPPT technique is specialized for PEMFC. The simulation is carried out using MATLAB Software, including the PEMFC functional system, predictive MPPT algorithm, and power electronics. The other types of FC are not included. For PEMFC, the electrical output power is the main focal point of the research. It focuses on the maximum power point instead of maximum power efficiency. The original chemical power from the reactance will not be discussed. For AC voltage control technique, the voltage is set to be $12Vac$ for validation instead of $240Vac$.

1.10 Thesis Outline

This thesis consists of five chapters. Chapter 1 is the introduction to the research. This chapter provides an overview of the research problem and its significance. It begins with a background on renewable energy sources and the role of PEMFCs in sustainable energy solutions. It also highlights the importance of MPPT systems in optimizing the performance of PEMFCs. The objectives of the research are clearly stated, followed by a description of the scope and structure of the thesis.

Chapter 2 presents the literature review related to the research. This chapter reviews the existing knowledge related to fuel cells, MPPT, and model predictive control (MPC). It starts with an overview of the fuel cell types and the mathematical model of PEMFC operation. It then examines various MPPT techniques applied to the PEMFC, including traditional methods and recent advancements. Since this research is investigating the

predictive MPPT technique, the MPC for power electronics is also summarized. These literature reviews raise the foundation for the proposed new MPPT design.

Chapter 3 introduces the research methodology. It illustrates the research design and methodology employed to achieve the research objectives. It begins with an explanation of the theoretical framework of tracking the MPP with mathematical computation underpinning the new MPPT design. Then, the design of the predictive MPPT approach is also explained in detail. Furthermore, the method of inverting the PEMFC DC power to AC power by the predictive voltage control technique is illustrated. This chapter describes the modeling and simulation tools used for the proposed MPPT and voltage control system.

Chapter 4 presents the results and discussions of the research methods introduced in Chapter 3. This chapter presents the findings of the research and provides an in-depth discussion of the results. All the simulation results are displayed. The performance of the new MPPT system is compared with existing techniques, highlighting improvements in accuracy, response time, and robustness. Any phenomenon and findings are provided with possible explanations.

Chapter 5 is the last chapter of the thesis that expresses the conclusion of the research. It summarizes the key findings of the research and reflects on the achievement of the research objectives. It reiterates the significance of the newly designed MPPT and its potential impact on PEMFC and the field of renewable energy. This chapter also discusses the limitations of the study and provides recommendations for future research.

CHAPTER 2

LITERATURE REVIEW

2.1 Introduction

This chapter provides information on the literature reviews that were carried out by other researchers. It is divided into several parts: the PEMFC, MPPT algorithm, and MPC. This can help gain knowledge of the PEMFC system and the MPPT technique carried out by other researchers. All these literature reviews will be written in detail in the following subsections.

2.2 Fuel Cell

FC is an electrical generator that converts the chemical energy of hydrogen and oxygen into electrical energy through oxidation (Gupta et al., 2021; Huang et al., 2020; Jawad et al., 2022; Menesy et al., 2020; Sultan, Menesy, Kamel, Hasanien, et al., 2020; Yaqoob et al., 2021). The best fuel for FC is pure hydrogen (Sadeghi & Baniasad Askari, 2020). It works similarly to the chemical battery but stores the hydrogen as fuel in an external container (Huang et al., 2020). The advantages of fuel cell technologies include environmental friendliness, high energy efficiency, reliability, durability, stability, and fast start-up (Abbassi et al., 2023; Menesy et al., 2020; Singla et al., 2023; Sultan, Menesy, Kamel, Hasanien, et al., 2020; Sultan, Menesy, Kamel, Tostado-Veliz, et al., 2020). Nowadays, the fuel cell application can be found in stationary and portable implementations such as electrical plants, industrial, distributed residential power generation, transportation, and backup power supply (Jawad et al., 2022; Menesy et al., 2020; Singla et al., 2023; Yaqoob et al., 2021). At present, fuel cells have gained a lot of attention due to their advantages over other RE sources. Currently, fuel cells can be categorized into six major

types based on their electrolyte material, fuel diversity, and operating temperature (Kheirandish, 2016). These six major types of fuel cells are explained in the sub-section below.

2.2.1 Proton Exchange Membrane Fuel Cell (PEMFC)

PEMFC was discovered by Willard Thomas Grubb and Leonard Niedrach in the early 1960s (Grubb & Niedrach, 1960). PEMFC is a more suitable energy technology for application in the transportation sectors, such as hybrid electric vehicles or portable power supply (Chowdhury et al., 2016; Ghenai et al., 2019; Obaid et al., 2018, 2019). Currently, the PEMFC system has provided outstanding performance for mobile applications as it can operate at lower temperatures and lower pressure with higher power density compared to other types of fuel cells (Daming, 2018). Besides, PEMFC can also be used in residential, commercial, and industrial (Hassani et al., 2018; Hossain & Jamal, 2015; Justin, 2017; K. A. Reddy et al., 2015). PEMFC has the advantages of fast start-up, high power density and efficiency, low operational temperature, and long life (Jawad et al., 2022). The PEMFC system leads to a rapid commissioning ability within an operating temperature range between $25 - 100°C$ (Ebrahimi et al., 2021). The chemical equations of a PEMFC are:

Anode: $H_2(g) \rightarrow 2H^+(aq) + 2e^-$

Cathode: $O_2(g) + 4H^+(aq) + 4e^- \rightarrow 2H_2O(l)$

Overall: $2H_2(g) + O_2(g) \rightarrow 2H_2O(l)$

2.2.2 Alkaline Fuel Cell (AFC)

The alkaline fuel cell is one of the most developed fuel cell powers in NASA's Apollo space program (Austin, 1976). AFC was first demonstrated by Francis Thomas

Bacon in 1969 (Bacon, 1969). It is similar to PEMFC, but the electrolyte is generally a porous matrix saturated with an aqueous alkaline solution such as potassium hydroxide (Daming, 2018). It has a structure made up of a gas diffusion layer and a hydroxyl ion exchange membrane that divides the anode and cathode (Ahmad et al., 2020). AFC is simple to operate, capable of using more abundant, non-platinum catalysts, and less expensive when compared to PEMFC (Jawad et al., 2022). However, it has a lower current density, short lifetime, and intolerance to carbon dioxide, poisoning the electrolyte (Kheirandish, 2016). AFC operates with a temperature range of between 25°C and 250°C (Ebrahimi et al., 2021). Its chemical reactions at the anode and cathode can be expressed as:

Anode: $2H_2(g) + 4OH^-(aq) \rightarrow 2H_2O(l) + 4e^-$

Cathode: $O_2(g) + 2H_2O(l) + 4e^- \rightarrow 4OH^-(aq)$

Overall: $2H_2 + O_2 \rightarrow H_2O + Electrical\ Energy + Heat$

2.2.3 Direct Methanol Fuel Cell (DMFC)

During 1960s and 1970s, Shell Research Limited and Exxon - Alsthom pioneered the DMFC (Andrew & David, 2018). It was designed based on PEMFC, but Hydrogen is replaced by methanol as the fuel. It can be considered an ideal energy source powered by liquid fuel. It has the advantages of low environmental impact, facile charging, low operational temperature, and quick refueling (Yaqoob et al., 2021). Methanol is a relatively stable liquid that is easy to transport and store, but it is a poisonous and flammable material. Moreover, the methanol oxidation process has the drawback of high manufacturing cost, slow reactions at the electrode, and lower power efficiency than other types of fuel cells. So, it is typically used in portable applications where energy density takes precedence over

power efficiency (Daming, 2018). In addition, DMFC has a wider operational temperature, which is between 25°C and 100°C (Ebrahimi et al., 2021). A DMFC has the following chemical equations:

Anode: $2CH_3OH(l) + 2H_2O(l) \rightarrow 12H^+(aq) + 12e^- + 2CO_2(g)$

Cathode: $3O_2(g) + 12H^+(aq) + 12e^- \rightarrow 6H_2O(l)$

Overall: $2CH_3OH(l) + 3O_2(g) \rightarrow 4H_2O(l) + 2CO_2(g)$

2.2.4 Solid Oxide Fuel Cell (SOFC)

In 1899, the development of SOFC was credited to Walther Hermann Nernst as recognizing that Zirconia (ZrO_2) is a conductor of oxygen ions (Andrew & David, 2018). It is named SOFC because its electrolyte is made of solid oxide or ceramic to conduct the oxygen ions from the cathode to the anode (Daming, 2018). The oxygen receives electrons when it passes over the cathode and dissociates into oxygen ions (Zhi et al., 2021). Then, it transfers to the anode through the electrolyte and reacts with hydrogen. The reaction generates electrons, and then the electrons pass through an external circuit. The chemical energy is transformed into electrical energy. SOFC has high efficiency and good fuel flexibility, but it needs time to start up the operation. Also, it requires a high operating temperature that may pose a risk of cell damage. The operational temperature of SOFC is 600°C to 1000°C (Ebrahimi et al., 2021). When the operational temperature drops, the resistance of SOFC will be increase dramatically (Wei et al., 2022). For SOFC, the chemical equations are expressed as:

Anode: $2H_2(g) + 2O^{2-}(aq) \rightarrow 2H_2O(l) + 4e^-$

Cathode: $O_2(g) + 4e^- \rightarrow 2O^{2-}(aq)$

Overall: $O_2(g) + 2H_2(g) \rightarrow 2H_2O(l)$

2.2.5 Molten Carbonate Fuel Cell (MCFC)

In 1921, Emil Baur developed a molten carbonate fuel cell by using a mixture of molten salts as the electrolyte of the fuel cell (Kheirandish, 2016). It is composed of a matrix separator that stores the electrolyte, which separates a porous lithiated NiO cathode and a Ni-based alloy anode (Young et al., 2021). MCFC has good fuel flexibility, high power efficiency, and stability (Başarır et al., 2021), but it is complex to manage the corrosive molten electrolyte. Besides, the other disadvantage of MCFC is that it has a short lifetime due to degradation (Ryan et al., 2016). Also, it is slow to start up an operation because it requires pre-heat before starting the operation. The operation temperature of MCFC is relatively high, which is between 620°C and 660°C (Ebrahimi et al., 2021). The chemical equations of an MCFC are:

Anode: $2CO_2(g) + O_2(g) + 4e^- \rightarrow 2CO_3^{2-}(aq)$

Cathode: $2H_2(g) + 2CO_3^{2-}(aq) \rightarrow 2H_2O(l) + 2CO_2(g) + 4e^-$

Overall: $2H_2(g) + O_2(g) \rightarrow 2H_2O(l)$

2.2.6 Phosphoric Acid Fuel Cell (PAFC)

In 1961, G. V. Elmore and H. A. Tanner discovered a PAFC by using liquid phosphoric acid as an electrolyte of the fuel cell (Elmore & Tanner, 1961). PAFC can use the compressed liquid hydrogen that is directly produced in situ from methanol (Jawad et al., 2022). PAFC can be used in both mobile and stationary applications, but generally in

stationary applications due to its simple and stable structure (Daming, 2018). PAFC is a reliable, stable, and mature technology (Ryan et al., 2016). Its disadvantages are large size, corrosive electrolyte, expensive electrolyte, and low output power. Its operational temperature is slightly higher than PEMFC which is between 150°C and 220°C (Ebrahimi et al., 2021). This is because its specific platinum electrolytes can withstand a higher temperature so that it can consume the hydrogen directly from the reformer (Sadeghi & Baniasad Askari, 2020). A PAFC has the following chemical equations:

Anode: $2H_2(g) \rightarrow 4H^+(aq) + 4e^-$

Cathode: $O_2(g) + 4H^+(aq) + 4e^- \rightarrow 2H_2O(l)$

Overall: $2H_2(g) + O_2(g) \rightarrow 2H_2O(l)$

2.2.7 Comparison of Fuel Cell Types

Six major types of fuel cells are discussed in this subtopic. All these fuel cells have their advantages and disadvantages. Therefore, it is crucial to study the fuel cell types so that a proper type of fuel cell is chosen to be used. Table 2.1 shows the comparison of the six types of fuel cells.

As mentioned in the research scope in chapter 1.8, this research only concentrates on the PEMFC. So, only PEMFC is considered in this research. Furthermore, the MPPT algorithm designed is based on the mathematical modeling of PEMFC, but not other types of fuel cells. Therefore, the newly designed MPPT algorithm is only suitable for a PEMFC system.

Table 2.1: Comparison of the Fuel Cell Types

Citation	Fuel cell Types	Operational Temperature	Advantages	Disadvantages
(Ebrahimi et al., 2021; Jawad et al., 2022)	Proton Exchange Membrane Fuel cell (PEMFC)	25°C - 100°C	• Low operational temperature • Quick start • Easy electrolyte management • High efficiency	• High sensitivity to fuel pureness • Expensive
(Ahmad et al., 2020; Ebrahimi et al., 2021)	Alkaline Fuel Cell (AFC)	25°C - 250°C	• Simple to operate • Smaller size • Low weight • Low operational temperature	• Lower current density • Short lifetime
(Ebrahimi et al., 2021; Yaqoob et al., 2021)	Direct Methanol Fuel Cell (DMFC)	25°C - 100°C	• Stable fuel • Easy for transportation and storage • High energy storage	• Lower power efficiency • Poisonous and flammable fuel
(Ebrahimi et al., 2021; Wei et al., 2022)	Solid oxide fuel cell (SOFC)	600°C - 1000°C	• High efficiency • Fuel flexibility	• Slow start-up • High operational temperature

Table 2.1 continued

(Başarır et al., 2021; Ebrahimi et al., 2021)	Molten carbonate fuel cell (MCFC)	620°C - 660°C	• High efficiency • Fuel flexibility • Suitable for combining heat and power	• Slow start-up • Complex electrolyte management • High operational temperature
(Ebrahimi et al., 2021; Sadeghi & Baniasad Askari, 2020)	Phosphoric acid fuel cell (PAFC)	150°C - 220°C	• High reliability • Stable • Mature technology	• Large size • Corrosive electrolyte • Expensive electrolyte • Low output power

2.3 Mathematical Modeling of PEMFC System

This is a section of pivotal importance in the study of the mathematical model of PEMFC. To simulate a PEMFC system, its mathematical model is significant because it expresses the behavior of the PEMFC. In simulation, the computed PEMFC model may approach the behavior of the real PEMFC if the mathematical model is highly accurate. There exists a very extensive literature on the topic of the mathematical model of PEMFC. Basically, the mathematical model of PEMFC includes the Nernst equation, activation overvoltage, ohmic overvoltage, and concentration overvoltage.

2.3.1 Nernst Equation

The energy obtained from the fuel cell is the thermodynamic energy produced from the electrochemical reactions released from the enthalpy of formation, ΔH (Saeed & Warkozek, 2015). This energy can be divided into two thermal energies, which are represented by Gibbs free energy, ΔG and specific entropy, ΔS. Gibbs free energy is affected by changes in partial pressures of the reactance in a specific volume inside the fuel cell. The equation of this relation can be represented by Equation 2.1 (Amphlett et al., 1995; Derbeli et al., 2018).

$$\Delta G = \Delta G^{\circ} - RT\left(\ln P_{H_2} + \frac{1}{2}\ln P_{O_2}\right) \qquad \text{Equation 2.1}$$

where $\Delta G^{\circ} = -237.17\ kJ\ mol^{-1}$ is the Gibbs free energy in the standard condition (Saeed & Warkozek, 2015), $R = 8.3143\ J\ (mol\ K)^{-1}$ is the gas constant, T is the operational temperature, P_{H_2} and P_{O_2} are the partial pressure of hydrogen and oxygen, respectively. The potential given by the fuel cell with the effect of changing temperature is defined as Equation 2.2 (Saeed & Warkozek, 2015).

$$\Delta E = \frac{\Delta S}{nF}\left(T - T_{ref}\right) \quad \text{Equation 2.2}$$

where $\Delta S = -164\, J\, mol^{-1}\, K^{-1}$ is the specific entropy, n is the number of electrons released from the anode electrode in the reaction, $F = 96485C$ is the Faraday constant, and $T_{ref} = 298.15°K$ is the standard temperature. For each fuel cell chemical reaction, there are two electrons released from the hydrogen gas, so n is equal to 2. Therefore, the electric potential of the cell, also known as the Nernst equation, is given by Equation 2.3 (Y. Li et al., 2021; Saeed & Warkozek, 2015).

$$E_{Nernst} = -\frac{\Delta G^{\circ}}{nF} + \frac{\Delta S}{nF}\left(T - T_{ref}\right) + \frac{RT}{nF}\ln P_{H_2} P_{O_2}^{0.5} \quad \text{Equation 2.3}$$

By substituting all the constants into Equation 2.3, the Nernst equation can be simplified as Equation 2.4.

$$E_{Nernst} = 1.229 - 8.5 \times 10^{-4}(T - 298.15) + 4.308 \times 10^{-5} T \ln P_{H_2} P_{O_2}^{0.5} \quad \text{Equation 2.4}$$

For the dynamic gas transportation model, the hydrogen and oxygen partial pressure, P_{H_2} and P_{O_2} can be rewritten in the time domain as shown in Equation 2.5 and Equation 2.6, respectively (Ahmadi et al., 2017; Fathy, Rezk, et al., 2021; Rana et al., 2019; Rezk & Fathy, 2020).

$$P_{H_2}(t) = \frac{1}{k_{H_2}}\left[q_{H_2}^{in} - 2k_r I_{FC}\left(1 - e^{\left(-\frac{t}{\tau_{H_2}}\right)}\right)\right] \quad \text{Equation 2.5}$$

$$P_{O_2}(t) = \frac{1}{k_{O_2}}\left[q_{O_2}^{in} - k_r I_{FC}\left(1 - e^{\left(-\frac{t}{\tau_{O_2}}\right)}\right)\right] \quad \text{Equation 2.6}$$

where t is the time domain, k_{H_2} and k_{O_2} are the hydrogen and oxygen valve molar constant, respectively, $k_r = {}^{N}/_{4F}$ is the modeling constant, τ_{H_2} and τ_{O_2} are the hydrogen and oxygen

time constants, respectively, q_{H_2} and q_{O_2} are the molar flow of hydrogen and oxygen, respectively.

This Nernst equation is the reversible thermodynamic potential, and it also represents the open-circuit voltage of the fuel cell. However, the fuel cell will lose voltage due to the rate of reactions on the electrodes, the resistance of proton flow in an electrolyte, and the reduction in the concentration of gases. So, the output voltage of a single cell can be defined as Equation 2.7 (Abdel-Basset et al., 2021; Fathy, Rezk, et al., 2021; C. Li & Hu, 2020; Y. Li et al., 2021; Rana et al., 2019; Ren et al., 2020; Rezk & Fathy, 2020).

$$V_{cell} = E_{nerst} - V_{act} - V_{ohm} - V_{conc} \qquad \text{Equation 2.7}$$

where V_{cell} is the output voltage of a single cell, V_{act} is the voltage loss due to the rate of reactions on the electrodes, V_{ohm} is the voltage drop from the resistance of proton flow in an electrolyte, V_{con} is the voltage loss from the reduction in concentration of gases.

2.3.2 Activation Overvoltage

The voltage loss at the rate of reactions on the electrodes is considered the ignition spark at the beginning of the reaction (Saeed & Warkozek, 2015). It is known as activation overvoltage that is described by the Tafel equation as shown in Equation 2.8 (Abdel-Basset et al., 2021; Ahmadi et al., 2017; Fathy, Rezk, et al., 2021; C. Li & Hu, 2020; Rana et al., 2019; Rezk & Fathy, 2020; Zhong et al., 2008).

$$V_{act} = \xi_1 + \xi_2 T + \xi_3 T \ln C_{O_2} + \xi_4 T \ln I_{FC} \qquad \text{Equation 2.8}$$

where ξ_1, ξ_2, ξ_3 and ξ_4 are parametric coefficients of the fuel cell model, I_{FC} is the fuel cell output current and C_{O_2} is the concentration of dissolved oxygen on the catalytic interface with Equation 2.9.

$$C_{O_2} = \frac{P_{O_2}}{(5.08 \times 10^6) e^{\frac{-498}{T}}} \quad \text{Equation 2.9}$$

2.3.3 Ohmic Overvoltage

The voltage loss due to the resistance of proton flow in the electrolyte is known as ohmic overvoltage, representing the voltage drop due to the resistance of the polymer membrane during the proton and electron transfer. The equation is similar to Ohm's law equation, defined as Equation 2.10 (Ahmadi et al., 2017; Fathy, Rezk, et al., 2021; Rana et al., 2019; Ren et al., 2020; Rezk & Fathy, 2020).

$$V_{ohm} = I_{FC} R_m \quad \text{Equation 2.10}$$

where the resistance of the electrode R_m can be expressed as Equation 2.11.

$$R_m = \frac{r_m t_m}{A} \quad \text{Equation 2.11}$$

From the equation, t_m is the length of the electrolyte that the proton flows, A is the area of the electrolyte through which the proton can flow, and r_m is the resistivity of the electrolyte, which can be expressed as Equation 2.12 (Mann et al., 2000; Springer et al., 1991).

$$r_m = 181.6 \times \frac{1 + 0.03\left(\frac{I_{FC}}{A}\right) + 0.062\left(\frac{T}{303}\right)^2 \left(\frac{I_{FC}}{A}\right)^{2.5}}{\left[\lambda_m - 0.634 - 3\left(\frac{I_{FC}}{A}\right)\right] e^{4.18\left(\frac{T-303}{T}\right)}} \quad \text{Equation 2.12}$$

where λ_m is the membrane water content that varies between 0 and 14. This value represents the relative humidity between 0% and 100%. Under ideal conditions, this parameter may have a value range between 14 and 20 (Ahmadi et al., 2017; Jiao & Cui, 2013; Rana et al.,

2019). The maximum possible value of λ_m can be as high as 23 under supersaturated condition (Ahmadi et al., 2017; Rana et al., 2019; Soltani et al., 2013).

2.3.4 Concentration Overvoltage

The voltage loss from the reduction in concentration of gases is known as concentration overvoltage. This voltage drop is due to the concentration gradient of reactants consumed in the reaction. This equation is expressed as Equation 2.13 (Ahmadi et al., 2017; Fathy, Rezk, et al., 2021; Rana et al., 2019; Rezk & Fathy, 2020; Zhong et al., 2008).

$$V_{con} = -\frac{RT}{nF}\ln\left(1 - \frac{I_{FC}}{i_L A}\right) \quad \text{Equation 2.13}$$

where i_L is the limiting current density of the fuel cell.

2.3.5 PEMFC Output Power

The output voltage of the fuel cell can be obtained by merging all the equations above. However, the voltage of one cell is very small. Therefore, a few cells must be connected in a bipolar plate to increase the output voltage. So, the output voltage of PEMFC is proportional to its number of cells, N, which is given by Equation 2.14 (Abdel-Basset et al., 2021; Ahmadi et al., 2017; Fathy, Rezk, et al., 2021; C. Li & Hu, 2020; Rana et al., 2019; Rezk & Fathy, 2020).

$$V_{FC} = NV_{cell} \quad \text{Equation 2.14}$$

Lastly, the output power of PEMFC is defined as Equation 2.15.

$$P_{FC} = V_{FC} I_{FC} \quad \text{Equation 2.15}$$

These mathematical equations are important because they represent the behavior of the PEMFC. Therefore, it is very crucial for designing the PEMFC system model.

2.4 Maximum Power Point Tracking (MPPT)

MPPT is a very important technique to track the maximum power point of the electrical generator. The MPPT algorithm has been widely applied to PV systems to obtain the maximum output power from a PV array. A similar technique can also be used for the fuel cell to determine the MPP since both systems have identical power curve characteristics. MPPT tracks the MPP for maximizing the output power. The electrical generator without the MPPT technique may not generate the electrical power at maximum, and it causes energy loss. There are various techniques for MPPT in the literature. This section introduces the existing MPPT techniques presented by other researchers.

2.4.1 Sliding Mode Control (SMC)

Sliding Mode Control (SMC) based MPPT with a DC-DC boost converter for a fuel cell power system was introduced (Abdi et al., 2012; Jiao & Cui, 2013). In general, sliding mode design consists of the design of the sliding surface and the selection of an appropriate control law. To track the MPP, the sliding surface is derived as the fuel cell electrical power derivative with respect to current. It ensures the system state reaches the surface and consistently produces maximum power generation. The sliding surface equation is expressed as Equation 2.16.

$$\sigma = \frac{dP_{FC}}{dI_{FC}} = \frac{d(V_{FC}I_{FC})}{dI_{FC}} = V_{FC} + \frac{dV_{FC}}{dI_{FC}} \qquad \text{Equation 2.16}$$

The duty cycle output control can be defined as Equation 2.17 based on the observation of duty cycle versus operation region as illustrated in Figure 2.1.

$$D(k) = \begin{cases} D + \Delta D \; for \; \sigma > 0 \\ D + \Delta D \; for \; \sigma < 0 \end{cases} \qquad \text{Equation 2.17}$$

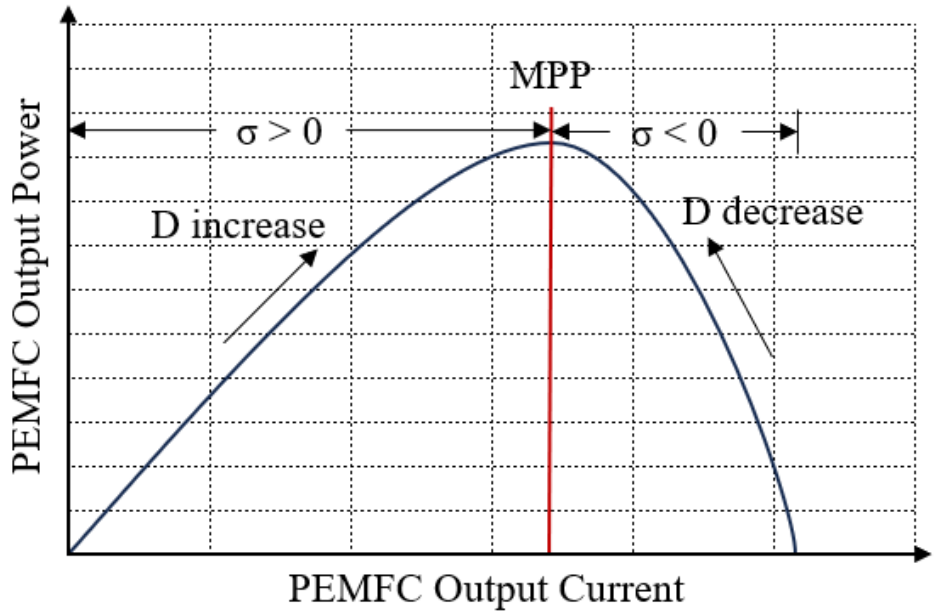


Figure 2.1: Duty Cycle Versus Operation Region (Abdi et al., 2012)

The sliding function regulates the duty cycle output control. The results showed the SMC approach can keep 99% of the maximum output power within $200ms$. In addition, it was robust to a variety of external conditions. Although this MPPT method has the advantages of fast-tracking speed and high stability, it has 30% of power ripple.

2.4.2 Twisting Algorithm-based High-Order SMC (HOSM-TA)

The SMC method with a robust high-order SMC (HOSM-TA) was developed based on the "Twisting Algorithm (Derbeli et al., 2020). Because of its high ability to combat the chattering phenomenon and switching control signals, it is an excellent solution for coping with the disadvantages of traditional SMC. For first-order sliding mode, the derivative of the sliding surface, $\dot{s}$ for a conventional DC-DC boost converter is defined as Equation 2.18.

$$\dot{s} = \frac{1}{L}(v - x_2) + \lambda e + \frac{x_2}{L}u \qquad \text{Equation 2.18}$$

where L is the inductance of the DC-DC boost converter, v is the fuel cell stack voltage, x_2 is the output voltage, λ is a positive constant, e is the control error, and u is the duty cycle.

For second-order sliding mode, a second derivative of the sliding surface by differentiating Equation 2.18 is expressed as Equation 2.19.

$$\ddot{s} = \frac{1}{L}[(u-1)\dot{x_2} + \dot{v} + \lambda(u-1)x_2 + \lambda v] + \frac{x_2}{L}\dot{u} \quad \text{Equation 2.19}$$

To ensure the tracking error converges to zero, the twisting algorithm is involved in the dynamic control law, $\dot{u}_{sw}$ with the Equation 2.20.

$$\dot{u}_{sw} = \frac{k_1 L}{x_2}\left(s + \beta sign(\dot{s})\right) \quad \text{Equation 2.20}$$

where β and k_1 are positive constants. Equation 2.19 can be simplified by substitution, as shown in Equation 2.21 and Equation 2.22.

$$\varphi = \frac{1}{L}[(u-1)\dot{x_2} + \dot{v} + \lambda(u-1)x_2 + \lambda v] \quad \text{Equation 2.21}$$

$$\gamma = \frac{x_2}{L} \quad \text{Equation 2.22}$$

Then, the equivalent control, $\dot{u}_{eq}$ can be defined as Equation 2.23.

$$\dot{u}_{eq} = \frac{\varphi}{\gamma} = \frac{1}{x_2}[(u-1)\dot{x_2} + \dot{v} + \lambda(u-1)x_2 + \lambda v] \quad \text{Equation 2.23}$$

The overall control law is expressed as Equation 2.24.

$$\dot{u} = \dot{u}_{sw} + \dot{u}_{eq} \quad \text{Equation 2.24}$$

To ensure the first-order and second-order sliding mode functions are converging to the MPP, the cost functions must converge to zero. Therefore, the derivative of the cost

function must be a semi-negative defined equation. Equation 2.25 proves that the derivative of the first-order sliding mode cost function, $\dot{V}_1$ is semi-negative defined,

$$\dot{V}_1 = s\left(\frac{1}{L}(v - x_2) + \lambda e + \frac{x_2}{L}\left(-\frac{\alpha L}{x_2} sign(s) - \frac{1}{x_2}(v + \lambda L e - x_2)\right)\right), \quad \text{Equation 2.25}$$

$$\dot{V}_1 = -s\alpha sign(s) = -\alpha|s|$$

where $sign()$ is a usual sign function. Then, the second-order sliding mode cost function is shown in Equation 2.26.

$$\dot{V}_2 = \dot{s}\left(k_1 s + \frac{1}{L}[(u-1)\dot{x_2} + \dot{v} + \lambda(u-1)x_2 + \lambda v]\right), \quad \text{Equation 2.26}$$

$$\dot{V}_2 = -\dot{s}k_1\beta sign(\dot{s}) = -|\dot{s}|k_1\beta$$

Since both the cost functions are always less than zero, their stability is ensured based on Lyapunov theory. Besides, the tracking point of sliding mode control will converge to the MPP because the tracking error of the sliding function tends to zero.

This HOSM-TA was designed to improve the power quality with a power ripple below 7% and to keep the fuel cell operating at an adequate power level. An experiment was done to compare the conventional SMC and HOSM-TA methods. From the results, the HOSM-TA method could control the PEMFC to generate electrical power with a lower power ripple.

2.4.3 Backstepping Algorithm

The MPPT for PEMFC using a backstepping algorithm based on current reference estimation was designed (Derbeli et al., 2018, 2019). The current that corresponds to the MPP represents the reference current. For the fuel cell's different operating temperatures and

pressures, the reference current can be obtained using the MPP curve. Then, the current reference estimation (CRE) curve can be constructed using the fitting function.

$$I_{mpp} = f(P) = a_1P^4 + a_2P^3 + a_3P^2 + a_4P + a_5 \qquad \text{Equation 2.27}$$

where $a_1 = -5041 \times 10^{-10}$, $a_2 = 1191 \times 10^{-7}$, $a_3 = -103 \times 10^{-4}$, $a_4 = 3943 \times 10^{-4}$, $a_5 = 8$. Figure 2.2 shows the PEMFC P-I curve for different operating temperatures and pressures. The MPP curve as the current reference estimation curve is also presented.

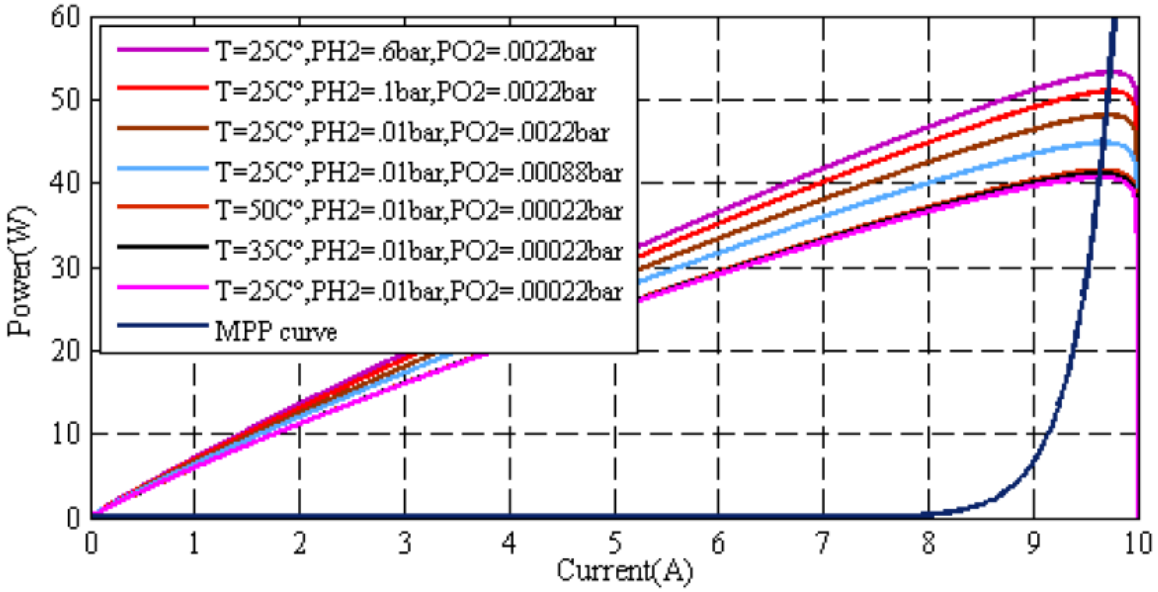


Figure 2.2: MPP Curve and P-I Curve for Different PEMFC Parameters (Derbeli et al., 2018)

From Figure 2.2, the MPP curve passes through the MPP of all P-I curves for different PEMFC parameters. Then, a Proportional-Integral (PI) controller is used to maintain the fuel cell output current at the MPP. The purpose of using a PI controller is to compare the desired output with the actual output, which is given by Equation 2.28.

$$s = K_p e(t) + K_i \int e(t)\, dt$$ Equation 2.28

The backstepping reduces the error between the output and the reference value. First, the current error is calculated by using the formula shown in Equation 2.29 and Equation 2.30.

$$e_1 = x_1 - I_{mpp}$$ Equation 2.29

$$\dot{e}_1 = -(1 - u_1)\frac{x_2}{L} + V_{Stack} - \dot{I}_{ref}$$ Equation 2.30

where $^{x_2}/_{L}$ is the virtual variable. Then, the Lyapunov function of V_1 is given as Equation 2.31 and Equation 2.32.

$$V_1 = \frac{1}{2} e_1^2$$ Equation 2.31

$$\dot{V}_1 = e_1 \dot{e}_1 = e_1 \left[-(1 - u_1)\frac{x_2}{L} + \frac{V_{Stack}}{L} - \dot{I}_{ref} \right]$$ Equation 2.32

From Equation 2.32, the $e_1 = 0$ is feasible when the virtual variable $^{x_2}/_{L} = \gamma_1$, where the equation is defined as Equation 2.33.

$$\gamma_1 = \frac{1}{1 - u_1}\left(b_1 e_1 + \frac{V_{Stack}}{L} - \dot{I}_{ref} \right)$$ Equation 2.33

where b_1 is a positive constant value. To eliminate the e_1, another error is defined with Equation 2.34.

$$e_2 = \frac{x_2}{L} - \gamma_1$$ Equation 2.34

Since the γ_1 and e_2 is defined, Equation 2.30 can be simplified as Equation 2.35.

$$\dot{e}_1 = -b_1 e_1 - (1 - u_1) e_2 \quad \text{Equation 2.35}$$

Lastly, the Lyapunov function of V_1 is expressed as Equation 2.36.

$$\dot{V}_1 = -b_1 e_1^2 - (1 - u_1) e_1 e_2 \quad \text{Equation 2.36}$$

To minimize the errors, the dynamics of e_2 is determined as Equation 2.37.

$$\dot{e}_2 = -\frac{\dot{u}_1 \gamma_1}{1 - u_1} + \Psi \quad \text{Equation 2.37}$$

$$\Psi = \frac{1}{1 - u_1}\left[b_1^2 e_1 + (1 - u_1) b_1 e_1^2 - \frac{\dot{V}_{Stack}}{L} + \dot{I}_{ref}\right] + \frac{1}{L}\left(\frac{1 - u_1}{C} x_1 - \frac{x_2}{RC}\right) \quad \text{Equation 2.38}$$

Then, a Lyapunov function candidate is applied to stabilize the control law, u_1 with Equation 2.39 and Equation 2.40.

$$V = V_1 + \frac{1}{2} e_2^2 = \frac{1}{2} e_1^2 + \frac{1}{2} e_2^2 \quad \text{Equation 2.39}$$

$$\dot{V} = \dot{V}_1 + e_2 \dot{e}_2 = -b_1 e_1^2 + e_2 [\dot{e}_2 - (1 - u_1) e_1] \quad \text{Equation 2.40}$$

The errors can be regulated to zero when the time derivative of the e_2 is set with Equation 2.41.

$$\dot{e}_2 = -b_2 e_2 + (1 - u_1) e_1 \quad \text{Equation 2.41}$$

where b_2 is another positive constant value. The final equation can be defined by solving Equation 2.37 and Equation 2.41.

$$\dot{u}_1 = \frac{1 - u_1}{\gamma_1} [b_2 e_2 - (1 - u_1) e_1 + \Psi] \quad \text{Equation 2.42}$$

This MPPT method showed satisfactory maximum power point tracking with settling time within $700ms$ and robustness toward external factor variations in the results.

2.4.4 Perturb and Observe (P&O)

Perturb and Observe (P&O) method is one of the most common MPPT techniques that has been used to track the MPP of the electrical generator. The P&O approach was applied to optimize PEMFC output power (Barhoumi et al., 2020; Naseri et al., 2018). This MPPT algorithm compares the rate of change of power and current at each instant according to the step perturbation chosen to generate a maximum power output. Therefore, the MPPT controller needs to measure the instantaneous reading of the fuel cell voltage and current. This MPPT technique controls the boost converter by regulating the duty cycle and keeping the fuel cell's power at maximum. Although this method has low complexity, it can track the MPP with accuracy as high as 98% within $500ms$. However, it has a high-power ripple recorded, which is around 10%. A diagram showing the steps in the process is shown in Figure 2.3.

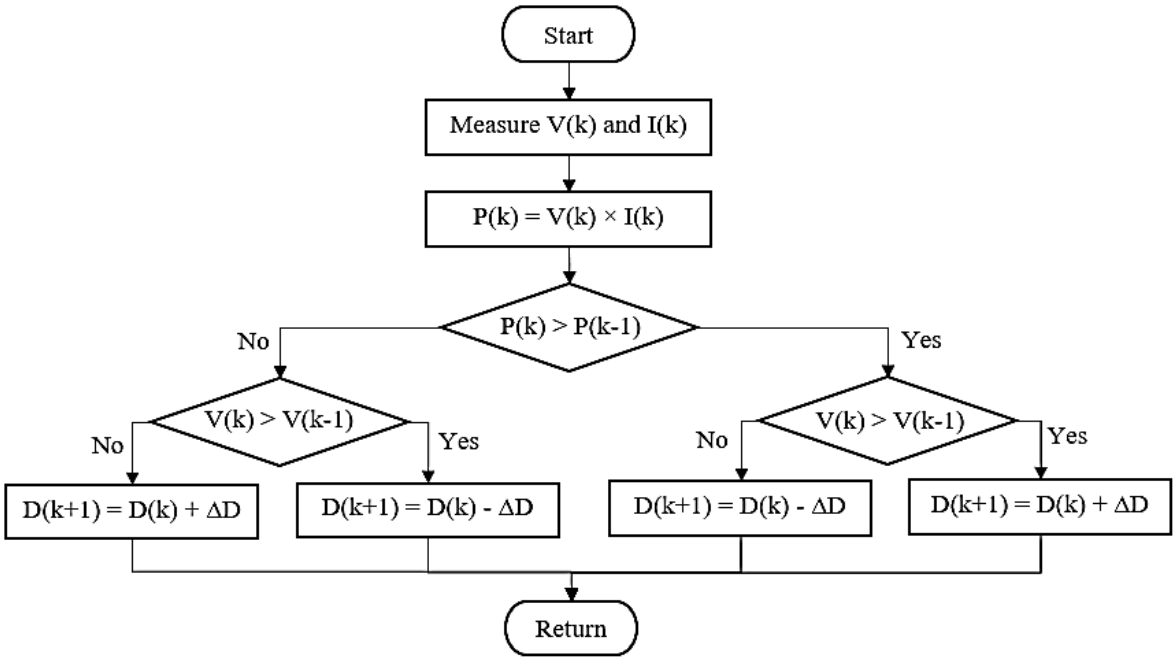


Figure 2.3: Flowchart for P&O-based MPPT Method (Barhoumi et al., 2020)

The P&O method has recently been modified to function as a higher-performance MPPT approach (Celikel et al., 2025). Rather than applying a constant duty cycle change, the method was improved by implementing variable duty cycle adjustments. It enhances the traditional P&O method by improving its MPP tracking speed, accuracy, and stability. For the enhanced P&O method, it can track the MPP within $80ms$ and the accuracy as high as 99.8%.

2.4.5 Increment Conductance Method (IC)

The Incremental Conductance (IC), also known as the increment resistance method, was used for MPPT to enhance output power (Karami et al., 2014). First, this IC method differentiates the fuel cell power with respect to the current. Then, maximum power is located at the point where the differentiation result is zero. To find the maximum power point, the MPPT controller must read the voltage and current. Then, the calculation of Equation 2.44 is performed.

$$\frac{dP_{FC}}{dI_{FC}} = \frac{d(V_{FC} \times I_{FC})}{dI_{FC}} = V_{FC} + I_{FC}\frac{dV_{FC}}{dI_{FC}} = 0 \qquad \text{Equation 2.43}$$

$$\frac{V_{FC}}{I_{FC}} = -\frac{dV_{FC}}{dI_{FC}} \qquad \text{Equation 2.44}$$

Then, the reference current is defined as the controller output used for the Pulse Width Modulation (PWM) control of the DC-DC converter connected to FC. Figure 2.4 shows the flowchart for the IC method for a synchronous DC-DC buck converter.

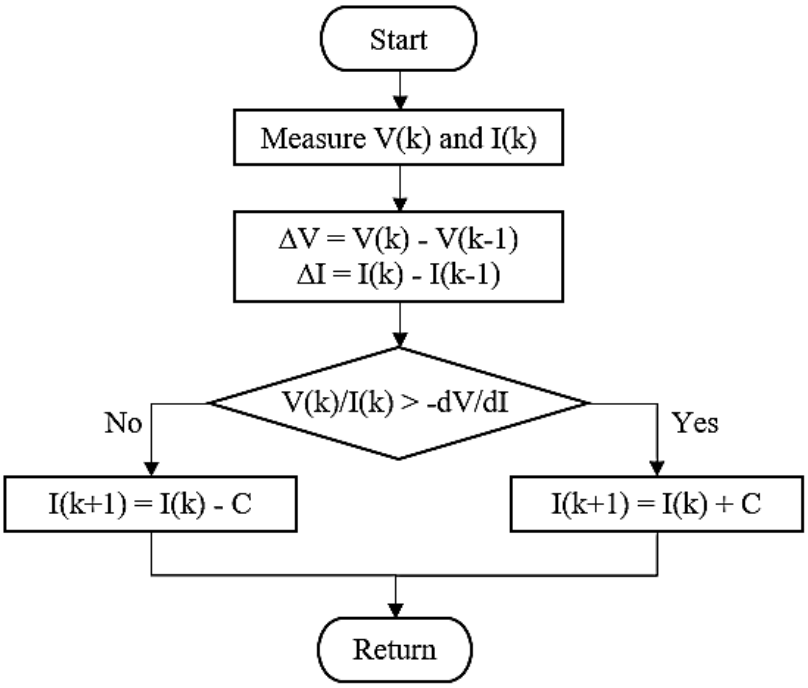


Figure 2.4: Flowchart for IC-based MPPT Method (Karami et al., 2014)

The performance of the IC method was compared with other MPPT techniques such as Perturb and Observe (P&O), SMC, and Particle Swarm Optimizer (PSO) methods (Ahmadi et al., 2017; Karami et al., 2014). From the comparison result, both the MPPT efficiencies of P&O and IC MPPT algorithms were almost the same, as they had similar accuracy around 98.5%. However, IC took less time and was more stable than the P&O method when there were external variations of factors. The IC method was enhanced with a variable step size (VSS) for output current determination (Rezk & Fathy, 2020). The performance surpassed all the other compared MPPT methods, with the highest output power, with 99.8% of accuracy reported.

2.4.6 Radial Basic Function Network (RBFN)

A Neural Network MPPT controller with a Radial Basic Function Network (RBFN) algorithm was proposed for the fuel cell system (K. J. Reddy & Sudhakar, 2017; Srinivasan

et al., 2021). A three-phase high voltage gain interleaved boost converter (IBC) was used to extract the electrical power from the fuel cell and power up an electrical vehicle application. The RBFN model is a feedforward neural network model with supervised and unsupervised learning phases. RBFN consists of three layers, which are the input layer, hidden layer, and output layer. The steps described below are depicted in Figure 2.5.

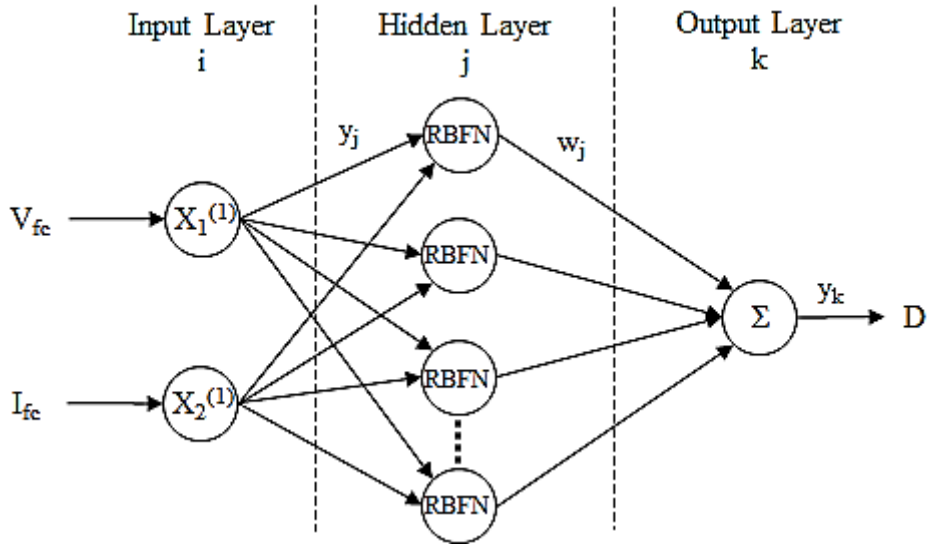


Figure 2.5: RBFN Structure (K. J. Reddy & Sudhakar, 2017)

The net input and output are expressed in Equation 2.45 and Equation 2.46, respectively.

$$x_i^{(1)}(n) = net_i^{(1)} \qquad \text{Equation 2.45}$$

$$y_i^{(1)}(n) = f_i^{(1)}\left[net_i^{(1)}(n)\right] = net_i^{(1)}(n), \quad i = 1,2 \qquad \text{Equation 2.46}$$

where $x_i^{(1)}$ is the input layer, $net_i^{(1)}$ is the sum of the input layer and $y_i^{(1)}$ is the hidden layer. For the hidden layer, the Gaussian function is expressed as Equation 2.47.

$$y_j^{(2)}(n) = f_j^{(2)}\left[net_j^{(2)}(n)\right] e^{net_j^{(2)}(n)}, \quad j = 1,2,\ldots \qquad \text{Equation 2.47}$$

The output layer includes a single node k with Equation 2.48.

$$y_k^{(3)} = f_k^{(3)}\left[net_k^{(3)}(n)\right] = net_k^{(3)}(n) \qquad \text{Equation 2.48}$$

For the fuel cell system, the voltage and current of the fuel cell are the inputs of the RBFN controller, the hidden layer is a non-linear radial basis activation function, and the duty cycle of the boost converter is the output. The performance of MPPT was compared when applied with conventional, quadratic, and reconfigured quadratic DC-DC boost converters (Srinivasan et al., 2021). This RBFN-based MPPT was compared with P&O and Fuzzy Logic Control (FLC) methods. The results showed that the RBFN-based MPPT controller could track the MPP of the fuel cell faster than the P&O and FLC methods. It has extremely quick tracking speed, which is around $20ms$ but its accuracy is not satisfied as 92% of maximum power was recorded. The reconfigured quadratic DC-DC boost converter excellently performed on DC power dissipation.

2.4.7 Fuzzy Logic Control (FLC)

Mamdani Fuzzy Logic Control (FLC) was implemented for the fuel cell stack (Luta & Raji, 2019b, 2019a). For Mamdani FLC, the "centre of gravity" defuzzification is used to determine the crisp output, y^{crisp} of the fuzzy system with Equation 2.49.

$$y^{crisp} = \frac{\sum_{i=1}^{R} q_i \int u^{Q^i}}{\sum_{i=1}^{R} \int u^{Q^i}} \qquad \text{Equation 2.49}$$

where Q^i is the consequent fuzzy set of rules i, characterized by membership u^{Q^i} and by defining the centre of areas of u^{Q^i} to be the point q_i in the universe. There are two inputs required for MPPT FLC, named error, e, and change in error Δe.

$$e(k) = \frac{P(k) - P(k-1)}{V(k) - V(k-1)} \qquad \text{Equation 2.50}$$

$$\Delta e = e(k) - e(k-1) \qquad \text{Equation 2.51}$$

Each input comprises five triangle membership functions with a normalized universe of discourse ranging from -2 to 2. The inputs include five variables named negative big (NB), negative small (NS), zero (Z), positive small (PS), and positive big (PB). For the Mamdani Inference System, the output has the universe of discourse ranging from 0 to 1. Figure 2.6 illustrates the input and output Membership Function (MF) of the Mamdani Inference System.

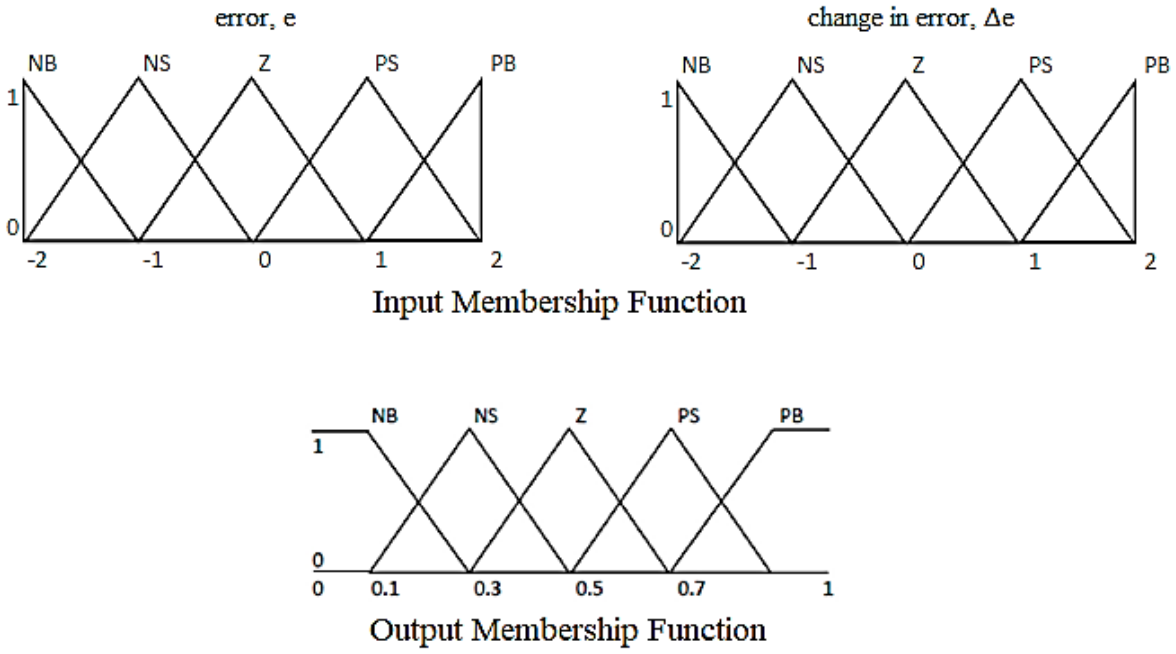


Figure 2.6: Input and Output Membership of Mamdani FLC (Luta & Raji, 2019b)

Its effectiveness is contingent on selecting the appropriate error computation in the rule table designed. The relationship between the inputs and outputs is displayed in Figure 2.7.

		Change in Error				
		NB	NS	Z	PS	PB
Error	NB	Z	Z	Z	PS	PB
	NS	Z	Z	NB	PS	PB
	Z	NB	NS	NS	PS	PB
	PS	NB	NS	NS	Z	Z
	PB	NB	NS	PS	Z	Z

Figure 2.7: Rules Table (Luta & Raji, 2019b)

The FLC-based MPPT was compared with fractional open-circuit voltage MPPT techniques. The FLC method had an extremely fast settling time for tracking the MPP of the PEMFC within $10.53ms$. However, the power extraction was slightly lower than the fractional open circuit voltage and PSO-based MPPT methods.

For FLC, it has recently been improved by optimizing the fuzzy MF design (Aly et al., 2023; Rezk et al., 2023). The literature demonstrated that FLC can be combined with optimization algorithms such as Success-History-based Adaptive Differential Evolution algorithm with linear population size reduction (LSHADE) or Gradient-based Optimization (GBO) to effectively track the MPP of the PEMFC. The purpose of involving the LSHADE algorithm is to solve various optimization problems, while GBO is used to minimize the objective function. The newly designed fuzzy MF points are illustrated in Figure 2.8.

The simulation results show that the LSHADE-FLC MPPT controller has high robustness to the PEMFC parameters change and has high stability with low power ripple

(Aly et al., 2023). For GBO-FLC MPPT control, it demonstrates a fast tracking speed of MPP for PEMFC within $5ms$ (Rezk et al., 2023). However, its main drawback is low stability, which results in noticeable power oscillation before the output is stabilized.

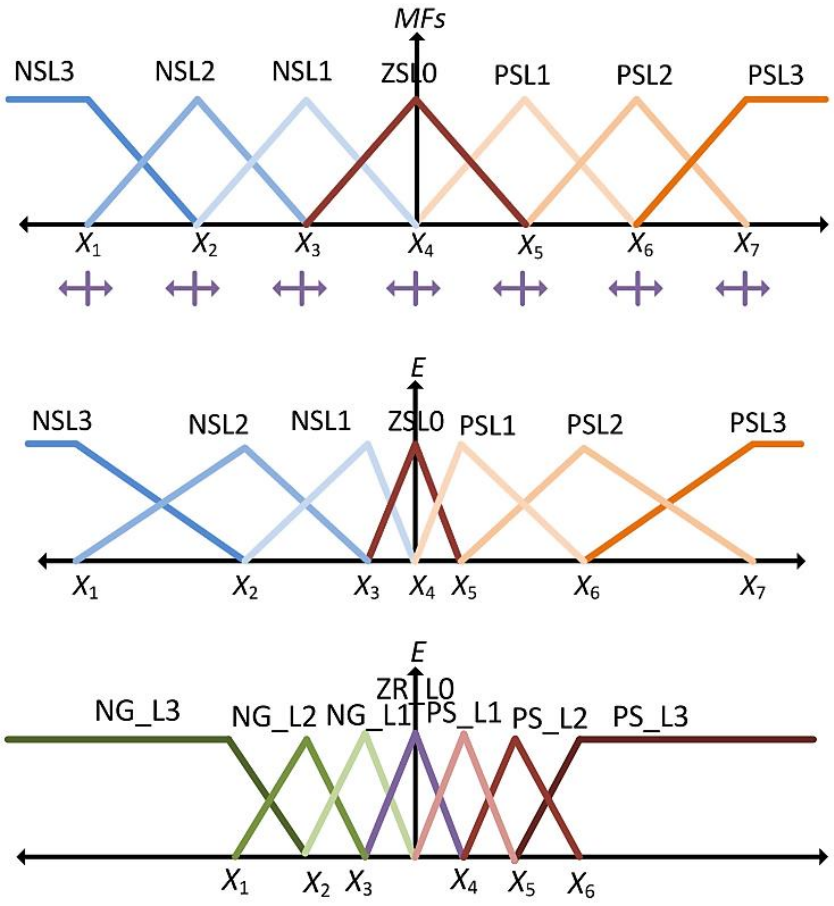


Figure 2.8: Fuzzy MF Design (Aly et al., 2023; Rezk et al., 2023)

2.4.8 Particle Swarm Optimizer (PSO)

A PSO-based MPPT for the PEMFC system was introduced, where PSO models group communication behavior with a target (Luta & Raji, 2019b). This group of organisms represents a potential solution called particles. Each particle has a position with a specified movement to find the best solution. Then, each particle updates its movement based on the

previous best position until the best solution can be determined. The particles are updated based on the formulae shown in Equation 2.52 and Equation 2.53.

$$v_i(k+1) = wv_i(k) + c_1 r_1\big(P_{best} - x_i(k)\big) + c_2 r_2\big(G_{best} - x_i(k)\big) \qquad \text{Equation 2.52}$$

$$x_i(k+1) = x_i(k) - v_i(k+1) \qquad \text{Equation 2.53}$$

where v_i and x_i are the velocity and position of the particle i, respectively, w is the inertia weight, c_1 and c_2 are the cognitive and social coefficients, respectively, r_1 and r_2 are the random variables uniformly distributed in the range between 0 and 1, P_{best} is the individual best particle position, G_{best} is the global best position for all the particles in the swarm.

Generally, a PSO algorithm's operational procedure consists of five steps. The first step is to initialize the particles randomly in the same distribution either over the search space or on grid nodes that span the search space in equidistant spots across the search space. The second stage involves evaluating the fitness of individual particles by providing a feasible solution to the objective function. In the third step, the values of P_{best} and G_{best} are updated by comparing previous values to newly calculated values and replacing P_{best} and G_{best} with their corresponding positions. In the fourth step, Equation 2.52 and Equation 2.53 are applied to update the velocity and position of particles in the swarm one by one. The final step is to check if the convergence condition is met before either terminating the operation or increasing the number of iterations by one and proceeding to step 2. The flowchart represented in Figure 2.9 is the basis for the PSO MPPT controller applied in PEMFC.

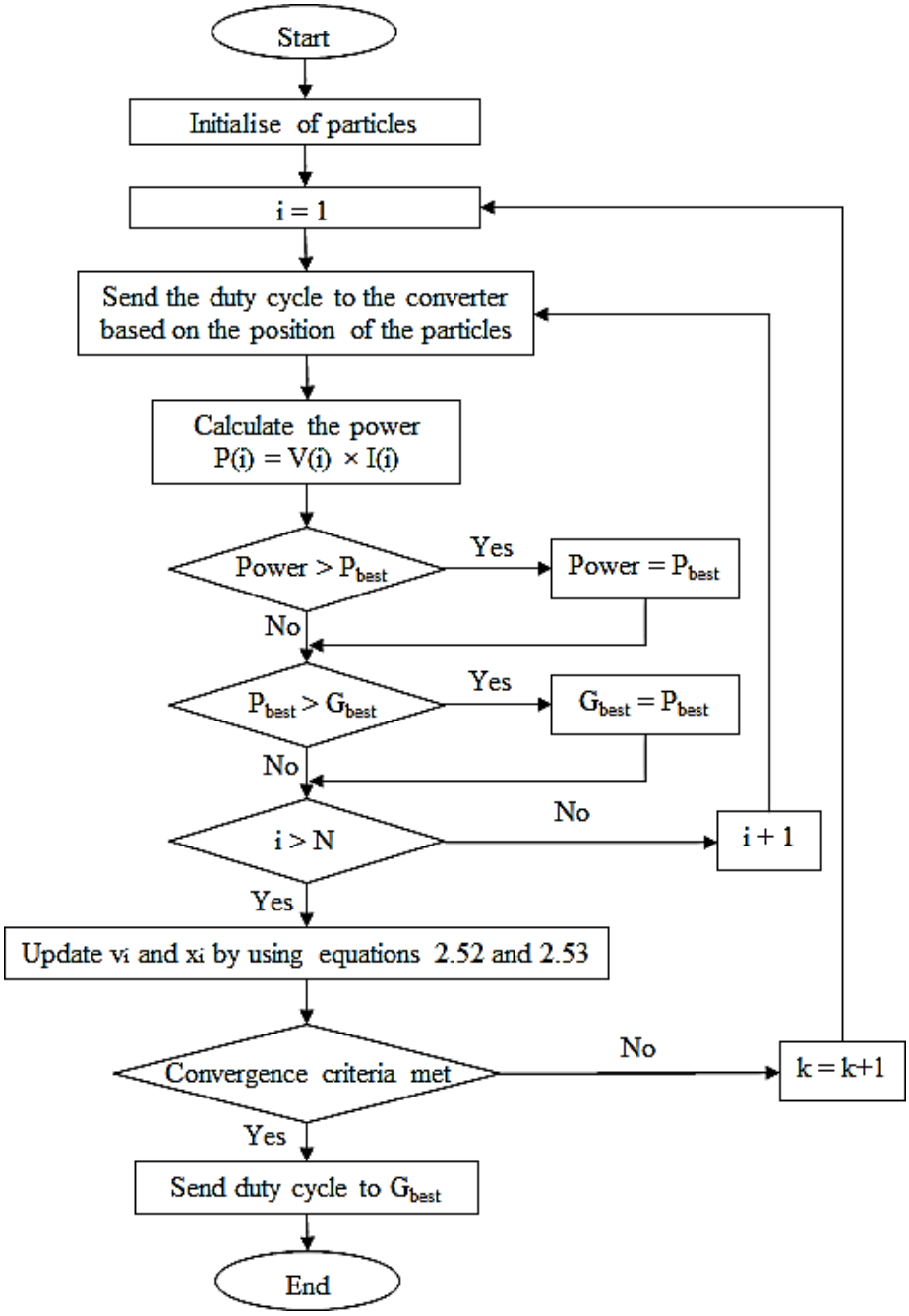


Figure 2.9: Flowchart of PSO MPPT Controller (Luta & Raji, 2019b)

A comparison of MPPT methods between FLC and PSO was presented (Luta & Raji, 2019b). The results showed that the PSO algorithm is better than the FLC controller with a lower current overshoot issue. On the other hand, FLC performed better in settling time and undershooting problems.

The PSO-based MPPT was improved using a Proportional-Integral-Derivative (PID) controller, resulting in the PSO-PID-based MPPT method (Ahmadi et al., 2017). The PID controller received the data from the PSO-based MPPT as the reference voltage. The reference voltage was then compared with the fuel cell voltage. Then, it regulated the fuel cell voltage by using a pulse generator connected to the metal-oxide-semiconductor field-effect transistor (MOSFET) in the boost converter. This technique could maintain the fuel cell voltage at MPP. The values of PID parameters were obtained by trial and error, with 0.043 for the proportional gain (K_P), 0.0001 for the integral gain (K_I), and 0.001 for the derivative gain (K_D). Then, the results were compared with the P&O and SMC methods. The PSO-PID algorithm performed the best in the simulation because it had high accuracy, fast time response, and very low power fluctuations when tracking the MPP under variable conditions.

2.4.9 Salp Swarm Algorithm (SSA)

An SSA-based MPPT with a PID controller to regulate the boost converter duty cycle was presented (Fathy, Abdelkareem, et al., 2021). The concept of SSA is that a free-swimming marine leader salp leads its followers in searching for the best food at the bottom of the ocean. During the food search, the location of each salp is updated based on information received from the leader, who adjusts its position using Equation 2.54.

$$X_j^{leader} = \begin{cases} F_j + c_1\left[\left(ub^j - lb^j\right)c_2 + lb^j\right]c_3 \geq 0 \\ F_j - c_1\left[\left(ub^j - lb^j\right)c_2 + lb^j\right]c_3 < 0 \end{cases} \quad \text{Equation 2.54}$$

where X_j^{leader} is the position of the leader at j^{th} dimension, F_j is the position of the food in j^{th} dimension, ub^j is the upper limit and lb^j is the lower limit at j^{th} dimension, c_1, c_2 and

c_3 are random values. The coefficient c_1 is decreased adaptively over iterations with Equation 2.55.

$$c_1 = 2e^{-\left(\frac{4\times Iter}{Max_{Iter}}\right)} \quad \text{Equation 2.55}$$

where $Iter$ is the number of the current iteration and Max_{Iter} is the maximum number of iterations. Based on the motion law of Newton, the positions of followers can be updated with Equation 2.56.

$$x_j^i = \frac{1}{2}\alpha t^2 + v_0 t, i = 2, 3 \cdots, dim - 1 \quad \text{Equation 2.56}$$

where x_j^i is the position of ith salp in jth dimension, α is the ratio between the final velocity and the initial velocity, t is the time, and v_0 is the initial velocity. In the SSA algorithm, t is the iteration number, and by assuming the zero initial velocity, the algorithm is expressed as Equation 2.57.

$$x_j^i = \frac{1}{2}\left(x_j^i + x_j^{i-1}\right), i = 2, 3 \cdots, dim - 1 \quad \text{Equation 2.57}$$

In SSA, the global optimum solution can track the value that represents the food. Figure 2.10 shows schematically the process of SSA.

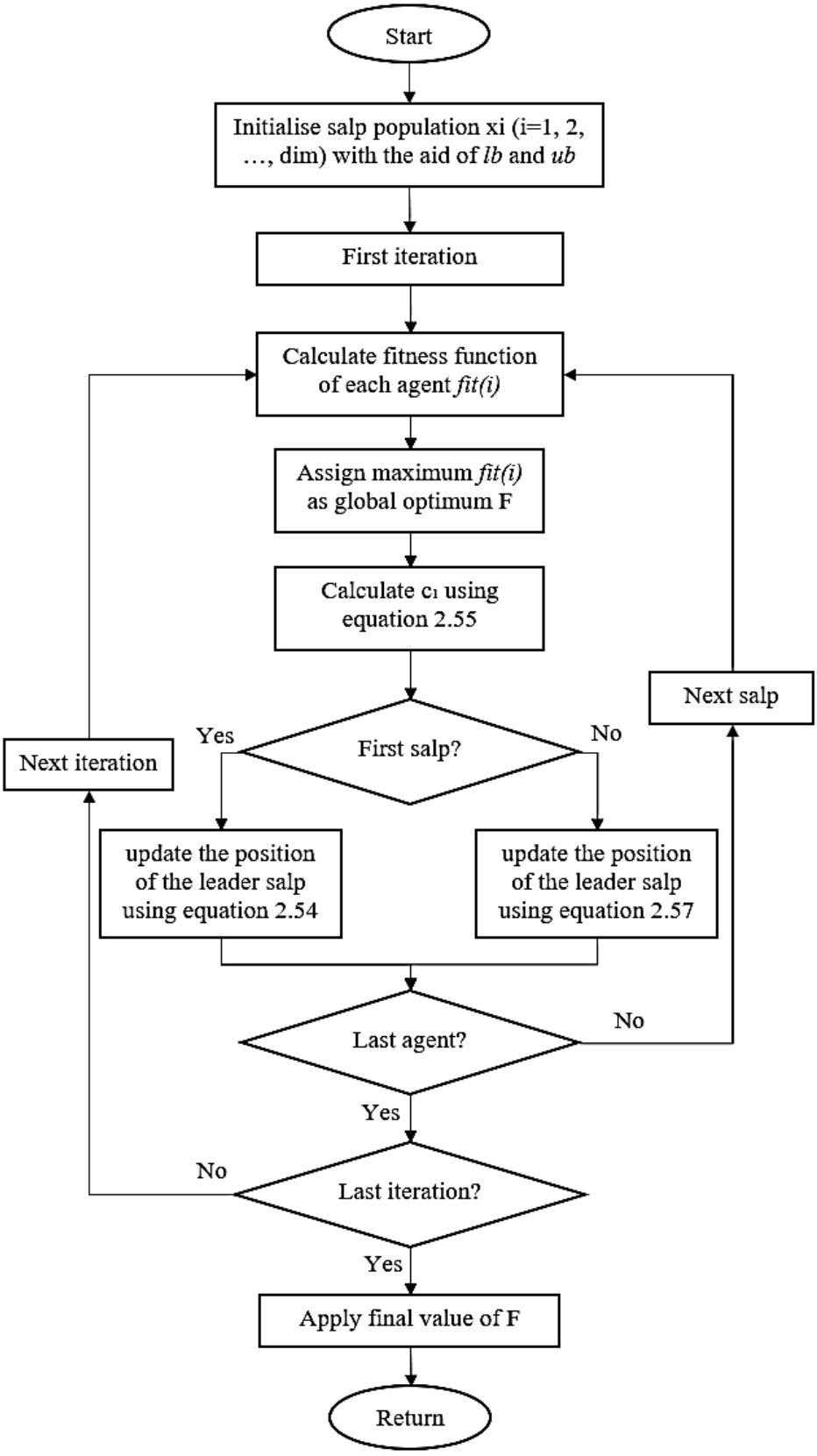


Figure 2.10: Flowchart of SSA (Fathy, Abdelkareem, et al., 2021)

This SSA with PID-based MPPT was compared with IC, FLC, grey wolf optimizer (GWO)-PID, antlion optimizer (ALO)-PID, and mine-blast algorithm (MBA)-PID for all studied cases (Fathy & Rezk, 2018; Rezk et al., 2017). The results revealed that the SSA-PID extracted slightly higher power than the FLC method within $170ms$. Besides, it is robust to the PEMFC changes under any operating conditions.

2.4.10 Forensic-based Investigation Algorithm (FBI)

A forensic-based investigation (FBI) algorithm combined with a fractional-order PID (FOPID) controller was introduced for PEMFC systems (Fathy, Rezk, et al., 2021). The FOPID is the improvement of the conventional PID, which has a better performance. It required two extra parameters than the conventional PID, which are the integrator (λ) and the order of derivative (μ). The transfer function of FOPID is expressed as Equation 2.58.

$$G_c(s) = \frac{U(s)}{E(s)} = K_p + K_i s^{-\lambda} + K_d s^{\mu}, \qquad \lambda, \mu > 0 \qquad \text{Equation 2.58}$$

where $U(s)$ is the output and $E(s)$ is the input of the FOPID controller. For the time domain, the output is defined as Equation 2.59.

$$u(t) = K_p e(t) + K_i D^{-\lambda} e(t) + K_d D^{-\mu} e(t) \qquad \text{Equation 2.59}$$

Then, the FBI algorithm is used to identify the optimal parameters for the FOPID controller. The concept of the FBI technique is the process of a suspected investigation carried out by a group of police officers to catch the perpetrators. For the location of ith suspect, X_{Ai}, each investigation team's police officer tries to find a new suspect, X_{A1i} with Equation 2.60.

$$X_{A1ij} = X_{Aij} + (2rand_1 - 1) \times \left(X_{Aij} - \frac{X_{Akj} + X_{Ahj}}{2}\right), \quad \text{Equation 2.60}$$

$$i, j, k \in \{1,2,\cdots,N_p\}$$

where $rand$ is the random number from 0 to 1 and i, k, h are three locations of suspects. The second step is to determine the direction of the perpetrators by comparing the location of each suspect, which is given by Equation 2.61.

$$X_{A2ij} = X_{best} + X_{Adj} + rand_5(X_{Aej} + X_{Afj}), \quad \text{Equation 2.61}$$

$$i, d, e, f \in \{1,2,\cdots,N_p\}$$

where X_{best} is the best location of the suspect obtained from Equation 2.60. Then, the pursuit team police officer updates the location with Equation 2.62.

$$X_{B1ij} = rand_6 \times X_{Bij} + rand_7(X_{best} - X_{Bij}) \quad \text{Equation 2.62}$$

At this moment, each agent B_i move toward the best location, but they are affected by each other by Equation 2.63 and Equation 2.64.

$$p_{Br} > B_r, \quad X_{B2ij} = X_{Brj} + rand_8(X_{Brj} - X_{Bij}) + rand_9(X_{best} - X_{Brj})r \quad \text{Equation 2.63}$$

$$p_{Br} < B_r, \quad X_{B2ij} = X_{Bij} + rand_{10}(X_{Bij} - X_{Brj}) + rand_{11}(X_{best} - X_{Bij})r \quad \text{Equation 2.64}$$

$$i \in \{1,2,\cdots,N_p\}$$

Finally, the police officers catch the perpetrators, and it represents the solution. The schematic flowchart of the FBI is presented in Figure 2.11.

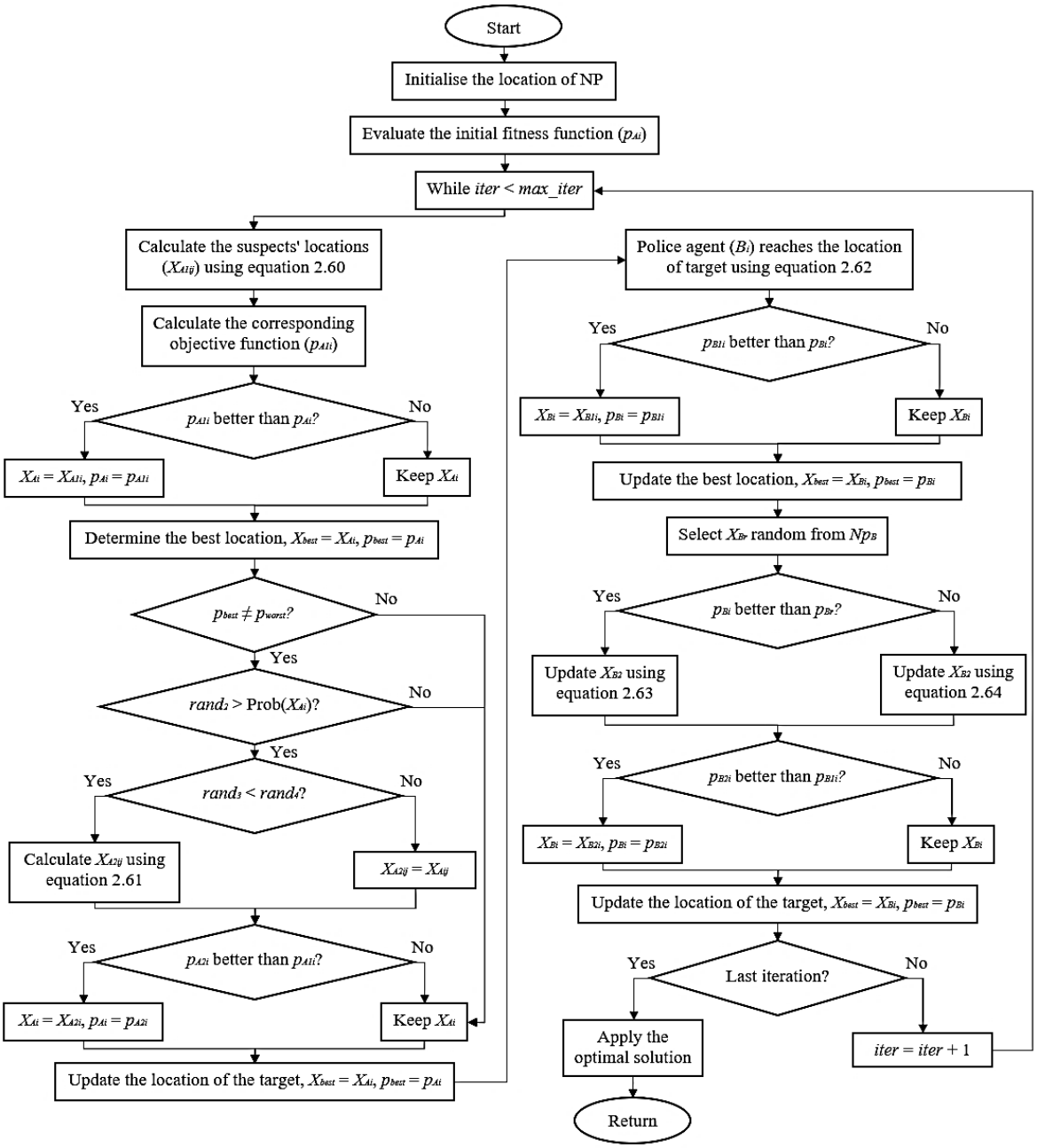


Figure 2.11: Flowchart of FBI (Fathy, Rezk, et al., 2021)

In the literature (Fathy, Rezk, et al., 2021), the other metaheuristic optimization approaches, such as PSO, invasive weed optimizer (IWO), artificial ecosystem optimizer (AEO), and sin-cosine algorithm (SCA) were combined with the FOPID controller. Then, the FBI-based MPPT approach was compared with IC and all other metaheuristic

optimization methods. The simulation results showed the FBI-FOPID technique could extract the highest power from the PEMFC. However, the tracking speed for the PEMFC to achieve the MPP was $700ms$, which is slower than the IC, PSO, IWO, and SCA methods.

2.4.11 Golden Jackal Optimization Algorithm (GJOA)

A new control strategy combines Proportional-Derivative (PD), PI controllers, and GJOA to extract the PEMFC maximum output power (Agwa et al., 2023). It searches for the optimal controller parameters by iteratively evaluating and updating candidate solutions based on a fitness function aimed at maximizing power stability and response speed. First, the location of a group of prey with Equation 2.65.

$$Prey(0) = \begin{bmatrix} L_{1,1} & \cdots & L_{1,dim} \\ \vdots & \ddots & \vdots \\ L_{pop,1} & \cdots & L_{pop,dim} \end{bmatrix} \quad \text{Equation 2.65}$$

where pop is the population and dim is the dimension. Then, evaluate the fitness function (FiFu) by minimizing the Integral-Time Absolute Error shown in Equation 2.66.

$$FiFu = minimize\left(\int_0^{t_{si}} t \cdot |V_o - V_{MP}| \cdot dt\right) \quad \text{Equation 2.66}$$

where t_{si} is the simulation time, V_o is the PEMFC output voltage and V_{MP} is the maximum power voltage. The FiFu is constrained to ensure that the PI-PD gains remain within its predefined limits shown in Equation 2.78.

$$u(t) = K_{p_2}\left(K_{p_1}e(t) + K_i\int e(t)dt\right) + K_d\frac{d}{dt}\left(K_{p_1}e(t) + K_i\int e(t)dt\right) \quad \text{Equation 2.67}$$

where $u(t)$ is the output control signal and $e(t)$ is the input error signal.

For GJOA, it computes the prey escaping energy, E with Equation 2.68.

$$E = c_1\left(1 - \frac{ite}{ite_{max}}\right)E_0 \quad \text{Equation 2.68}$$

where c_1 is a constant value, E_0 is the value from -1 to 1 and ite, ite_{max} are the iteration and the maximum iteration, respectively. At the last process, it updates the location of the prey by Equation 2.69 until Equation 2.72.

$$L_1(ite) = L_M(ite) - E|L_M(ite) - rlPrey(ite)| \quad \text{Equation 2.69}$$

$$L_2(ite) = L_{FM}(ite) - E|L_{FM}(ite) - rlPrey(ite)| \quad \text{Equation 2.70}$$

$$L_3(ite) = L_M(ite) - E|rlL_M(ite) - Prey(ite)| \quad \text{Equation 2.71}$$

$$L_4(ite) = L_{FM}(ite) - E|rlL_{FM}(ite) - Prey(ite)| \quad \text{Equation 2.72}$$

where $L_1(ite)$, $L_2(ite)$, $L_3(ite)$ and $L_4(ite)$ are updated locations of the jackals, $L_M(ite)$ and $L_{FM}(ite)$ are the locations of male and female jackals, respectively. Another algebra rl represents a vector number which involves random value computation by the Levy flight function. A schematic flowchart of GJOA is revealed in Figure 2.12.

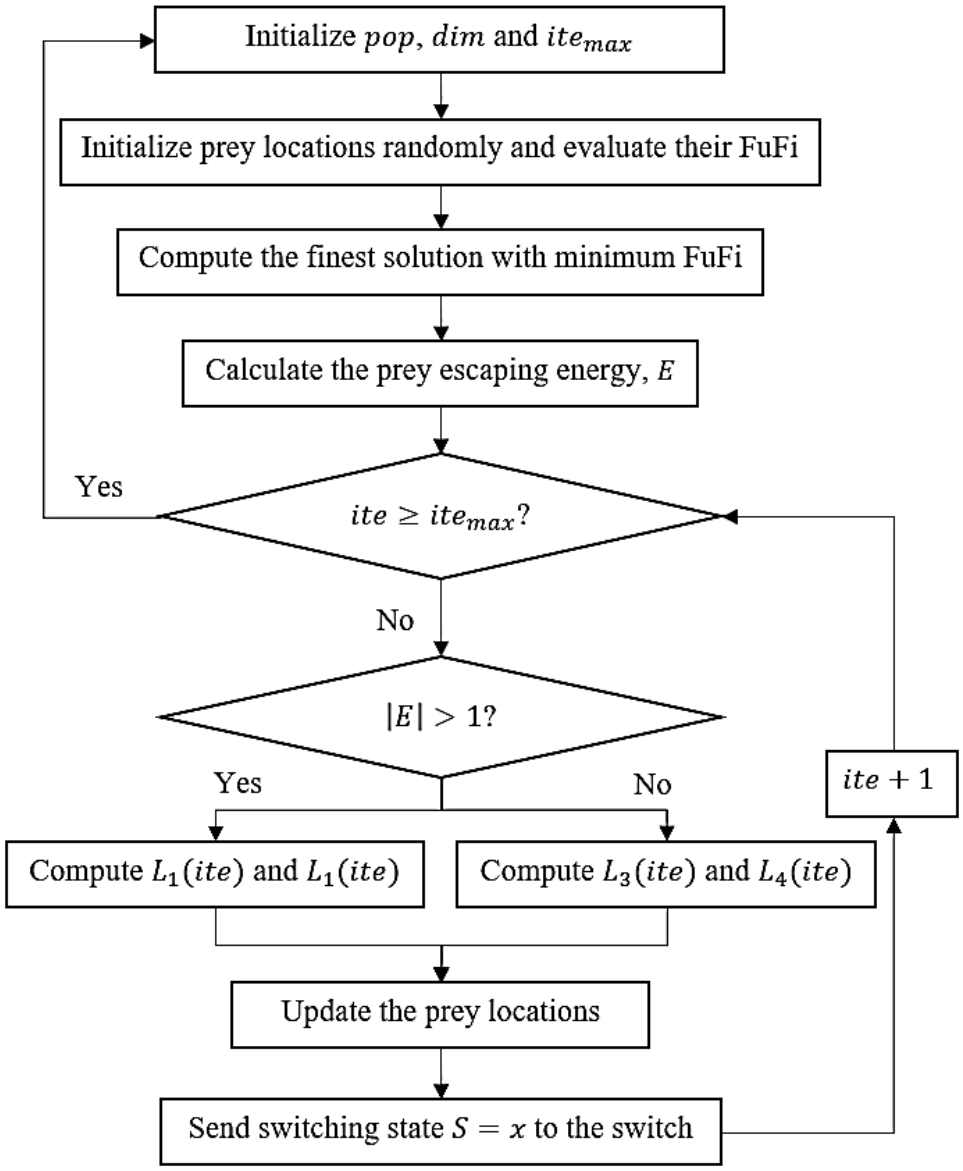


Figure 2.12: Flowchart of GJOA (Agwa et al., 2023)

The performance of this MPPT method exhibits minimal overshoot within 0.2% and has negligible oscillations, leading to stable tracking under various operating conditions. However, it requires 700ms to track the MPP.

2.4.12 Artificial Bee Colony Algorithm (ABC)

The ABC algorithm has recently been implemented in the PEMFC system (Fan & Ma, 2022). It is a population-based optimization technique inspired by the nectar foraging behavior of honeybees. It starts with a population of employed, onlooker bees, and scouts with parameters. The employed bees search for the food and update the position with Equation 2.73.

$$V_{i,j} = X_{i,j} + \varphi_{i,j}\left(X_{i,j} - X_{k,j}\right) \quad \text{Equation 2.73}$$

where $V_{i,j}$ is the updated food position, $X_{i,j}$ is the current food position, $\varphi_{i,j}$ is the random value from -1 to 1, and i, j, k are the random positive integers limited to the dimension of the problem and the number of solutions in the colony. Onlooker bees are responsible for sharing the information from employed bees and determining the food source with a computed probability formula shown in Equation 2.74.

$$p_i = \frac{f_i}{\sum_{i=1}^{S_N} f_i} \quad \text{Equation 2.74}$$

where f_i is the fitness function and S_N is the number of solutions in the colony. The scout bees act as the leader to monitor the changes in the solution for each iteration. If it fails to lock the food position, a new random solution will be computed using Equation 2.75.

$$X_{i,j} = X_{min,j} + rand[0,1]\left(X_{max,j} - X_{min,j}\right) \quad \text{Equation 2.75}$$

The ABC algorithm was merged with the FLC to enhance its performance. The fuzzy controller receives inputs related to the PEMFC's operating conditions and adjusts the duty cycle of the power converter. The ABC-FLC method was compared with P&O, VSS-IC, and the original ABC algorithm. Its accuracy is as high as 99.8% tracked within $30ms$. It

performed the best in accuracy and tracking speed. However, there was a 2.6% power ripple recorded.

2.4.13 Summary of MPPT in Literature Review

The MPPT methods that are applied to the fuel cells are introduced. All the MPPT methods discussed are listed in Table 2.2.

Table 2.2: Summary of the MPPT Techniques

Citation	Approach	Converter	Advantages	Disadvantages
(Abdi et al., 2012; Derbeli et al., 2020; Jiao & Cui, 2013)	SMC	Boost	• High accuracy (around 99% of theoretical MPP) • Low complexity due to the direct application of the equation without iteration	• Slow tracking speed (requires $200ms$ to track the MPP) • Low stability due to high power ripple (the highest power ripple recorded is 30%)
(Derbeli et al., 2020)	HOSM-TA	Boost	• High accuracy (almost the same as SMC) • Low complexity due to the direct application of the equation without iteration	• Slow tracking speed (requires $1200ms$ to track the new MPP) • Low stability due to high power ripple (the highest power ripple recorded is 7%)
(Derbeli et al., 2018, 2019)	Backstepping	Boost	• High stability due to low power undershoot and overshoot during fast variation of PEMFC parameters or load resistance • Low complexity due to the direct application of the equation without iteration	• Slow tracking speed (requires $700ms$ to track the MPP) • Excessive data is required to determine the CRE curve

Table 2.2 continued

(Naseri et al., 2018)	P&O	Boost	• High accuracy (slightly higher than IC) • Low complexity due to the direct application of the equation without iteration	• Slow tracking speed (requires $500ms$ to track the MPP) • Low stability due to high power ripple (the highest power ripple recorded is around 10%)
(Barhoumi et al., 2020)		Interleaved Boost		
(Celikel et al., 2025)	Modified P&O	Boost	• High accuracy (around 99.8% of theoretical MPP) • Fast tracking speed (within $80ms$) • Low complexity due to the direct application of the equation without iteration	• Low stability due to high power undershoot during fast variation of operating temperature (the highest power undershoot recorded is around 80%)
(Karami et al., 2014)	IC	Synchronous Buck	• High accuracy (around 98.5% of theoretical MPP) • Low complexity due to the direct application of the equation without iteration	• Slow tracking speed (requires $700ms$ to track the MPP) • Low stability due to high power ripple (the highest power ripple recorded is around 2%)

Table 2.2 continued

(Rezk & Fathy, 2020)	VSS-IC	Boost	• High accuracy (around 99.8% of theoretical MPP) • Low complexity due to the direct application of the equation without iteration	• Slow tracking speed (requires $15000ms$ to track the MPP) • Low stability due to high power undershoot during fast variation of operating temperature (the highest power undershoot recorded is around 20%)
(K. J. Reddy & Sudhakar, 2017)	RBFN	Interleaved Boost	• Fast tracking speed (within $20ms$) • Low complexity due to the direct application of the equation without iteration	• Low accuracy (around 92% of theoretical MPP) • Low stability due to high power ripple (the highest power ripple recorded is around 4.3%) • Excessive data is required before applying the method
(Srinivasan et al., 2021)	RBFN	Reconfigured quadratic boost		

Table 2.2 continued

(Luta & Raji, 2019a, 2019b)	FLC	Boost	• High accuracy (slightly lower than PSO) • Fast tracking speed (within $10.53ms$) • Low complexity due to the direct application of the equation without iteration	• Low stability (around 70% of power overshoot is recorded before the output power is stable)
(Aly et al., 2023)	LSHADE-FLC	Boost	• High accuracy (slightly lower than original FLC) • High stability due to no power undershoot, overshoot, and low power ripple	• High complexity with two combined algorithms
(Rezk et al., 2023)	GBO-FLC	Boost	• High accuracy (similar to original FLC) • Fast tracking speed (within $5ms$)	• Lower stability due to oscillation found before the output is stabilized • High complexity with two combined algorithms

Table 2.2 continued

(Luta & Raji, 2019b)	PSO	Boost	• High accuracy (slightly higher than SMC) • Fast tracking speed (within $20ms$)	• Low stability (around 70% of power overshoot is recorded before the output power is stable) • High complexity because it involves iterations in the algorithm
(Ahmadi et al., 2017)	PSO-PID	Boost	• High accuracy (slightly higher than SMC) • Fast tracking speed (within $20ms$) • High stability due to no power undershoot, overshoot, and low power ripple	• High complexity because it involves iterations in the algorithm
(Fathy, Abdelkareem, et al., 2021)	SSA-PID	Boost	• High accuracy (higher than FLC) • High stability due to no power undershoot, overshoot, and low power ripple	• Slow tracking speed (requires $170ms$ to track the MPP) • High complexity because it involves iterations in the algorithm

Table 2.2 continued

(Fathy, Rezk, et al., 2021)	FBI-FOPID	Boost	• High accuracy (slightly higher than PSO) • High stability due to no power undershoot, overshoot, and low power ripple	• Slow tracking speed (requires $700ms$ to track the MPP) • High complexity because it involves iterations in the algorithm
(Agwa et al., 2023)	GJOA-PI-PD	Boost	• High stability with negligible oscillations	• Slow tracking speed (requires $700ms$ to track the MPP) • High complexity because it involves iterations in the algorithm
(Fan & Ma, 2022)	ABC-FLC	Boost	• High accuracy (around 99.8% of theoretical MPP) • Fast tracking speed (within $30ms$)	• Low stability due to high power ripple (the highest power ripple recorded is around 2.6%) • High complexity with two combined algorithms

2.5 Model Predictive Control (MPC)

MPC is a control strategy that was discovered by Zadeh and Whalen (Zadeh & Whalen, 1962). It uses a dynamic model of the system to predict the future system behavior of the controllable variables over a finite prediction horizon (Khalilzadeh et al., 2021; Rodriguez & Cortes, 2012; Schwenzer et al., 2021). It is an optimal control strategy that involved the time domain since the 1960s (Karamanakos et al., 2020; Khalilzadeh et al., 2021; Rodriguez & Cortes, 2012). MPC has been widely studied and applied in various industries due to its ability to handle complex systems with constraints and uncertainties effectively in the late 1970s (Karamanakos et al., 2020; Rodriguez & Cortes, 2012). In the 1980s, the potential of MPC was investigated for power electronics applications in high-power systems, but with low switching frequency (Rodriguez & Cortes, 2012). In the 2000s, the development of higher switching frequency power semiconductors and powerful microprocessors allowed the MPC to break its applicability and perceived benefit (Karamanakos et al., 2020; Rodriguez & Cortes, 2012). Nowadays, MPC is widely used in power electronics applications in the fields of active filters, renewable energy, and distributed power generation (Borreggine et al., 2019; Khalilzadeh et al., 2021).

Power electronics MPC methods can be divided into two primary groups based on the existence of separate modulators (Karamanakos et al., 2020). The first group of MPC is named as indirect MPC, which includes a modulator to receive the duty ratio and send the switching signal. The second group is known as direct MPC. It can directly command the switch by sending the ON or OFF signal. MPC is predicated on repeatedly optimizing a mathematical system model in real time (Schwenzer et al., 2021). Therefore, the mathematical system model is crucial for a functional MPC. The model must be discretized

for prediction with the basic state space model expressed as Equation 2.76 and Equation 2.77 (Khalilzadeh et al., 2021; Rodriguez & Cortes, 2012; Toledo et al., 2022).

$$x(k+1) = Ax(k) + Bu(k) \quad \text{Equation 2.76}$$

$$y(k) = Cx(k) + Du(k) \quad \text{Equation 2.77}$$

where x is the state vector, u is the input variable, and k is the number of discrete sampling steps. Then, the MPC will optimize the switching selection by comparing the predicted value and the reference value with a cost function shown in Equation 2.78 (Khalilzadeh et al., 2021; Rodriguez & Cortes, 2012; Toledo et al., 2022).

$$J = f[x(k), u(k), \cdots, u(k+N)] \quad \text{Equation 2.78}$$

There are various advantages of using MPC due to the implicit formulation, flexibility, and explicit usage of models (Schwenzer et al., 2021). It can be used with numerous types of systems, including multivariable cases and non-linear models. In addition, it can be modified and expanded upon based on the needs of individual applications due to its comprehensible and intuitive concepts (Rodriguez & Cortes, 2012). However, MPC requires a high-performance microcontroller to compute a large prediction calculation within a short sampling time (Borreggine et al., 2019; Rodriguez & Cortes, 2012).

This section reviews the MPC techniques used in power electronics. Currently, MPCs are developed to control the switches of the power electronics and regulate the output voltage, current, or power of an electrical system. It can control the output of both DC and AC electrical power systems, including single-phase and three-phase circuits. It provides high-quality power for the electric appliances. The literature is reviewed to introduce the MPC methods that could be used in power electronics.

2.5.1 MPC for DC-DC Buck Converter

MPC was applied in a conventional DC-DC buck converter (Gaouzi et al., 2017; Pathan, 2020). A DC-DC buck converter can reduce the DC voltage to a lower level, which is widely used in DC voltage supply (Gaouzi et al., 2017). It can be considered as the DC motor starter and speed regulator (Gaouzi et al., 2017; Wu et al., 2017). It consists of a switch, a diode, an inductor, and a capacitor. A schematic of a DC-DC buck converter is shown in Figure 2.13.

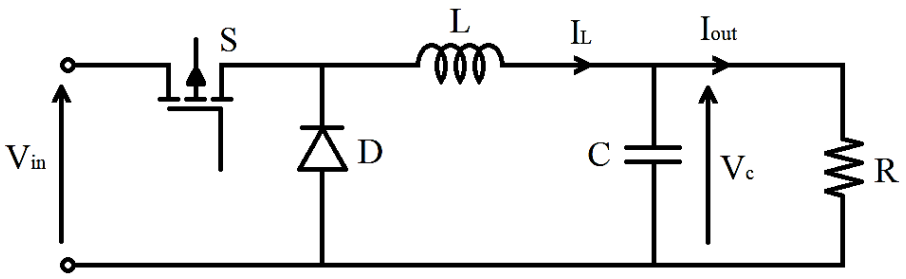


Figure 2.13: DC-DC Buck Converter Circuit Topology

Since there is a switch, the output can be controlled by the duty ratio of the switch. By applying Kirchhoff's Law, the mathematical model when the switch is OFF can be expressed as Equation 2.79 and Equation 2.80.

$$\frac{dI_L}{dt} = -\frac{1}{L}V_c \qquad \text{Equation 2.79}$$

$$\frac{dV_c}{dt} = \frac{1}{C}I_L - \frac{1}{RC}V_c \qquad \text{Equation 2.80}$$

When the switch is ON, the mathematical model of the DC-DC buck converter is defined as in Equation 2.81 and Equation 2.82, respectively.

$$\frac{dI_L}{dt} = -\frac{1}{L}V_c + \frac{V_{in}}{L} \quad \text{Equation 2.81}$$

$$\frac{dV_c}{dt} = \frac{1}{C}I_L - \frac{1}{RC}V_c \quad \text{Equation 2.82}$$

Therefore, the final switching model equations of the DC-DC buck converter can be expressed as Equation 2.83 and Equation 2.84.

$$\frac{dI_L}{dt} = -\frac{1}{L}V_c + \frac{V_{in}}{L}u \quad \text{Equation 2.83}$$

$$\frac{dV_c}{dt} = \frac{1}{C}I_L - \frac{1}{RC}V_c \quad \text{Equation 2.84}$$

$$u = \begin{cases} 1, & 0 \le t \le t_{ON} \\ 0, & t_{OFF} < t \le T \end{cases} \quad \text{Equation 2.85}$$

where u is the duty ratio for the switch to ON in one cycle and R is the resistance of the load. Based on the general discretized prediction mathematical model of MPC in Equation 2.76, the general equation of the operational DC-DC boost converter is defined as Equation 2.86.

$$\frac{d}{dt}\begin{pmatrix} I_L \\ V_c \end{pmatrix} = \begin{pmatrix} 0 & -\frac{1}{L} \\ \frac{1}{C} & -\frac{1}{RC} \end{pmatrix}\begin{pmatrix} I_L \\ V_c \end{pmatrix} + \begin{pmatrix} \frac{V_{in}}{L} \\ 0 \end{pmatrix}u \quad \text{Equation 2.86}$$

For a discretized mathematical model, the equation can be reformulated by Euler's expansion. The discretized equation for output voltage control is shown in Equation 2.87.

$$V_c(k+1) = T_s\left[\frac{I_L(k)}{C} + \left(1 - \frac{1}{RC}\right)V_c u(k)\right] \quad \text{Equation 2.87}$$

where T_s is the sampling time.

After the $V_{out}(k+1)$ is defined, the output voltage can be predicted. This prediction can be used to regulate the output voltage by comparing it with the reference voltage, V_{ref}. The output voltage control can be achieved by minimizing the cost function shown in Equation 2.88.

$$g_S = \left|V_{ref} - V_c(k+1)\right| \qquad \text{Equation 2.88}$$

The output voltage control of MPC was compared with that of a PID controller (Pathan, 2020). The MPC showed an excellent result for output voltage control with high stability and short settling time. The PID controller also had high stability, but it had a slower settling time. MPC with a Generalized Proportional Integral Observer (GPIO) was applied to a DC motor system for angular velocity regulation (Wu et al., 2017). The performance of the MPC was compared with that of the PID controller. The simulation results showed that the MPC was more stable than the PID controller when there was a fast variation of force acting on the motor.

2.5.2 MPC for DC-DC Boost Converter

The MPC technique was applied in a DC-DC boost converter (Bououden et al., 2014; Cheng et al., 2017, 2016). A DC-DC boost converter functions as the opposite of a buck converter. It increases the voltage level instead of reducing it. Its components are the same as a buck converter, but the different arrangement results in a contrary output. A diagram of a DC-DC boost converter is illustrated in Figure 2.14.

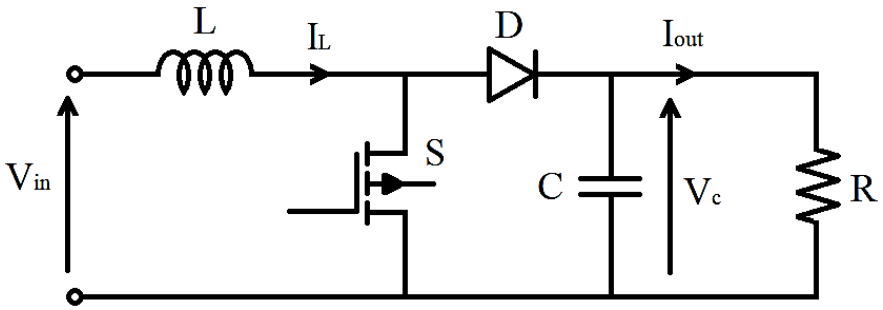


Figure 2.14: DC-DC Boost Converter Circuit Topology

The control of the boost converter output is also similar to the buck converter, which regulates the output by controlling the switch. When the switch is OFF, the mathematical model equation of the DC-DC boost converter can be expressed as the equations shown in Equation 2.89 and Equation 2.90.

$$\frac{dI_L}{dt} = \frac{V_{in}}{L} \qquad \text{Equation 2.89}$$

$$\frac{dV_c}{dt} = -\frac{1}{RC}V_c \qquad \text{Equation 2.90}$$

When the switch is ON, the mathematical model equations of the DC-DC boost converter are defined as in Equation 2.91 and Equation 2.92.

$$\frac{dI_L}{dt} = -\frac{1}{L}V_c + \frac{V_{in}}{L} \qquad \text{Equation 2.91}$$

$$\frac{dV_c}{dt} = \frac{1}{C}I_L - \frac{1}{RC}V_c \qquad \text{Equation 2.92}$$

Considering the duty ratio, the final mathematical model equations can be simplified as Equation 2.93 and Equation 2.94.

$$\frac{dI_L}{dt} = -(1-u)\frac{1}{L}V_c + \frac{V_{in}}{L} \quad \text{Equation 2.93}$$

$$\frac{dV_c}{dt} = (1-u)\frac{1}{C}I_L - \frac{1}{RC}V_c \quad \text{Equation 2.94}$$

Therefore, the rate of change of the inductor current and the output voltage can be expressed as Equation 2.95.

$$\frac{d}{dt}\begin{pmatrix} I_L \\ V_c \end{pmatrix} = \begin{pmatrix} 0 & -\frac{1-u}{L} \\ \frac{1-u}{C} & -\frac{1}{RC} \end{pmatrix}\begin{pmatrix} I_L \\ V_c \end{pmatrix} + \begin{pmatrix} \frac{V_{in}}{L} \\ 0 \end{pmatrix}u \quad \text{Equation 2.95}$$

For a discretized mathematical model, the equation can be reformulated by Euler's expansion. The discretized equation for output voltage control is shown in Equation 2.96.

$$x(k+1) = (I + T_s A)x(k) + T_s B \quad \text{Equation 2.96}$$

An accurate MPC application that considered inductor internal resistance was introduced (Cheng et al., 2017, 2016). The final discretized model of equations are defined as Equation 2.97 and Equation 2.98.

$$I_L(k+1) = \left(1 - \frac{T_s R}{L}\right)I_L(k) + (u-1)\frac{T_s}{L}V_c(k) + \frac{T_s}{L}V_{in}(k) \quad \text{Equation 2.97}$$

$$V_c(k+1) = \frac{T_s}{C}I_L(k) + \left[1 - \frac{T_s}{R}\right]V_c(k) + \frac{uT_s}{C}I_L(k) \quad \text{Equation 2.98}$$

After the output prediction is defined, the output voltage can be regulated. By comparing it with the reference voltage, the output control can be achieved by minimizing the cost function.

Simulation results demonstrated that MPC could regulate output voltage to the reference within $3ms$ (Cheng et al., 2017, 2016). The Takagi-Sugeno fuzzy approach was

merged with MPC and compared against the conventional MPC method (Bououden et al., 2014). The simulation showed that the fuzzy MPC had a faster settling time than the conventional MPC method. MPC was also used in a DC-DC boost converter to control PEMFC output current in the literature (Derbeli et al., 2021). The results were compared with the PID controller. In conclusion, the MPC had a faster reaction and settling time in regulating the PEMFC output current.

MPC with GPIO was implemented on a Two-Phase Interleaved Boost Converter (TIBC) (Niu et al., 2023). The interleaved boost converter has another inductor, switch, and diode connected in parallel to the original one. The schematic diagram of this interleaved boost converter is shown in Figure 2.15.

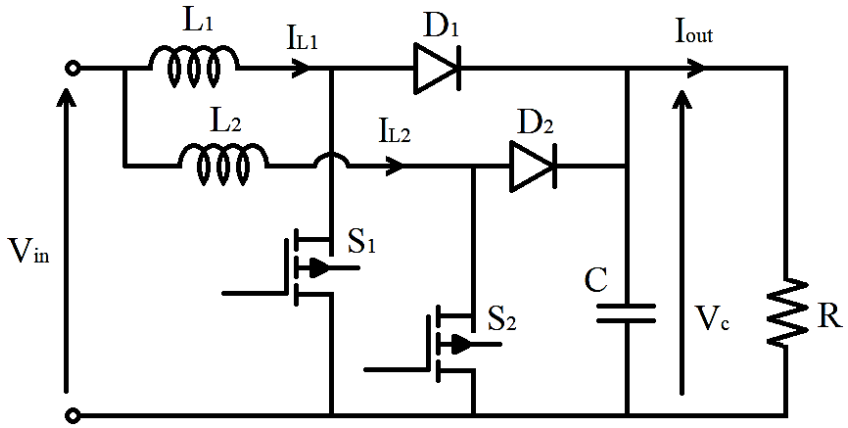


Figure 2.15: Two-Phase Interleaved Boost Converter Circuit Topology

Based on the circuit topology, the static model mathematical equations of the interleaved boost converter for continuous conduction mode can be expressed as Equation 2.99 and Equation 2.100.

$$V_c = \frac{V_{in}}{1 - D}$$ Equation 2.99

$$I_{out} = 2I_L(1 - D)$$ Equation 2.100

where D is the duty cycle. Then, the dynamic model of TIBC can be expressed as Equation 2.101 and Equation 2.102.

$$L\frac{dI_L}{dt} = V_{in} - (1 - D_i)V_C$$ Equation 2.101

$$C\frac{dV_c}{dt} = \sum(1 - D_i)I_L - \frac{V_c}{R}$$ Equation 2.102

where $i = 1, 2$.

A Three-Level Boost Converter (TLBC) was presented, and the MPC was used to control the real-time PEMFC output current (Kanouni et al., 2024). It can divide the input voltage into three levels. Figure 2.16 illustrates the circuit topology of TLBC.

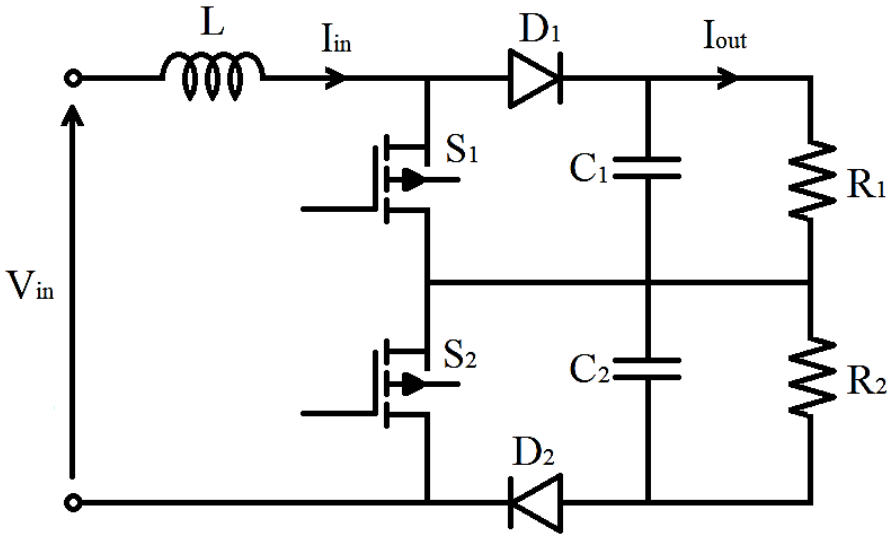


Figure 2.16: Three-Level Boost Converter Circuit Topology

Based on the circuit topology, the dynamic model of the TLBC for a discrete mathematical model for MPC can be expressed as Equation 2.103.

$$\begin{bmatrix} I_{in}(k+1) \\ V_{C_1}(k+1) \\ V_{C_2}(k+1) \end{bmatrix} = \begin{bmatrix} 0 & -\frac{T_s}{L}(1-S_1) & -\frac{T_s}{L}(1-S_2) \\ \frac{T_s}{C_1}(1-S_1) & 0 & 0 \\ \frac{T_s}{C_2}(1-S_2) & 0 & 0 \end{bmatrix} \begin{bmatrix} I_{in}(k) \\ V_{C_1}(k) \\ V_{C_2}(k) \end{bmatrix} + \begin{bmatrix} \frac{T_s}{L} & 0 & 0 \\ 0 & -\frac{T_s}{C_1} & 0 \\ 0 & 0 & -\frac{T_s}{C_2} \end{bmatrix} \begin{bmatrix} V_{in}(k) \\ I_{01}(k) \\ I_{02}(k) \end{bmatrix} \quad \text{Equation 2.103}$$

The TLBC can predict the next PEMFC output current as the input of the power converter using the MPC algorithm. The controlling approach was merged with the FLC to regulate the PEMFC output current. This controller was proven with an experimental validation.

2.5.3 MPC for DC-DC Buck-Boost Converter

A DC-DC buck-boost converter can either step up or step down the output DC voltage and current. Output voltage control with a DC-DC buck-boost converter was achieved using MPC (Albira et al., 2020). Same as a buck or boost converter, it consists of a switch, a diode, an inductor, and a capacitor. The conventional DC-DC buck-boost converter gives an inverting output voltage. However, this does not affect the application in the electronics field. Figure 2.17 illustrates the conventional model of a DC-DC buck-boost converter.

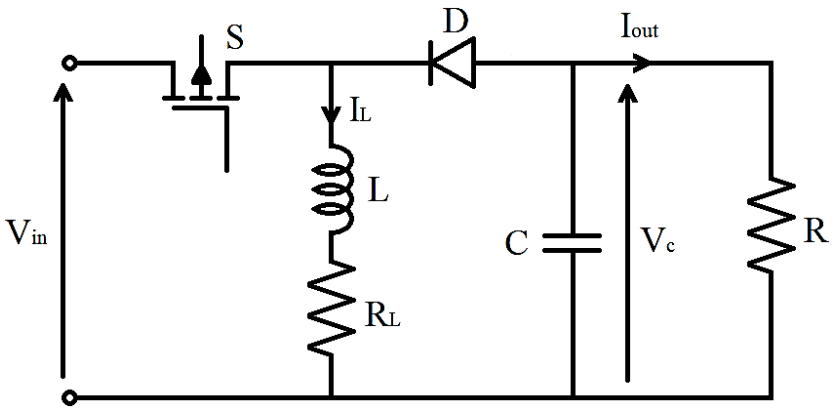


Figure 2.17: DC-DC Buck-Boost Converter Circuit Topology

It is important to compute the mathematical model of the buck-boost converter because the control of the switch may step up or step down the output DC voltage. When the switch is OFF, the mathematical model equation of the DC-DC buck-boost converter is defined as Equation 2.104 and Equation 2.105.

$$\frac{dI_L}{dt} = -\frac{R_L}{L}I_L + \frac{1}{L}V_c \qquad \text{Equation 2.104}$$

$$\frac{dV_c}{dt} = -\frac{1}{C}I_L - \frac{1}{RC}V_c \qquad \text{Equation 2.105}$$

When the switch is ON, the mathematical model equation is expressed as Equation 2.106 and Equation 2.107.

$$\frac{dI_L}{dt} = -\frac{R_L}{L}I_L + \frac{1}{L}V_{in} \qquad \text{Equation 2.106}$$

$$\frac{dV_c}{dt} = -\frac{1}{RC}V_c \qquad \text{Equation 2.107}$$

When the duty ratio is involved, the final mathematical model equations of the buck-boost converter are shown in Equation 2.108 and Equation 2.109.

$$\frac{dI_L}{dt} = -\frac{R_L}{L} I_L + (1-u)\frac{1}{L} V_c + u\frac{1}{L} V_{in} \quad \text{Equation 2.108}$$

$$\frac{dV_c}{dt} = -(1-u)\frac{1}{C} I_L - \frac{1}{RC} V_c \quad \text{Equation 2.109}$$

$$u = \begin{cases} 1, & 0 \le t < t_{ON} \\ 0, & t_{OFF} < t \le T \end{cases} \quad \text{Equation 2.110}$$

By using the MPC algorithm, the rate of change of the inductor current and the output voltage can be expressed in matrix form as Equation 2.111.

$$\frac{d}{dt}\begin{pmatrix} I_L \\ V_c \end{pmatrix} = \begin{pmatrix} -\frac{R_L}{L} & \frac{u-1}{L} \\ \frac{u-1}{C} & \frac{1}{RC} \end{pmatrix}\begin{pmatrix} I_L \\ V_c \end{pmatrix} + \begin{pmatrix} \frac{V_{in}}{L} \\ 0 \end{pmatrix} u \quad \text{Equation 2.111}$$

For the discretized mathematical model, the matrix equation for output prediction can be expressed by using the same formula as Equation 2.96.

Simulation results of the DC-DC buck-boost converter controlled by MPC were presented (Albira et al., 2020). It can regulate the output voltage in both step-up and step-down conversion. However, the output voltage showed some oscillations before it became stable.

A non-inverting buck-boost converter was introduced (Ghamari et al., 2022). It requires an extra switch and a diode to build the converter. Its circuit topology is the combination of a buck converter and a boost converter, which is shown in Figure 2.18.

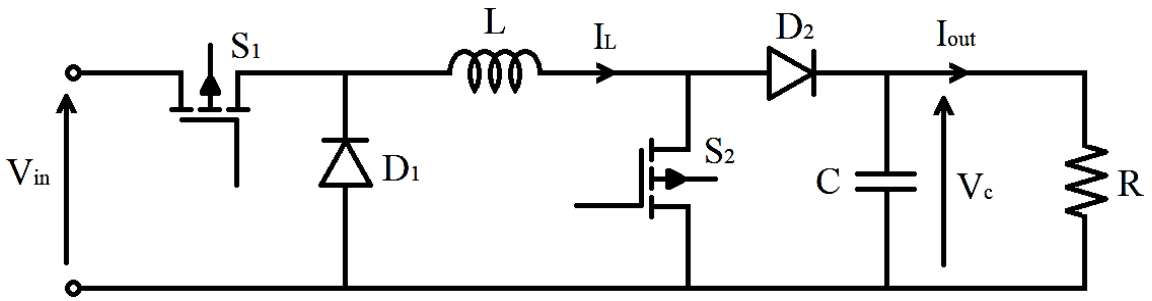


Figure 2.18: Non-Inverting DC-DC Buck-Boost Converter Circuit Topology

The feature of this converter is that it can either step up or step down the DC voltage without getting the output inverted. However, this converter has two switches, and it requires two signals to control the switches. The converter performs buck and boost mode with a transfer function shown in Equation 2.112 and Equation 2.113, respectively.

$$\widehat{V_c} = \frac{\frac{V_{in}}{LC}}{s^2 + \frac{s}{RC} + \frac{1}{LC}}\hat{u} + \frac{\frac{D_1}{LC}}{s^2 + \frac{s}{RC} + \frac{1}{LC}}\widehat{V_{in}} \qquad \text{Equation 2.112}$$

$$\widehat{V_c} = \frac{\frac{I_L}{C}\left(\frac{V_{in}}{LI_L} - s\right)}{s^2 + \frac{s}{RC} + \frac{(1-D_2)^2}{LC}}\hat{u} + \frac{\frac{1-D_1}{LC}}{s^2 + \frac{s}{RC} + \frac{(1-D_2)^2}{LC}}\widehat{V_{in}} \qquad \text{Equation 2.113}$$

where D_1 and D_1 are the duty cycle. Then, a generalized model predictive controller (GPC) is designed with a discrete transfer function shown in Equation 2.114.

$$G(z) = \frac{Y(z)}{U(z)} = \frac{b_0 z + b_1}{z^2 + a_1 z + a_2 z} \qquad \text{Equation 2.114}$$

2.5.4 MPC for Single-Phase AC-DC Converter

A single-phase AC-DC power converter controlled by MPC was proposed (Jun et al., 2020). From the literature, the electrical energy source was supplied from a single-phase AC generator. Then, a three-level neutral point clamped (NPC) converter was used to

convert the AC power to DC power. During the conversion, the MPC was used to balance the DC capacitor voltage at the load side. The purpose of balancing the capacitor voltage was to stabilize the voltage supply to the DC load. The circuit topology diagram is shown in Figure 2.19.

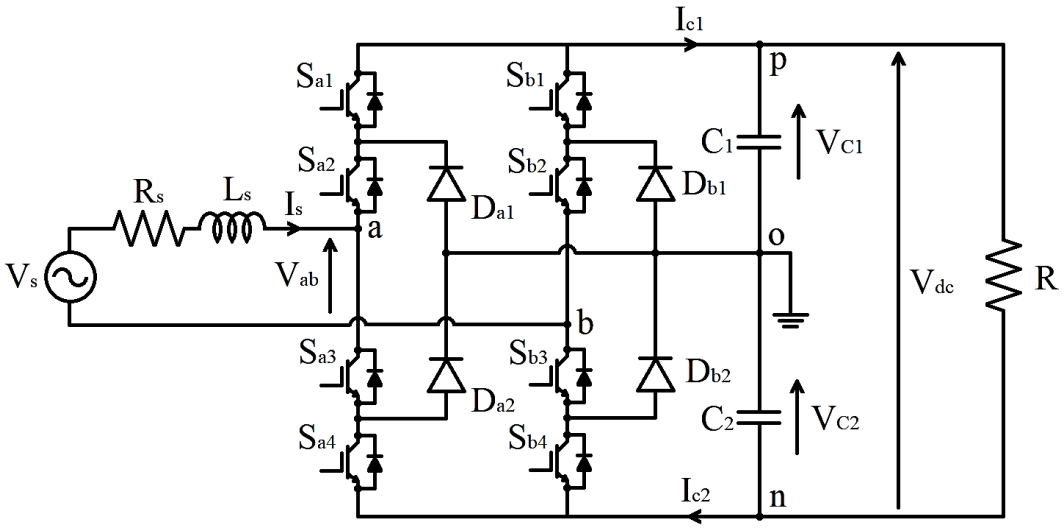


Figure 2.19: Single-Phase Three-Level Neutral Point Clamped Converter Circuit Topology

From Figure 2.19, the AC voltage source is connected to two capacitors at the load side through eight switches with four antiparallel diodes. Since there are eight switches, there are several combinations to control the switches for regulating the output DC voltage. The combinations of the switching can be expressed as Equation 2.115.

$$S_x = \begin{cases} 1, & S_{x1}, S_{x2}: ON \\ 0, & S_{x2}, S_{x3}: ON \\ -1, & S_{x3}, S_{x4}: ON \end{cases}, \qquad x = a, b \qquad \text{Equation 2.115}$$

By using the combination in Equation 2.115, the current of I_{C1} and I_{C2} can be defined as Equation 2.116 and Equation 2.117.

$$I_{C1} = \frac{S_a(S_a + 1) - S_b(S_b + 1)}{2} I_S \quad \text{Equation 2.116}$$

$$I_{C2} = \frac{S_a(S_a - 1) - S_b(S_b - 1)}{2} I_S \quad \text{Equation 2.117}$$

To predict the capacitor voltage of the converter, the equation can be finalized as Equation 2.118.

$$\frac{dv_{cx}}{dt} = \frac{i_{cx}}{C} \quad \text{Equation 2.118}$$

where $x = 1, 2$. Lastly, the mathematical equation is discretized by Euler's expansion for the MPC algorithm to compute the prediction and determine the switching combination.

$$v_{cx}(k + 1) = v_{cx}(k) + \frac{T_s i_{cx}(k)}{C} \quad \text{Equation 2.119}$$

At the AC voltage source side, the source voltage can be expressed as Equation 2.120.

$$V_s = R_s I_s + L_s \frac{dI_s}{dt} + V_{ab} \quad \text{Equation 2.120}$$

Then, the AC source current can be predicted by discretizing Equation 2.120 in terms of current. Lastly, the prediction of source current can be computed with Equation 2.121.

$$I_s(k + 1) = 1 - \frac{R_s T_s}{L_s} I_s(k) + \frac{T_s}{L_s} [V_s(k) - V_{ab}(k)] \quad \text{Equation 2.121}$$

After the output voltage and source current prediction algorithm are computed, the output voltage can be regulated with consideration of the source current. The cost function shown in Equation 2.122 includes the source current and the capacitor voltage balancing control.

$$g = |I_s^*(k+1) - I_s(k+1)| + \lambda_c |v_{c1}(k+1) - v_{c2}(k+1)| \qquad \text{Equation 2.122}$$

where I_s^* is the reference current and λ_c is the weighing factor for capacitor voltage balance.

The result of this literature showed that the MPC could regulate the output DC voltage while balancing the capacitor voltage. It showed an excellent result with extremely short computational time and low source current total harmonic distortion (THD).

2.5.5 MPC for Three-Phase AC-DC Converter

MPC was applied to a three-phase AC-DC power converter (Shi et al., 2019; Yang et al., 2020). This converter rectifies the three-phase AC voltage to a DC voltage. The circuit topology of a three-phase AC-DC converter is illustrated in Figure 2.20.

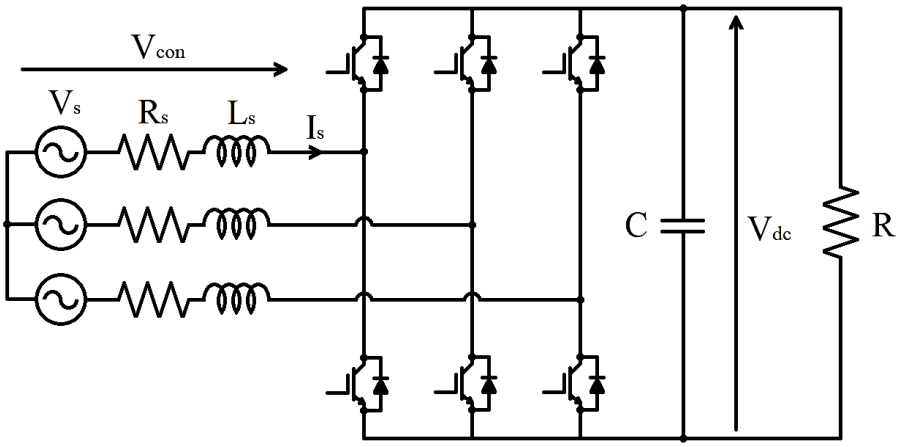


Figure 2.20: Three-Phase AC-DC Converter Circuit Topology

The converter consists of resistors and inductor filters at the source, six switches, and a capacitor at the load side. Under balanced conditions, the circuit formulation can be expressed as Equation 2.123 and Equation 2.124.

$$V_s = L_s \frac{dI_s}{dt} + R_s I_s + V_{con} \quad \text{Equation 2.123}$$

$$V_{con} = S_{con} V_{dc} \quad \text{Equation 2.124}$$

where S_{con} is the switching state vector that can be defined as Equation 2.125.

$$S_{con} = \frac{3}{2}\left(S_a + S_b e^{j\frac{2}{3}\pi} + S_c e^{-j\frac{2}{3}\pi}\right) \quad \text{Equation 2.125}$$

Then, the prediction of source voltage and current are defined as Equation 2.126 and Equation 2.127, respectively.

$$\frac{dV_s}{dt} = j\omega V_s \quad \text{Equation 2.126}$$

$$\frac{dI_s}{dt} = \frac{1}{L_s}(V_s - V_{con} - R_s I_s) \quad \text{Equation 2.127}$$

The apparent power, S and its first derivative produced by the three-phase AC source can be defined as Equation 2.128 and Equation 2.129, respectively.

$$S = \frac{2}{3}(I_s)^* V_s \quad \text{Equation 2.128}$$

$$\frac{dS}{dt} = \frac{1}{L_s}\left[\frac{3}{2}(V_s^2 - (V_{con})^* V_s) - (R_s - j\omega L_s)S\right] \quad \text{Equation 2.129}$$

where $*$ is the conjugate operator. The prediction of apparent power can be computed after the discretization by Euler's expansion.

$$S(k+1) = S(k) + \frac{T_s}{L_s}\left[\frac{3}{2}\left(V_s^2(k) - (V_{con})^* V_s(k)\right) - (R_s - j\omega L_s)S(k)\right] \quad \text{Equation 2.130}$$

This prediction can control the input power from the source while regulating the output voltage.

MPC was used to convert three-phase AC power into a DC source (Fang et al., 2021). The switches used in the converter were bidirectional Insulated Gate Bipolar Transistor (IGBT). The circuit topology is schematically shown in Figure 2.21.

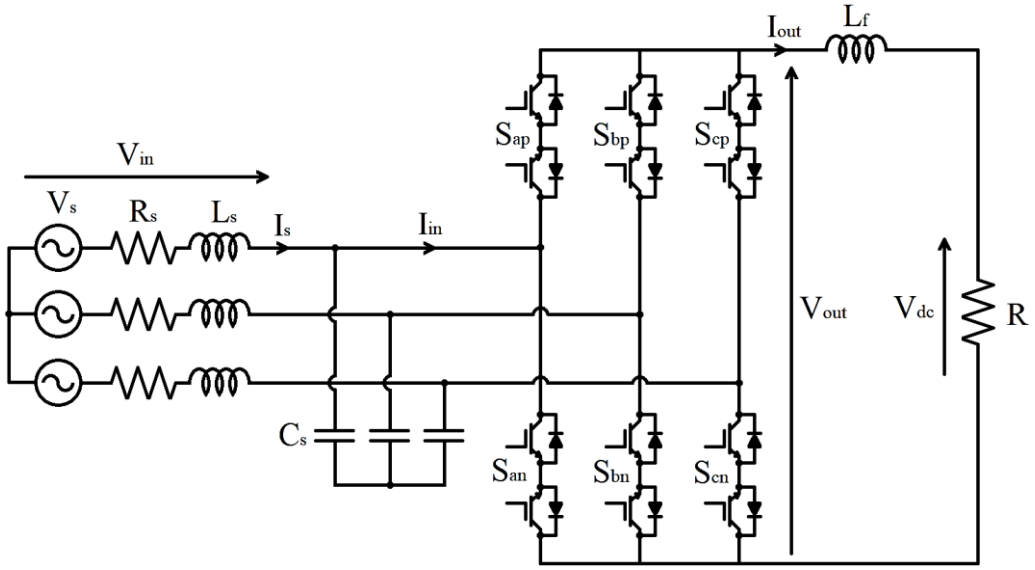


Figure 2.21: Bidirectional Switches Controlled Three-Phase AC-DC Converter Circuit Topology

Using forward Euler's expansion, the final predictive formula for source current, input voltage, and output current can be defined as Equation 2.131 to Equation 2.133.

$$I_s(k+1) = I_s(k) + \frac{T_s}{L_s}[V_s(k) - V_{in}(k) - R_s I_s(k)] \quad \text{Equation 2.131}$$

$$V_{in}(k+1) = V_{in}(k) + \frac{T_s}{C_s}[I_s(k) - I_{in}(k)] \quad \text{Equation 2.132}$$

$$I_{out}(k+1) = I_{out}(k) + \frac{T_s}{L_f}[V_{out}(k) - V_{dc}(k)] \quad \text{Equation 2.133}$$

2.5.6 MPC for Single-Phase DC-AC Inverter

A simple inverter for converting DC to single-phase AC was developed using MPC (X. Li et al., 2017). This inverter consists of an H-bridge and a secondary resistor-indictor-capacitor (RLC) filter between the DC source and the load. The structure of the inverter is shown in Figure 2.22.

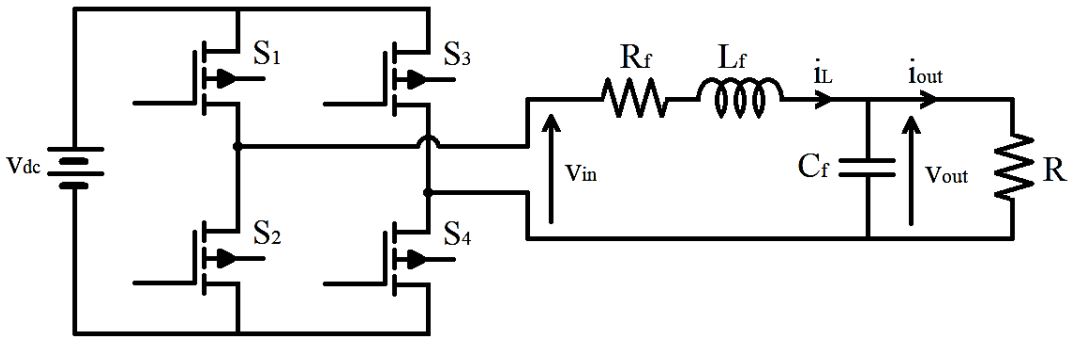


Figure 2.22: Single-Phase DC-AC Inverter Circuit Topology

There are four switches connected in the H-bridge. The different switching combinations will either cause the v_{in} become 0, v_{dc} or $-v_{dc}$. At the secondary filter side, the filter inductor current can be expressed as Equation 2.134 to Equation 2.136.

$$\frac{di_L}{dt} = \frac{1}{L_f}\left(v_{in} - v_{out} - i_L R_f\right) \quad \text{Equation 2.134}$$

$$\frac{dv_{out}}{dt} = \frac{1}{C_f}(i_L - i_{out}) \quad \text{Equation 2.135}$$

$$i_{out} = i_L - C_f \frac{dv_{out}}{dt} \quad \text{Equation 2.136}$$

The prediction of output voltage and current can be computed by discretizing the equations above by forward Euler's formula. The predicted output voltage and current can be defined as Equation 2.138 and Equation 2.139, respectively.

$$i_L(k+1) = i_L(k) + \frac{T_s}{L_f}\left[v_{in}(k) - v_{out}(k) - i_L(k)R_f\right] \quad \text{Equation 2.137}$$

$$v_{out}(k+1) = v_{out}(k) + \frac{T_s}{C_f}[i_L(k) - i_{out}(k)] \quad \text{Equation 2.138}$$

$$i_{out}(k+1) = i_L(k+1) - C_f\frac{v_{out}(k+1) - v_{out}(k)}{T_s} \quad \text{Equation 2.139}$$

This MPC algorithm can either control the output voltage or current with a reference AC waveform. Simulation results showed that the inverter could generate a pure sinusoidal AC voltage with constant amplitude and frequency (X. Li et al., 2017).

MPC was applied to a single-phase quasi-Z source inverter (Saavedra et al., 2023). This inverter contains a quasi-Z network between the DC source and the H-bridge switches. A visual representation of this inverter can be seen here in Figure 2.23.

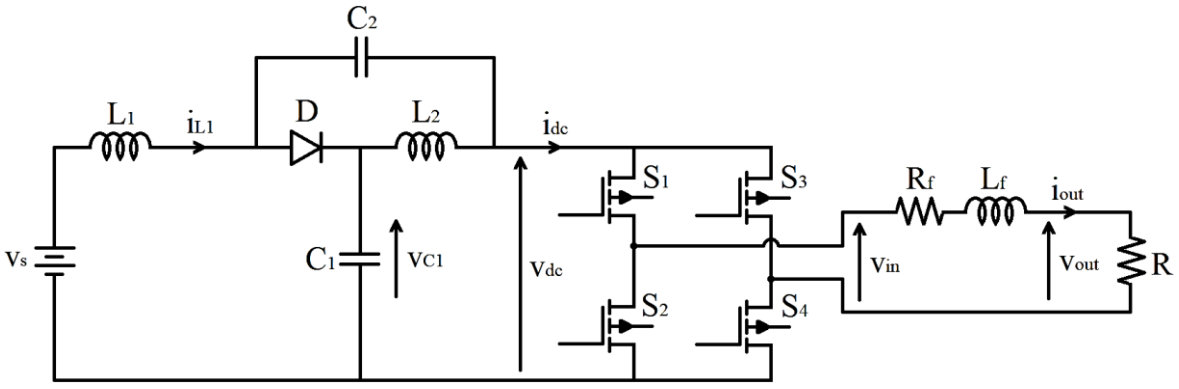


Figure 2.23: Single-Phase Quasi-Z Source Inverter Circuit Topology

The quasi-Z source inverter has two models of operation, which are known as shoot-through (ST) mode and non-shoot-through (nST) mode. The operation model is determined by the current flow through the diode. If the diode is reverse-biased, the inverter is in shoot-through mode. On the contrary, the inverter becomes a non-shoot-through mode when the diode is forward-biased. Therefore, a conditional variable is affected by the model operation of the inverter with Equation 2.140.

$$S_{ST} = \begin{cases} 0, & nST \\ 1, & ST \end{cases} \qquad \text{Equation 2.140}$$

Then, the rate of change of inductors current and capacitors voltage are defined in Equation 2.141 to Equation 2.144. For the output, the rate of change of current can be expressed as Equation 2.145.

$$\frac{di_{L1}}{dt} = \frac{1}{L_1}[(1 - S_{ST})(v_s - v_{C1}) + S_{ST}(v_s - v_{C2})] \qquad \text{Equation 2.141}$$

$$\frac{di_{L2}}{dt} = \frac{1}{L_2}[(1 - S_{ST})(-v_{C2}) + S_{ST}v_{C1}] \qquad \text{Equation 2.142}$$

$$\frac{dv_{C1}}{dt} = \frac{1}{C_1}[(1 - S_{ST})(i_{L1} - i_{dc}) - S_{ST}i_{L2}] \qquad \text{Equation 2.143}$$

$$\frac{dv_{C2}}{dt} = \frac{1}{C_2}[(1 - S_{ST})(i_{L2} - i_{dc}) - S_{ST}i_{L1}] \qquad \text{Equation 2.144}$$

$$\frac{di_{out}}{dt} = \frac{1}{L_f}\left(v_{in} - i_{out}R_f - i_{out}R\right), \qquad v_{in} = \begin{cases} v_{dc}, & S_1, S_4: ON \\ 0, & S: OFF, nST \\ -v_{dc}, & S_2, S_3: ON \end{cases} \qquad \text{Equation 2.145}$$

Lastly, the prediction of the MPC algorithm can be discretized by the forward-Euler expansion method. The capacitor voltage, v_{C1}, inductor current, i_{L1} and output current, i_{out} are expressed as Equation 2.146 to Equation 2.148.

$$i_{L1}(k+1) = i_{L1}(k) + \frac{T_s}{L_1}\left[(1 - S_{ST})\left(v_s(k) - v_{C1}(k)\right) + S_{ST} v_{C1}(k)\right] \quad \text{Equation 2.146}$$

$$v_{C1}(k+1) = v_{C1}(k) + \frac{T_s}{C_1}\left[(1 - S_{ST})\left(i_{L1}(k) - i_{dc}(k)\right) - S_{ST} i_{L1}(k)\right] \quad \text{Equation 2.147}$$

$$i_{out}(k+1) = i_{out}(k) + \frac{T_s}{L_f}\left[2v_{C1}(k) - v_{in}(k) - i_{out}(k)\left(R_f + R\right)\right] \quad \text{Equation 2.148}$$

The MPC algorithm can determine the switching control by comparing the predicted value with the reference values.

MPC was implemented in a single-phase five-level hybrid Active Neutral-Point-Clamped (ANPC) inverter (Najjar et al., 2021). It divides the DC voltage into five levels for the MPC algorithm to determine which level to select. The circuit topology of this inverter is shown in Figure 2.24.

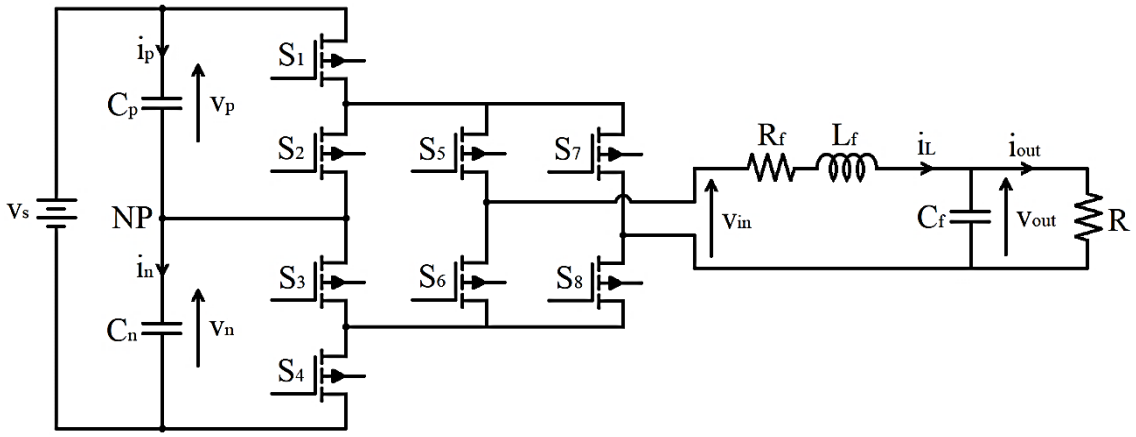


Figure 2.24: Single-Phase Five-Level ANPC Inverter

The different switching combinations will determine the AC voltage, v_{in}. Eight switching combinations resulting in voltage, v_{in} in five levels. Table 2.3 shows the different

switching states of each switch with the corresponding v_{in} based on each switching combinations.

Table 2.3: Switching Combinations of Single-Phase Five-Level ANPC Inverter

Vector	Switching State								v_{in}
	S_1	S_2	S_3	S_4	S_5	S_6	S_7	S_8	
1	1	0	0	1	1	0	0	1	v_s
2	1	0	1	0	1	0	0	1	$0.5 \times v_s$
3	0	1	0	1	1	0	0	1	$0.5 \times v_s$
4	0	1	1	0	1	0	0	1	0
5	0	1	1	0	0	1	1	0	0
6	1	0	1	0	0	1	1	0	$-0.5 \times v_s$
7	0	1	0	1	0	1	1	0	$-0.5 \times v_s$
8	1	0	0	1	0	1	1	0	$-v_s$

By using the table above, the AC voltage can be divided into $-v_s$, $-0.5v_s$, 0, $0.5v_s$ and v_s. Then, the AC voltage regulation can be done at the filter part by the MPC algorithm. The rate of change of the inductor filter current and capacitor filter voltage can be expressed as Equation 2.149 and Equation 2.150, respectively.

$$\frac{di_L}{dt} = \frac{1}{L_f}\left(v_{in} - i_L R_f - v_{out}\right) \qquad \text{Equation 2.149}$$

$$\frac{dv_{out}}{dt} = \frac{1}{C_f}(i_L - i_{out}) \qquad \text{Equation 2.150}$$

The prediction of the output voltage can be computed by determining the next step of v_{out} as shown in Equation 2.152.

$$i_L(k+1) = i_L(k) + \frac{T_s}{L_f}\left[v_{in} - i_L(k)R_f - v_{out}(k)\right] \quad \text{Equation 2.151}$$

$$v_{out}(k+1) = v_{out}(k) + \frac{T_s}{C_f}[i_L(k) - i_{out}(k)] \quad \text{Equation 2.152}$$

This method performs a high accuracy of voltage control with a pure sinusoidal signal. It has a low THD because the AC voltage can be divided into five levels. The MPC algorithm can select the optimum voltage for filtering. The THD can become extremely low, within 0.2% when the MPC is enhanced with a constant switching frequency.

2.5.7 MPC for Three-Phase DC-AC Inverter

MPC was introduced in the general model of three-phase DC-AC inverters (Estrada et al., 2021; Rodriguez et al., 2020; Shan et al., 2019). A three-phase DC-AC inverter can change a single DC power source to three-phase AC power with controlled voltage and frequency for three distribution lines or loads. A general model of a three-phase consists of six switches to invert the DC voltage to a three-phase AC voltage. In addition, a secondary resistor-inductor (RL) filter is important to enhance the power quality by regulating the AC voltage approaching the pure sinusoidal waveform. Figure 2.25 shows a basic model of a three-phase inverter.

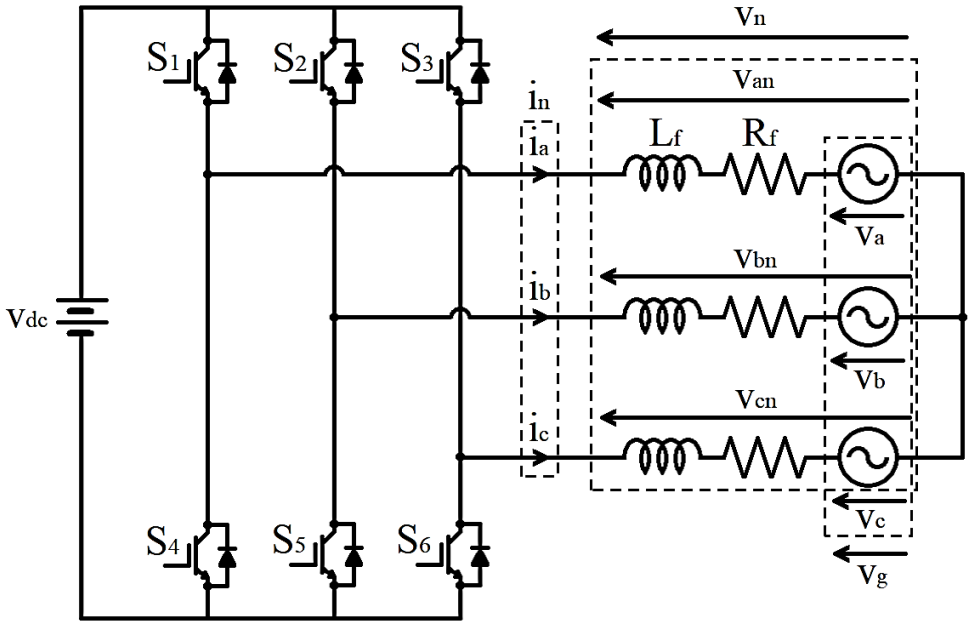


Figure 2.25: General Model of Three-Phase DC-AC Inverter Circuit Topology

There are six switches, which are divided into 3 pairs. Each pair of switches is complementary. Therefore, eight switching combinations affect the changes in the voltage. The AC voltage before the filter is defined in a complex form shown in Equation 2.153.

$$v_n = \begin{cases} \frac{2}{3} v_{dc}^{*} e^{j(i-1)\frac{\pi}{3}}, & i = 1,2,3,4,5,6 \\ 0, & i = 0,7 \end{cases} \qquad \text{Equation 2.153}$$

A schematic diagram of this equation is shown in Figure 2.26.

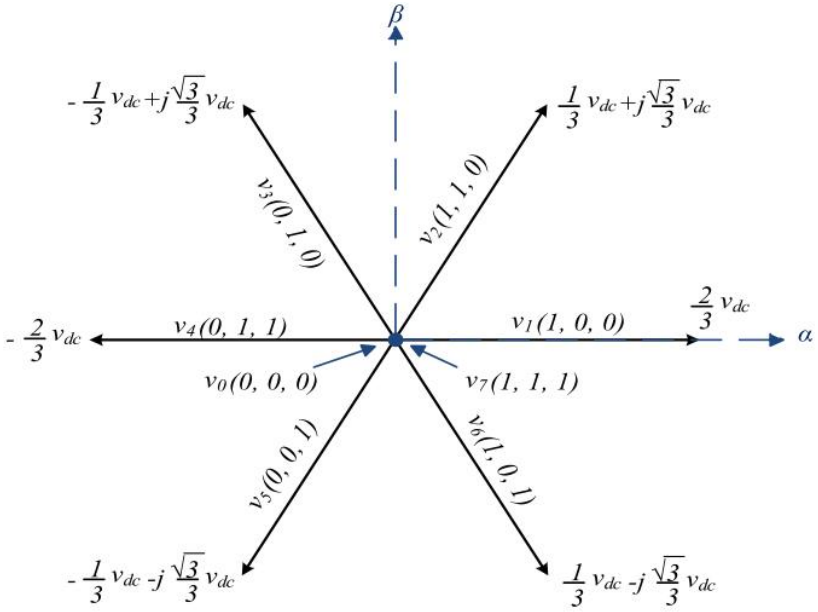


Figure 2.26: Switching Combination Responding to AC Voltage for Three-Phase Inverter (Rodriguez et al., 2020)

From Figure 2.25, the mathematical equation at the AC side can be determined by Kirchhoff's Voltage Law, which is shown in Equation 2.154.

$$v_n = L_f \frac{di_n}{dt} + i_n R_f + v_g \qquad \text{Equation 2.154}$$

Then, the output current can be computed to predict the next step by using the MPC algorithm. The prediction of the output current of each phase is defined as shown in Equation 2.155 to Equation 2.157.

$$i_a(k+1) = i_a(k) + \frac{T_s}{L_f}\left(v_{an}(k) - i_a(k)R_f - v_a(k)\right) \qquad \text{Equation 2.155}$$

$$i_b(k+1) = i_b(k) + \frac{T_s}{L_f}\left(v_{bn}(k) - i_b(k)R_f - v_b(k)\right) \qquad \text{Equation 2.156}$$

$$i_c(k+1) = i_c(k) + \frac{T_s}{L_f}\left(v_{cn}(k) - i_c(k)R_f - v_c(k)\right) \qquad \text{Equation 2.157}$$

This method showed its characteristic in controlling the output current from a DC source to an AC power. Simulation results confirmed that three-phase AC could be regulated into a pure sinusoidal waveform with constant amplitude and frequency (Estrada et al., 2021; Rodriguez et al., 2020; Shan et al., 2019).

A three-phase DC-AC inverter was improved into a five-level active NPC inverter (Liu et al., 2020). The power quality was improved due to the five-level division of the DC source input voltage. This inverter requires many switches to control the input voltage of the three-phase circuit. The design of this inverter is shown in Figure 2.27.

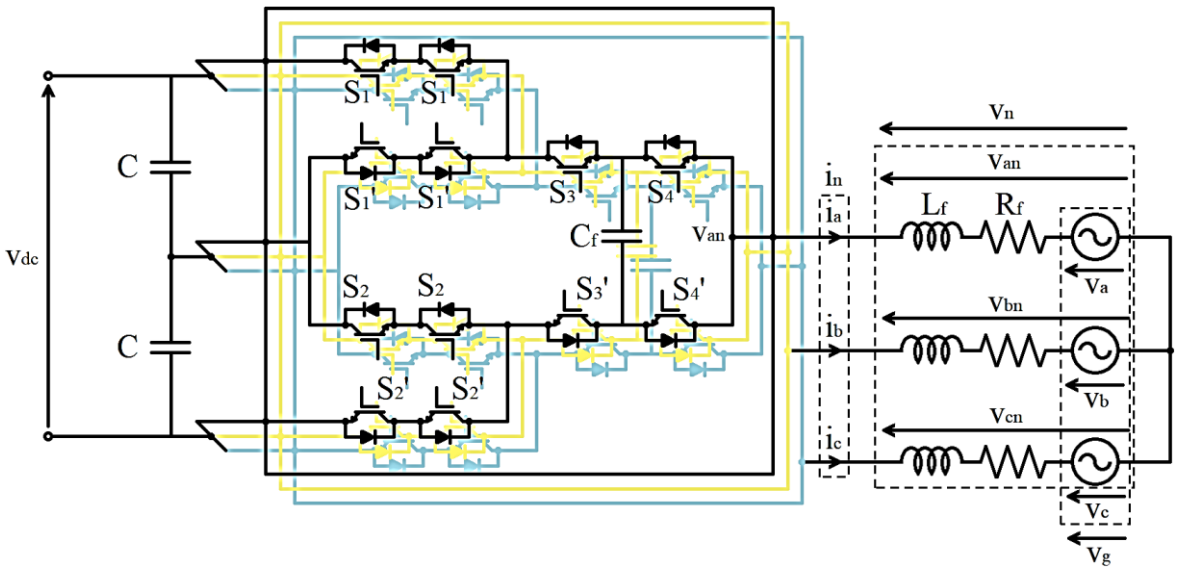


Figure 2.27: Three-Phase Five-Level Active NPC Inverter Circuit Topology

This inverter is similar to the single-phase five-level active NPC inverter (Najjar et al., 2021). However, this inverter was designed for three-phase electrical power distribution.

Its switching combination will determine the level of voltage at v_n. The switching state corresponding to v_n for each switching combinations are listed in Table 2.4.

Table 2.4: Switching Combinations of Three-Phase Five-Level ANPC Inverter

Vector	Switching State				Voltage Level
	S_1	S_2	S_3	S_4	
0	1	0	0	1	v_s
1	1	0	1	0	$0.5 \times v_s$
2	0	1	0	1	$0.5 \times v_s$
3	0	1	1	0	0
4	0	1	1	0	0
5	1	0	1	0	$-0.5 \times v_s$
6	0	1	0	1	$-0.5 \times v_s$
7	1	0	0	1	$-v_s$

The three-phase five-level inverter used the same MPC prediction algorithm as in earlier studies (Estrada et al., 2021; Rodriguez et al., 2020; Shan et al., 2019). The difference of this inverter is that there are five levels of input voltage for the MPC algorithm to select the optimum voltage. The switching combination responding to AC voltage can be illustrated in Figure 2.28.

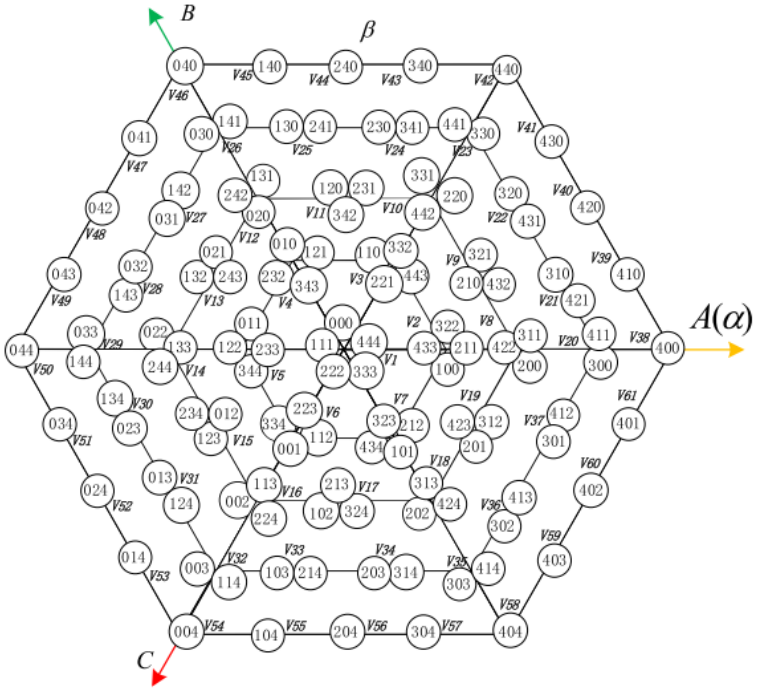


Figure 2.28: Switching Combination Responding to AC Voltage for Three-Phase Five-Level Inverter (Liu et al., 2020)

Another three-phase inverter with four pairs of switches controlled by MPC was introduced, including one additional pair compared to the general model (Fayyaz et al., 2023). It has one extra pair of switches more than the general model of a three-phase inverter. The extra pair of switches is connected to the neutral of the three-phase load. This enables the inverter to control the neutral current of the load. The advantage of the three-phase four-legged inverter is that it can handle both balanced and unbalanced loads in the three-phase electrical circuit. Its circuit topology is schematically shown in Figure 2.29.

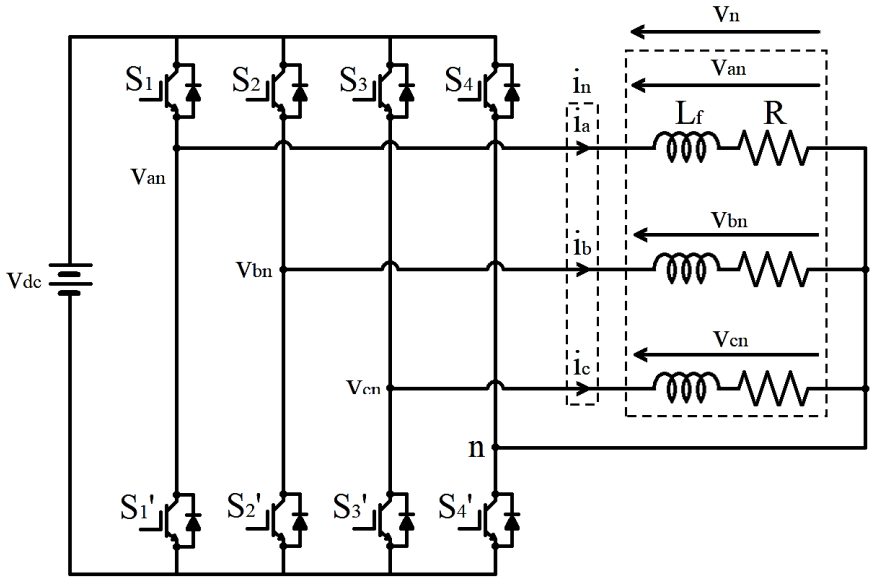


Figure 2.29: Three-Phase Four-Legged Inverter Circuit Topology

For a three-phase four-legged inverter, the voltage of each phase can be controlled by its switches. The mathematical model for the input voltage of each phase can be expressed as shown in Equation 2.158 to Equation 2.160.

$$v_{an} = (S_1 - S_4)v_{dc} \qquad \text{Equation 2.158}$$

$$v_{bn} = (S_2 - S_4)v_{dc} \qquad \text{Equation 2.159}$$

$$v_{cn} = (S_3 - S_4)v_{dc} \qquad \text{Equation 2.160}$$

Using Kirchhoff's Voltage Law, the voltage at the filter and load side can be defined as Equation 2.161.

$$v_n = L_f \frac{di_n}{dt} + i_n R \qquad \text{Equation 2.161}$$

From Equation 2.161, the prediction of the output AC can be computed as Equation 2.162.

$$i_n(k+1) = i_n(k) + \frac{T_s}{L_f}(v_n(k) - i_n(k)R) \quad \text{Equation 2.162}$$

2.5.8 MPC for Three-Phase AC Output Control

A three-phase direct matrix converter was developed to regulate AC supply output (Toledo et al., 2022; Vijayagopal et al., 2017; Zhang et al., 2019). A three-phase direct matrix converter can control output to a desired value by MPC. It consists of an RLC filter at the input side and nine switches connected as a matrix converter. The circuit topology of the three-phase direct matrix converter is shown in Figure 2.30.

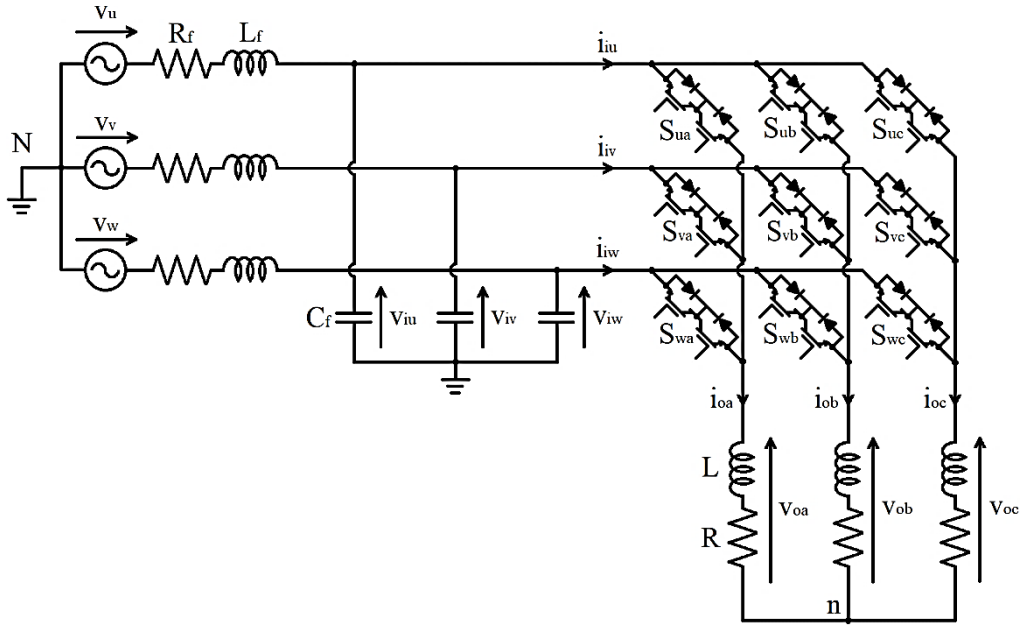


Figure 2.30: Three-Phase Direct Matrix Converter Circuit Topology

Since the switches are connected as a 3×3 matrix converter, the output voltage of the converter can be defined as Equation 2.163.

$$\begin{pmatrix} v_{oa} \\ v_{ob} \\ v_{oc} \end{pmatrix} = \begin{pmatrix} S_{ua} & S_{va} & S_{wa} \\ S_{ub} & S_{vb} & S_{wb} \\ S_{uc} & S_{vc} & S_{wc} \end{pmatrix} \begin{pmatrix} v_{iu} \\ v_{iv} \\ v_{iw} \end{pmatrix} \quad \text{Equation 2.163}$$

Using the same MPC algorithm, the prediction of output current can be computed as Equation 2.164.

$$i_o(k+1) = i_o(k) + \frac{T_s}{L}(v_o(k) - v_{nN}(k) - i_o(k)R) \qquad \text{Equation 2.164}$$

$$v_{nN}(k) = \frac{v_{aN}(k) + v_{bN}(k) + v_{cN}(k)}{3} \qquad \text{Equation 2.165}$$

The performance of MPC in AC output current control was reported (Zhang et al., 2019). The simulation results showed that the MPC can regulate the AC according to the reference current with a THD within 5%. The simulation results are validated by the experimental results. It showed a similar performance to the simulation results.

A three-phase AC output current control using MPC was also presented (Basri & Mekhilef, 2022). The power converter used in this literature is the combination of the bidirectional switches controlled three-phase AC to DC converter and the three-phase four-legged inverter through a dual-buck switching circuit. This power converter is schematically shown in Figure 2.31.

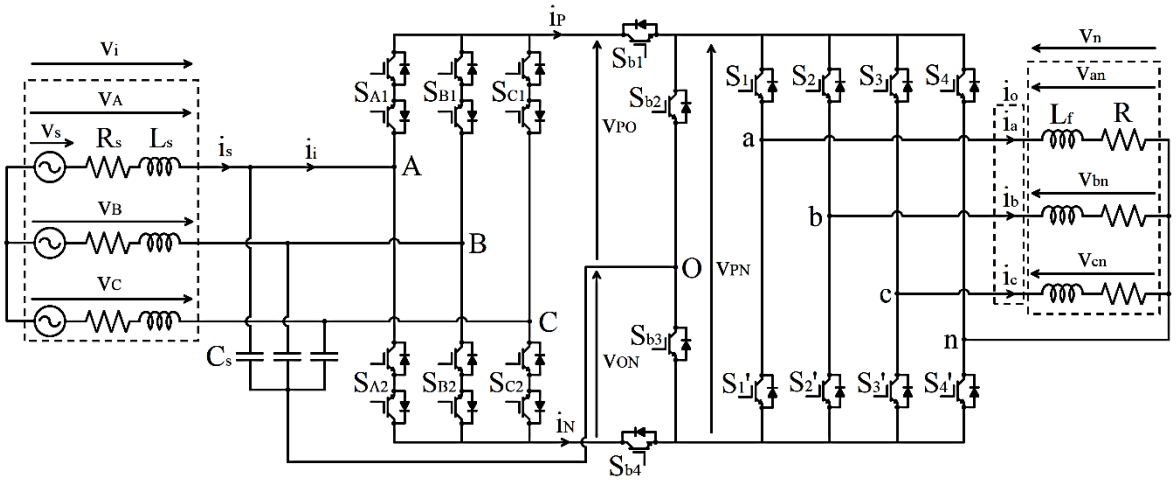


Figure 2.31: Three-level Four-Leg Indirect Matrix Converter

At the AC power supply side, the RLC filter mitigates the THD by the MPC algorithm, which is shown in Equation 2.166.

$$\frac{d}{dt}\begin{pmatrix} v_i \\ i_s \end{pmatrix} = \begin{pmatrix} 0 & \frac{1}{C_s} \\ -\frac{1}{L_s} & -\frac{R_s}{L_s} \end{pmatrix}\begin{pmatrix} v_i \\ i_s \end{pmatrix} + \begin{pmatrix} 0 & \frac{1}{C_s} \\ \frac{1}{L_s} & 0 \end{pmatrix}\begin{pmatrix} v_s \\ i_i \end{pmatrix} \quad \text{Equation 2.166}$$

Then, the forward step prediction of the source current and filter voltage can be computed as Equation 2.167.

$$\begin{bmatrix} v_i(k+1) \\ i_s(k+1) \end{bmatrix} = e^{AT_s}\begin{bmatrix} v_i(k) \\ i_s(k) \end{bmatrix} + A^{-1}(e^{AT_s} - I_{2\times 2})B\begin{bmatrix} v_s(k) \\ i_i(k) \end{bmatrix} \quad \text{Equation 2.167}$$

After the AC voltage is rectified, the dual-buck switches divide the DC voltage in half, as Equation 2.168.

$$\begin{pmatrix} v_{PO} \\ v_{ON} \end{pmatrix} = \begin{pmatrix} S_{A1} & S_{B1} & S_{C1} \\ S_{A2} & S_{B2} & S_{C2} \end{pmatrix}\begin{pmatrix} v_A \\ v_B \\ v_C \end{pmatrix} \quad \text{Equation 2.168}$$

From the equation, the voltage is divided into two potential differences, named as v_{PO} and v_{ON}. The purpose is to increase the number of voltage levels for the MPC algorithm to select the optimum voltage level. Therefore, the input voltage for the four-legged inverter is dependent on the switching of the dual-buck switches, which is defined as Equation 2.169.

$$v_{PN} = \begin{pmatrix} S_{b1} & S_{b4} \end{pmatrix}\begin{pmatrix} v_{PO} \\ v_{ON} \end{pmatrix} \quad \text{Equation 2.169}$$

After that, the AC voltage of the inverter can be controlled by the four-legged switches. The MPC algorithm is the same as the method introduced from Equation 2.158 to Equation 2.162.

The experimental results proved that the MPC was able to manage the three-phase AC output under an unbalanced voltage source and an unbalanced load (Basri & Mekhilef,

2022). Although the three-phase input voltage was unbalanced, the MPC algorithm could regulate the load current to the reference current with a low THD below 9%.

2.6 Chapter Summary

This chapter discusses the existing types of fuel cells and their basic information. Since this research is focusing on the PEMFC, the mathematical model of the PEMFC is explained based on the literature review. The fully functional mathematical model of the PEMFC is significant in representing its features in simulation. This research includes the simulation of the PEMFC and the investigation of its MPPT method. Therefore, the mathematical model of PEMFC is studied and computed in MATLAB / Simulink based on the mathematical equation in Section 2.3.

In the present study, an MPPT should be addressed with high priority for the PEMFC system to operate with the highest efficiency. Many MPPT techniques applied to the PEMFC are also introduced to gain knowledge of the research on the electrical power generation and power efficiency of PEMFC. This research also includes the development of the MPPT for PEMFC using the MPC method. Therefore, a new predictive MPPT technique will be designed for the PEMFC to generate the maximum electrical power.

The MPC is widely used in electrical, electronic, and mechanical fields. Since the power electronics are necessary for a PEMFC to achieve the MPP, the use of MPC in power electronics is also discussed in this chapter. In this research, a standard DC-DC boost converter is applied as the power converter to regulate the DC output voltage of the PEMFC. The design of the MPC algorithm for a DC-DC boost converter is shown in Figure 2.14. It is expected that the DC-DC boost converter works with the predictive MPPT control and leads the PEMFC to generate the electrical power at MPP.

Besides MPPT, the MPC also enables the power conversion of DC to AC through an inverter. In this research, a single-phase DC-AC inverter by the MPC algorithm is designed to provide a standard AC voltage with constant amplitude and frequency. This is crucial for an electrical appliance to function with an AC power supply. Therefore, an H-bridge inverter with a secondary filter is designed for inverting the DC power to AC source. For this inverter, the MPC algorithm for filter voltage follows Equation 2.167 for generating the pure sinusoidal AC voltage waveform.

CHAPTER 3

RESEARCH METHODOLOGY

3.1 Introduction

In this chapter, the methodology of the research is explained in detail. This research investigates a predictive MPPT technique and a predictive AC voltage control method for a PEMFC system. Simulation helps to understand the concepts, theories, equations, and algorithms applied in a PEMFC system. It also allows ideas to be verified by producing the results from different variables. Therefore, a new design concept can be proved in the simulation by using MATLAB software.

The whole PEMFC simulation system includes fully functional mathematical modeling of PEMFC, DC-DC power converter, predictive MPPT control, and predictive voltage control. The DC-DC power converter is the main power electronic component that is connected between the PEMFC system and the load. The predictive MPPT controller either directly controls the switch of the DC-DC power converter or commands the switch through a Pulse Width Modulation (PWM) generator to manipulate the switching state. So, the output voltage of the fuel cell will be regulated by the DC-DC boost converter according to the MPPT algorithm. Figure 3.1(a) shows the configuration of the PEMFC system with the Predictive MPPT Controller. When the predictive voltage control is included, the load voltage can be converted to AC voltage with constant amplitude and frequency. This configuration is presented in Figure 3.1(b).

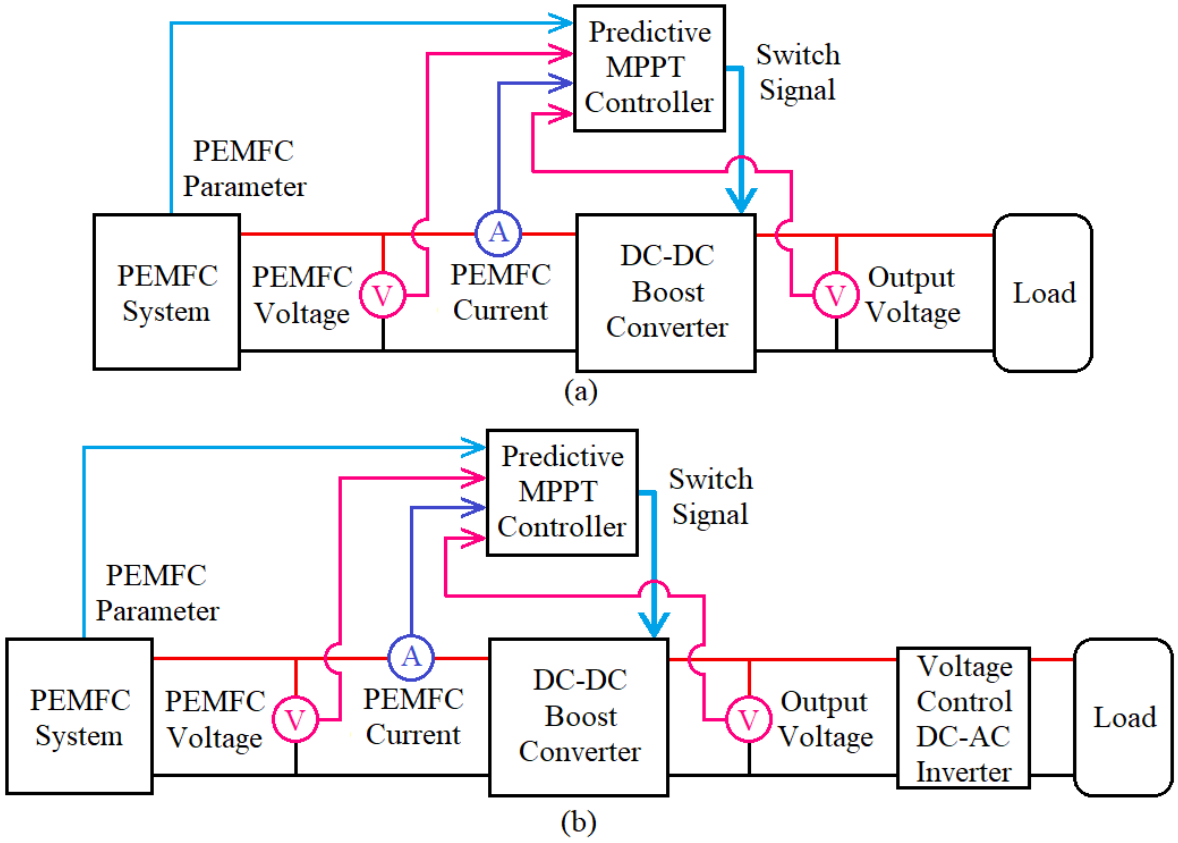


Figure 3.1: PEMFC System and Predictive MPPT Controller Configuration (a) Without Predictive Voltage Control Inverter, (b) With Predictive Voltage Control Inverter

3.2 Mathematical Model of PEMFC

To simulate the PEMFC system with an MPPT technique, the first step is to construct an accurate PEMFC model. The fully functional mathematical PEMFC model can be developed by using the equations from Equation 2.4 to Equation 2.15. The mathematical model of PEMFC is programmed in MATLAB software, which represents the fuel cell system. A snapshot of the PEMFC mathematical model designed in MATLAB/Simulink is shown in Figure 3.2.

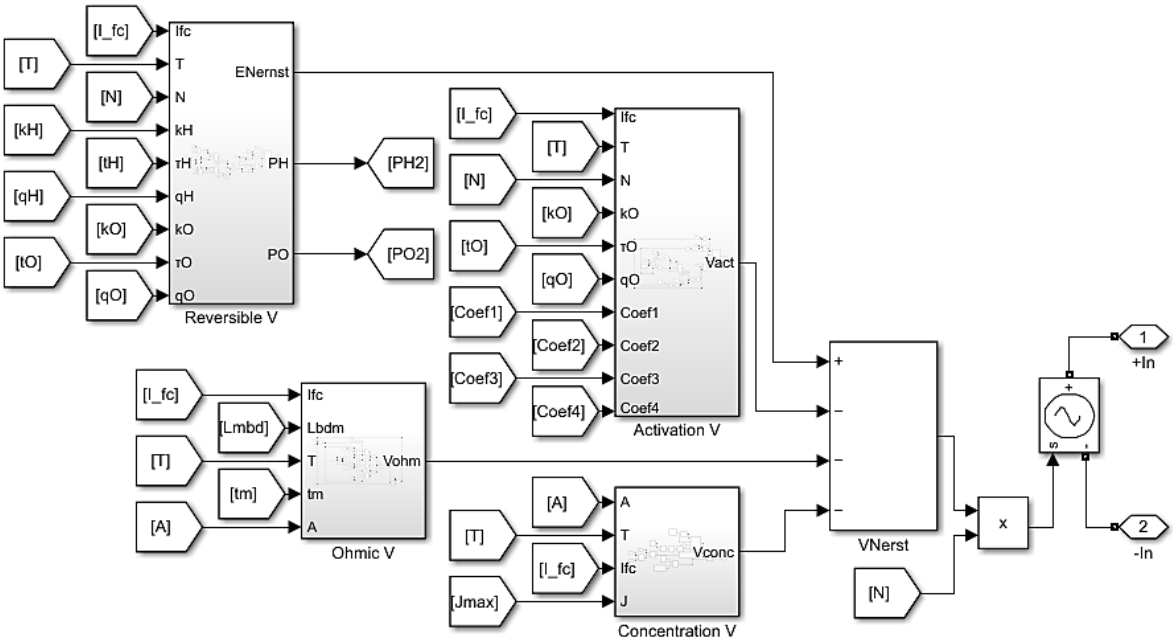


Figure 3.2: Fully Functional Mathematical Modeling of PEMFC System

After constructing a PEMFC model, it is important to determine which parameters of PEMFC highly affect the polarization curve. The PEMFC model can be simulated in MATLAB with varying parameters such as partial pressure of oxygen and hydrogen, relative humidity, and operational temperature. From the simulation, a different polarization curve can be created, and the MPP will be different.

3.3 Maximum Power Point Tracker

As mentioned, the environmental parameters will affect the operation of the PEMFC. It indicates that changing the parameters will also change the MPP of the PEMFC during operation. Therefore, it is important to track the MPP and control the output power at that particular point.

3.3.1 Newton–Raphson Method

Due to the equation involving logarithm and polynomial function, the Newton–Raphson method is suitable to solve the non-linear equation. Therefore, an MPP tracker has been implemented using the Newton–Raphson Method. Newton–Raphson method is a quick approximation of the root of a non-linear equation. The concept of Newton–Raphson method is to approximate the root and reduce the approximation error in the next iteration. It starts with an initial guess of the root and computes the next approximation, which is better than the initial guess. This step can be iterated until the approximation converges to the actual root. Figure 3.3 shows that the root estimation becomes more precise as the number of calculation iterations increases. The basic equation of Newton–Raphson method is shown in Equation 3.1.

$$x_{i+1} = x_i - \frac{f(x_i)}{f'(x_i)} \qquad \text{Equation 3.1}$$

where x is the root to be found and i is the number of iterations.

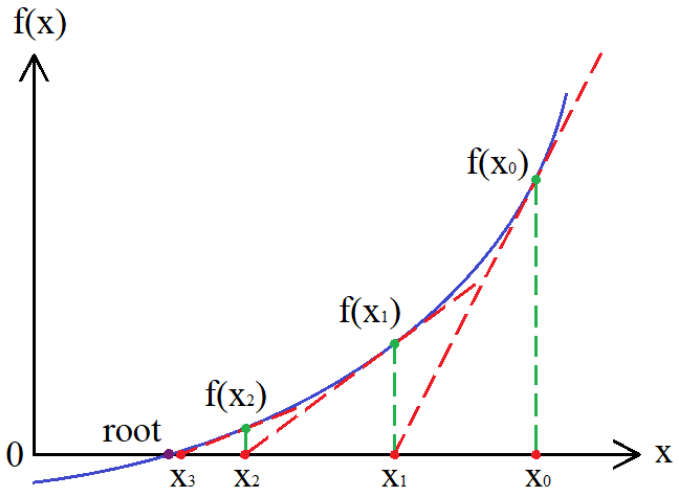


Figure 3.3: Newton–Raphson Approximation Concept

By substituting the equations from Equation 2.7 to Equation 2.14 into Equation 2.15, the PEMFC output power is shown in Equation 3.2. The first derivative of PEMFC output power is required to determine the current at MPP. The MPP is located at the point when $dP_{FC}/dI_{FC} = 0$ and the MPP current can be defined. However, the non-linear equation is difficult to solve. Therefore, Newton–Raphson method is implemented to solve the root of the first derivative of PEMFC output power. In this case, the second derivative of PEMFC output power is required to accomplish the algorithm. Its first derivative and second derivative are expressed as Equation 3.3 and Equation 3.4, respectively.

$$P_{FC} = N(I_{FC}E_{nerst} - I_{FC}V_{act} - I_{FC}V_{ohm} - I_{FC}V_{conc}) \quad \text{Equation 3.2}$$

$$\frac{dP_{FC}}{dI_{FC}} = N\frac{d(I_{FC}E_{nerst} - I_{FC}V_{act} - I_{FC}V_{ohm} - I_{FC}V_{conc})}{dI_{FC}} \quad \text{Equation 3.3}$$

$$\frac{d^2P_{FC}}{dI_{FC}^{\ 2}} = N\frac{d^2(I_{FC}E_{nerst} - I_{FC}V_{act} - I_{FC}V_{ohm} - I_{FC}V_{conc})}{dI_{FC}^{\ 2}} \quad \text{Equation 3.4}$$

Since the first and second derivatives of PEMFC output power are essential in Newton–Raphson method, they must also be derived to compute the equation.

3.3.2 First Derivative of Reversible Thermodynamic Power

This section derives the first derivative of reversible thermodynamic power $(I_{FC}E_{nerst})$. By substituting Equation 2.4 into the equation, the first derivative of the reversible thermodynamic power of the PEMFC is derived as Equation 3.6.

$$\frac{dI_{FC}E_{nerst}}{dI_{FC}} = \frac{dI_{FC}\left[1.229 - 8.5 \times 10^{-4}(T - 298.15) + 4.308 \times 10^{-5}T\ln P_{H_2}P_{O_2}^{0.5}\right]}{dI_{FC}} \quad \text{Equation 3.5}$$

$$\frac{dI_{FC}E_{nerst}}{dI_{FC}} = 1.229 - 8.5 \times 10^{-4}(T - 298.15) + a_1 + b_1 \quad \text{Equation 3.6}$$

where $a_1 = 4.308 \times 10^{-5} T \left[\frac{-2k_r I_{FC}\left(1-e^{\left(-\frac{t}{\tau_{H_2}}\right)}\right)}{q_{H_2}^{in}-2k_r I_{FC}\left(1-e^{\left(-\frac{t}{\tau_{H_2}}\right)}\right)} + \ln \frac{q_{H_2}^{in}-2k_r I_{FC}\left(1-e^{\left(-\frac{t}{\tau_{H_2}}\right)}\right)}{k_{H_2}} \right]$ and

$b_1 = 2.154 \times 10^{-5} T \left[\frac{-k_r I_{FC}\left(1-e^{\left(-\frac{t}{\tau_{O_2}}\right)}\right)}{q_{O_2}^{in}-k_r I_{FC}\left(1-e^{\left(-\frac{t}{\tau_{O_2}}\right)}\right)} + \ln \frac{q_{O_2}^{in}-k_r I_{FC}\left(1-e^{\left(-\frac{t}{\tau_{O_2}}\right)}\right)}{k_{O_2}} \right]$.

3.3.3 First Derivative of Activation Power Loss

This section derives the first derivative of activation power loss on the electrodes ($I_{FC}V_{act}$). By substituting Equation 2.8 into the equation, the first derivative of power loss at the rate of reactions on the electrodes is derived as Equation 3.8.

$$\frac{dI_{FC}V_{act}}{dI_{FC}} = \frac{dI_{FC}\left(\xi_1 + \xi_2 T + \xi_3 T \ln C_{O_2} + \xi_4 T \ln I_{FC}\right)}{dI_{FC}} \qquad \text{Equation 3.7}$$

$$\frac{dI_{FC}V_{act}}{dI_{FC}} = \xi_1 + \xi_2 T + a_2 + \xi_4 T(1 + \ln I_{FC}) \qquad \text{Equation 3.8}$$

where $a_2 = \xi_3 T \left[\frac{-k_r I_{FC}\left(1-e^{\left(-\frac{t}{\tau_{O_2}}\right)}\right)}{q_{O_2}^{in}-k_r I_{FC}\left(1-e^{\left(-\frac{t}{\tau_{O_2}}\right)}\right)} + \ln \frac{q_{O_2}^{in}-k_r I_{FC}\left(1-e^{\left(-\frac{t}{\tau_{O_2}}\right)}\right)}{k_{O_2}(5.08\times10^6)e^{\frac{-498}{T}}} \right]$.

3.3.4 First Derivative of Ohmic Power Loss

This section derives the first derivative of the ohmic power loss ($I_{FC}V_{ohm}$). By substituting Equation 2.10, Equation 2.11, and Equation 2.12 into the equation, the first derivative of power loss on resistance of proton flow in the electrodes is derived as Equation 3.10.

$$\frac{dI_{FC}V_{ohm}}{dI_{FC}} = \frac{d\left[I_{FC}^2 \times \frac{t_m}{A} \times 181.6 \times \frac{1 + 0.03\left(\frac{I_{FC}}{A}\right) + 0.062\left(\frac{T}{303}\right)^2\left(\frac{I_{FC}}{A}\right)^{2.5}}{\left[\lambda_m - 0.634 - 3\left(\frac{I_{FC}}{A}\right)\right]e^{4.18\left(\frac{T-303}{T}\right)}}\right]}{dI_{FC}} \quad \text{Equation 3.9}$$

$$\frac{dI_{FC}V_{ohm}}{dI_{FC}} = \frac{b_3\frac{da_3}{dI_{FC}} - a_3\frac{db_3}{dI_{FC}}}{b_3^2} \quad \text{Equation 3.10}$$

where

$$a_3 = 181.6t_m\left[I_{FC}^2 + 0.03\left(\frac{I_{FC}^3}{A}\right) + 0.062\left(\frac{T}{303}\right)^2\left(\frac{I_{FC}^{4.5}}{A^{2.5}}\right)\right],$$

$$\frac{da_3}{dI_{FC}} = 363.2t_mI_{FC} + 16.344t_m\left(\frac{I_{FC}^2}{A}\right) + 5.51867 \times 10^{-4}t_mT^2\left(\frac{I_{FC}^{3.5}}{A^{2.5}}\right),$$

$$b_3 = (\lambda_mA - 0.634A - 3I_{FC})e^{4.18\left(\frac{T-303}{T}\right)},$$

$$\frac{db_3}{dI_{FC}} = -3e^{4.18\left(\frac{T-303}{T}\right)}.$$

3.3.5 First Derivative of Concentration Power Loss

This section derives the first derivative of the concentration power loss ($I_{FC}V_{conc}$). By substituting Equation 2.13 into the equation, the first derivative of power loss from the reduction in concentration gases is derived as Equation 3.12.

$$\frac{dI_{FC}V_{conc}}{dI_{FC}} = \frac{dI_{FC}\left[-\frac{RT}{nF}\ln\left(1 - \frac{I_{FC}}{i_LA}\right)\right]}{dI_{FC}} \quad \text{Equation 3.11}$$

$$\frac{dI_{FC}V_{conc}}{dI_{FC}} = \frac{RT}{nF}\left[\frac{I_{FC}}{i_LA - I_{FC}} - \ln\left(1 - \frac{I_{FC}}{i_LA}\right)\right] \quad \text{Equation 3.12}$$

3.3.6 Second Derivative of Reversible Thermodynamic Power

This section derives the second derivative of reversible thermodynamic power. From the equation of the first derivative of reversible thermodynamic power (Equation 3.6), the second derivative of reversible thermodynamic power of the PEMFC is derived as Equation 3.14.

$$\frac{d^2 I_{FC} E_{nerst}}{dI_{FC}{}^2} = \frac{d[1.229 - 8.5 \times 10^{-4}(T - 298.15) + a_1 + b_1]}{dI_{FC}} \qquad \text{Equation 3.13}$$

$$\frac{d^2 I_{FC} E_{nerst}}{dI_{FC}{}^2} = \frac{da_1}{dI_{FC}} + \frac{db_1}{dI_{FC}} \qquad \text{Equation 3.14}$$

where $\frac{da_1}{dI_{FC}} = 4.308 \times 10^{-5} T \left(\frac{I_{FC}\left[2k_r\left(1-e^{\left(-\frac{t}{\tau_{H_2}}\right)}\right)\right]^2 - 4q_{H_2}^{in} k_r\left(1-e^{\left(-\frac{t}{\tau_{H_2}}\right)}\right)}{\left[q_{H_2}^{in} - 2k_r I_{FC}\left(1-e^{\left(-\frac{t}{\tau_{H_2}}\right)}\right)\right]^2} \right)$ and

$\frac{db_1}{dI_{FC}} = 2.154 \times 10^{-5} T \left(\frac{I_{FC}\left[k_r\left(1-e^{\left(-\frac{t}{\tau_{O_2}}\right)}\right)\right]^2 - 2q_{O_2}^{in} k_r\left(1-e^{\left(-\frac{t}{\tau_{O_2}}\right)}\right)}{\left[q_{O_2}^{in} - k_r I_{FC}\left(1-e^{\left(-\frac{t}{\tau_{O_2}}\right)}\right)\right]^2} \right)$.

3.3.7 Second Derivative of Activation Power Loss

This section derives the second derivative of activation power loss. From the equation of the first derivative of activation power loss (Equation 3.8), the second derivative of power loss at the rate of reactions on the electrodes is derived as Equation 3.16.

$$\frac{d^2 I_{FC} V_{act}}{dI_{FC}{}^2} = \frac{d[\xi_1 + \xi_2 T + a_2 + \xi_4 T(1 + \ln I_{FC})]}{dI_{FC}} \qquad \text{Equation 3.15}$$

$$\frac{d^2 I_{FC} V_{act}}{dI_{FC}{}^2} = \frac{da_2}{I_{FC}} + \frac{\xi_4 T}{I_{FC}} \qquad \text{Equation 3.16}$$

where $\frac{da_2}{I_{FC}} = \xi_3 T \left(\frac{I_{FC}\left[k_r\left(1-e^{\left(-\frac{t}{\tau_{O_2}}\right)}\right)\right]^2 - 2q_{O_2}^{in} k_r\left(1-e^{\left(-\frac{t}{\tau_{O_2}}\right)}\right)}{\left[q_{O_2}^{in} - k_r I_{FC}\left(1-e^{\left(-\frac{t}{\tau_{O_2}}\right)}\right)\right]^2} \right)$.

3.3.8 Second Derivative of Ohmic Power Loss

This section derives the second derivative of the ohmic power loss. From the equation of the first derivative of ohmic power loss (Equation 3.10), the second derivative of power loss on the resistance of proton flow in the electrodes is derived as Equation 3.18.

$$\frac{d^2 I_{FC} V_{ohm}}{dI_{FC}{}^2} = \frac{d\left[\frac{b_3 \frac{da_3}{dI_{FC}} - a_3 \frac{db_3}{dI_{FC}}}{b_3^2}\right]}{dI_{FC}} \qquad \text{Equation 3.17}$$

$$\frac{d^2 I_{FC} V_{ohm}}{dI_{FC}{}^2} = \frac{b_3^2\left(b_3 \frac{d^2 a_3}{dI_{FC}{}^2}\right) - \frac{db_3^2}{dI_{FC}}\left(b_3 \frac{da_3}{dI_{FC}} - a_3 \frac{db_3}{dI_{FC}}\right)}{b_3^4} \qquad \text{Equation 3.18}$$

where $\frac{d^2 a_3}{dI_{FC}{}^2} = 363.2 t_m + 32.688 t_m \left(\frac{I_{FC}}{A}\right) + 1.93153 \times 10^{-3} t_m T^2 \left(\frac{I_{FC}^{2.5}}{A^{2.5}}\right)$ and

$\frac{db_3^2}{dI_{FC}} = (18 I_{FC} + 3.804A - 6\lambda_m A)\left[e^{4.18\left(\frac{T-303}{T}\right)}\right]^2$.

3.3.9 Second Derivative of Concentration Power Loss

This section derives the second derivative of concentration power loss. From the equation of the first derivative of concentration power loss (Equation 3.12), the second

derivative of the reversible thermodynamic power of the PEMFC is derived as Equation 3.20.

$$\frac{d^2 I_{FC} V_{conc}}{dI_{FC}{}^2} = \frac{d\left[\frac{RT}{nF}\left[\frac{I_{FC}}{i_L A - I_{FC}} - \ln\left(1 - \frac{I_{FC}}{i_L A}\right)\right]\right]}{dI_{FC}} \quad \text{Equation 3.19}$$

$$\frac{d^2 I_{FC} V_{conc}}{dI_{FC}{}^2} = \frac{RT}{nF}\left[\frac{2 i_L A - I_{FC}}{(i_L A - I_{FC})^2}\right] \quad \text{Equation 3.20}$$

3.3.10 Newton–Raphson Equation

For PEMFC, the maximum power point current can be tracked by implementing Newton–Raphson method with Equation 3.21.

$$I_{track+1} = I_{track} - \left.\frac{dP_{FC}}{dI_{FC}}\right/\frac{d^2 P_{FC}}{dI_{FC}{}^2} \quad \text{Equation 3.21}$$

where I_{track} is the approximated current at MPP. Lastly, the algorithm for MPPT is derived by combining all the related equations (Equation 3.1 – Equation 3.20). The approximation of the current at MPP by the Newton–Raphson method is accurate due to the negligible error after a few iterations. This approximated current is computed to represent the reference current for the PEMFC to achieve its maximum power.

3.4 DC-DC Power Converter

A DC-DC power converter is a necessary component to track the MPP of PEMFC because it allows the output voltage to be changed (Karami et al., 2014). In this research, a DC-DC boost converter is used to regulate the output voltage of the PEMFC. A DC-DC boost converter is an electronic system that can be used to raise a DC electrical voltage level to a higher level (Derbeli et al., 2019). The main components of a DC-DC boost converter

are the inductor (L), switch (S), diode (D), and capacitor (C). In this research, the DC-DC boost converter is assumed to be an ideal converter. So, there is no power loss at the diode and the switch. The inductance and capacitance values are set as $10mH$ and $3mF$ respectively. Figure 3.4 illustrates the circuit diagram of the DC-DC boost converter.

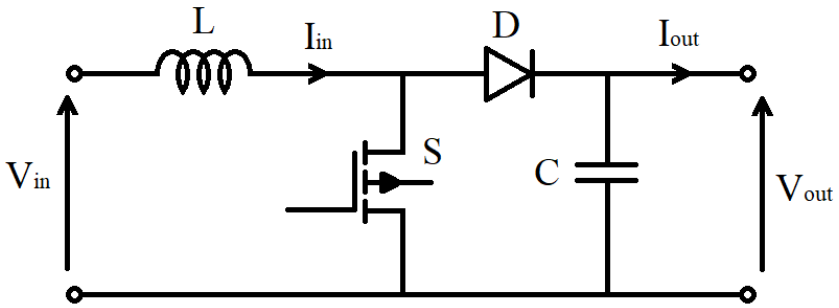


Figure 3.4: DC-DC Boost Converter

The DC-DC boost converter has two operation modes, which are the ON switching state and the OFF switching state. When the switch is ON, it creates a short circuit with zero resistance to current flow. The diode becomes reverse-biased, and the current will not flow through the output. Instead, all current will flow through the switch and back to the DC input source. Figure 3.5 represents the circuit diagram of the DC-DC boost converter when the switch is ON.

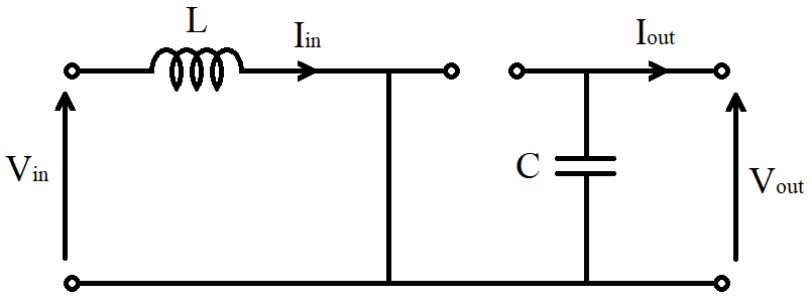


Figure 3.5: DC-DC Boost Converter for ON Switching State

By applying Kirchhoff's Voltage Law, when the switch is ON, the equation can be described as Equation 3.22.

$$V_{in}(t) = L\frac{dI_{in}(t)}{dt} \qquad \text{Equation 3.22}$$

where V_{in} is the input voltage, I_{in} is the input current, and t is the operation time. Because the input current is always equal to the inductor current, the change in inductor current is defined by Equation 3.23.

$$dI_L(t) = \frac{V_{in}(t)D\tau}{L} \qquad \text{Equation 3.23}$$

where I_L is the inductor current, τ is the period for one complete switching cycle, and D is the duty cycle representing the ratio of the ON switching state to the complete switching cycle.

When the switch is OFF, the diode becomes forward-biased to provide a path for inductor current. The inductor current cannot change instantaneously, so the polarity of the inductor is reversed. The energy stored in the inductor is released and dissipated to the output. Figure 3.6 shows the circuit diagram of the DC-DC boost converter when the switch is OFF.

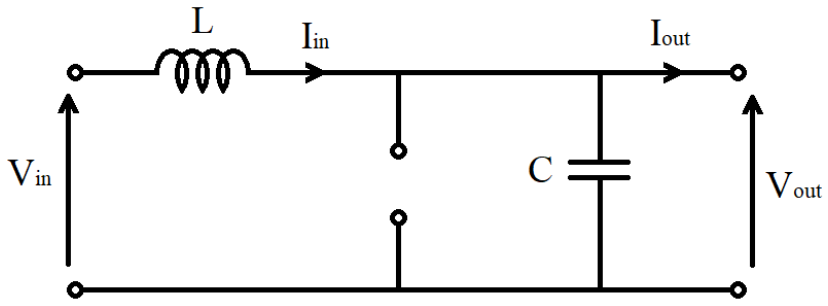


Figure 3.6: DC-DC Boost Converter for OFF Switching State

During the OFF switching state, the equation can be described as Equation 3.24.

$$V_{in}(t) = L\frac{dI_{in}(t)}{dt} + V_{out}(t) \qquad \text{Equation 3.24}$$

where V_{out} is the output voltage. Because the switch is OFF for $(1 - D)\tau$, the change in inductor current is computed as Equation 3.25.

$$dI_L(t) = \frac{\big(V_{in}(t) - V_{out}(t)\big)(1 - D)\tau}{L} \qquad \text{Equation 3.25}$$

In one complete cycle, the inductor current rises from a value with a positive slope to a maximum value during the ON state and then falls back to the initial value with a negative slope during the OFF state. As a result, the net change of the inductor current is zero across any whole cycle during the steady-state operation. The inductor voltage alternates between positive and negative voltages because of the change in polarity. The changes in inductor voltage and current are illustrated in Figure 3.7.

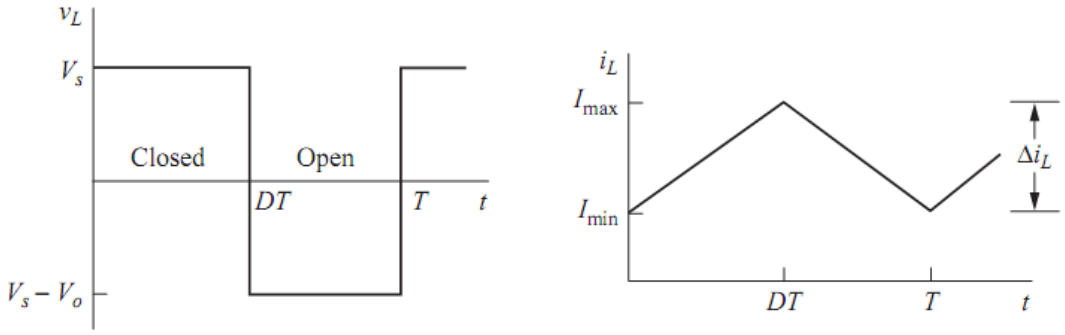


Figure 3.7: Change in Inductor Voltage and Current

Because the net change of the inductor current is zero under steady-state operation, the output voltage can be computed from Equation 3.23 and Equation 3.25, which is shown in Equation 3.26.

$$\frac{V_{in}(t)D\tau}{L} + \frac{\big(V_{in}(t) - V_{out}(t)\big)(1-D)\tau}{L} = 0 \qquad \text{Equation 3.26}$$

Therefore, the final equation for output voltage is defined by Equation 3.27.

$$V_{out}(t) = \frac{V_{in}(t)}{1-D} \qquad \text{Equation 3.27}$$

From Equation 3.27, the DC-DC boost converter steps up the DC output voltage by increasing the duty cycle. The longer the time for the ON state, the higher the electrical energy stored in the inductor. Therefore, the output voltage will be increased when the duty cycle is increased.

3.5 Predictive Maximum Power Point Tracking Method

The MPPT control process is crucial to achieving good efficiency in a PEMFC power system. From the mathematical modeling of PEMFC, either the changes in load or the parameters of the fuel cell can highly affect the output power of the fuel cell. Therefore, MPPT control is necessary to force the PEMFC system to generate the highest output power in any condition. However, the MPPT algorithm technique is needed to work together with the DC-DC boost converter. The MPPT algorithm will control the switch of the boost converter and regulate the output voltage of the fuel cell to a maximum power voltage.

In this research, a predictive MPPT technique will be designed and applied to the PEMFC system. This predictive MPPT technique involves the FCS-MPC strategy in the DC-DC boost converter, which is introduced in section 2.5.2. The key feature of Model Predictive Control (MPC) is to predict the future behavior of the controlled variables (Rodriguez & Cortes, 2012). To design the predictive MPPT algorithm, relevant equations need to be expressed as a discrete-time model. In this way, the algorithm can predict the fuel

cell's next behavior step at the next sampling time. The predictive MPPT algorithm can predict the fuel cell output voltage and current to compute the one-step prediction of the fuel cell power.

3.5.1 Discrete-time Model Equation

When the DC-DC boost converter is connected to the PEMFC, the output voltage of the fuel cell becomes the input voltage of the DC-DC boost converter. Therefore, Equation 3.22 and Equation 3.24 can be simplified as Equation 3.28 and Equation 3.29, respectively.

$$S = 0, \qquad V_{FC}(t) = L\frac{dI_{FC}(t)}{dt} + V_{out}(t) \qquad \text{Equation 3.28}$$

$$S = 1, \qquad V_{FC}(t) = L\frac{dI_{FC}(t)}{dt} \qquad \text{Equation 3.29}$$

where $S = 0$ when the switching state is OFF and $S = 1$ when the switching state is ON. Then, the final equation can be concluded as Equation 3.30.

$$V_{FC}(t) = L\frac{dI_{FC}(t)}{dt} + \bar{S}V_{out}(t) \qquad \text{Equation 3.30}$$

By rearranging Equation 3.30, the rate of change of fuel cell current can be derived as Equation 3.31.

$$\frac{dI_{FC}(t)}{dt} = \frac{V_{FC}(t) - \bar{S}V_{out}(t)}{L} \qquad \text{Equation 3.31}$$

In the discrete-time model, the rate of change of current is assumed to be a small change of fuel cell current in one sampling step. Therefore, the rate of change of current can be expressed as Equation 3.32.

$$\frac{dI_{FC}(t)}{dt} = \frac{I_{FC}(k+1) - I_{FC}(k)}{T_s} \quad \text{Equation 3.32}$$

where k is the number of discrete sampling steps and T_s is the sampling time. For Equation 3.31, the time domain, t can also be discretized to the sampling step domain, k.

3.5.2 Predictive Switching State Control Technique

Predictive switching state control is a technique to predict the future behavior of the next sampling step and select a unique switching state. It controls the switching state inside the DC-DC power converter to maximize the fuel cell output power. By substituting Equation 3.32 into Equation 3.31, the predicted PEMFC output current in the discrete-time model can be expressed as Equation 3.33.

$$I_{FC}(k+1) = \frac{T_s}{L}\left(V_{FC}(k) - \bar{S}V_{out}(k)\right) + I_{FC}(k) \quad \text{Equation 3.33}$$

This equation includes two conditions, which are the ON switching state and the OFF switching state. By using Equation 3.33, the predicted fuel cell currents for both ON and OFF switching state conditions can be calculated. The predictive MPPT technique requires the DC-DC boost converter output voltage, PEMFC output voltage, and current at the present step to predict the next fuel cell output current.

3.5.3 Predictive Duty Cycle Control Technique

Predictive duty cycle control predicts the future behavior of the next sampling step and controls the duty cycle of the DC-DC boost converter instead of selecting a unique switching state. One-step prediction of the PEMFC output current can be derived from Equation 3.33. Since the switch is OFF for $1 - D$ period of the sampling time and it considers the output voltage, the equation of PEMFC current prediction can be expressed in

Equation 3.34. For the ON switching state, the output voltage does not affect the PEMFC current, so the equation can be expressed in Equation 3.35.

$$S = 0, \qquad I_{FC}(k+1)_{S=0} = \frac{(1-D)T_S}{L}\left(V_{FC}(k) - V_{out}(k)\right) + I_{FC}(k) \qquad \text{Equation 3.34}$$

$$S = 1, \qquad I_{FC}(k+1)_{S=1} = \frac{DT_S}{L}V_{FC}(k) + I_{FC}(k) \qquad \text{Equation 3.35}$$

The predictive MPPT algorithm will first measure the DC-DC boost converter output voltage, PEMFC output voltage, and current at the present step. Subsequently, it applies a large range of duty cycles for calculation and predicts the next PEMFC output current for ON and OFF switching states. The duty cycle is started from 0 to 1 with an increment of 0.05. The average PEMFC output current is then defined as Equation 3.36 by calculating the average current obtained in Equation 3.34 and Equation 3.35.

$$I_{FC}(k+1) = \frac{I_{FC}(k+1)_{S=0} + I_{FC}(k+1)_{S=1}}{2} \qquad \text{Equation 3.36}$$

3.6 Cost Function

To maximize the output power of PEMFC, the PEMFC output current must converge to the maximum power point current. It can be computed through the cost function by minimizing the error between the predicted current and the maximum power point current. The maximum power point current (I_{MPP}) is derived in Equation 3.21, while the predicted current is derived in Equation 3.33 or Equation 3.36 based on the predictive technique. Then, the equation of the cost function is expressed as Equation 3.37.

$$g_S = |I_{MPP} - I_{FC}(k+1)| \qquad \text{Equation 3.37}$$

The minimum cost function indicates the switching state or the duty cycle having the nearest PEMFC output current to I_{MPP}.

3.7 Switching Frequency Reduction Technique

The predictive MPPT algorithm may control the switch in the DC-DC power converter with a very high switching frequency due to the small sampling time. However, a high switching frequency in the DC-DC power converter may cause the switching power loss that affects the power conversion efficiency. The Technique for Order of Preference by Similarity to Ideal Solution (TOPSIS) algorithm will be designed to reduce the switching frequency. If the switching frequency is reduced to a very low switching rate, the power fluctuation may become high. This will also cause the power conversion efficiency to be reduced. Therefore, the TOPSIS algorithm with a suitable weightage between fuel cell output power and switching frequency will be defined. The calculation in the TOPSIS algorithm includes the normalization of values, positive and negative ideal solutions, and lastly, choosing the best alternatives based on the performance score. The steps below are essential to understand the mechanism and integration.

3.7.1 Construction of Decision Matrix

To deal with multiple criteria decision-making (MCDM) problems, the first step is to figure out how many attributes or criteria exist in the problem. This research deals with two criteria, which are output power and switching frequency. For output power, it is represented by the cost function calculated in Equation 3.37. The lower the cost function, the higher the output power. For the switching frequency, it is compared with the previous switching state. It is set as 1 if the switching state is changed and 0 if the switching state is unchanged. Therefore, a 2×2 matrix is constructed as shown in Table 3.1.

Table 3.1: Decision Matrix

Switching State	Cost Function (Output Power)	Switching Changes (Switching Frequency)
OFF	x_{11}	x_{12}
ON	x_{21}	x_{22}

3.7.2 Normalized Decision Matrix Construction

A specific normalization technique will be chosen to bring all the criteria to the same scale. It is necessary to normalize it and transform it into a dimensionless matrix, which allows the comparison of the various criteria. In this work, the element of the decision matrix is normalized using Equation 3.38.

$$r_{ij} = \frac{x_{ij}}{\sqrt{\sum_{i=1}^{n} x_{ij}^2}} \qquad \text{Equation 3.38}$$

3.7.3 Weighted Normalized Decision-making Construction

The concept of the weighting factor w_j will be introduced to set priority to each criterion so that a good trade-off between each criterion will be obtained. The matrix is a product of the normalized decision score with its associated weight, as shown in Equation 3.39.

$$v_{ij} = w_j r_{ij}, \qquad w_j = \text{weighting factor of each criterion} \qquad \text{Equation 3.39}$$

where w_j is the weighting factor of each criterion. At this stage, the decision matrix becomes the weighted and normalized decision matrix. Since the output power is more important than the switching frequency, the weighting factor for output power must be higher than the

switching frequency. The sum of the weighting factors must be equal to 1. Then, the weighted normalized decision matrix becomes:

Table 3.2: Weighted Normalised Decision Matrix

Switching State	Cost Function (Output Power)	Switching Changes (Switching Frequency)
OFF	v_{11}	v_{12}
ON	v_{21}	v_{22}

3.7.4 Determining the PIS and NIS

Next, the algorithm will identify the positive-ideal solutions (PIS) and negative-ideal solutions (NIS), which cover all the beneficial criteria and the non-beneficial criteria, respectively. In this research, the cost function is a non-beneficial criterion because it represents the accuracy of the maximum power point by minimizing its value. Switching changes as the switching frequency is also a non-beneficial criterion. In this case, the lowest cost function, v_1^+ and the lowest switching change, v_2^+ will be selected as the PIS. On the contrary, the highest cost function, v_1^- and the highest switching change, v_2^- will be selected as the NIS. Then, the matrix for PIS and NIS is presented as shown in Table 3.3.

Table 3.3: PIS and NIS Matrix

Ideal Solution	Cost Function (Output Power)	Switching Changes (Switching Frequency)
PIS	v_1^+	v_2^+
NIS	v_1^-	v_2^-

3.7.5 Calculating the Distances of Each Alternative to the PIS and NIS

This step consists of calculating the relative distance of each solution from the positive ideal solution, S_i^+ and to the negative ideal solution, S_i^-. The Euclidean distance between the positive ideal solution and the negative ideal solution to each switching state will be evaluated to determine how much they deviate from NIS and PIS. The equations used to calculate S_i^+ and S_i^- are given as Equation 3.40 and Equation 3.41, respectively.

$$S_i^+ = \sqrt{\sum_{i=1}^{m} \left(v_i^+ - v_{ij}\right)^2} \quad \text{Equation 3.40}$$

$$S_i^- = \sqrt{\sum_{i=1}^{m} \left(v_i^- - v_{ij}\right)^2} \quad \text{Equation 3.41}$$

Then, the Euclidean distance matrix can be constructed as Table 3.4.

Table 3.4: Euclidean Distance Matrix

Switching State	**Euclidean distance from PIS, S_i^+**	**Euclidean distance from NIS, S_i^-**
OFF	S_1^+	S_1^-
ON	S_2^+	S_2^-

3.7.6 Calculate the Relative Closeness

The last step of TOPSIS is to calculate the relative closeness of each alternative to the ideal solution. The equation is given by Equation 3.42.

$$C_i = \frac{S_i^-}{S_i^- + S_i^+}$$ Equation 3.42

After the relative closeness of each alternative to the ideal solution is computed, the relative closeness index for the ON and OFF switching states can be presented.

Table 3.5: Relative Closeness Index for ON and OFF Switching State

Switching State	**Relative closeness index, C_i**
OFF	C_1
ON	C_2

Finally, the TOPSIS algorithm will select the solution with the higher relative closeness index. Therefore, the next switching state can be determined.

3.7.7 Frequency Reduction by TOPSIS in MPPT Technique

The predictive MPPT technique calculates the predicted current by using Equation 3.33. Then, the maximum power is determined by minimizing the cost function in Equation 3.37. For the beginning of the TOPSIS algorithm, it first receives the cost function as the output power of both ON and OFF switching states from the predictive MPPT algorithm. After that, the TOPSIS algorithm will determine the next switching state by comparing the output power difference and current switching state with the process in Sections 3.7.1 to 3.7.6. The flowchart of the TOPSIS in the MPPT technique is presented in Figure 3.8.

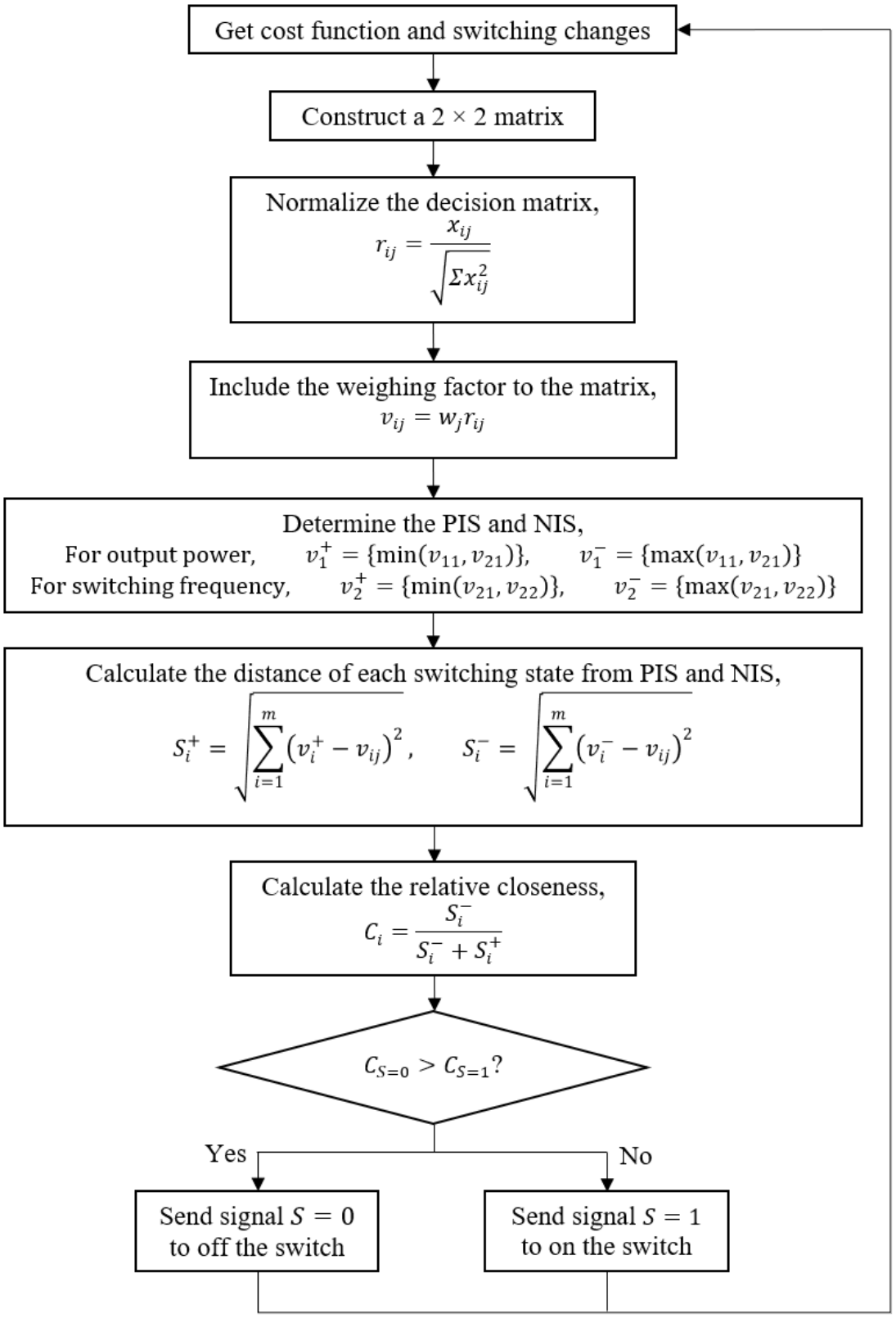


Figure 3.8: TOPSIS Flowchart

3.8 Summary of MPPT Technique in Simulation

For simulation, the MPPT techniques are implemented using the MATLAB software with the Simulink environment. As mentioned in Section 3.2, the mathematical model is constructed as shown in Figure 3.2. Whatever input parameter changes will affect the output power of the PEMFC. Therefore, the Newton–Raphson algorithm introduced in Section 3.3.1 is developed to track the maximum output power current as the reference current. Then, the predictive MPPT technique algorithm is implemented to achieve the maximum power. In this research, there are three predictive MPPT methods introduced. Each method is simulated, and the results are compared.

3.8.1 Process Flow of Predictive MPPT by Switching State Control Technique

The first predictive MPPT method is the predictive MPPT by switching state control. This method is explained in Section 3.5.2, which maximizes the PEMFC output power by controlling the switching state. The algorithm determines the switching state in each sampling step and keeps the output current approaching the reference current. In this case, the cost function is computed to determine the next decision. Due to the switching state may be changed for each sampling step, the switching frequency may be high. The flowchart of the predictive MPPT by switching state control technique is presented in Figure 3.9.

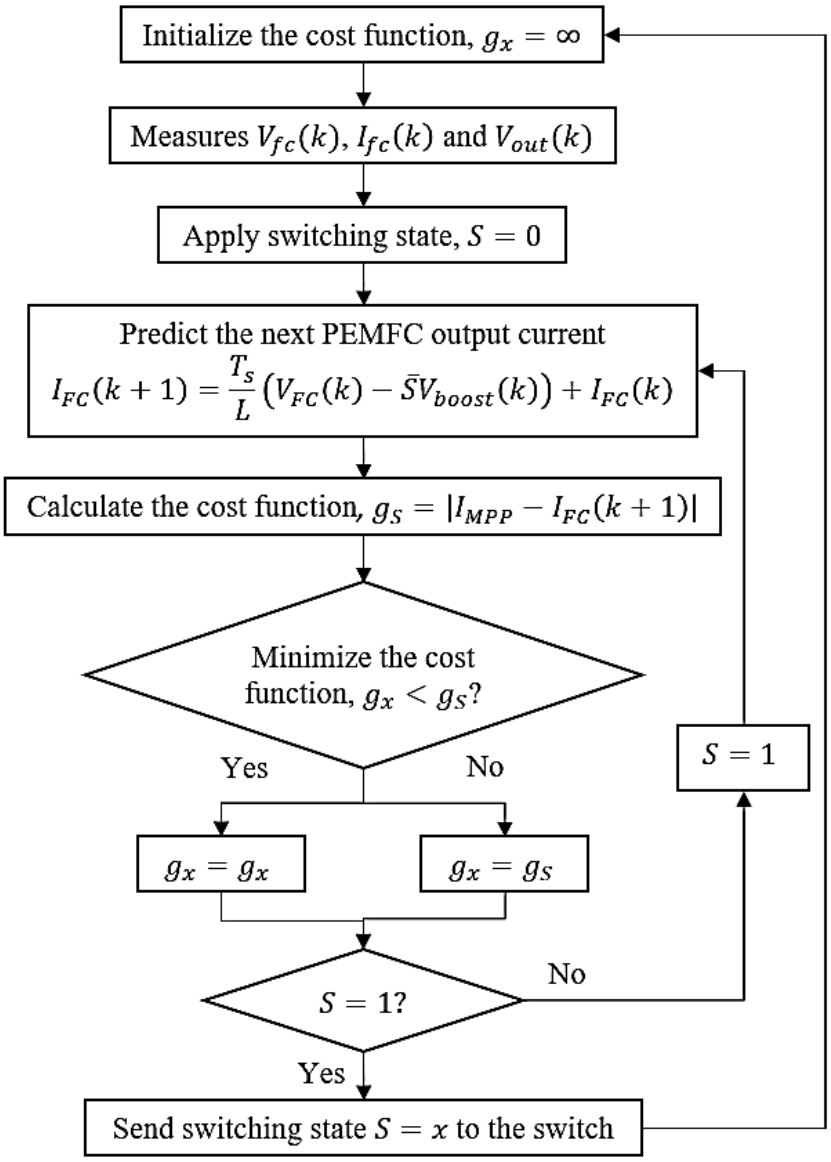


Figure 3.9: Predictive MPPT by Switching State Control Flowchart

3.8.2 Process Flow of Predictive MPPT by Duty Cycle Control Technique

The second predictive MPPT method is the predictive MPPT by duty cycle control, which is mentioned in Section 3.5.3. It regulates the duty cycle of the switch inside the power converter to maximize the PEMFC output power. The predicted output current is computed by Equation 3.34 to Equation 3.36. Then, the cost function is minimized to determine the

next duty cycle. This method has a constant switching which is has been set. The flowchart of the predictive MPPT by duty cycle control technique is presented as Figure 3.10.

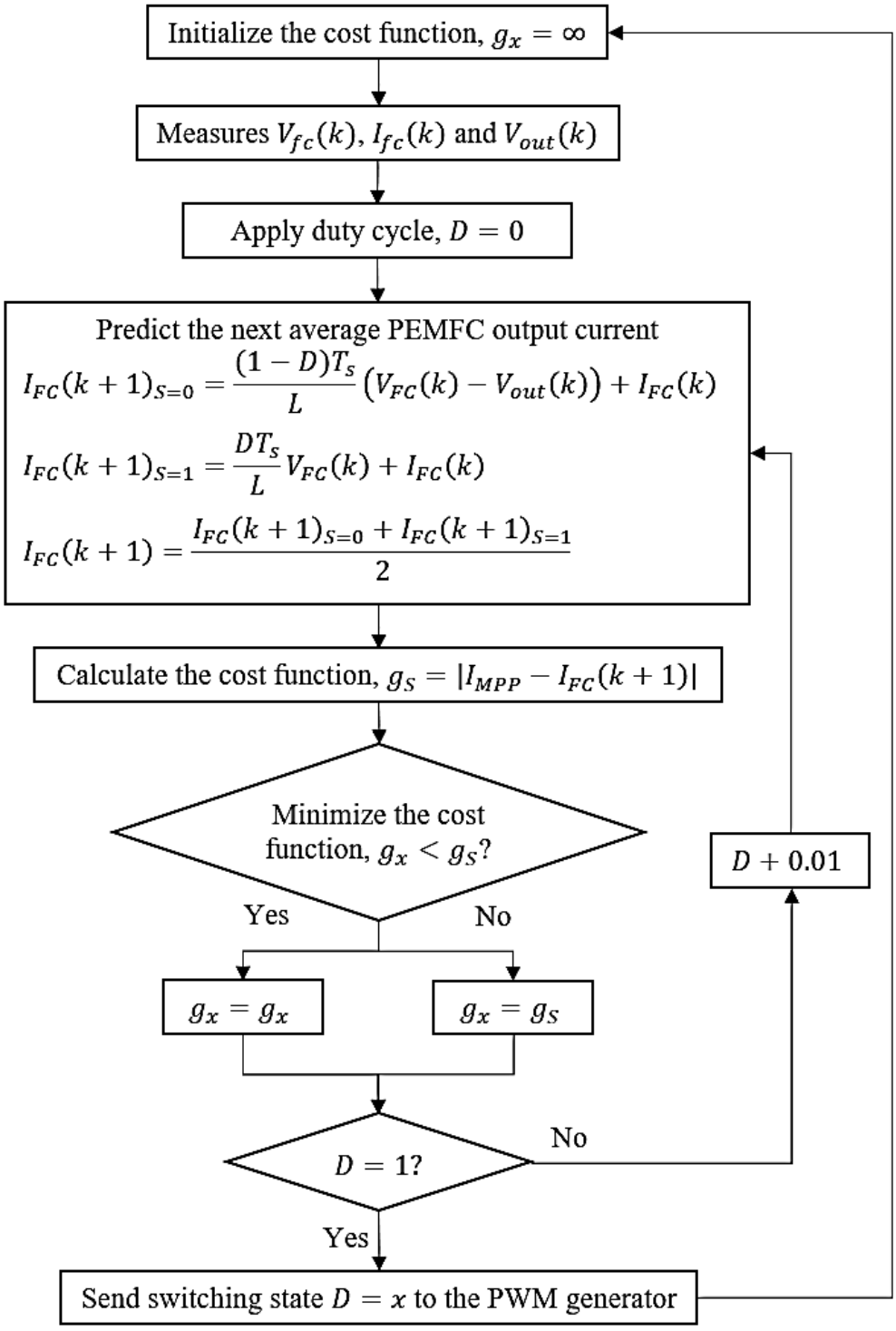


Figure 3.10: Predictive MPPT by Duty Cycle Control Flowchart

3.8.3 Process Flow of Predictive MPPT with Switching Frequency Reduction Technique

The third predictive MPPT method is the predictive MPPT by switching state control merging with the switching frequency reduction algorithm. The switching frequency reduction technique is the TOPSIS algorithm described in section 3.7. Since the technique in section 3.8.1 may have a high switching frequency, the switching frequency reduction technique is applied to decrease the switching frequency while maximizing the output power. The flowchart of the predictive MPPT with the switching frequency reduction technique is presented in Figure 3.11.

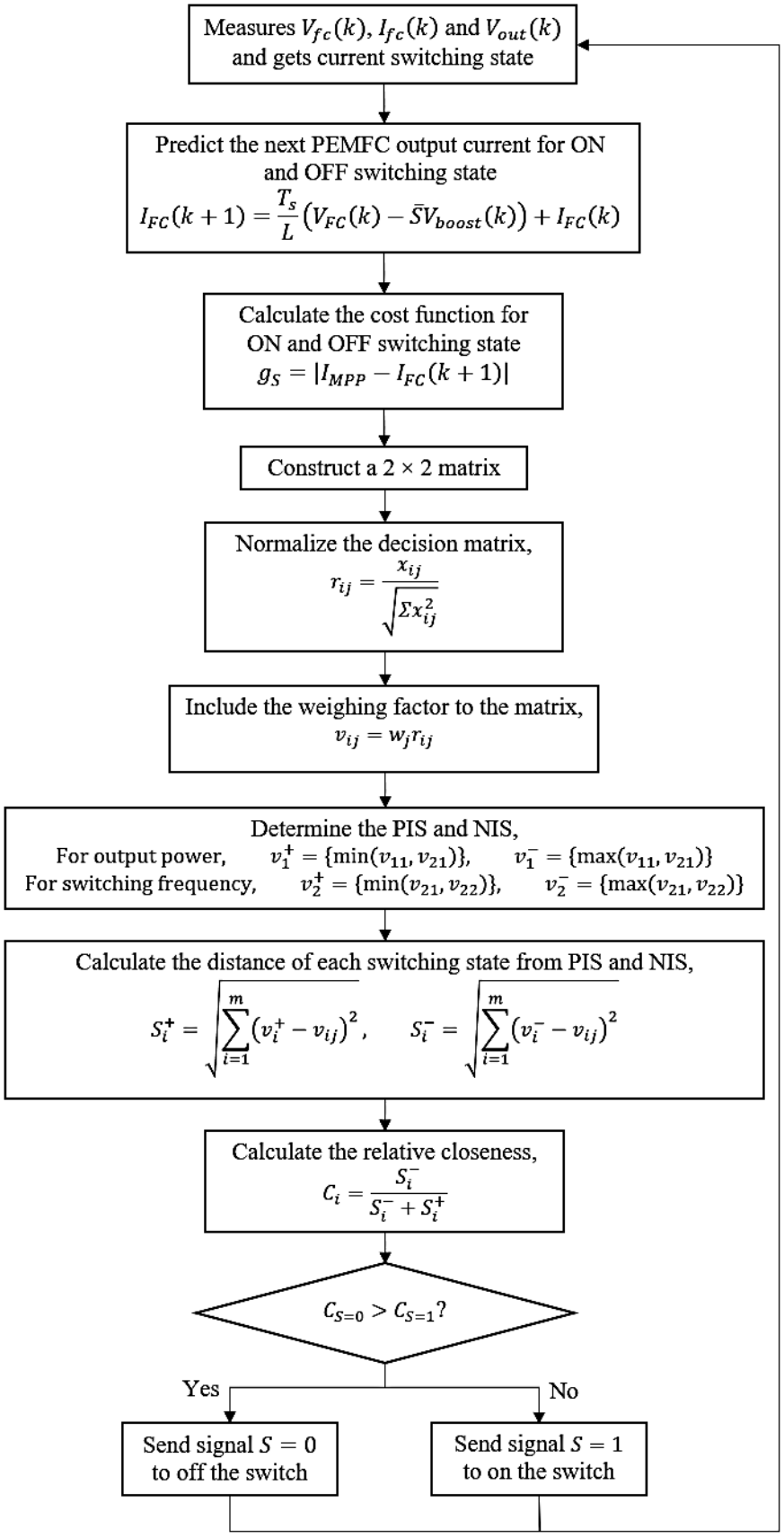


Figure 3.11: Predictive MPPT by Switching with TOPSIS Control Flowchart

3.9 Predictive Voltage Control Technique

The voltage control technique is crucial for the load to operate at its voltage rating. A voltage control technique by FCS-MPC is also presented to convert the boosted DC voltage into a pure sinusoidal AC voltage. For DC to AC conversion, a four-switch H-bridge inverter with a second-order input filter is used.

3.9.1 H-Bridge Inverter

The H-Bridge inverter consists of four switches arranged in an "H" configuration with two pairs of power switches in a complementary manner. It is commonly used to convert DC power into alternating current AC power. To implement the MPC, a secondary filter of an RLC circuit is required to discretize the equation of the output voltage. Therefore, the secondary RLC filter is necessary to regulate the output waveform by the MPC technique. The circuit diagram of the power converter is schematically shown in Figure 3.12.

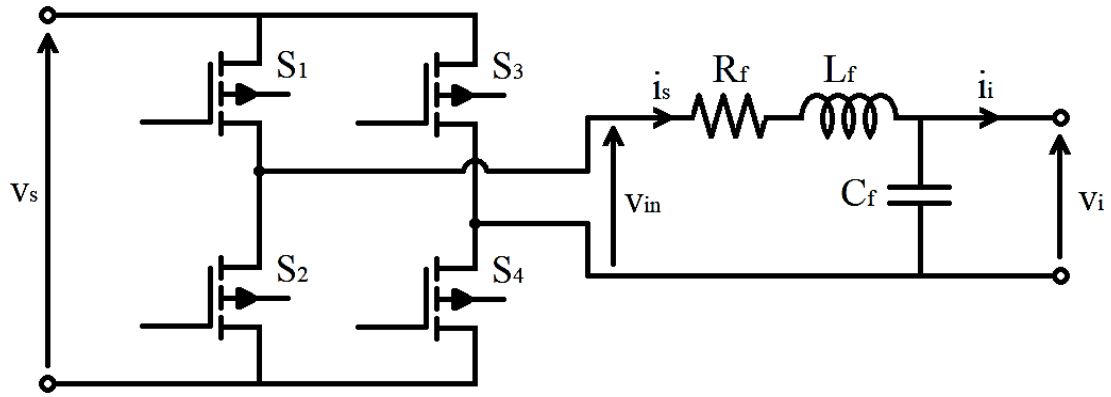


Figure 3.12: H-bridge Inverter with Second-order Input Filter

For the H-bridge inverter, S_1 and S_2 operate in complementary modes. Likewise, S_3 and S_4 also operate in the same mode. The inverter must avoid a short circuit at the input

side. Therefore, there are only four switching sequences. Table 3.6 shows the 4 possible switching states and the corresponding v_s based on each possible switching state.

Table 3.6: Possible Switching States Responding to v_s

i	Switching State				v_{in}
	S1	S2	S3	S4	
1	0	1	0	1	0
2	1	0	0	1	v_s
3	1	0	1	0	0
4	0	1	1	0	$-v_s$

3.9.2 Voltage Control Algorithm

The H-Bridge inverter consists of four switches with two pairs of power switches. From Table 3.6, v_s is either 0, v_{in} or $-v_{in}$ which is a square wave. Therefore, an RLC filter is merged with the H-bridge inverter to modify the square AC voltage waveform to a pure sinusoidal waveform. In addition, this second-order input filter helps to mitigate harmonic distortion and improve power quality. Its dynamic behavior in the time domain is described as Equation 3.43 and Equation 3.44 (Basri & Mekhilef, 2022).

$$\frac{d}{dt}\begin{bmatrix} v_i \\ i_s \end{bmatrix} = A\begin{bmatrix} v_i \\ i_s \end{bmatrix} + B\begin{bmatrix} v_s \\ i_i \end{bmatrix} \quad \text{Equation 3.43}$$

$$A = \begin{bmatrix} 0 & \frac{1}{C_f} \\ -\frac{1}{L_f} & -\frac{R_f}{L_f} \end{bmatrix}, \qquad B = \begin{bmatrix} 0 & -\frac{1}{C_f} \\ \frac{1}{L_f} & 0 \end{bmatrix} \quad \text{Equation 3.44}$$

Then, the time domain equation is converted to a discrete-time model equation to apply the FCS-MPC. The FCS-MPC can predict the one-step future output voltage and current with Equation 3.45 (Basri & Mekhilef, 2022).

$$\begin{bmatrix} v_i(k+1) \\ i_s(k+1) \end{bmatrix} = A_q \begin{bmatrix} v_i(k) \\ i_s(k) \end{bmatrix} + B_q \begin{bmatrix} v_s(k) \\ i_i(k) \end{bmatrix} \quad \text{Equation 3.45}$$

where k is the sampling step, $A_q = e^{ATs}$ and $B_q = A^{-1}(e^{ATs} - I_{2\times2})B$. A_q and B_q are the 2×2 conversion matrix, which can be easily obtained by computing the "c2d" function in MATLAB. For voltage control, the equation only involves $v_i(k+1)$ as the control variable with Equation 3.46.

$$v_i(k+1) = A_{q_{11}} v_i(k) + A_{q_{12}} i_s(k) + B_{q_{11}} v_s(k) + B_{q_{12}} i_i(k) \quad \text{Equation 3.46}$$

By using the same technique, FCS-MPC predicts the next output voltage of all the possible switching states listed in Table 3.6. The predicted output voltage is compared with the reference voltage, which is the ideal sinusoidal waveform. A cost function is defined to determine the optimal switching state by minimizing the cost function shown in Equation 3.47.

$$g = \left| v_{ref} - v_i(k+1) \right| \quad \text{Equation 3.47}$$

where v_{ref} is the reference voltage. The flowchart for the predictive voltage control algorithm is presented in Figure 3.13.

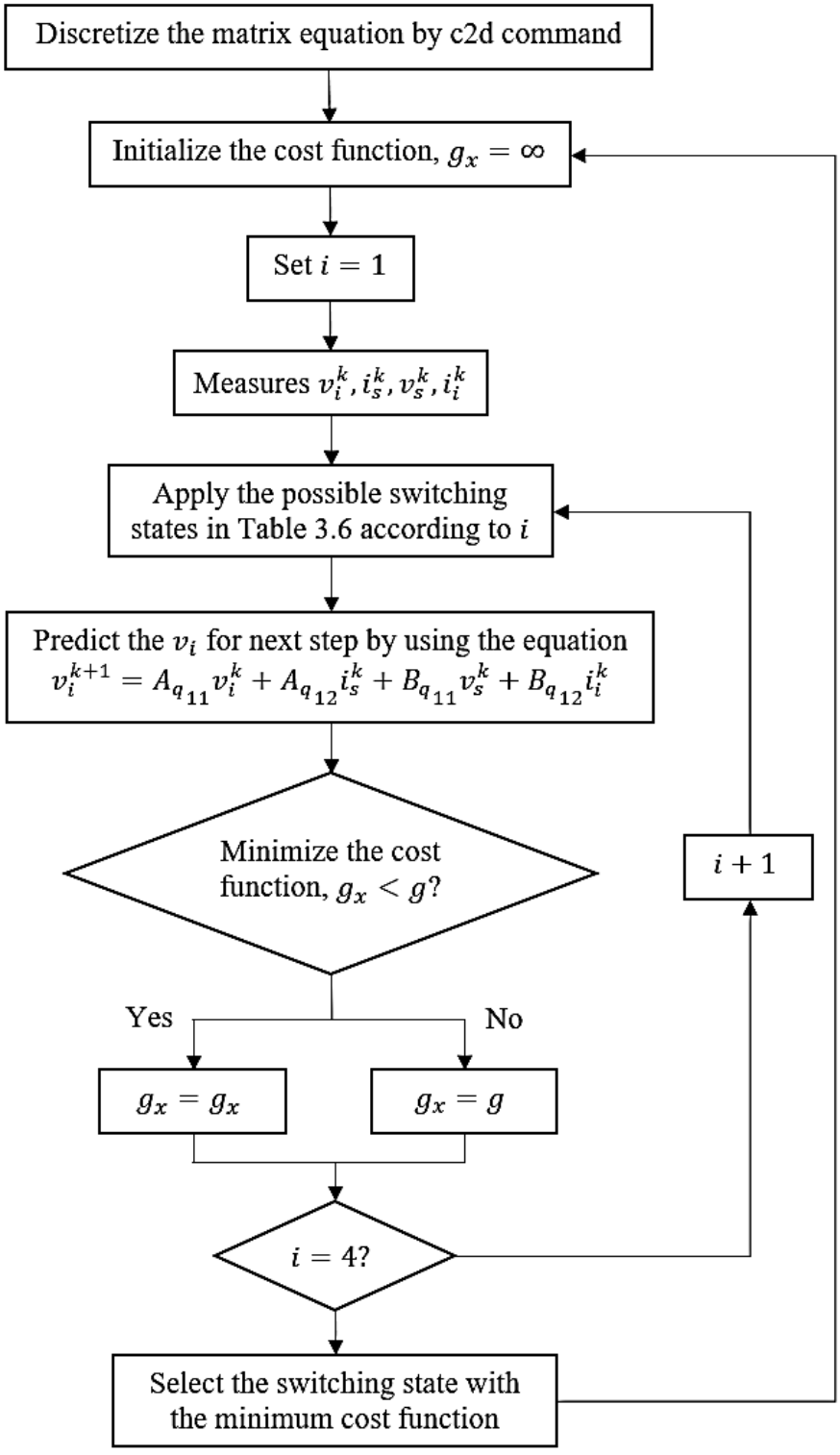


Figure 3.13: Predictive Voltage Control Technique Flowchart

Based on Equation 3.43 and Equation 3.44, the components of the RLC filter highly affect the conversion matrix of the FCS-MPC algorithm. The components and the conversion matrix value to be applied are listed in Table 3.7.

Table 3.7: Parameters for Predictive Voltage Control Technique

Components and Conversion Matrix	Value
Resistance (R)	0.539Ω
Inductor (L)	$3.92mH$
Capacitor (C)	$400\mu F$
$A_{q_{11}}$	1
$A_{q_{12}}$	0.025
$B_{q_{11}}$	3.1873×10^{-5}
$B_{q_{12}}$	-0.025

3.9.3 Fuel Control Algorithm

For the predictive voltage control technique, the voltage control algorithm will always regulate the AC voltage to a constant amplitude and frequency. When the AC voltage is supplied to the load, the power consumption is based on the load resistance. Based on the law of conservation of energy, all the electrical energy produced by the PEMFC must be consumed by the load. Otherwise, the energy will be stored inside the capacitor of the DC-DC boost converter. If the electrical power generated by the PEMFC is higher than the load consumption, the capacitor will charge continuously, and the capacitor voltage may exceed its limiting voltage in just a few seconds. On the contrary, the capacitor voltage will drop,

and the energy may not be enough to supply a stable AC voltage. Therefore, the electrical power generated by the PEMFC should not be constant.

Based on Equation 2.4, Equation 2.7, Equation 2.14, and Equation 2.15, the PEMFC output power is affected by the partial pressure of the hydrogen and oxygen gases. From Equation 2.5 and Equation 2.6, the mathematical equations show that the partial pressures are influenced by the input flow rate of the gases. When the input flow rates are high, the partial pressure will be high, resulting in high PEMFC output power. Since the input flow rate of the reactant gases can directly affect the PEMFC output power, an algorithm to control the input flow rate of the fuel is introduced in this section. This algorithm will control the input flow rate of the fuel by referring to two parameters. The first parameter is the boosted DC voltage that can be measured from the capacitor voltage inside the DC-DC boost converter. Another parameter is the setting voltage, known as the reference voltage. The purpose of this algorithm is to adjust the input flow rate of the fuel so that the capacitor voltage will approach the reference voltage. When the capacitor voltage is lower than the reference voltage, the controller will supply a suitable flow rate of the fuel so that the PEMFC can generate enough power and increase the capacitor voltage. If the capacitor voltage is too high, the controller will limit the fuel to decrease the output power. This algorithm may provide sufficient fuel for the PEMFC to generate enough power for the load and keep the capacitor voltage at a specific value. The initial fuel control algorithms are listed in Equation 3.48 to Equation 3.51.

$$For\ V_{ref} - V_c(k) \geq 0\ and\ V_c(k) - V_c(k-1) \geq 0, \qquad \text{Equation 3.48}$$

$$q_a^{in} = q_{H_2}^{in}(k) - \left[V_{ref} - V_c(k)\right] \times \left[V_c(k) - V_c(k-1)\right] \times StepSize1$$

$For\ V_{ref} - V_c(k) \geq 0\ and\ V_c(k) - V_c(k-1) < 0,$ Equation 3.49

$$q_b^{in} = q_{H_2}^{in}(k) + \left[V_{ref} - V_c(k)\right] \times \left[V_c(k) - V_c(k-1)\right] \times StepSize1$$

$For\ V_{ref} - V_c(k) < 0\ and\ V_c(k) - V_c(k-1) \geq 0,$ Equation 3.50

$$q_c^{in} = q_{H_2}^{in}(k) + \left[V_{ref} - V_c(k)\right] \times \left[V_c(k) - V_c(k-1)\right] \times StepSize2$$

$For\ V_{ref} - V_c(k) < 0\ and\ V_c(k) - V_c(k-1) < 0,$ Equation 3.51

$$q_d^{in} = q_{H_2}^{in}(k) + \left[V_{ref} - V_c(k)\right] \times \left[V_c(k) - V_c(k-1)\right] \times StepSize3$$

Where V_{ref} is the reference voltage, V_c is the capacitor voltage, and $StepSize1,2,3$ are the steps to increase or decrease the input flow rate.

To avoid the rapid decrease in the input flow of the fuel when the flow rate is approaching zero, q_a^{in} and q_c^{in} are divided by a scale factor. Therefore, the final fuel control algorithms are shown in Equation 3.52 and Equation 3.53.

$For\ V_{ref} - V_c(k) \geq 0,$ Equation 3.52

$$q_{H_2}^{in}(k+1) = \begin{cases} q_a^{in} \times \dfrac{q_a^{in}}{ScaleFactor}, & V_c(k) - V_c(k-1) \geq 0 \\ q_b^{in}, & V_c(k) - V_c(k-1) < 0 \end{cases}$$

$For\ V_{ref} - V_c(k) < 0,$ Equation 3.53

$$q_{H_2}^{in}(k+1) = \begin{cases} q_c^{in} \times \dfrac{q_c^{in}}{ScaleFactor}, & V_c(k) - V_c(k-1) \geq 0 \\ q_d^{in}, & V_c(k) - V_c(k-1) < 0 \end{cases}$$

The flowchart of the fuel control algorithm is presented in Figure 3.14. For the fuel control algorithm, the parameters are listed in Table 3.8.

Table 3.8: Parameters for Predictive Fuel Control Algorithm

Parameters	Value
$StepSize1$	10^{-10}
$StepSize2$	10^{-11}
$StepSize3$	10^{-8}
$ScaleFactor$	10^{-7}

The limit of the input flow rate of hydrogen gas is set between $0\ kmol\ s^{-1}$ and $10^{-5}\ kmol\ s^{-1}$. For the input flow rate of oxygen gas, it is always half of the input flow rate of hydrogen gas due to the chemical reaction of forming water from hydrogen and oxygen, as explained in Section 2.2.1.

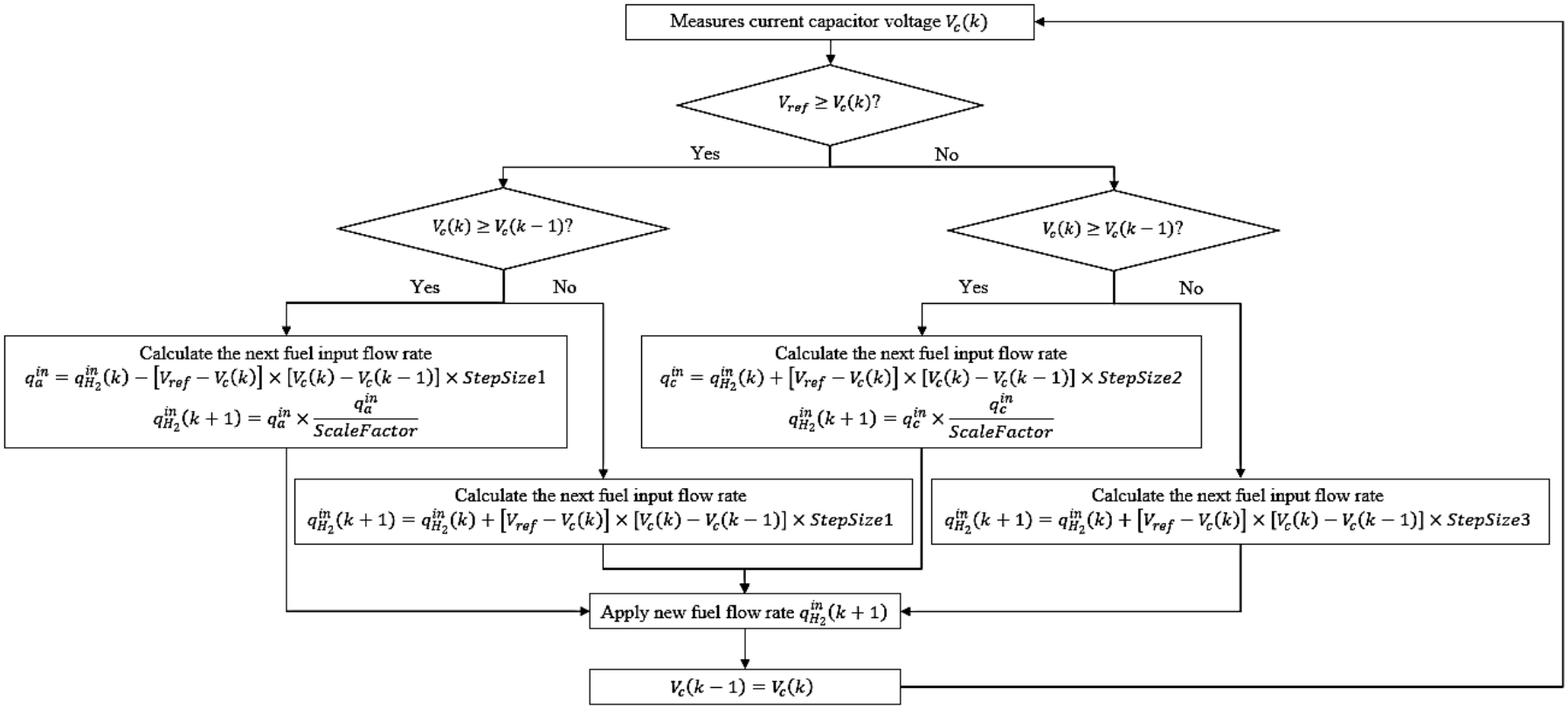


Figure 3.14: Fuel Control Algorithm Flowchart

3.10 Chapter Summary

To sum up this section, it has been demonstrated that a PEMFC for simulation can be constructed by a fully functional mathematical model of PEMFC. Sections 3.3, 3.5, 3.6, and 3.7 illustrate a review of MPPT techniques used in PEMFC. The purpose of controlling the PEMFC output voltage is to maintain the fuel cell power at the MPP. Sections 3.4 and 3.9 set out the theories that underpin the power electronics used in output voltage regulation. In section 3.4, a DC-DC boost converter has been selected as the power converter to control the voltage generated from the PEMFC system. Then, the designed predictive MPPT technique sends signals to command the IGBT of the DC-DC boost converter to control the PEMFC output voltage. In this way, the MPPT algorithm controls the DC-DC boost converter to extract the maximum power from the PEMFC. In section 3.9, the AC output voltage control was also introduced for supplying a constant AC voltage to the load. The robustness of the proposed fuel cell predictive MPPT control scheme over an operating range will be verified through simulations in the MATLAB/Simulink environment. It is expected that the proposed predictive MPPT method has excellent performance and is robust to PEMFC parameter changes and load resistance changes.

In this research, the Newton–Raphson method was selected because it is a highly accurate root-approximation technique for solving nonlinear equations. It is suitable to estimate the current at which the PEMFC power reaches its maximum. MPC was adopted as the control framework due to its fast and accurate response when regulating systems that can be described by mathematical models. Since the PEMFC and power converter can be modeled mathematically, MPC is an advanced tool to manage the PEMFC system. For the MCDM, the TOPSIS method was chosen because it allows efficient computation using a simple 2×2 decision matrix in this case, thus it minimizes the computational burden. After

the PEMFC output power has been maximized, the single-phase power inverter implemented with MPC converts the DC power into AC power to the load. The integration of Newton–Raphson, MPC, TOPSIS, and predictive voltage control inverter within a unified control framework represents the novelty of this research and contributes to the body of knowledge in predictive control of fuel cell systems.

CHAPTER 4

RESULTS AND DISCUSSION

4.1 Introduction

This chapter discusses a detailed evaluation of the results by simulation. In each section, each simulation provides the results for each different case. For the simulation part, MATLAB/Simulink software was used to simulate the system. The predictive MPPT without voltage control was validated by changing the PEMFC parameters and the total load resistance. The PEMFC should always produce power at MPP. Then, predictive voltage control was included to invert the DC voltage to AC voltage with a constant amplitude and frequency.

4.2 PEMFC Characteristics in Simulation

Before starting the simulation, the PEMFC parameters need to be set. This is because each PEMFC parameter will significantly affect the output voltage, current, and power. For the simulations, a $50W$ PEMFC was constructed, and its parameters are shown in Table 4.1. The PEMFC parameters are benchmarked with the previous study from two papers (Ahmadi et al., 2017; Derbeli et al., 2020).

Table 4.1: PEMFC Parameters

Parameters	Symbol & Unit	Value
Temperature	$T\ (K)$	323
Membrane water content	λ_m	10
Number of cells	N	10
Active area	$A\ (cm^2)$	104.04
Hydrogen valve molar constant	$k_{H_2}\ (kmol\ atm^{-1}\ s^{-1})$	4.22×10^{-6}
Oxygen valve molar constant	$k_{O_2}\ (kmol\ atm^{-1}\ s^{-1})$	2.11×10^{-6}
Hydrogen time constant	$\tau_{H_2}(s)$	3.37
Oxygen time constant	$\tau_{O_2}(s)$	6.74
Hydrogen input flow	$q_{H_2}(kmol\ \ s^{-1})$	1×10^{-5}
Oxygen input flow	$q_{O_2}(kmol\ \ s^{-1})$	5×10^{-6}
Membrane thickness	$t_{\ m}(cm)$	1.78×10^{-2}
Coefficient 1	$\xi_1\ (V)$	9.44×10^{-1}
Coefficient 2	$\xi_2\ (V\ K^{-1})$	-3.54×10^{-3}
Coefficient 3	$\xi_3\ (V\ K^{-1})$	-1.68×10^{-4}
Coefficient 4	$\xi_4\ (V\ K^{-1})$	1.96×10^{-4}
Limiting current density	$i_L\ (A\ cm^{-2})$	0.1

By using the parameters in Table 4.1, the PEMFC indicates a maximum power of $50.06W$ at MPP. The MPP voltage and current are $4.963V$ and $10.09A$ respectively. The PEMFC was simulated, and the V-I and P-I curves are also presented in Figure 4.1.

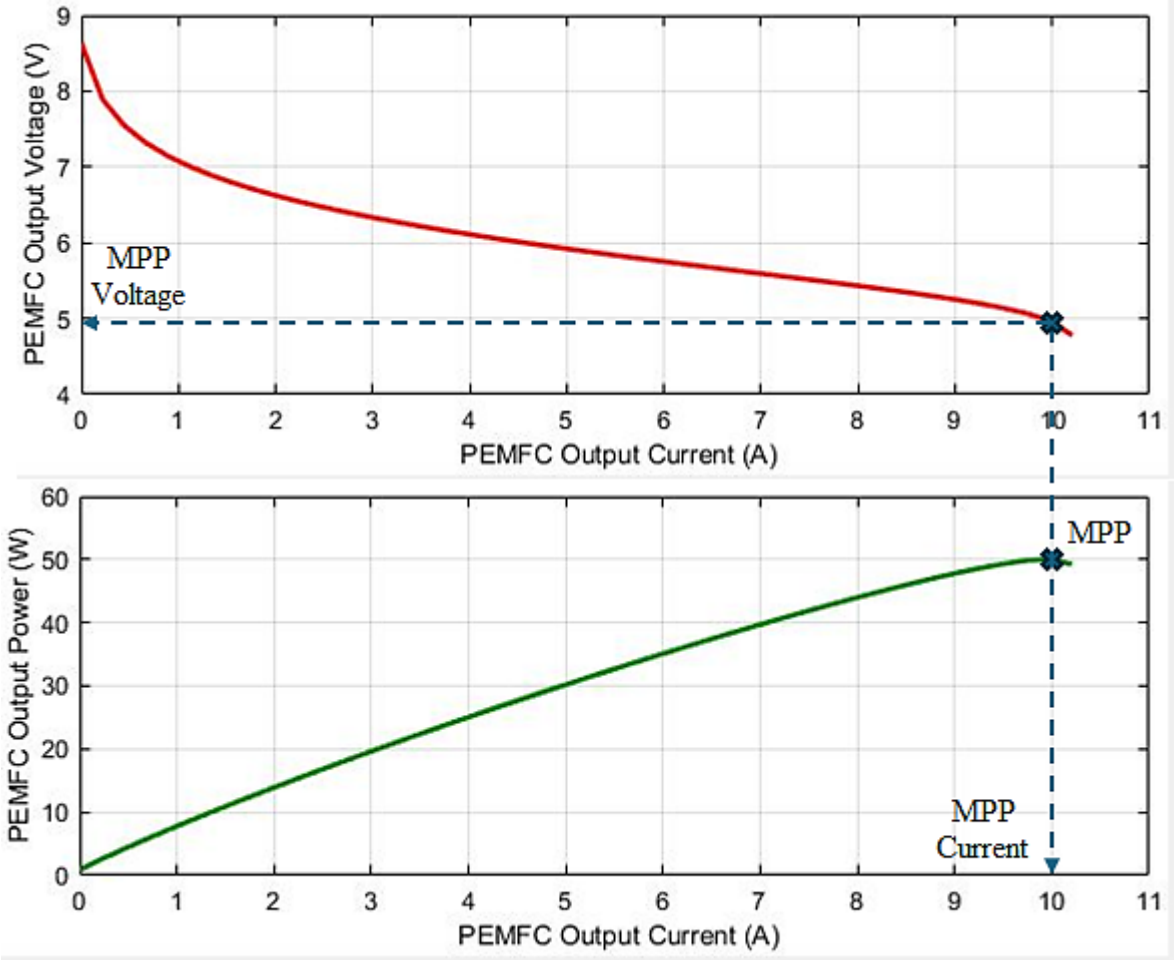


Figure 4.1: V-I and P-I Characteristics for 50W PEMFC

4.3 Simulation with Constant PEMFC Parameters and Constant Load

Since the MPP of the PEMFC is $50.06W$, the PEMFC should generate an electrical power of around $50.06W$ when the predictive MPPT technique is implemented. In this simulation, the predictive MPPT method was applied to the PEMFC and connected to a 12Ω load. In this section, the simulations were operated for $1s$ to observe the behavior of the PEMFC and the load. All the simulation results by applying predictive MPPT with switching state, duty cycle, and switching state with frequency reduction techniques are presented.

4.3.1 Simulation with Constant PEMFC Parameters by Predictive Switching State MPPT Technique

This section provides the simulation results of the PEMFC using predictive switching state MPPT control. Figure 4.2 illustrates the PEMFC output voltage, current, and power.

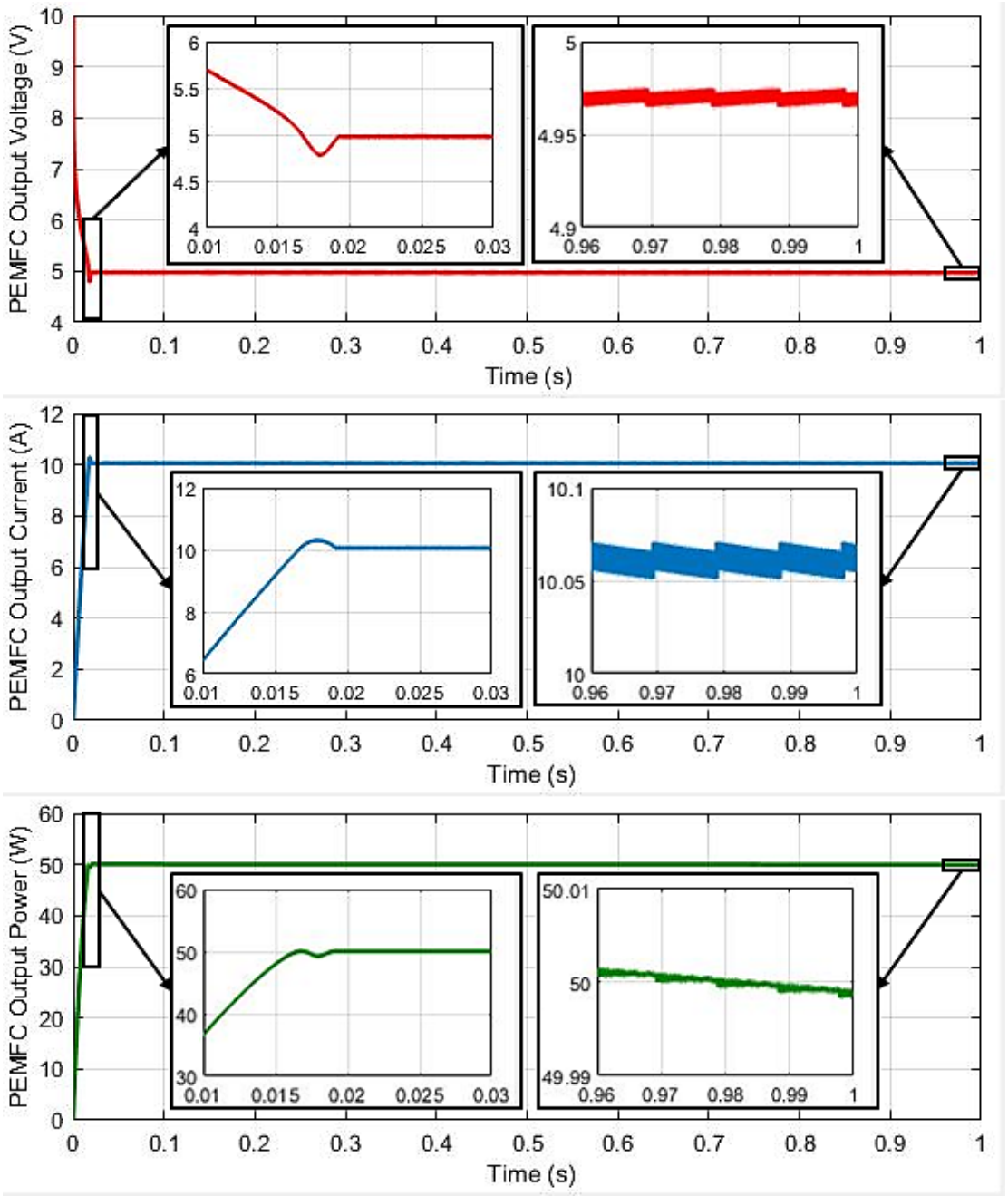


Figure 4.2: Simulation Results of PEMFC for Predictive Switching State MPPT under Constant PEMFC Parameters

From the simulation results shown in Figure 4.2, the output power reached $50W$ within $0.02s$. When the output power was optimized, the fuel cell generated the output voltage at $4.97V$ with a current of $10.06A$. The output power was approaching the MPP, $50.06W$ which shown in Figure 4.1. From these results, it is clear that the MPPT algorithm regulated the PEMFC output current to $10.06A$ and obtained the maximum power output from the fuel cell. The accuracy of the MPPT technique is about 99.88%. The outcomes indicate that the proposed predictive MPPT approach achieves rapid MPP tracking and extracts the highest possible power from the PEMFC system.

Before reaching the maximum power, the output experienced a 3.96% voltage undershoot, 2.44% of current overshoot, and 1.59% of power undershoot. It is found that the transient was quite low with an extremely short period. In addition, there were 0.20% of voltage ripple, 0.20% of current ripple, and 0.0016% of power ripple. These results prove that the PEMFC output power was stable due to the negligible power ripple. In conclusion, this method shows an excellent performance in tracking the MPP with low power ripple.

This predictive MPPT technique determines the switching state instead of the duty cycle. The main feature to note is that the switching state does not have a fixed frequency. At each sampling time, the predictive MPPT controller can send a signal to change the switching state. Therefore, the switching state is not constrained by the duty cycle. This shows the advantage of having fewer power oscillations and ripples. The shorter the sampling time, the smaller the ripples produced. Therefore, a very small sampling time may result in negligible ripple. Figure 4.3 shows the switching state of the DC-DC boost converter when the predictive MPPT algorithm by switching state is applied.

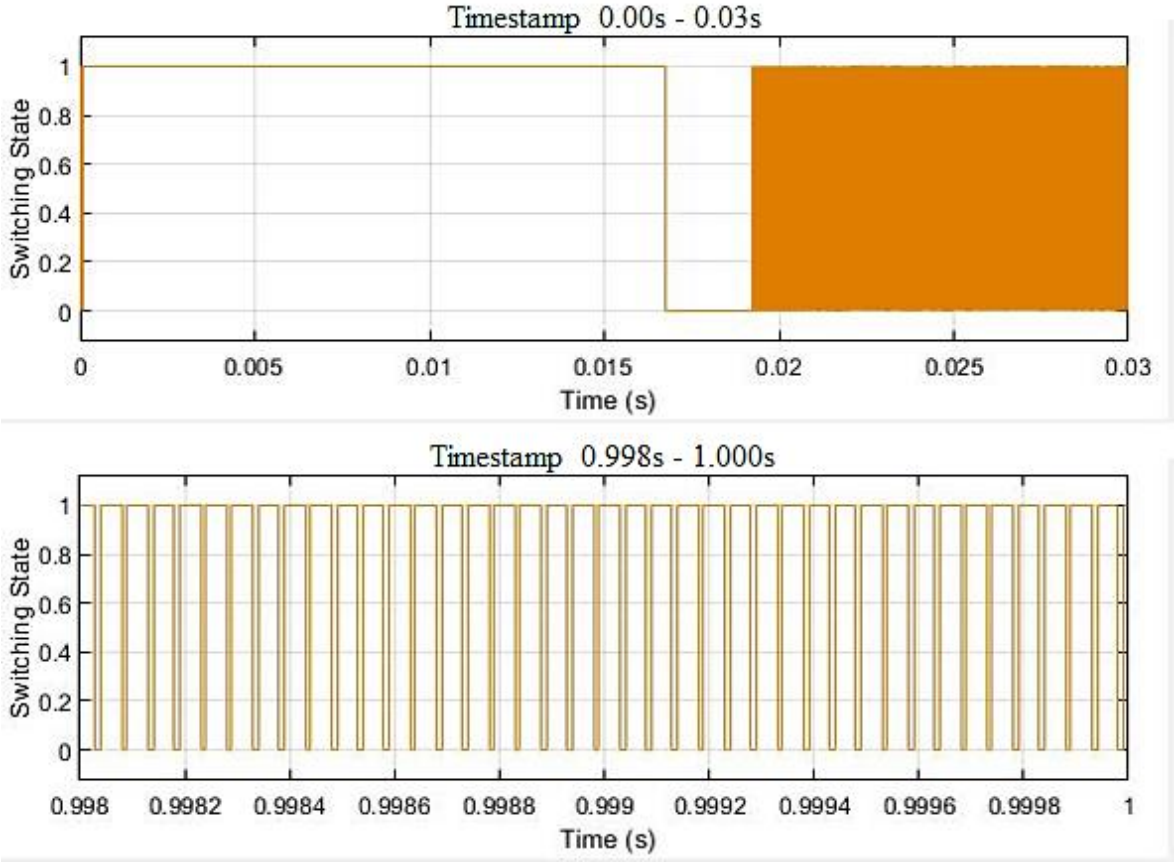


Figure 4.3: Simulation Results of Switching State for Predictive Switching State MPPT under Constant PEMFC Parameters

From the operation time $0s$ to $0.0165s$, the switching state was always ON. At the same time, the PEMFC output current was increased from $0A$ to $10.06A$. Then, the switching state was OFF after $0.0165s$. At this period, the PEMFC output current existed the maximum power current before it reached the MPP, and causing the output power to undershoot. When the output current is higher than the maximum power current, the switching state remained OFF to reduce the PEMFC output current until it was backed to the maximum power current. At this moment, the PEMFC output power was maximized. After $0.019s$, the switching state started to switch ON and OFF alternatively and kept the PEMFC output power at MPP. As shown in Figure 4.3, one can see that there are 20

switching cycles between $0.999s$ and $1s$. This means that the switching frequency is approximately $20kHz$.

At the load side, the load absorbed $48.1W$ of power from the PEMFC. The load voltage, current, and power are presented in Figure 4.4.

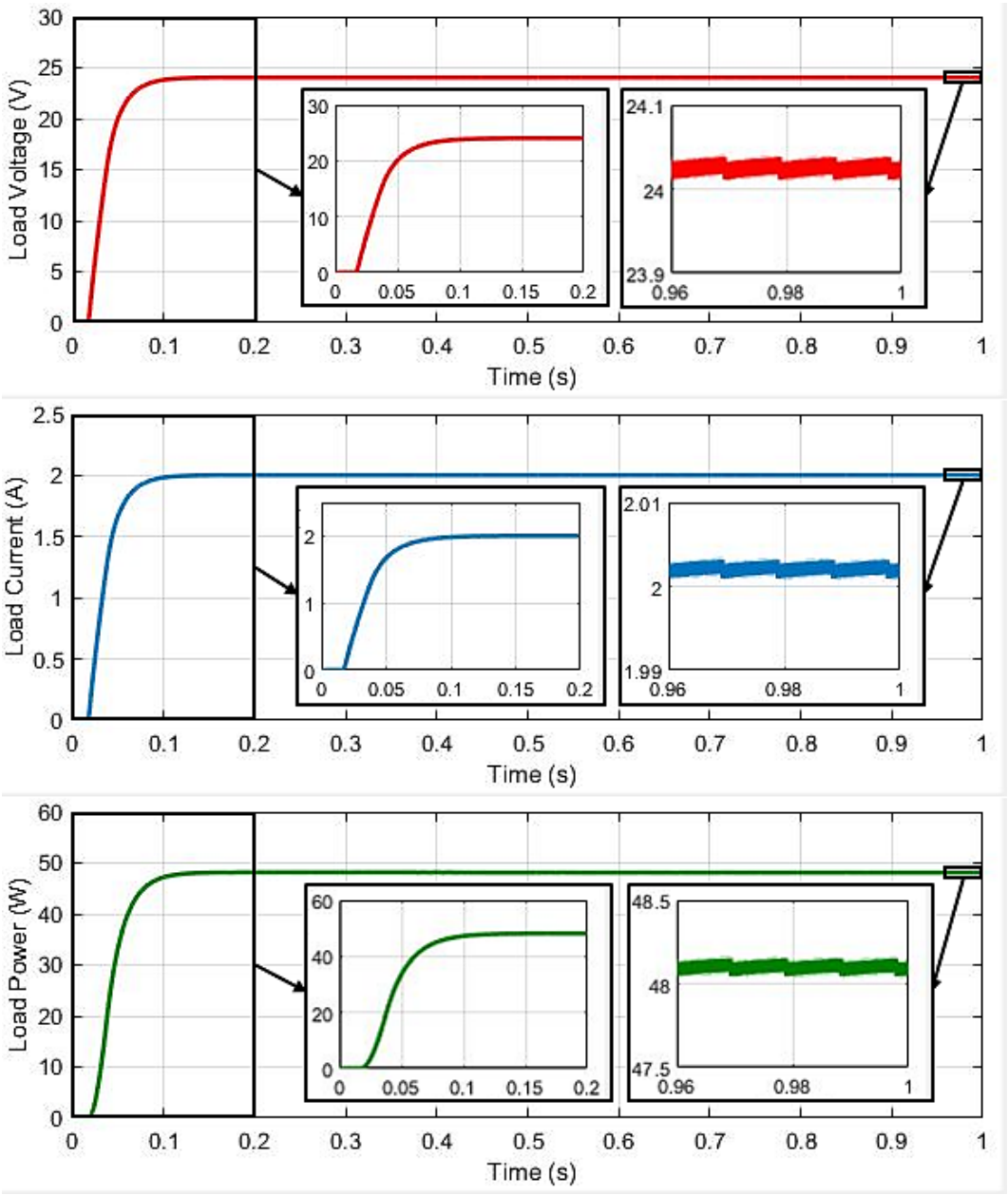


Figure 4.4: Simulation Results of Load for Predictive Switching State MPPT under Constant PEMFC Parameters

The initial load voltage was zero, and it started to increase after $0.0165s$. After that, it started to increase and reached $24.03V$ at $0.14s$ without overshoot. At the same time, the load current reached $2A$ and the load power reached $48.1W$. There are 0.11% voltage ripple, 0.11% current ripple, and 0.22% power ripple. These results prove that the DC-DC converter regulated a stable voltage with negligible ripple.

4.3.2 Simulation with Constant PEMFC Parameters by Predictive Duty Cycle MPPT Technique

This section presents the simulation results for the PEMFC implemented with predictive duty cycle MPPT control. For the predictive duty cycle MPPT technique, the maximum switching frequency can be fixed. In this section, the simulation of $10kHz$, $20kHz$, and $30kHz$ switching frequencies were applied. The simulation results of the PEMFC are illustrated in Figure 4.5, Figure 4.6, and Figure 4.7.

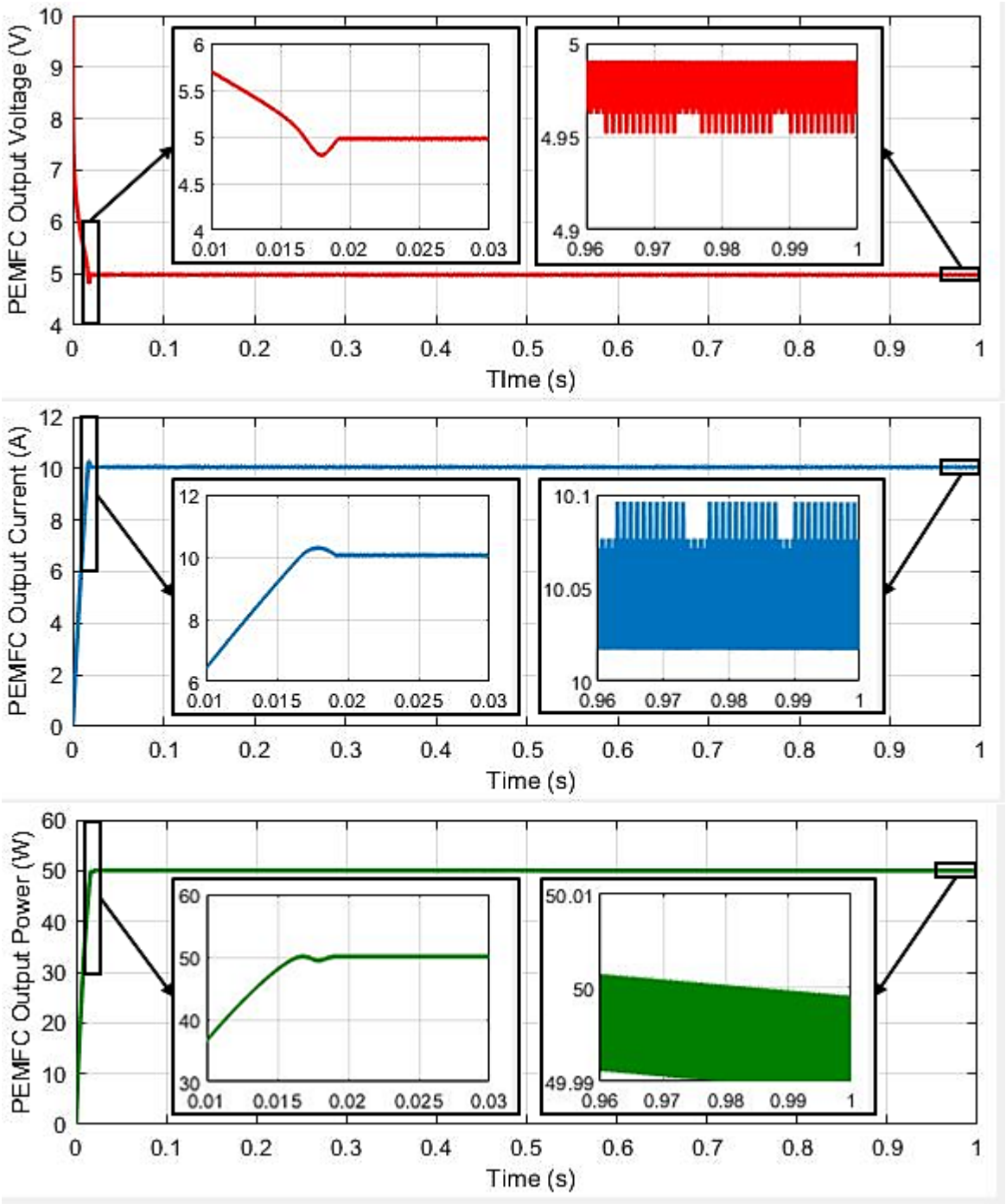


Figure 4.5: Simulation Results of PEMFC for Predictive Duty Cycle MPPT with $10kHz$ Frequency under Constant PEMFC Parameters

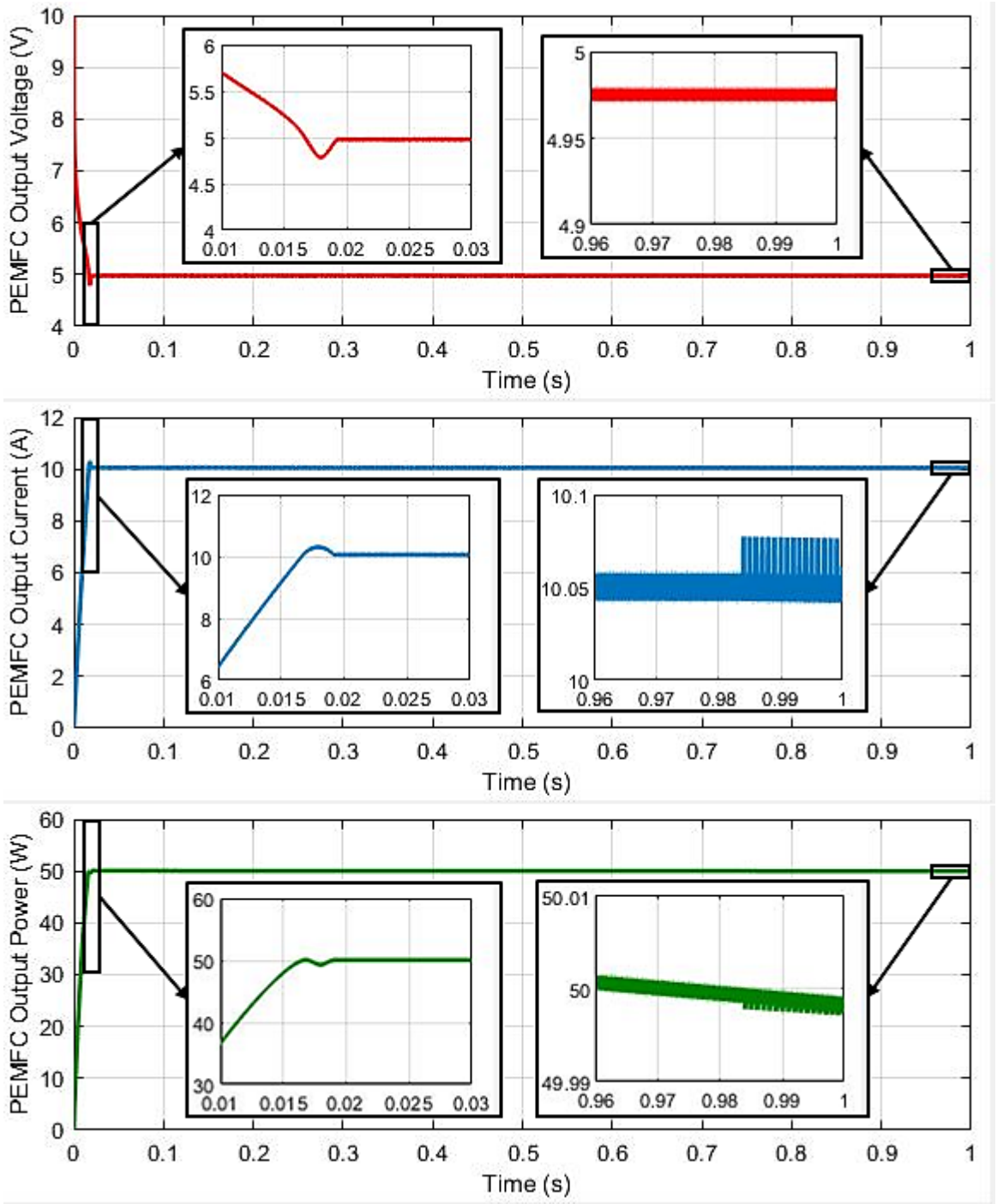


Figure 4.6: Simulation Results of PEMFC for Predictive Duty Cycle MPPT with $20kHz$ Frequency under Constant PEMFC Parameters

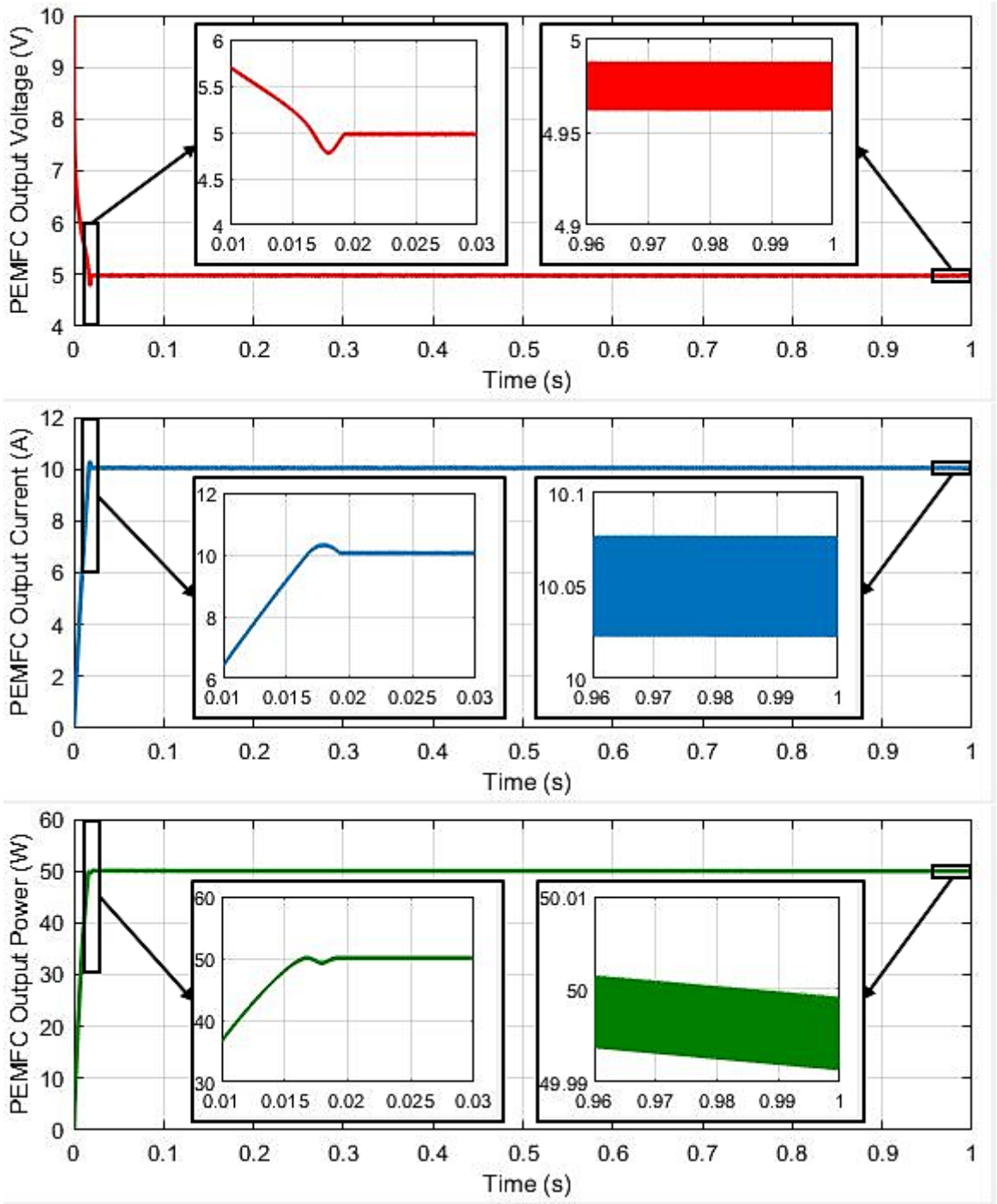


Figure 4.7: Simulation Results of PEMFC for Predictive Duty Cycle MPPT with $30kHz$ Frequency under Constant PEMFC Parameters

The simulation results above show that the PEMFC output power also reaches $50W$ within $0.02s$. The results are similar to the predictive MPPT by the switching state method.

However, the power quality produced by the PEMFC in each simulation was different due to the different power ripple and different power undershoot. First, the predictive duty cycle MPPT with $10kHz$ frequency method shows a 3.52% voltage undershoot, 2.28% current overshoot, and 1.28% power undershoot. For predictive duty cycle MPPT with $20kHz$ frequency method, it shows 3.89% of voltage undershoot, 2.41% of current overshoot, and 1.53% of power undershoot. The predictive duty cycle MPPT with $30kHz$ frequency method has slightly higher undershoot and overshoot issues. There were a 4.01% voltage undershoot, 2.45% current overshoot, and 1.62% power undershoot recorded. It is quite a surprise to find that the lower frequency method performs better than the higher frequency, with a lower power undershoot issue. Nevertheless, the power undershoot is considered low, and the power loss is negligible.

Another finding to be reported is the output ripple of the PEMFC. From the simulation results, the predictive MPPT by $10kHz$ frequency duty cycle method reported 0.78% voltage ripple, 0.8% current ripple, and 0.021% power ripple. For predictive MPPT by $20kHz$, the voltage ripple, current ripple, and power ripple were 0.35%, 0.35%, and 0.0041% respectively. For predictive MPPT by $30kHz$, there are 0.53% voltage ripple, 0.54% current ripple, and 0.0157% power ripple recorded. From the results, the predictive MPPT by $20kHz$ frequency duty cycle control had the best performance in terms of power ripple. Unexpectedly, the highest frequency control did not surpass the lower frequency. However, these negligible power ripples were insufficient to affect the power quality. It is found that such an approach produces good quality results in power quality.

This predictive MPPT technique determines the duty cycle with a fixed frequency. The controller computes the data and sends the duty cycle signal to the PWM generator at

every sampling stage. Then, the PWM generator sends the signal to the switch of the DC-DC boost converter. The determination of the duty cycle for each simulation is presented in Figure 4.8.

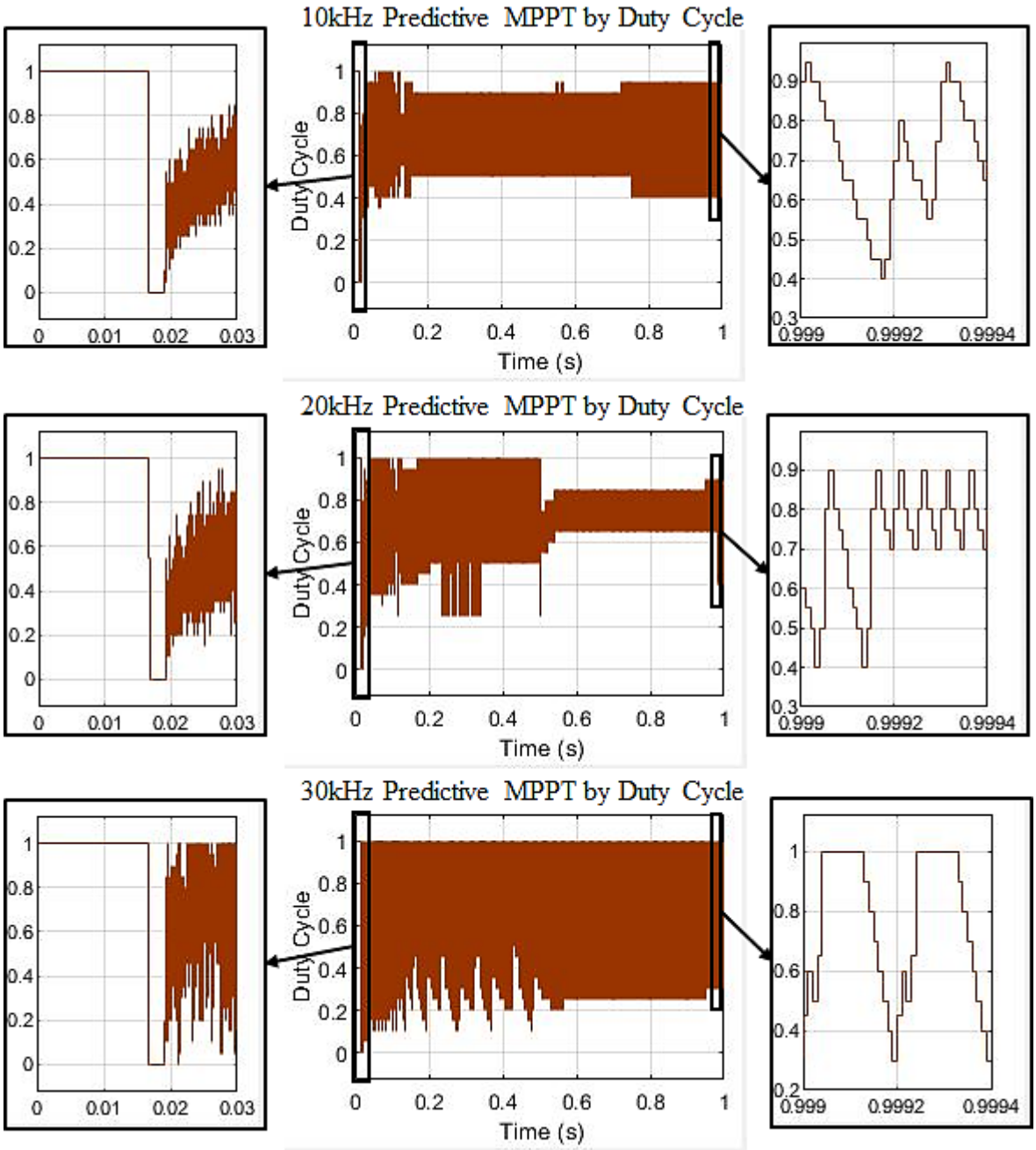


Figure 4.8: Simulation Results of Duty Cycle for Predictive Duty Cycle MPPT under Constant PEMFC Parameters

Figure 4.8 shows that the duty cycle was always equal to 1 before $0.0165s$. This led the switch to always turn ON. The phenomenon is similar to the previous results, which raise the output power to the maximum. Then, the duty cycle was varied from 0.4 to 0.95 according to the algorithm. The value of the duty cycle was always a number in multiples of 0.05. This is because the algorithm is designed with the duty cycle selection from 0 to 1 with an increment of 0.05 as discussed in section 3.5.3. The duty cycle was received by the PWM generator and sent the signal to the switch. The switching state of the DC-DC boost converter is displayed in Figure 4.9, Figure 4.10, and Figure 4.11.

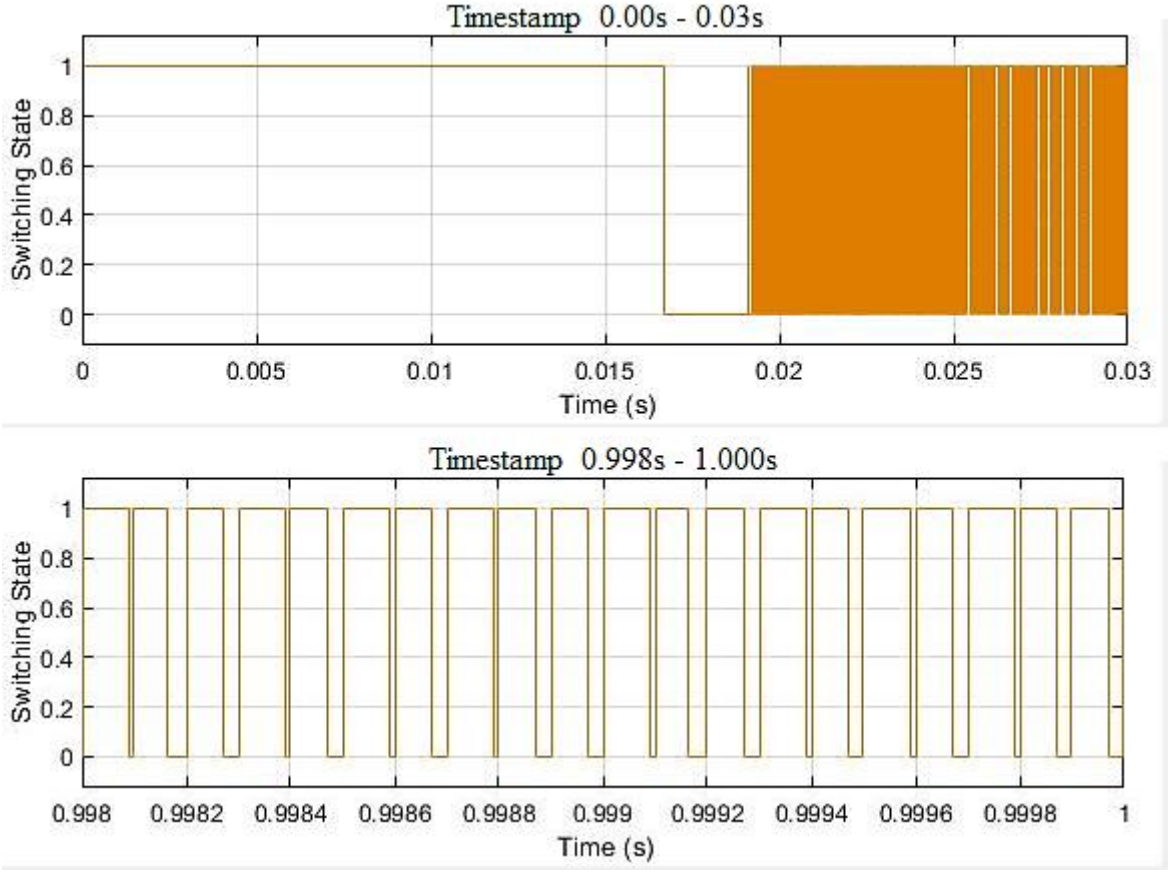


Figure 4.9: Simulation Results of Switching State for Predictive Duty Cycle MPPT with $10kHz$ Frequency under Constant PEMFC Parameters

The switching state controlled by the predictive MPPT by duty cycle with $10kHz$ frequency shows 10 switching cycles between $0.999s$ and $1s$. This means that it had a constant switching of $10kHz$. The difference between the switch ON and switch OFF periods in each switching cycle was determined by the duty cycle.

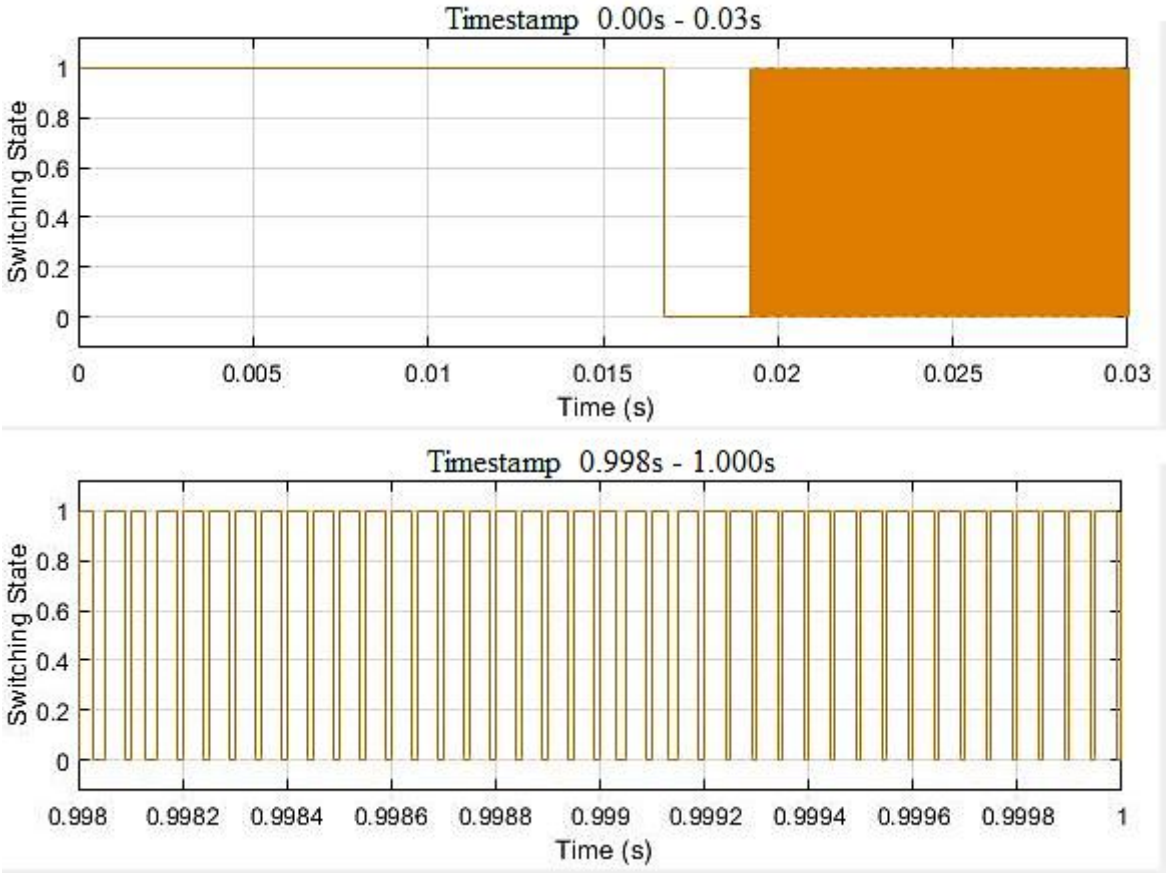


Figure 4.10: Simulation Results of Switching State for Predictive Duty Cycle MPPT with $20kHz$ Frequency under Constant PEMFC Parameters

Figure 4.10 displays the switching state controlled by the predictive MPPT by duty cycle with $20kHz$ frequency. There are 20 switching cycles between $0.999s$ and $1s$. This proves that the switching frequency is $20kHz$.

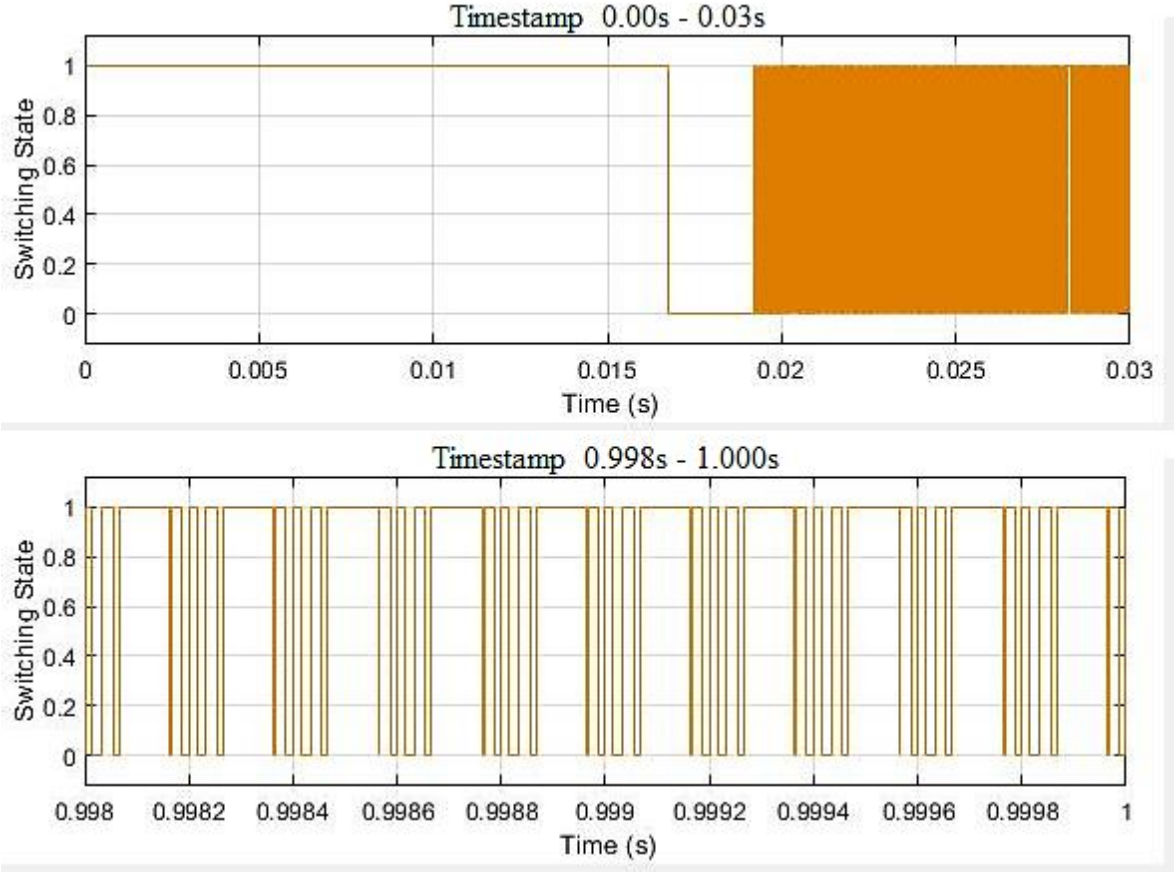


Figure 4.11: Simulation Results of Switching State for Predictive Duty Cycle MPPT with $30kHz$ Frequency under Constant PEMFC Parameters

In Figure 4.11, the predictive MPPT by duty cycle with $30kHz$ frequency did not perform exactly $30kHz$ of switching frequency. Although the method is designed to have a maximum switching frequency of $30kHz$, the actual frequency may falling below this value. Based on the simulation results shown in Figure 4.8, the duty cycle ranged from 0.3 to 1. When the controller selected the duty cycle as 1, the switch remained ON continuously. In this scenario, the switch did not experience any OFF-ON transitions within that switching cycle, leading to a reduction in the switching frequency. From Figure 4.11, only 20 ON-OFF cycles were observed between $0.999s$ and $1s$, indicating that the switching frequency was reduced to $20kHz$ instead of the intended $30kHz$.

Similar to the simulation results in section 4.3.1, the load also absorbed $48.1W$ of electrical power from the PEMFC. The load voltage, current, and power are presented in Figure 4.12, Figure 4.13, and Figure 4.14.

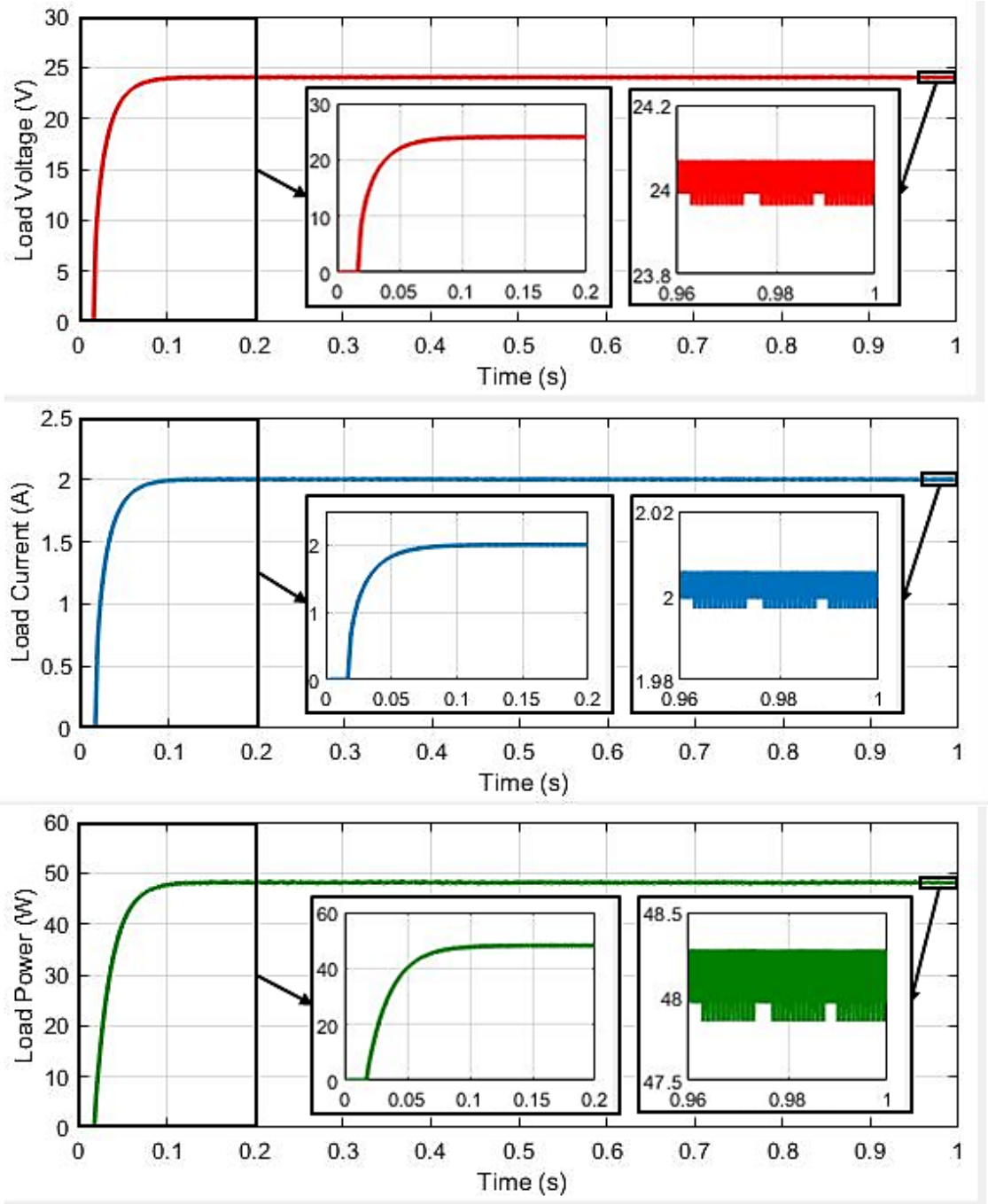


Figure 4.12: Simulation Results of Load for Predictive Duty Cycle MPPT with $10kHz$ Frequency under Constant PEMFC Parameters

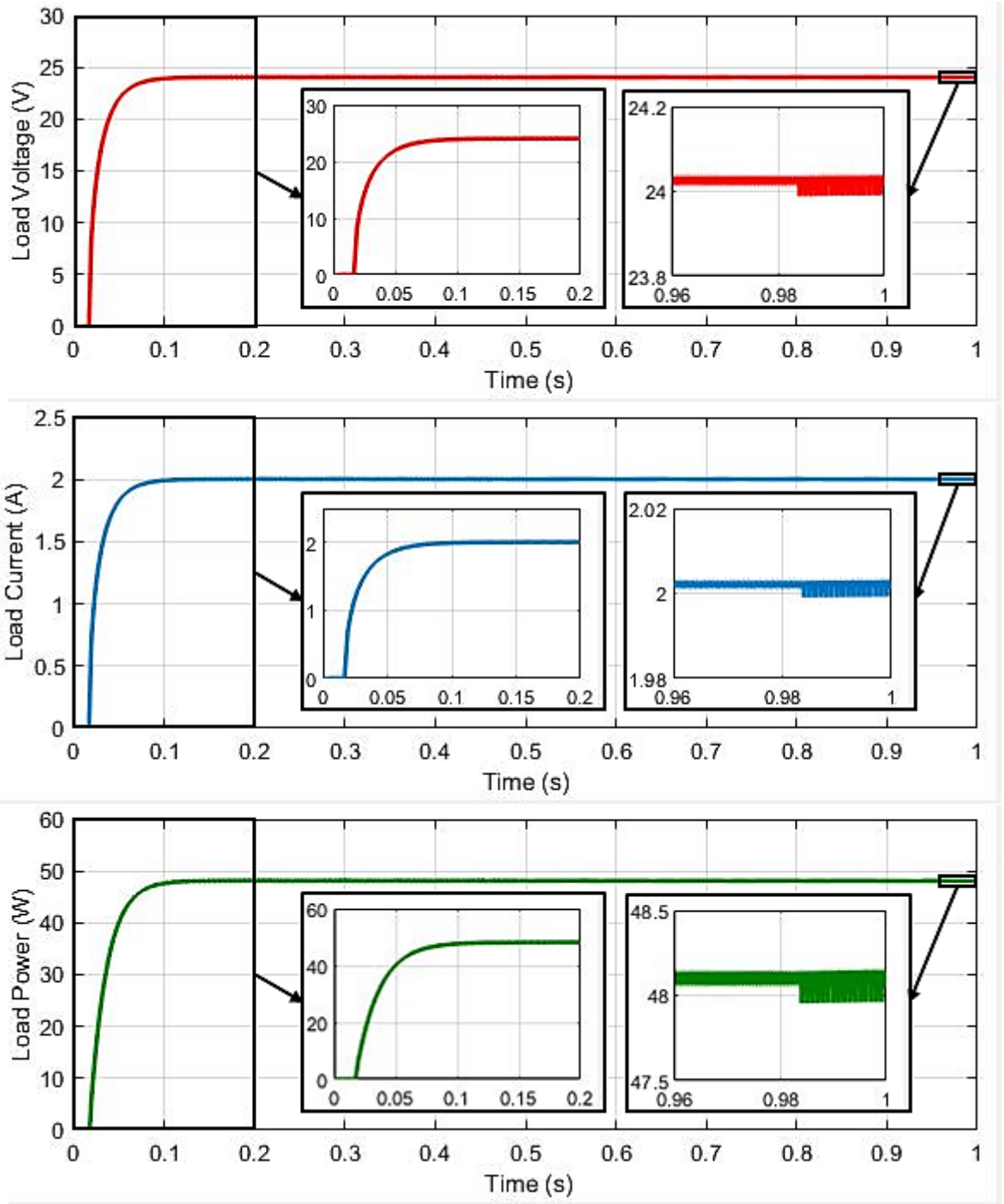


Figure 4.13: Simulation Results of Load for Predictive Duty Cycle MPPT with $20kHz$ Frequency under Constant PEMFC Parameters

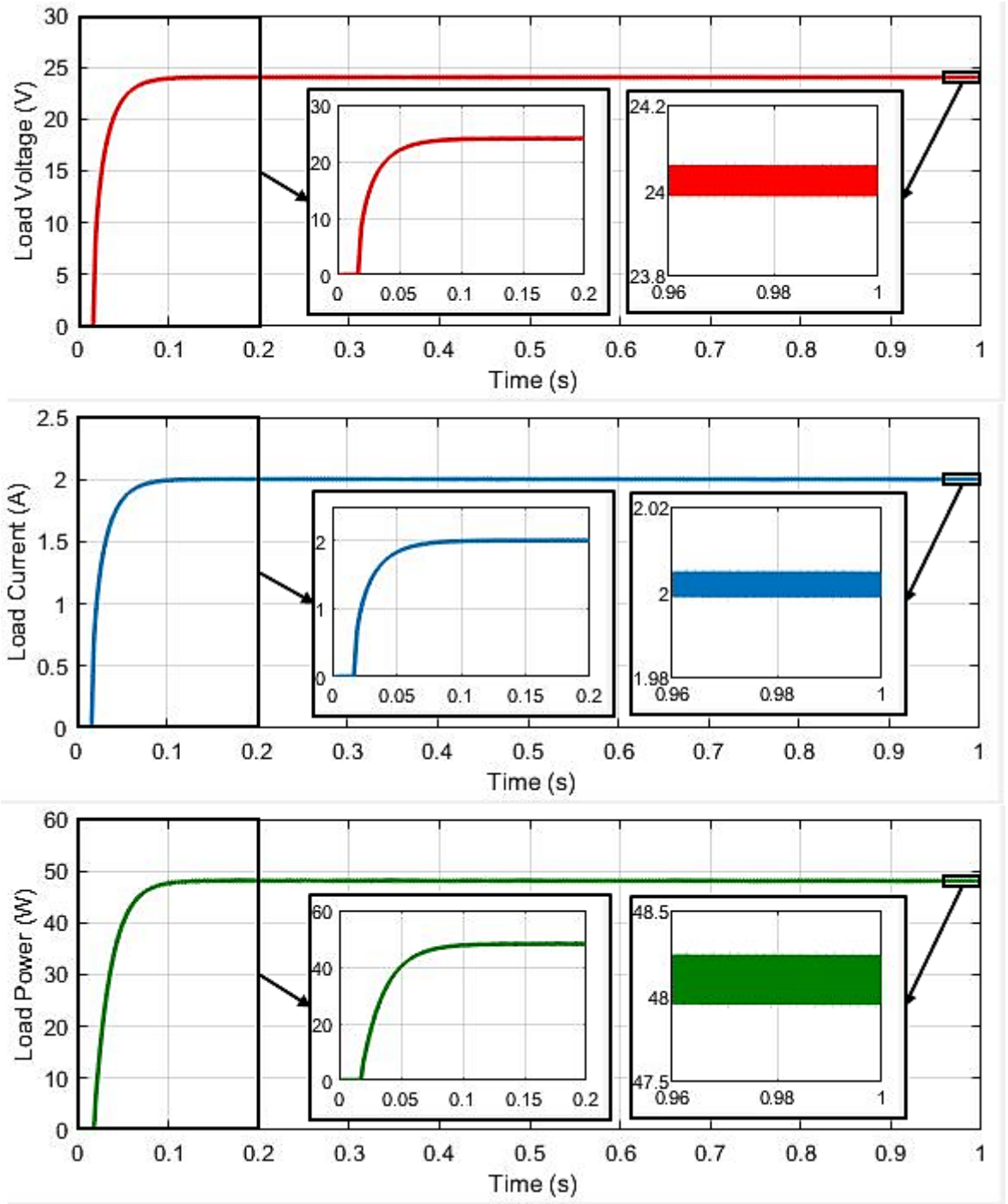


Figure 4.14: Simulation Results of Load for Predictive Duty Cycle MPPT with $30kHz$ Frequency under Constant PEMFC Parameters

The simulation results of the load are similar. Same as the previous method, the load voltage reached $24.03V$ and the load current reached $2A$ at $0.14s$ without overshooting.

There was a 0.45% voltage ripple, 0.44% current ripple, and 0.89% power ripple for $10kHz$ frequency method. For $20kHz$ frequency method, there was a 0.2% voltage ripple, 0.19% current ripple, and 0.37% power ripple. The $30kHz$ frequency method had the smallest ripple with 0.3% voltage ripple, 0.3% current ripple, and 0.61% power ripple. These ripples are insignificant to affect the power quality of the load.

4.3.3 Simulation with Constant PEMFC Parameters by Predictive Switching State MPPT with Frequency Reduction Technique

This section provides the simulation results of the PEMFC system with the predictive switching state MPPT with frequency reduction technique. This technique includes the switching frequency reduction technique in the predictive MPPT method with an adjustable weighting factor. If the weighting factor is high, the predictive control will place more emphasis on the switching frequency reduction. This weighting factor must not be too high because it may lose its goal of tracking the MPP. In this section, the simulations were done with the 0.1, 0.2, and 0.3 of weightage applied. The simulation results of the PEMFC are illustrated in Figure 4.15, Figure 4.16, and Figure 4.17.

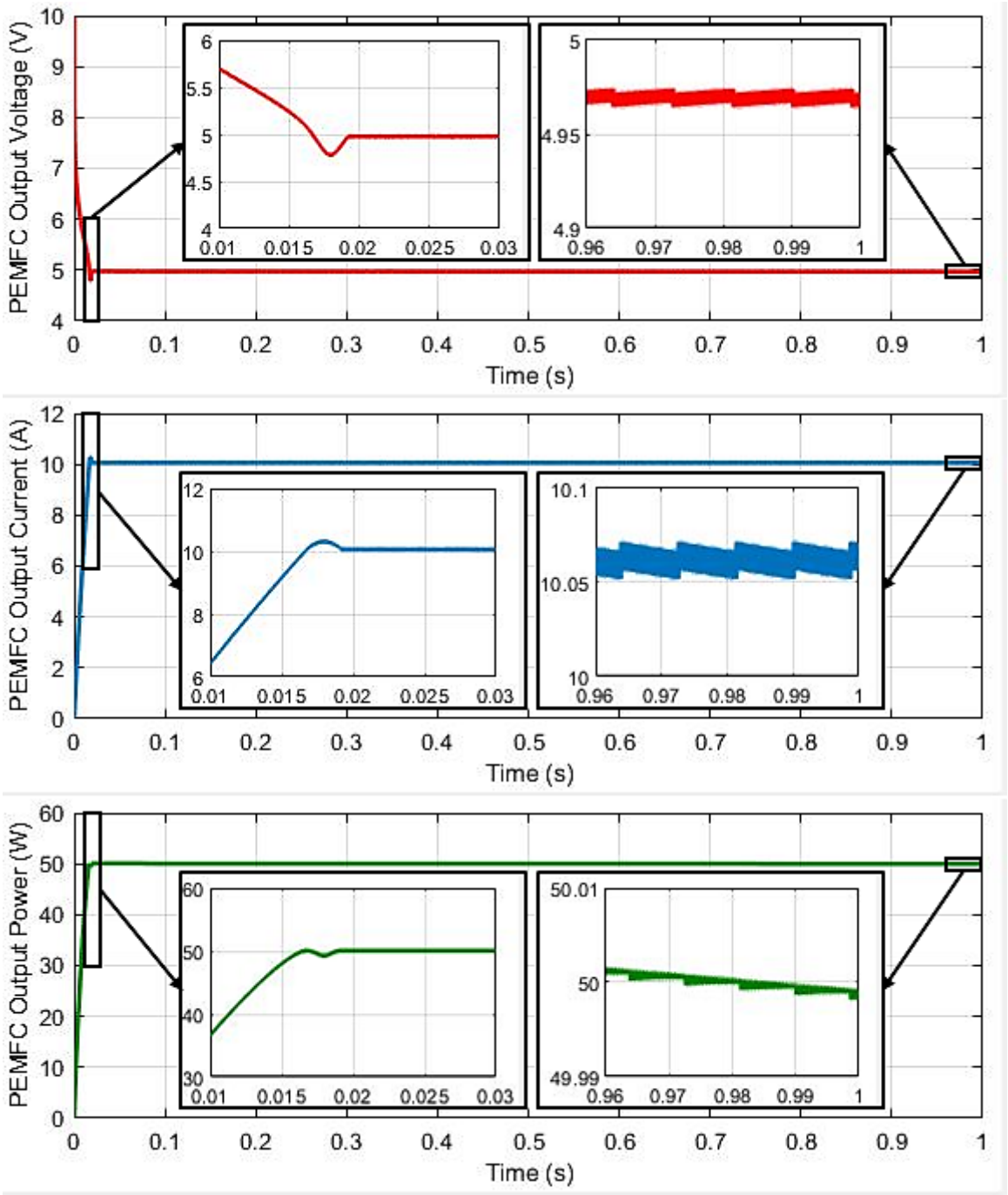


Figure 4.15: Simulation Results of PEMFC for Predictive Switching State MPPT with 0.1 Weighting Factor of Frequency Reduction under Constant PEMFC Parameters

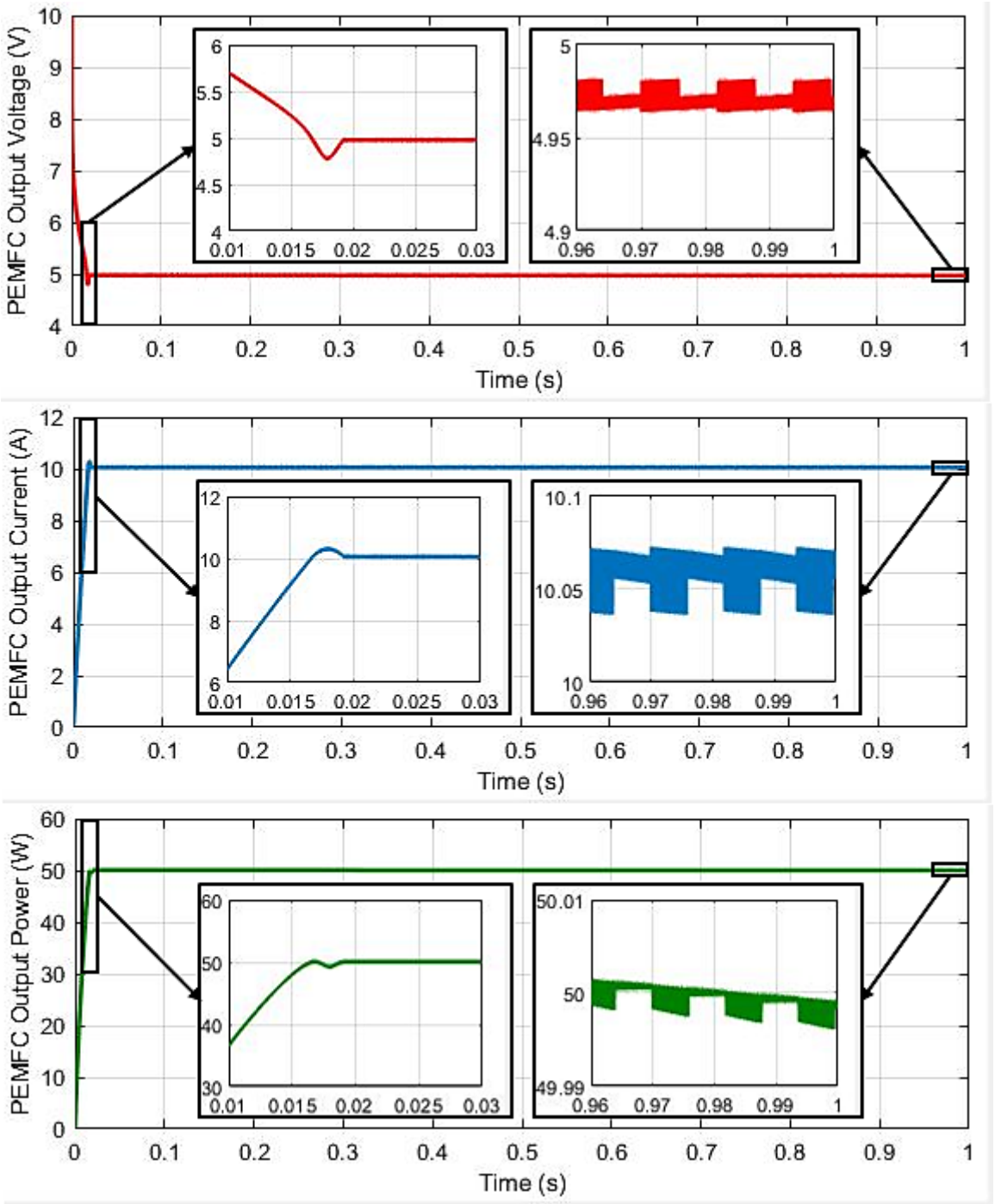


Figure 4.16: Simulation Results of PEMFC for Predictive Switching State MPPT with 0.2 Weighting Factor of Frequency Reduction under Constant PEMFC Parameters

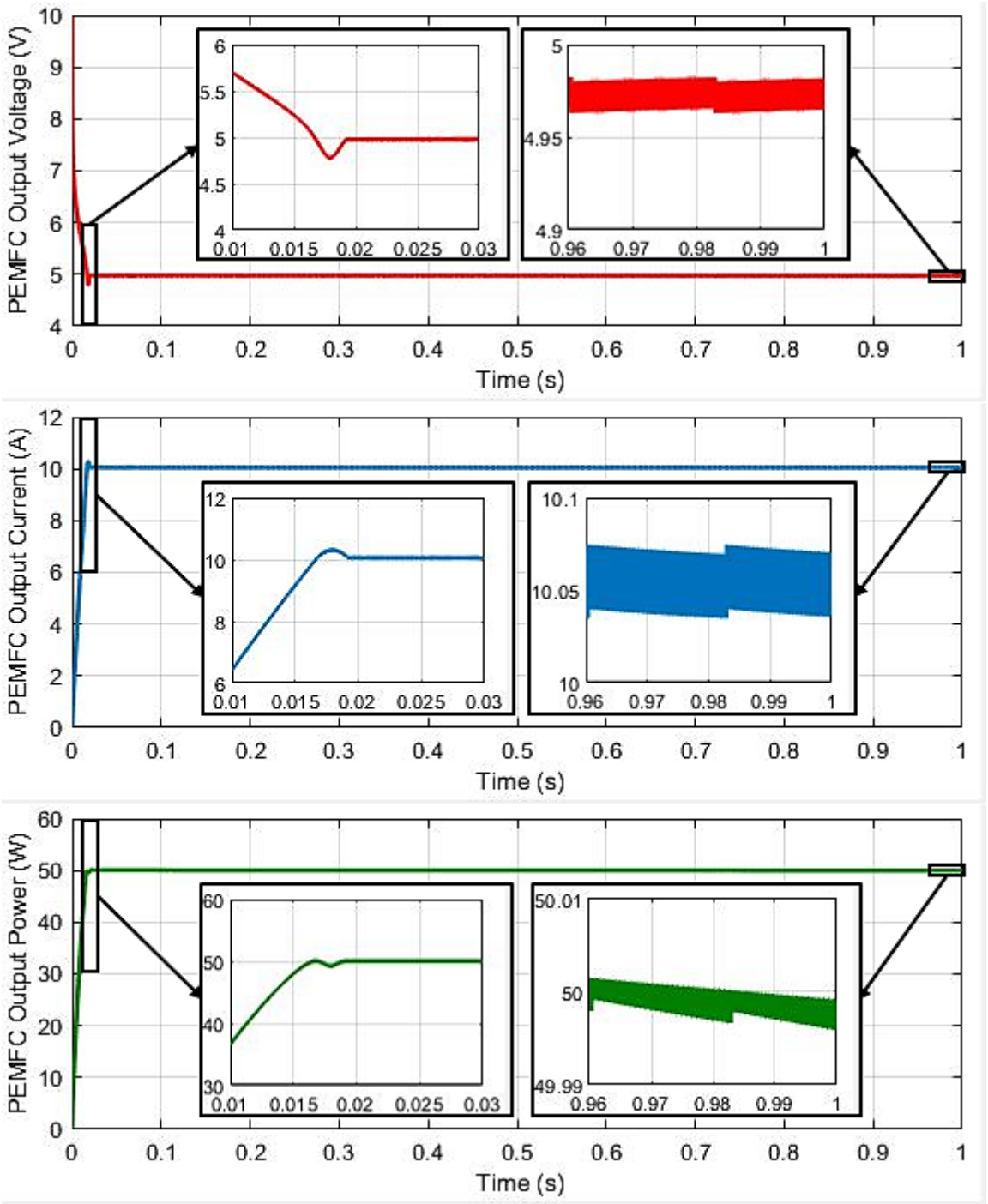


Figure 4.17: Simulation Results of PEMFC for Predictive Switching State MPPT with 0.3 Weighting Factor of Frequency Reduction under Constant PEMFC Parameters

The predictive switching state MPPT with frequency reduction technique has the same accuracy and tracking speed as the predictive MPPT by pure switching state and duty

cycle methods. Its voltage undershoot, current overshoot, and power undershoot are also the same as those of the predictive MPPT by the pure switching state method. However, its power quality depends on the weighing factor of the switching frequency reduction. The predictive switching state MPPT with a 0.1 weighting factor of frequency reduction had 0.2% voltage ripple, 0.2% current ripple, and 0.002% power ripple. For the 0.2 weighting factor of frequency reduction, there are 0.34% voltage ripple, 0.35% current ripple, and 0.006% power ripple reported. The predictive switching state MPPT with a 0.3 weighting factor of the frequency reduction technique has the same voltage and current ripple as the 0.2 weighting factor of frequency reduction, but its power ripple recorded is 0.007%. This finding is expected, since the higher weighting factor of switching frequency reduction may lead to higher output power fluctuations.

Similar to the predictive switching state MPPT technique, the controller directly manipulates the switching state inside the DC-DC boost converter. The simulation results of the switching state of the predictive switching state MPPT with 0.1, 0.2, and 0.3 weighting factor frequency reduction are illustrated in Figure 4.18, Figure 4.19, and Figure 4.20, respectively. From the simulation results, the switching frequency of the predictive switching state MPPT with 0.1, 0.2, and 0.3 weighting factor frequency reduction were approximately $20kHz$, $15kHz$ and $10kHz$, respectively.

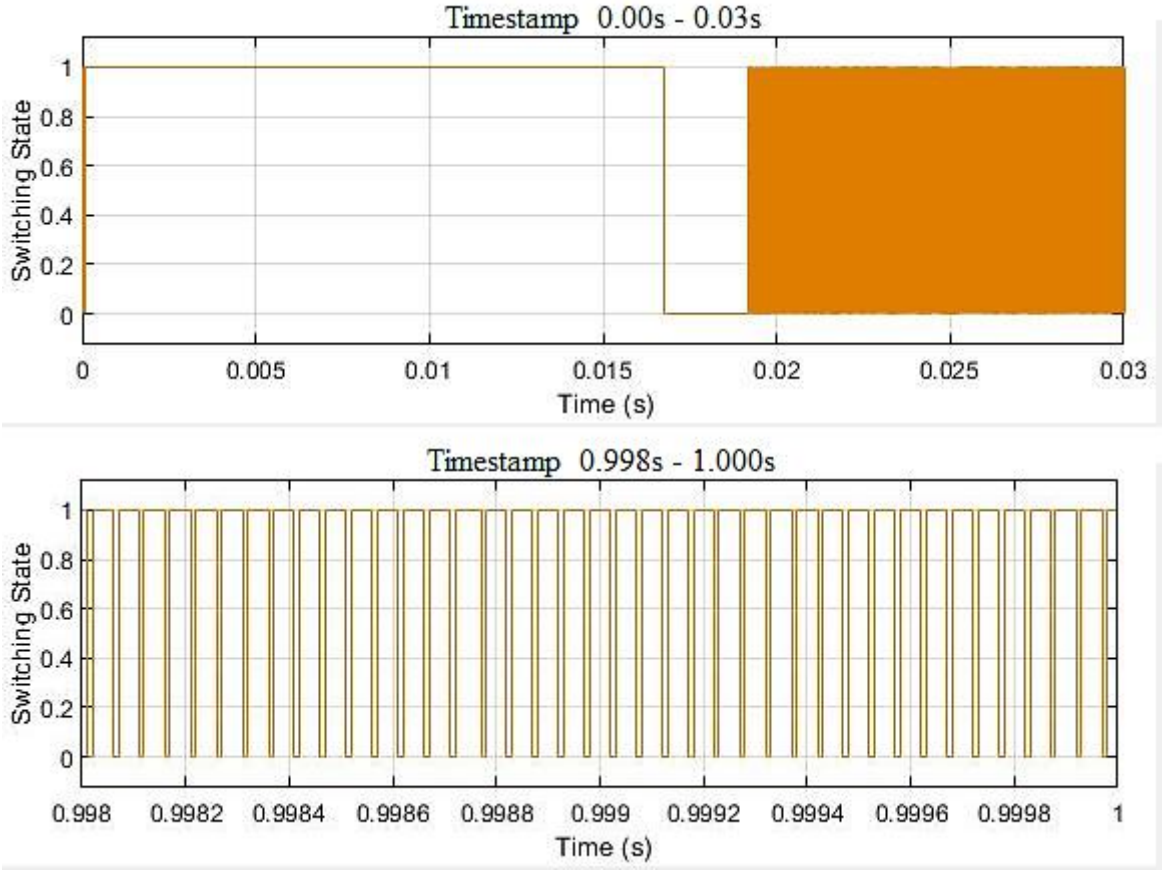


Figure 4.18: Simulation Results of Switching State for Predictive Switching State MPPT with 0.1 Weighting Factor of Frequency Reduction under Constant PEMFC Parameters

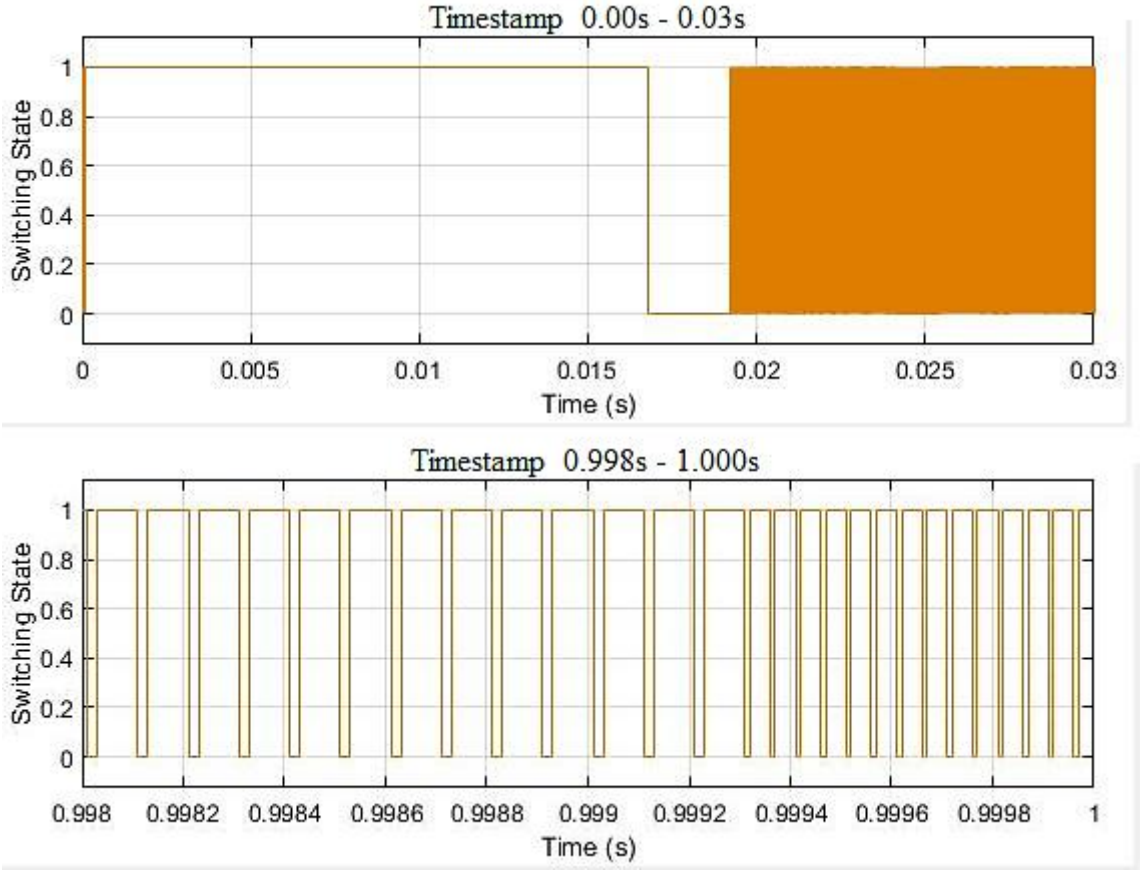


Figure 4.19: Simulation Results of Switching State for Predictive Switching State MPPT with 0.2 Weighting Factor of Frequency Reduction under Constant PEMFC Parameters

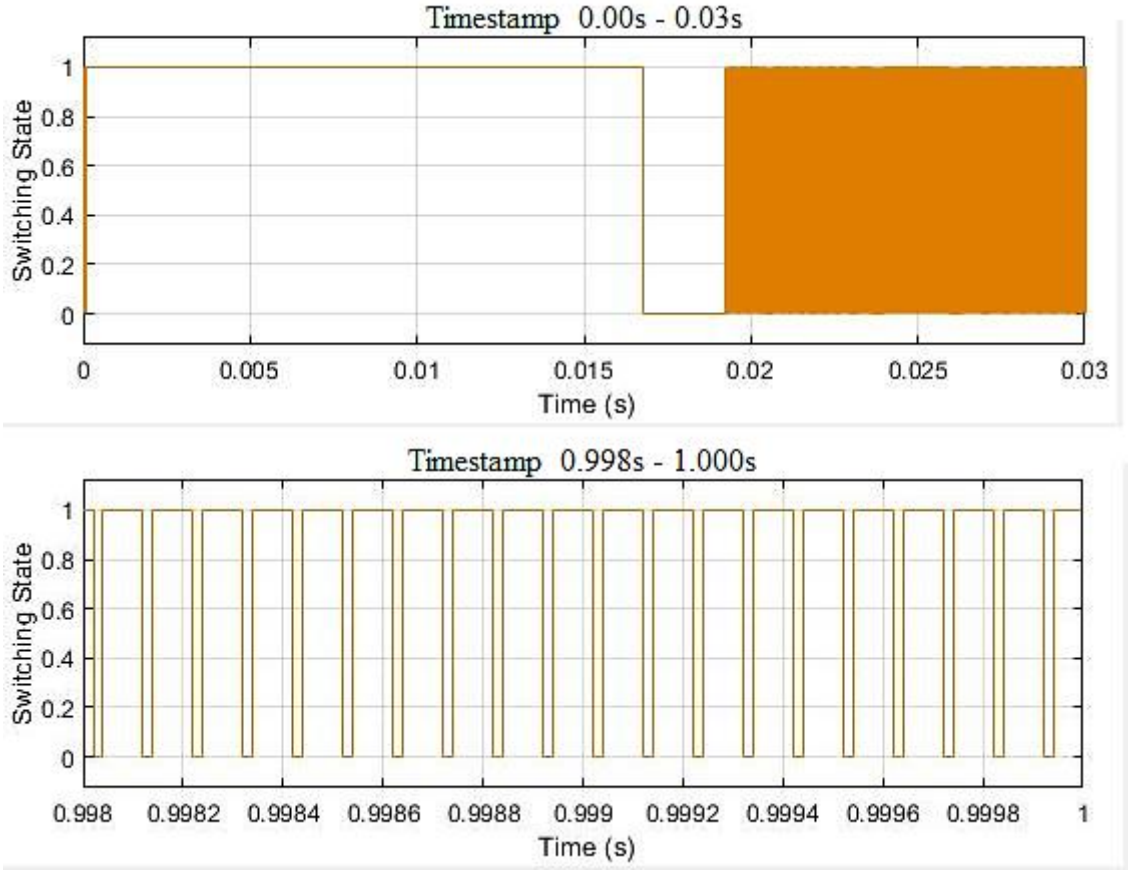


Figure 4.20: Simulation Results of Switching State for Predictive Switching State MPPT with 0.3 Weighting Factor of Frequency Reduction under Constant PEMFC Parameters

For the load, $48.1W$ of electrical power was consumed by the 12Ω load. Figure 4.21, Figure 4.22, and Figure 4.23 show the simulation results of the load voltage, current, and power for each simulation.

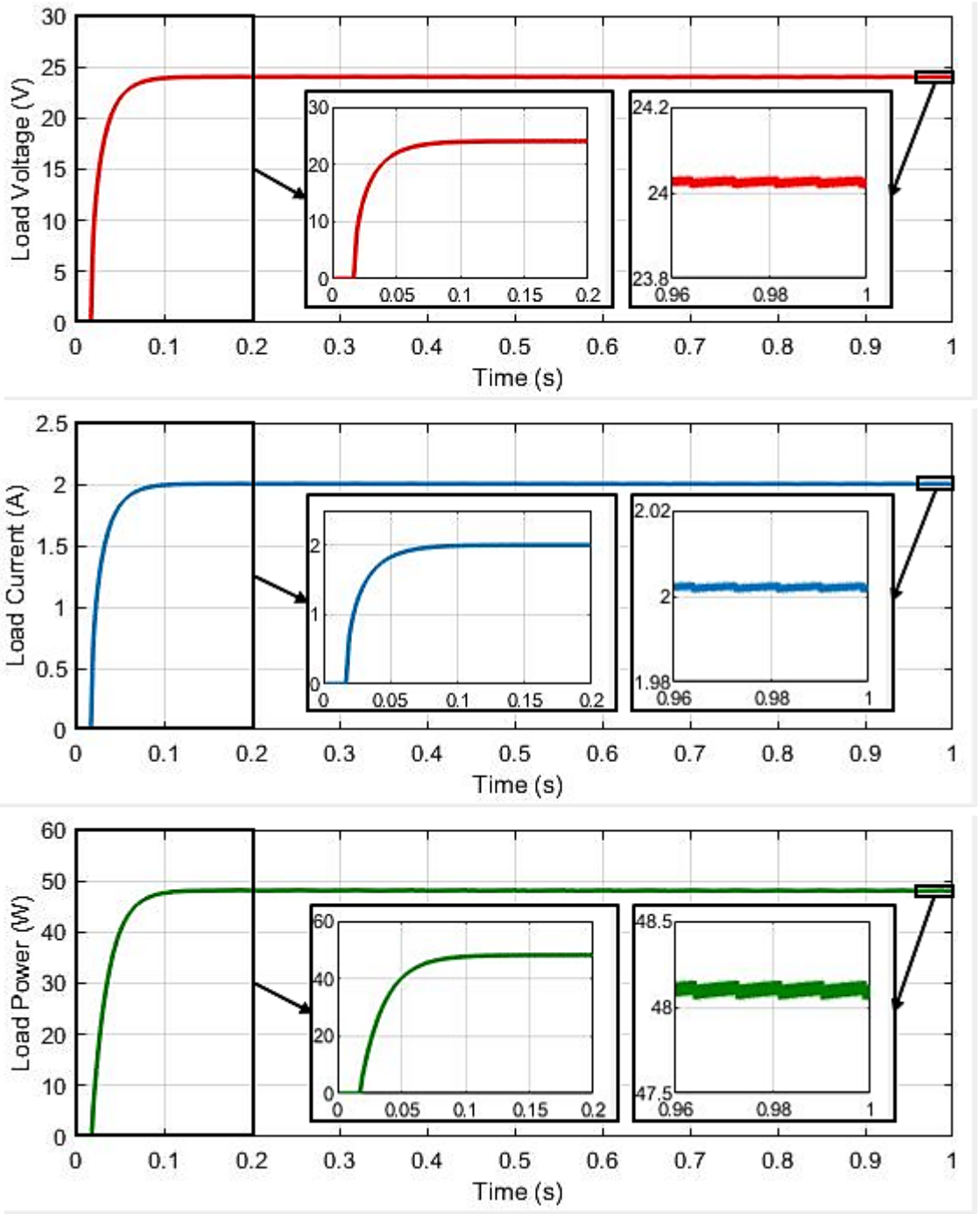


Figure 4.21: Simulation Results of Load for Predictive Switching State MPPT with 0.1 Weighting Factor of Frequency Reduction under Constant PEMFC Parameters

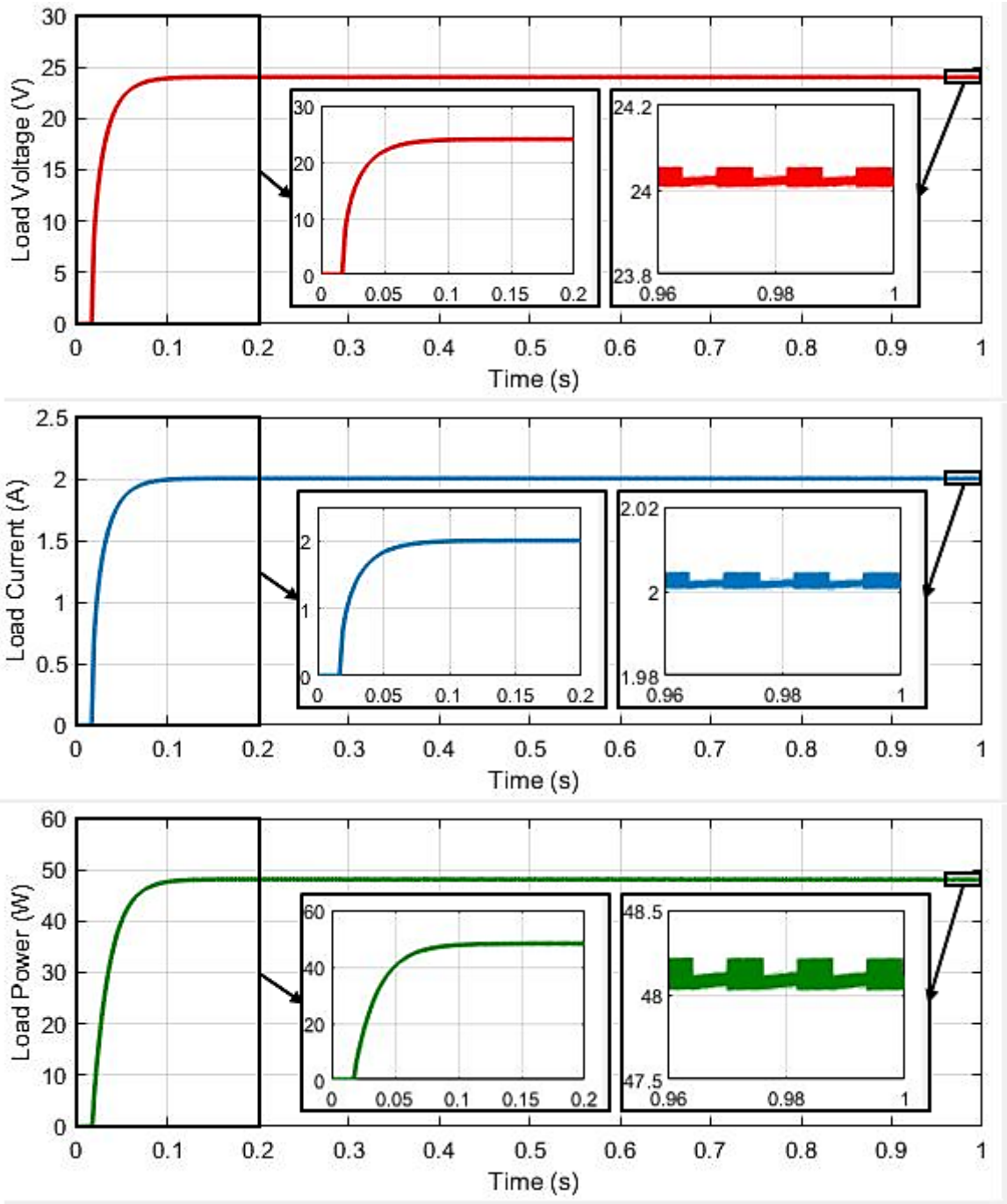


Figure 4.22: Simulation Results of Load for Predictive Switching State MPPT with 0.2 Weighting Factor of Frequency Reduction under Constant PEMFC Parameters

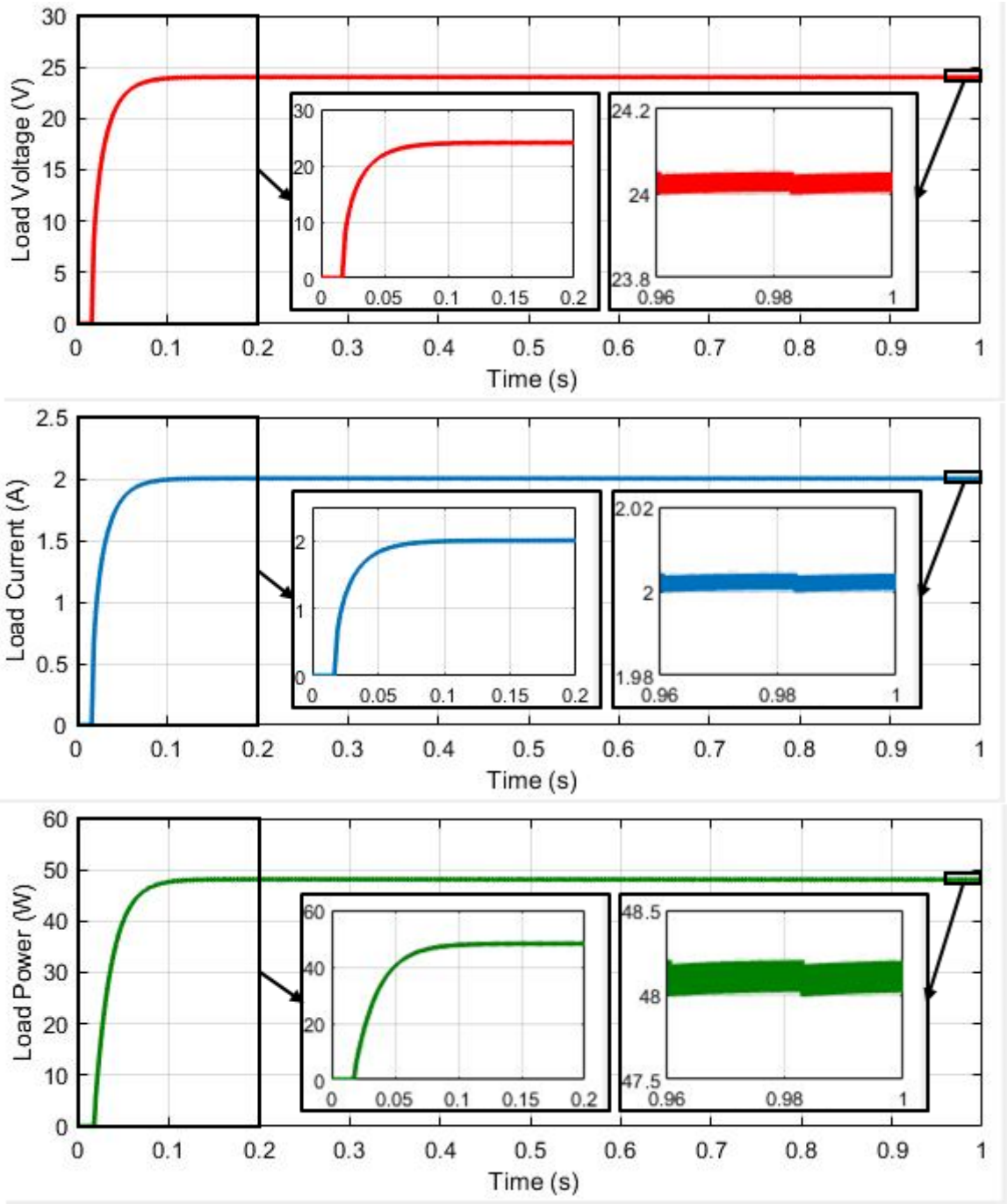


Figure 4.23: Simulation Results of Load for Predictive Switching State MPPT with 0.3 Weighting Factor of Frequency Reduction under Constant PEMFC Parameters

On average, the load voltage, current, and power reached $24.03V$, $2A$, and $48.1W$ at $0.14s$ without overshooting. The predictive switching state MPPT with a 0.1 weighting

factor of the frequency reduction method had the smallest ripple with 0.11% voltage ripple, 0.11% current ripple, and 0.22% power ripple. For predictive switching state MPPT with 0.2 and 0.4 weighting factors of frequency reduction methods, there was a 0.20% voltage ripple, 0.19% current ripple, and 0.39% power ripple. These ripples are insignificant to affect the power quality of the load.

4.3.4 Summary of Simulation Results with Constant PEMFC Parameters

The results of the simulation are summarised in this section. Based on Figure 4.2, Figure 4.5, Figure 4.6, Figure 4.7, Figure 4.15, Figure 4.16, and Figure 4.17, the PEMFC output power was decreasing with time. This was because the partial pressures of the fuel reduced over time as the process progressed. According to Equation 2.5, hydrogen has a partial pressure of $q_{H_2}^{in}/k_{H_2}$ at initial, and then reduced by $2k_r I_{FC}\left[1-e^{\left(-\frac{t}{\tau_{H_2}}\right)}\right]/k_{H_2}$ with time. After a long period of operation, the final partial pressure will become $q_{H_2}^{in}-2k_r I_{FC}/k_{H_2}$. For oxygen, its partial pressure also follows the same pattern. According to the mathematical equation, the output power of PEMFC will be decreased if the partial pressure of hydrogen and oxygen is decreased. This phenomenon is illustrated in Figure 4.24.

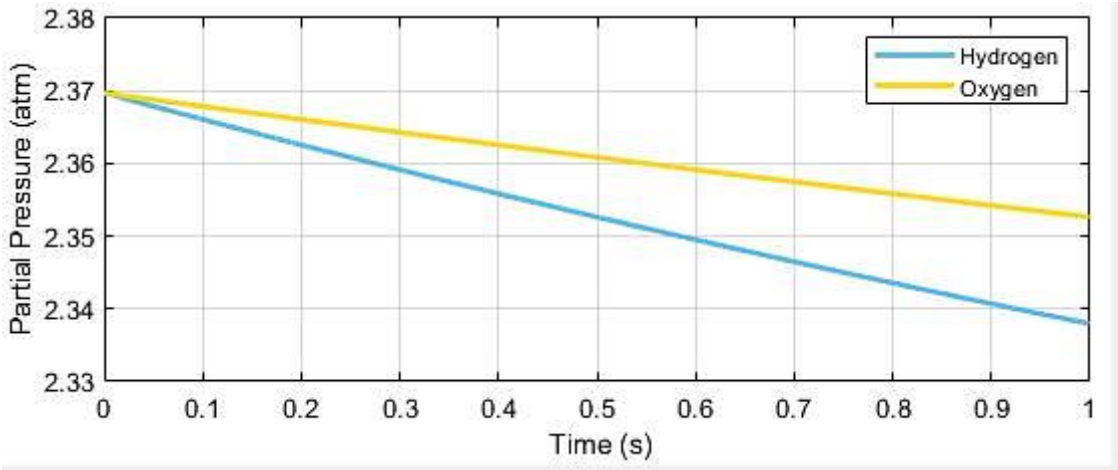


Figure 4.24: Partial Pressure of Hydrogen and Oxygen during Operation

Theoretically, the starting maximum power is $50.06W$. After the PEMFC operates for a long time, the maximum power will be reduced to $49.66W$. Figure 4.25 displays the starting P-I curve and final P-I curve. The difference points of the MPPs are also shown in Figure 4.25.

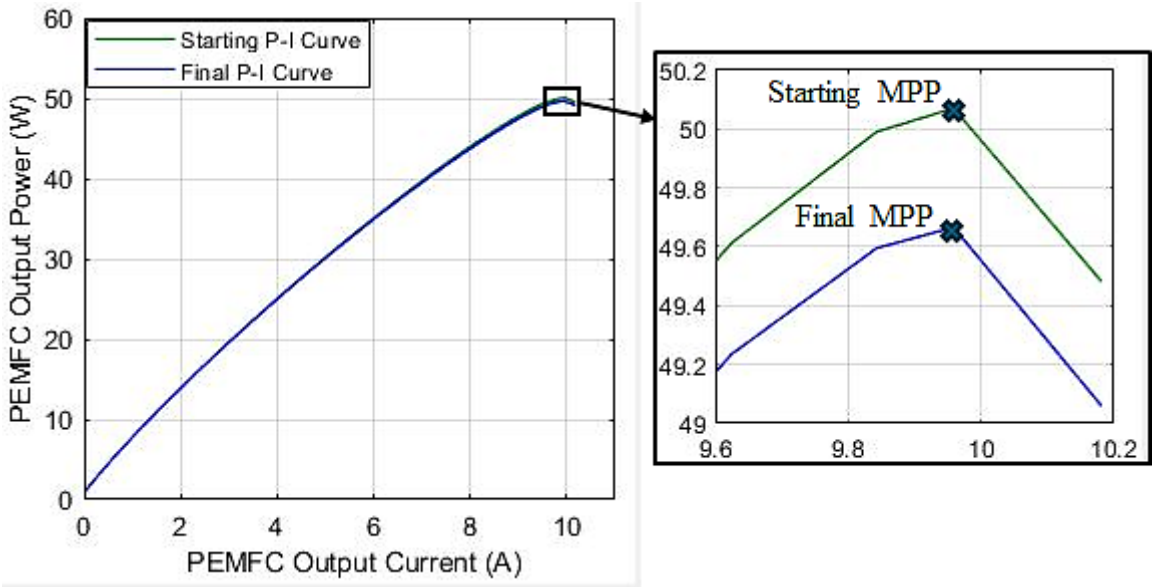


Figure 4.25: Starting and Final PEMFC P-I Curve

Figure 4.3, Figure 4.9, Figure 4.10, Figure 4.11, Figure 4.18, Figure 4.19, and Figure 4.20 show that the switching state was always ON before the PEMFC output power achieved the maximum power. At this moment, the PEMFC output current was increased to the maximum power current, and the energy was stored in the inductor with Equation 4.1.

$$E = \frac{1}{2}LI^2 \qquad \text{Equation 4.1}$$

where E is the electrical energy, L is the inductance, and I is the current. After $0.0165s$, the current flow through the inductor exceeded the maximum power current at $10.06A$ after the PEMFC reached MPP and caused the output power to undershoot. Therefore, the predictive MPPT controller selected the switching state or duty cycle as 0 so that the switch was OFF and forced the inductor to release the electrical energy to the load. However, the PEMFC output current overshoot still occurred due to the unstable load voltage and current. At $0.019s$, the output power reached MPP again. This was the moment that the MPP was tracked. Then, the predictive MPPT algorithm determined the alternative of switching state to keep the output power at MPP.

From Figure 4.4, Figure 4.12, Figure 4.13, Figure 4.14, Figure 4.21, Figure 4.22, and Figure 4.23, the load voltage, current, and power were approximately zero before $0.0165s$. This was because the switch in the DC-DC converter was always ON before 0.0165s. This caused the PEMFC to short-circuit to the inductor of the DC-DC converter. At this period, the electrical energy was only transmitted to the inductor, and no electrical power was transmitted to the load. In addition, the initial capacitor voltage was zero. Therefore, there was no current flow between the capacitor and the load. The current flow of the electrical circuit is described in Figure 4.26.

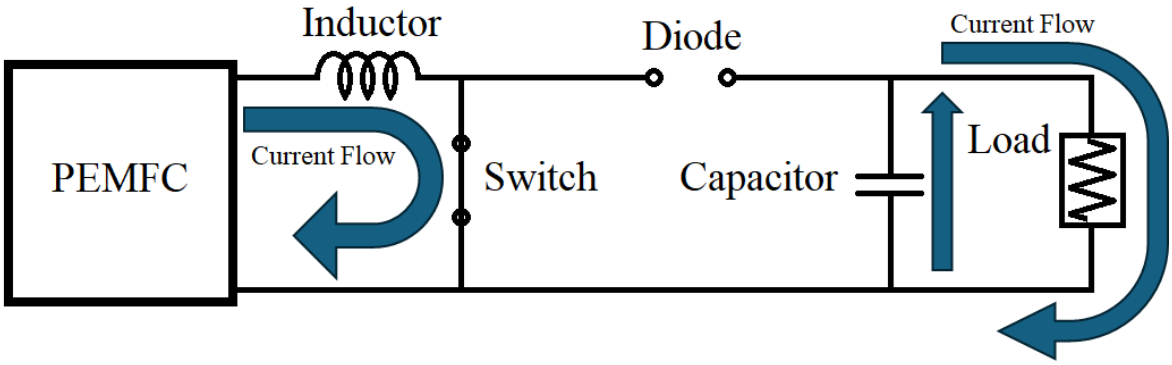


Figure 4.26: Current Flow in DC-DC Boost Converter when Switch is ON

After the PEMFC reached the maximum power, the switch was OFF until $0.019s$. At this moment, the load voltage started to increase because the electrical power started to be transmitted to the load when the switch was OFF. At the same time, the capacitor started to charge, and the voltage started to increase. The energy stored in the capacitor is expressed as Equation 4.2.

$$E = \frac{1}{2}CV^2 \qquad \text{Equation 4.2}$$

The current flow when the switch was OFF is illustrated in Figure 4.27.

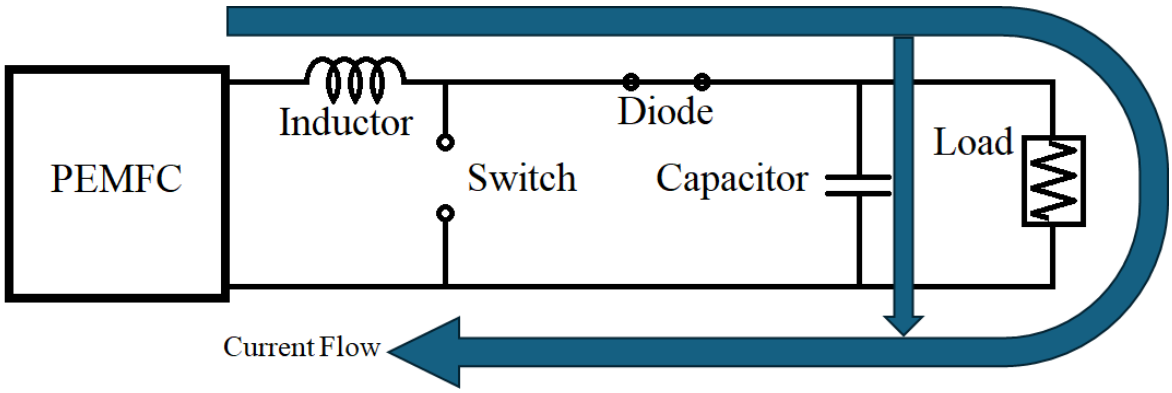


Figure 4.27: Current Flow in DC-DC Boost Converter when Switch is OFF

When there was energy stored in the capacitor, the load could continuously absorb the electrical power either from the PEMFC, inductor, or capacitor. After $0.019s$, the switch was ON and OFF rapidly to keep the PEMFC output current at maximum power current. The determination of the switching state was controlled by the predictive MPPT controller. The load voltage did not drop to zero when the switch was ON for an instantaneous period because the capacitor opposed the abrupt voltage changes. Figure 4.26 and Figure 4.27 illustrate the electrical power was only distributed to the capacitor and load when the switch was OFF. It means the PEMFC output power was divided into multiple portions of energy and then transmitted to the capacitor and load. Figure 4.28 shows the simulation results comparing the PEMFC output power and the electrical power distributed to the capacitor and load.

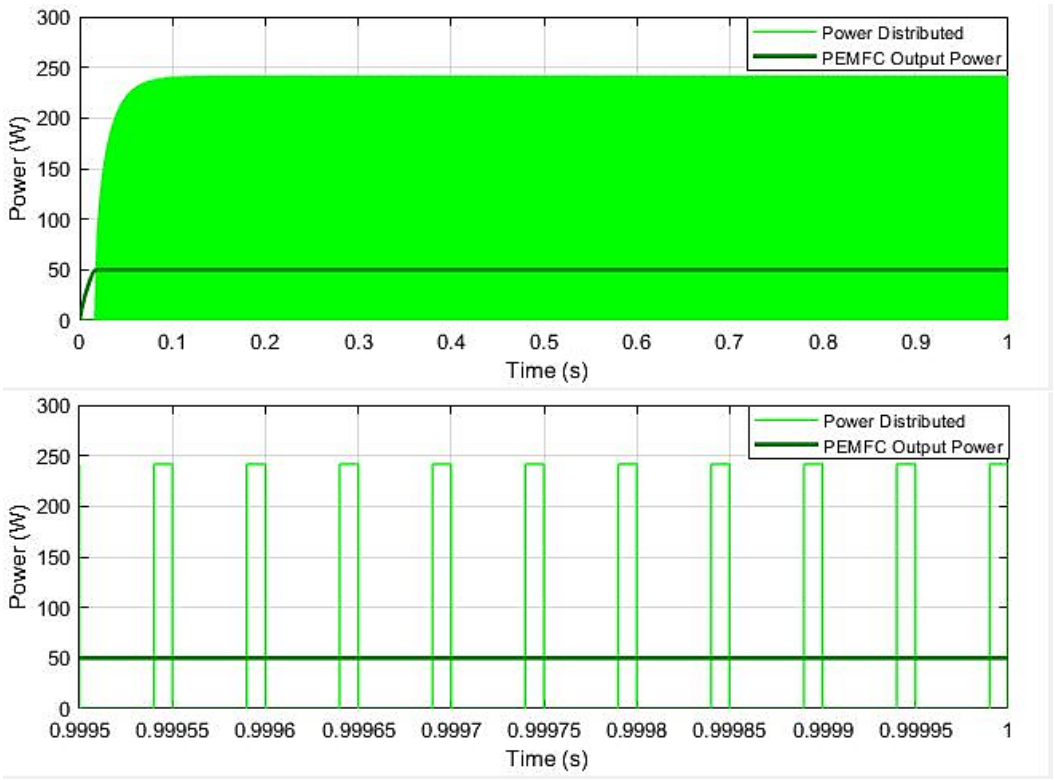


Figure 4.28: Simulation Results of Electrical Power Absorbed by Capacitor and Load vs PEMFC Output Power

Figure 4.28 illustrates the electrical power distributed to the capacitor and the load, which was divided into multiple portions with higher power. There were ten portions of energy with $241.75W$ of power within $10\mu s$. The total electrical energy can be determined by calculating the area under the graph.

$$E = \int P \ dt \qquad \text{Equation 4.3}$$

By calculation, the energy distributed was approximately the same as a continuous power of $48.35W$, which is close to the maximum capacity of the $50W$ PEMFC output power.

The simulation results of all the predictive MPPT techniques are presented in Table 4.2, and their performances are compared. The main focal points of these predictive MPPT techniques are the accuracy and the speed of tracking the MPP. Secondly, it is to provide a stable and high power quality with a low power ripple. From the comparison in Table 4.2, the tracking rate of all the techniques can be considered at the same speed. For voltage undershoot, current overshoot, and power undershoot issues, the predictive duty cycle MPPT method performed slightly better than the predictive switching state MPPT with or without the frequency reduction technique.

The predictive duty cycle MPPT with $20kHz$ and $30kHz$ frequency methods had the same switching frequency, which is $20kHz$. Figure 4.8 shows that the duty cycle for predictive duty cycle MPPT with $10kHz$ and $20kHz$ frequency always selected the duty cycle between 0.4 and 0.95. The switch was always ON and OFF alternatively in each switching cycle. Therefore, the switching frequency was the same as the setting frequency. For predictive duty cycle MPPT with $30kHz$ frequency, the duty cycle varied from 0.1 to 1.

When the duty cycle was 1, the switch was maintained at the ON switching state. This caused the switching frequency to be reduced to $20kHz$. It did not reach the full switching frequency setting. It is estimated that one-third of its duty cycle was selected as 1. Even though the maximum switching frequency setting of the predictive duty cycle MPPT control was $30kHz$, the simulated switching frequency was only $20kHz$.

Table 4.2: Comparison of Proposed Predictive MPPT Techniques under Constant PEMFC Parameters

Comparison	**Predictive Switching State MPPT**	**Predictive Duty Cycle MPPT**			**Predictive Switching State MPPT with Frequency Reduction**		
		$10kHz$	**$20kHz$**	**$30kHz$**	**0.1 Weighing Factor**	**0.2 Weighing Factor**	**0.3 Weighing Factor**
Accuracy	99.88%	99.88%	99.88%	99.88%	99.88%	99.88%	99.88%
MPP Tracking Time	$0.0192s$	$0.0191s$	$0.0192s$	$0.0192s$	$0.0192s$	$0.0192s$	$0.0192s$
Switching Frequency	$\approx 20kHz$	$10kHz$	$20kHz$	$\approx 20kHz$	$\approx 20kHz$	$\approx 15kHz$	$\approx 10kHz$
PEMFC Voltage Undershoot	3.96%	3.52%	3.89%	4.01%	3.96%	3.96%	3.96%
PEMFC Current Overshoot	2.44%	2.28%	2.41%	2.45%	2.44%	2.44%	2.44%
PEMFC Power Undershoot	1.59%	1.28%	1.53%	1.62%	1.59%	1.59%	1.59%
PEMFC Voltage Ripple	0.20%	0.78%	0.35%,	0.53%	0.20%	0.34%,	0.34%
PEMFC Current Ripple	0.20%	0.80%	0.35%	0.54%	0.20%	0.35%	0.35%
PEMFC Power Ripple	0.0016%	0.0210%	0.0041%	0.0157%	0.0020%	0.0060%	0.0070%

Among the duty cycle methods, the predictive duty cycle MPPT with $20kHz$ frequency had the lowest power ripple. However, the predictive switching state MPPT method surpassed the duty cycle method with extremely low power ripple. Although they had approximately the same switching frequency, the power ripple of the predictive duty cycle MPPT method was 2.56 times higher than that of the predictive switching state MPPT method. For the predictive switching state MPPT with a 0.1 weighting factor frequency reduction technique, its performance was almost the same as the pure predictive switching state MPPT method, but its power ripple is slightly higher than that of the pure predictive switching state MPPT method. When a higher weighting factor of the switching frequency reduction was set, the switching frequency was reduced, and the power ripple was increased. If the predictive control was more emphasized on the switching frequency reduction, the power quality may be sacrificed. From the results, the predictive switching state MPPT with a 0.3 weighting factor frequency reduction method had the most satisfying performance because it cut the switching frequency to around half while maintaining the high power quality. Its performance was outstanding when it was compared with the predictive duty cycle MPPT method. By comparison, its power ripple was 3 times lower than the predictive duty cycle MPPT with $10kHz$ frequency, although they had approximately the same switching frequency.

For predictive duty cycle MPPT with $30kHz$ frequency method, the actual switching frequency is only around $20kHz$. This phenomenon has been explained in section 4.3.2. However, this does not mean that the proposed predictive duty cycle MPPT method was not able to manage the switching frequency to $30kHz$. The switching frequency is dependent on the load resistance. Based on the formula of electrical power shown in Equation 4.4, a load

with higher resistance requires a higher voltage to consume the same amount of electrical power.

$$P = VI, \qquad P = \frac{V^2}{R}, \qquad P = I^2R \qquad \text{Equation 4.4}$$

Based on Equation 3.27, the switch inside the DC-DC boost converter must have a longer ON switching state than the OFF switching state. Due to the characteristics of the MPC, the predictive duty cycle MPPT controller will not directly compute the duty cycle, but it predicts and selects the optimum condition in each sampling step. If the load is changed to a load with lower resistance, the predictive duty cycle MPPT controller can manage the switching frequency as high as $30kHz$. After the testing by simulation, the predictive duty cycle MPPT with $30kHz$ frequency method controls the duty cycle of the switch in DC-DC boost converter with $30kHz$ of switching frequency when the load resistance is reduced to 3Ω.

The proposed predictive MPPT methods maintain a high and stable power quality while extracting the electrical power from the PEMFC. For all the proposed predictive MPPT methods, the power ripples of the PEMFC are lower than 0.022%. This can be considered as an extremely low power ripple. However, there was a simulation showing that the power ripple can be as low as 0.000006% while operating a $7kW$ PEMFC (Harrag & Messalti, 2018). Besides, the tracking time for MPP of the proposed MPPT approach was extremely short. The performance of the proposed MPPT technique is compared with the methods used in the previous study of literature (Fathy, Abdelkareem, et al., 2021). This study simulates a PEMFC with a maximum power output of $7563W$. To ensure a fair comparison, the PEMFC parameters reported in the reference study were replicated. Under

these same conditions, the PEMFC was then simulated using the proposed predictive MPPT technique. The comparison results are tabulated in Table 4.3.

Table 4.3: Comparison of Proposed MPPT Technique with Other Techniques

MPPT Technique	Accuracy	Tracking Time
Predictive MPPT Method (proposed)	99.58%	$0.090s$
Increment Conductance Method	47.35%	$0.100s$
Fuzzy MPPT Method	90.97%	$0.236s$
GWO-PID Method	56.95%	$0.020s$
ALO-PID Method	91.11%	$0.187s$
MBA-PID Method	91.12%	$0.205s$
SSA-PID Method	95.99%	$0.186s$

Table 4.3 presents that the results achieved surpass the earlier work in this area in terms of accuracy and MPP tracking time. The suggested predictive MPPT method attains the maximum power with the highest percentage of accuracy within the shortest time. If the MPP tracking time is quick, the PEMFC can reach the maximum output power instantaneously. If the PEMFC can generate power at MPP rapidly, there is less energy loss. Additionally, the suggested predictive MPPT approach's tracking accuracy is superior to the other MPPT techniques listed in Table 4.3, attaining $7531W$ of PEMFC output power which is 99.58% of the theoretical maximum power within $0.090s$. Although the proposed predictive MPPT techniques does not work as as well as a low power PEMFC, the results achieved surpass the earlier work in this area in both accuracy and tracking time.

On the load side, Figure 4.4, Figure 4.12, Figure 4.13, Figure 4.14, Figure 4.21, Figure 4.22, and Figure 4.23 show the load consumed $48.1W$ of electrical power. From the figures, the 12Ω load obeyed the Ohm's Law. When the load voltage was increased, the load current was also increased. This is due to Ohm's Law, which is defined as Equation 4.5.

$$V = IR \qquad \text{Equation 4.5}$$

where V is the voltage, I is the current, and R is the resistance. In these simulation results, the load voltage was exactly 12 times higher than the load current. In addition, the load also obeyed the formula of electrical power stated in Equation 4.4.

The power quality consumed by the load is also an emphasis to be discussed. The speed of load power stabilization and the power ripples for both MPPT techniques are compared in Table 4.4. From the comparison, the load consumed the same amount of electrical power, which is $48.1W$. Besides, all simulations had the same settling time of $0.14s$. This means that there was around $1.9W$ of electrical power loss to the DC-DC boost converter. However, the power consumption of the load achieved 96.2% which was considered a high power efficiency.

From the comparison in Table 4.4, it is apparent that the predictive switching state MPPT method provided the best power quality for the load. However, the other predictive MPPT methods have a slightly higher power ripple than the predictive switching state MPPT method. Considering the switching frequency, the predictive switching state MPPT with a 0.3 weighting factor frequency reduction method surpassed the other predictive MPPT methods with a lower switching frequency while maintaining the high power quality.

Table 4.4: Comparison of Load Power Quality under Constant PEMFC Parameters

Comparison	**Predictive Switching State MPPT**	**Predictive Duty Cycle MPPT**			**Predictive Switching State MPPT with Frequency Reduction**		
		$10kHz$	**$20kHz$**	**$30kHz$**	**0.1 Weighing Factor**	**0.2 Weighing Factor**	**0.3 Weighing Factor**
Load Power	$48.1W$	$48.1W$	$48.1W$	$48.1W$	$48.1W$	$48.1W$	$48.1W$
Settling Time	$0.14s$	$0.14s$	$0.14s$	$0.14s$	$0.14s$	$0.14s$	$0.14s$
Load Voltage Ripple	0.11%	0.45%	0.20%	0.30%	0.11%	0.20%	0.20%
Load Current Ripple	0.11%	0.44%	0.19%	0.30%	0.11%	0.19%	0.19%
Load Power Ripple	0.22%	0.89%	0.37%	0.61%	0.22%	0.39%	0.39%

4.4 Simulation with Variable PEMFC Parameters and Constant Load

The previous section presents the proposed method applied to PEMFC with constant parameters. In this section, the robustness of the proposed predictive MPPT methods is examined by changing the PEMFC parameters. This simulation was done to provide the best quality evidence for the effectiveness of the suggested MPPT approach across different parameters. The simulation was conducted under fast variations of PEMFC parameters. In this simulation, the initial input flow rates of hydrogen and oxygen were set to be $1 \times 10^{-5}\ kmol\ s^{-1}$ and $5 \times 10^{-6}\ kmol\ s^{-1}$, respectively. It was assumed that these values are the 100% input flow rate of the hydrogen and oxygen gases. Then, the input flow rates of both gases were reduced to half of the original flow rate at $0.25s$. After that, it was reduced to 10% of the original flow rate at $0.5s$. Lastly, it returned to the original flow rate at $0.75s$. Figure 4.29 shows schematically the variations of hydrogen and oxygen input flow rates in this simulation.

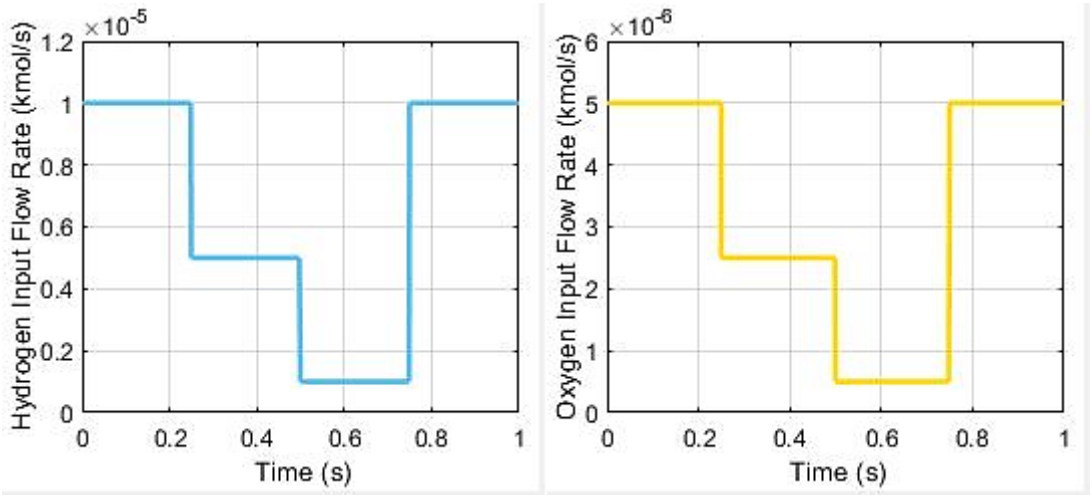


Figure 4.29: Variations of Hydrogen and Oxygen Input Flow Rates

Based on Equation 2.5 and Equation 2.6, the input flow rates will affect the partial pressure of the reactant gases. If the partial pressure is reduced, it will cause a decrease in output power. Figure 4.30 illustrates the V-I and P-I polarization curves with different amounts of hydrogen and oxygen input flow rates.

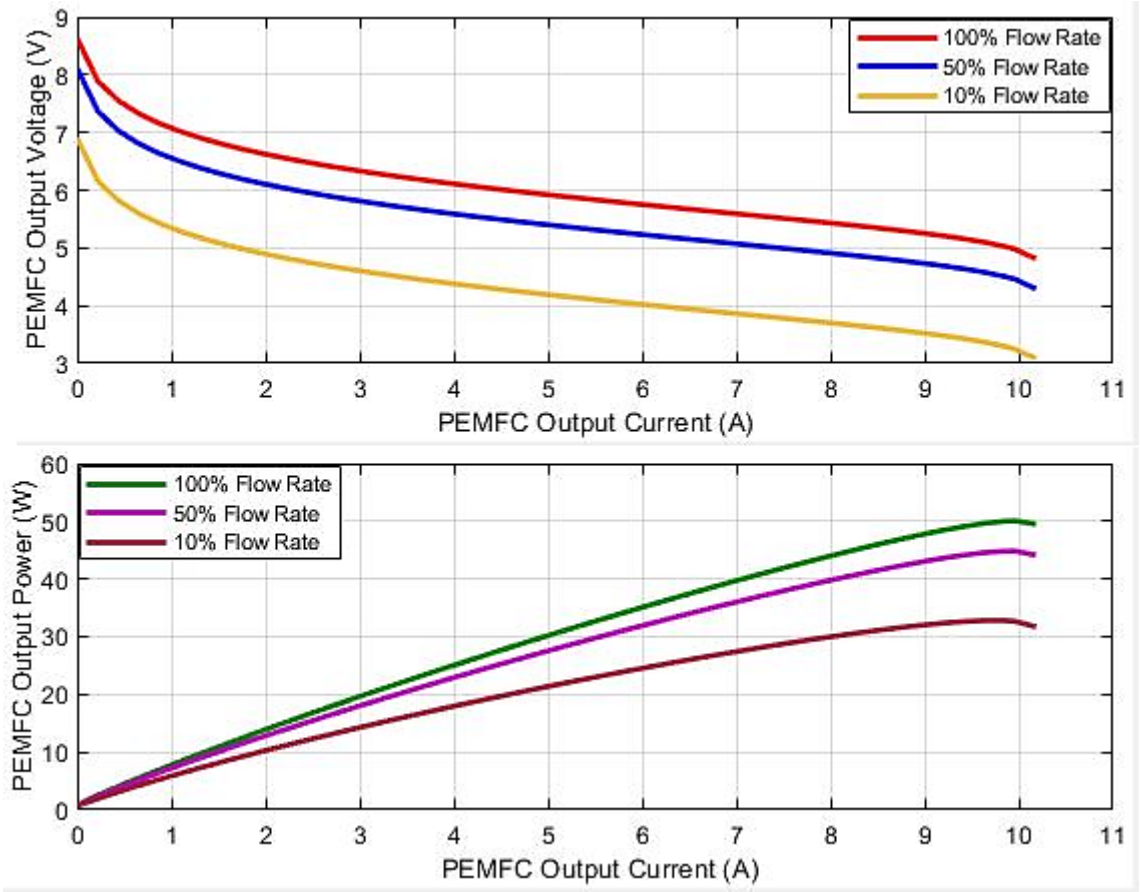


Figure 4.30: PEMFC P-I Polarization Curve under Different Input Flow Rates

When the flow rate is 100%, 50%, and 10%, the MPP of the PEMFC is $50.06W$, $44.83W$, and $32.79W$, respectively. Figure 4.30 represents a diagram to understand this process, where the drop in the input flow rate will decrease the maximum power of the PEMFC.

4.4.1 Simulation with Variable PEMFC Parameters by Predictive Switching State MPPT Technique

This section concerns the simulation results of the PEMFC under fast variations of hydrogen and oxygen input flow rates. Figure 4.31, Figure 4.32, and Figure 4.33 illustrate the simulation results of the predictive switching state MPPT technique.

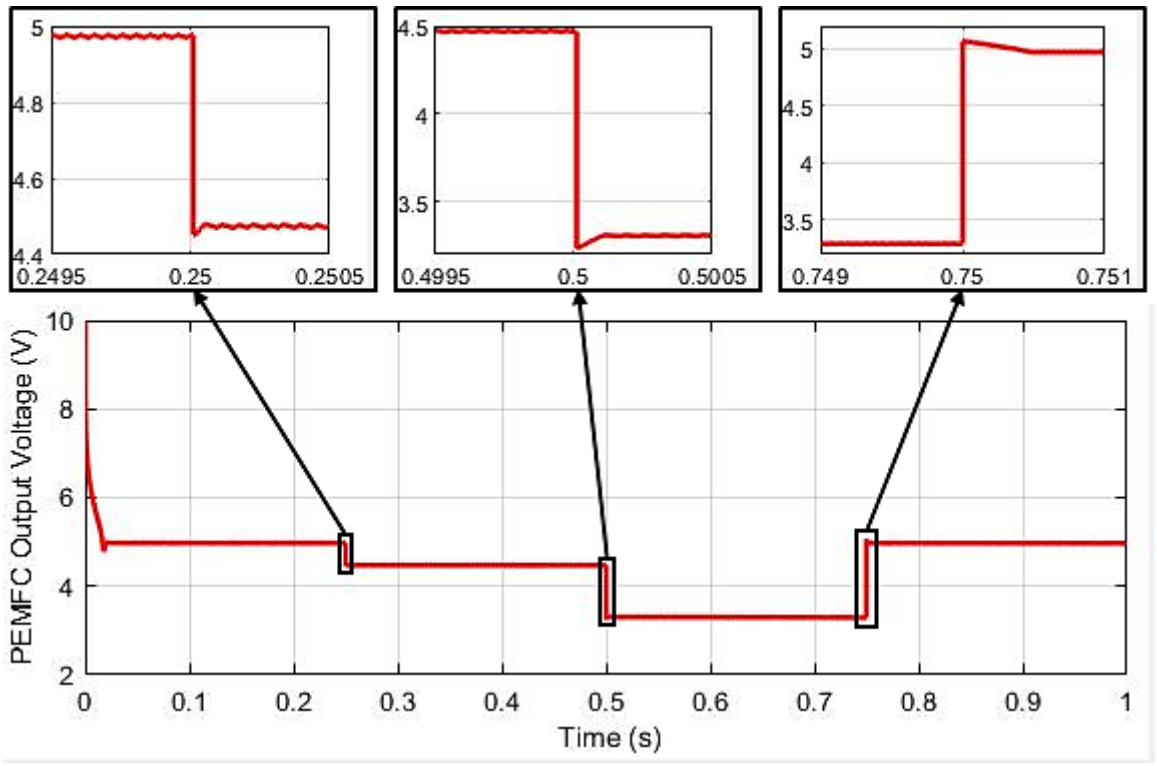


Figure 4.31: Simulation Results of PEMFC Output Voltage for Predictive Switching State MPPT under Variable PEMFC Parameters

The PEMFC output voltage achieved $4.976V$ at the beginning. When the input flow rates of the reactant gases were reduced to 50%, the PEMFC output voltage dropped to $4.475V$ with a 0.51% voltage undershoot within $0.05ms$. At $0.5s$, the input flow rates of hydrogen and oxygen were dropped to 10% of the original flow rate. At this period, the PEMFC output voltage dropped to $3.306V$ with 2.15% of voltage undershoot within $0.1ms$. The input flow rates returned to the original value at $0.75s$ where the PEMFC output

voltage returned to $4.971V$ with 1.93% of voltage overshoot within $0.5ms$. When 50% and 10% of the input flow rate were applied, the voltage ripple recorded was 0.18% and 0.17% respectively.

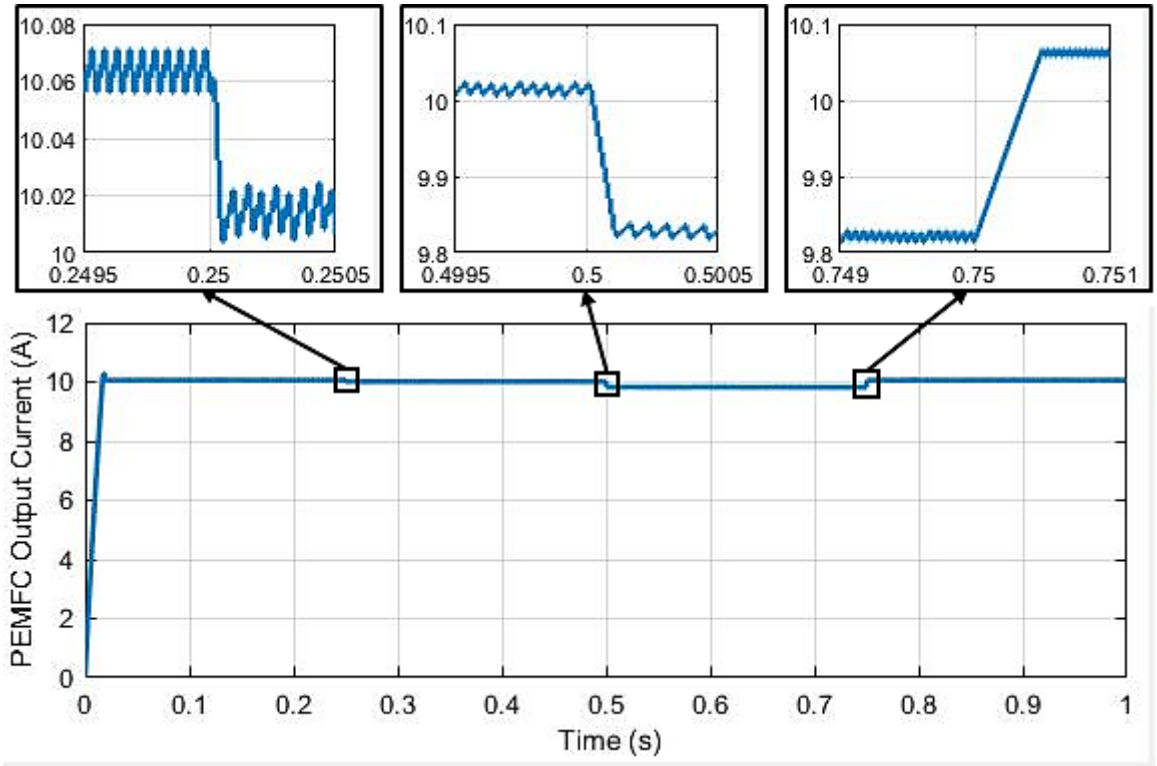


Figure 4.32: Simulation Results of PEMFC Output Current for Predictive Switching State MPPT under Variable PEMFC Parameters

For PEMFC output current, it dropped from $10.06A$ to $10.01A$ when the input flow rates of hydrogen and oxygen were reduced from 100% to 50%. The current ripple recorded at this period was 0.18%. Then, it dropped to $9.83A$ with a ripple of 0.16% after the input flow rate varied to 10%. At $0.75s$, the PEMFC output current returned to $10.06A$ after the input flow rates applied were 100%. The PEMFC output current did not experience any undershoot or overshoot. However, the change in PEMFC output current during the fast variation of PEMFC parameters was within $0.5ms$.

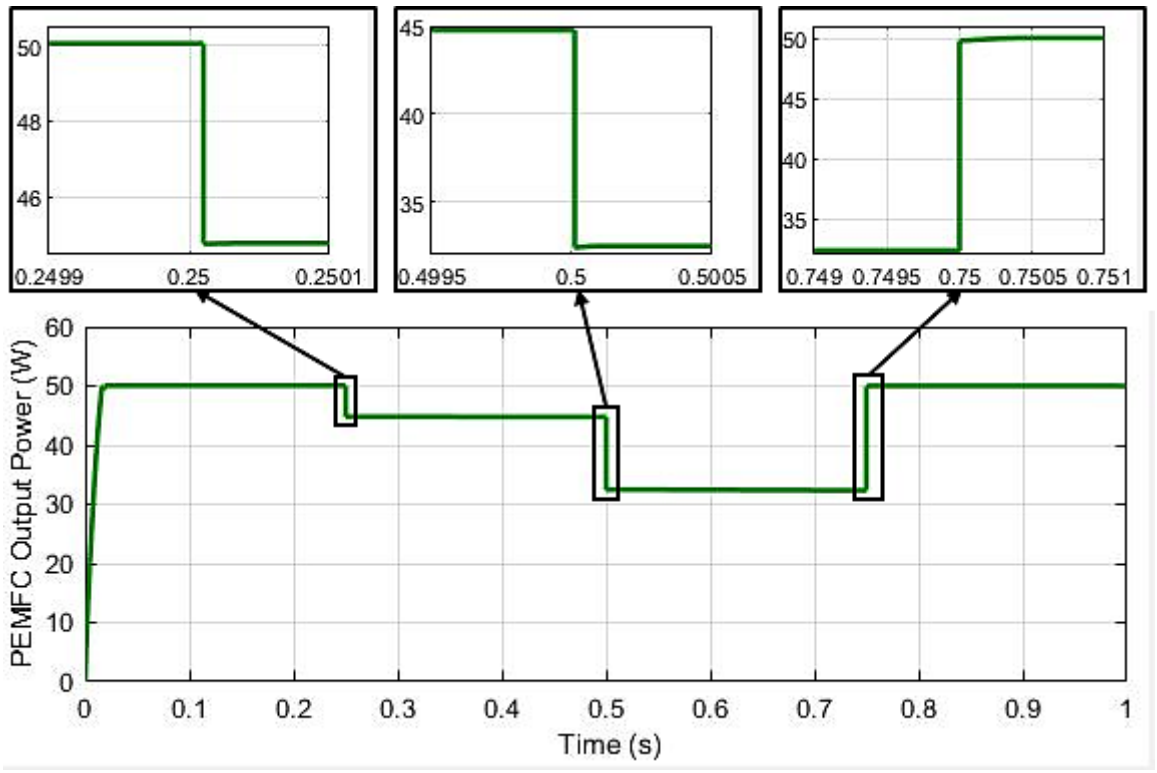


Figure 4.33: Simulation Results of PEMFC Output Power for Predictive Switching State MPPT under Variable PEMFC Parameters

The observation in Figure 4.33 with achieving $50W$ output power within $0.02s$ is similar to that investigated in previous simulation results. The PEMFC output power dropped to $44.8W$ with a 0.022% power undershoot within $0.05ms$ when the input flow rates of the reactant gases were reduced to 50%. At $0.5s$, the PEMFC output power dropped to $32.49W$ with 0.31% of power undershoot within $0.1ms$. Lastly, the PEMFC output power returned to $50W$ without any power undershoot when the input flow rate returned to the original value. The power ripple recorded was 0.0013% and 0.0006% when the hydrogen and oxygen input flow rates were 50% and 10% respectively.

Since the switching frequency of the predictive switching state MPPT method is not fixed, the switching frequency may not always be constant. It may be different when the

PEMFC parameters are changed. Figure 4.34 displays the switching state when different input flow rates were utilized.

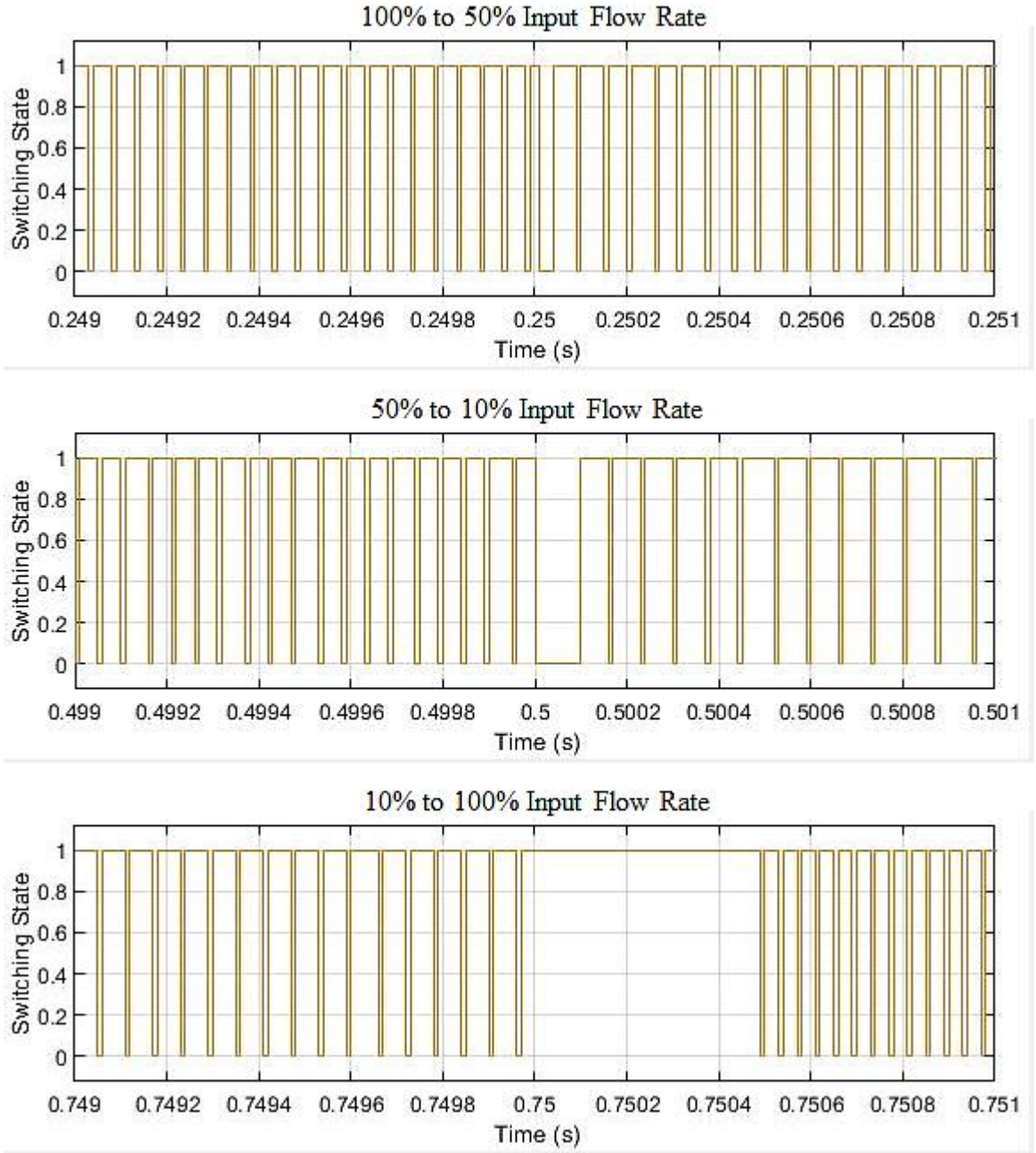


Figure 4.34: Simulation Results of Switching State for Predictive Switching State MPPT under Variable PEMFC Parameters

Figure 4.34 clearly shows that the different input flow rates affect the determination of the predictive MPPT controller. This is because different PEMFC parameters lead to different MPPs. The predictive MPPT algorithm makes the optimum switching state determination to achieve the MPP. From the simulation results, the switching frequencies for 100% flow rate, 50% flow rate, and 10% flow rate were $20kHz$, $19kHz$ and $16kHz$ respectively. When the input flow rates were changed from high to low, the switching was OFF for a longer period to regulate the PEMFC output current to the MPP current. At $0.75s$, the input flow rates changed from low to high, and the switching state was always ON to increase the PEMFC output current to MPP current.

At the load side, the load absorbed $48.15W$ of power from the PEMFC before $0.25s$. After that, the load power was reduced to $43W$ and then to $30.85W$. The power drop corresponded to the reduction of the input flow rate of the reactant gases. Figure 4.35, Figure 4.36, and Figure 4.37 depict the load voltage, current, and power under fast variations of hydrogen and oxygen input flow rates.

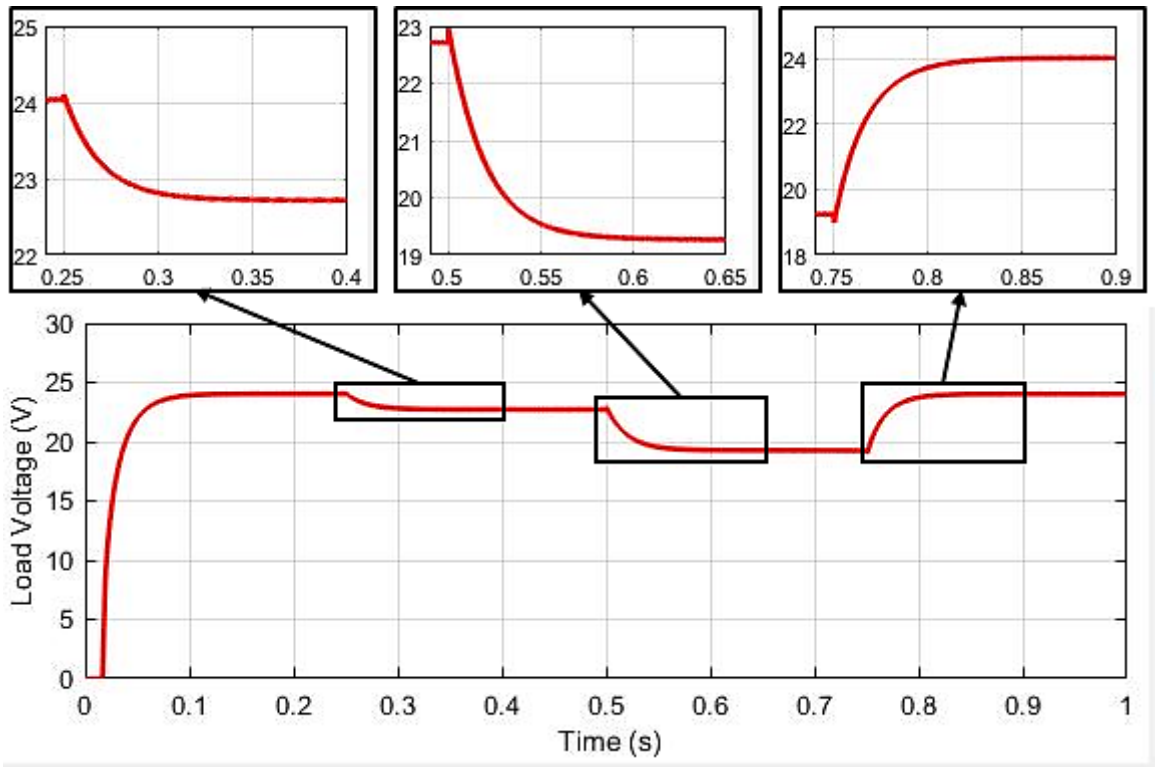


Figure 4.35: Simulation Results of Load Voltage for Predictive Switching State MPPT under Variable PEMFC Parameters

At the start of the operation, the same phenomenon as the previous simulation was observed. The load voltage only started to increase after $0.0165s$. This phenomenon is already discussed in section 4.3.4. Before $0.25s$, the load voltage raised to $24.03V$. Then, the load experienced a 0.32% voltage overshoot, and the voltage started to decrease until $22.71V$ with 0.12% of ripple. At $0.5s$, the load experienced another voltage overshoot with 1.1% and then started to decrease until $19.24V$ with 0.14% of ripple. Lastly, the load experienced a 1.3% voltage undershoot and then returned to $24.03V$.

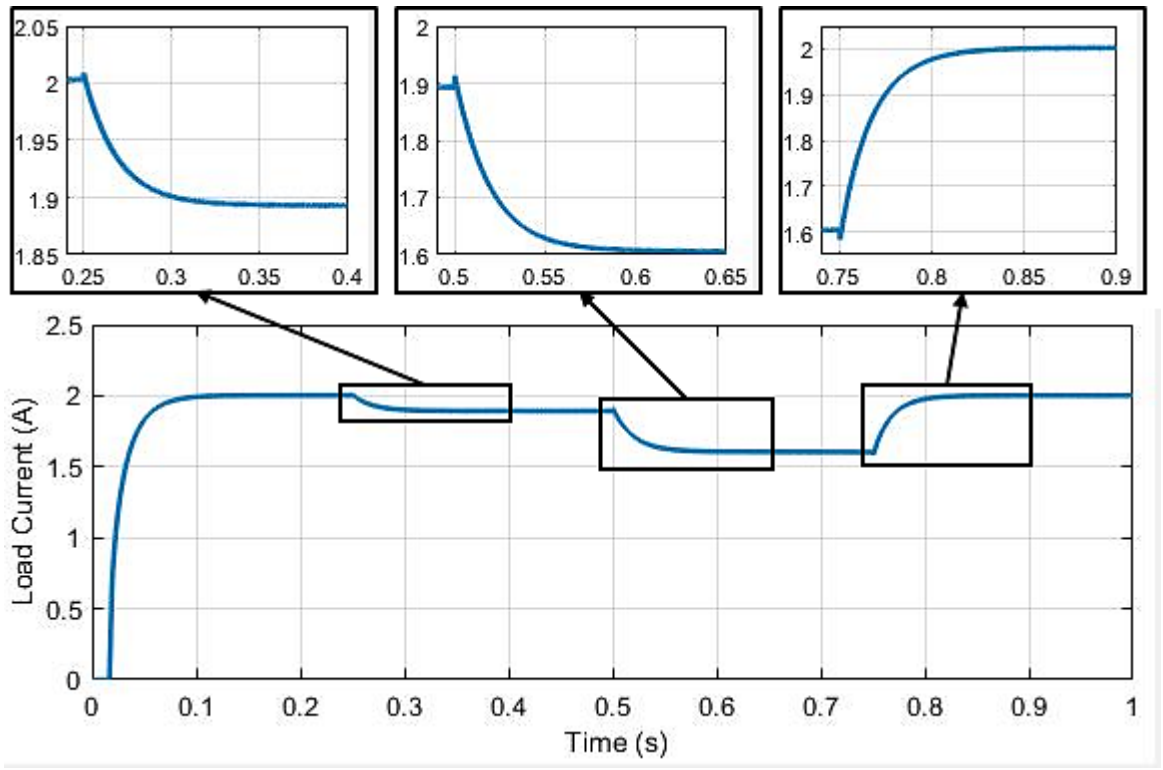


Figure 4.36: Simulation Results of Load Current for Predictive Switching State MPPT under Variable PEMFC Parameters

The load current had a similar pattern to the load voltage because the load obeys Ohm's Law. The load current decreased from $2.003A$ to $1.893A$, and it experienced a 0.32% current overshoot. Then, the load current experienced another 1.11% current overshoot and decreased to $1.604A$. When the input flow rates of hydrogen and oxygen were 50% and 10%, the current ripple was 0.11% and 0.14% respectively. Lastly, the load experienced a 1.34% current undershoot, and then the current returned to $2.002A$.

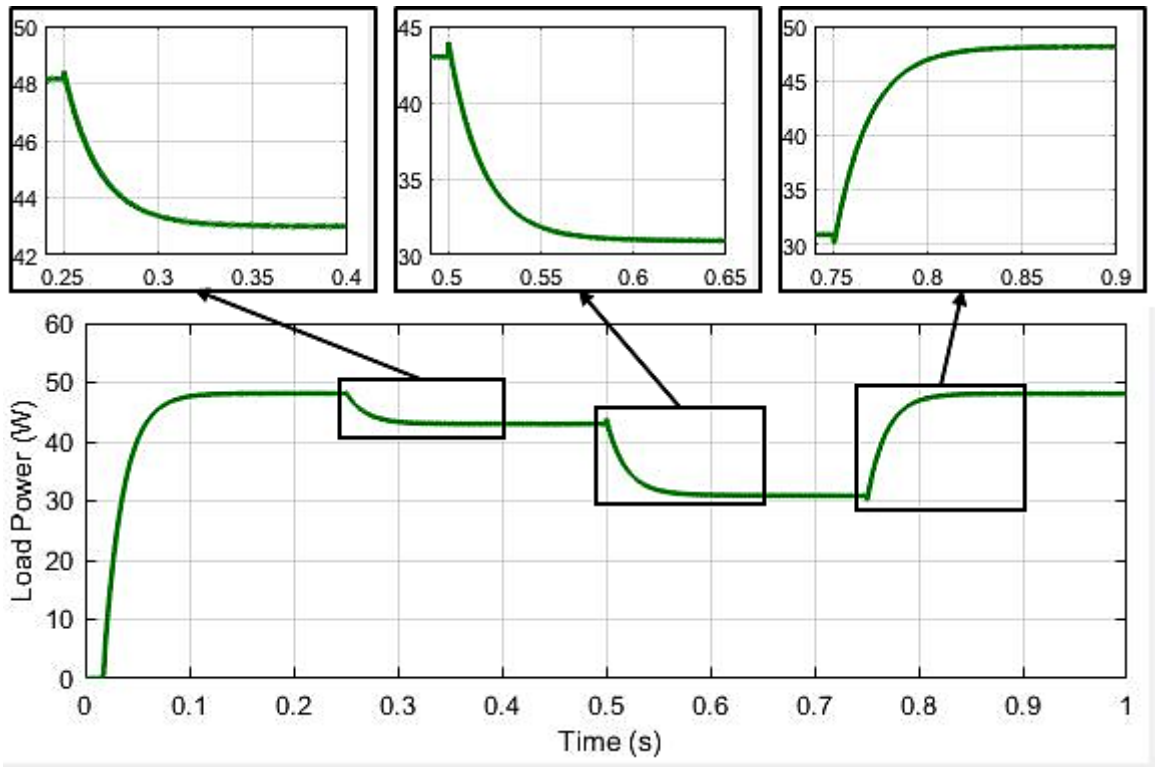


Figure 4.37: Simulation Results of Load Power for Predictive Switching State MPPT under Variable PEMFC Parameters

The load power corresponds to the PEMFC output power. When the PEMFC output power was decreased, the load power was also decreased. Figure 4.37 shows that the load power was decreased from $48.1W$ to $43.0W$ with 0.23% of ripple after a 0.62% power overshoot. At $0.5s$, the load experienced 2.21% of power overshoot and started to decrease until $30.9W$ with 0.27% of ripple. At $0.75s$, the load experienced a 2.62% power undershoot, and the load power returned to $48.1W$.

4.4.2 Simulation with Variable PEMFC Parameters by Predictive Duty Cycle MPPT Technique

The simulation results for the predictive duty cycle MPPT technique in section 4.3.2 show that the performance of $20kHz$ frequency performed the best in reducing the power ripple. In this section, the predictive duty cycle MPPT control with $20kHz$ frequency is

chosen for the simulation. The simulation results for PEMFC are shown in Figure 4.38, Figure 4.39, and Figure 4.40.

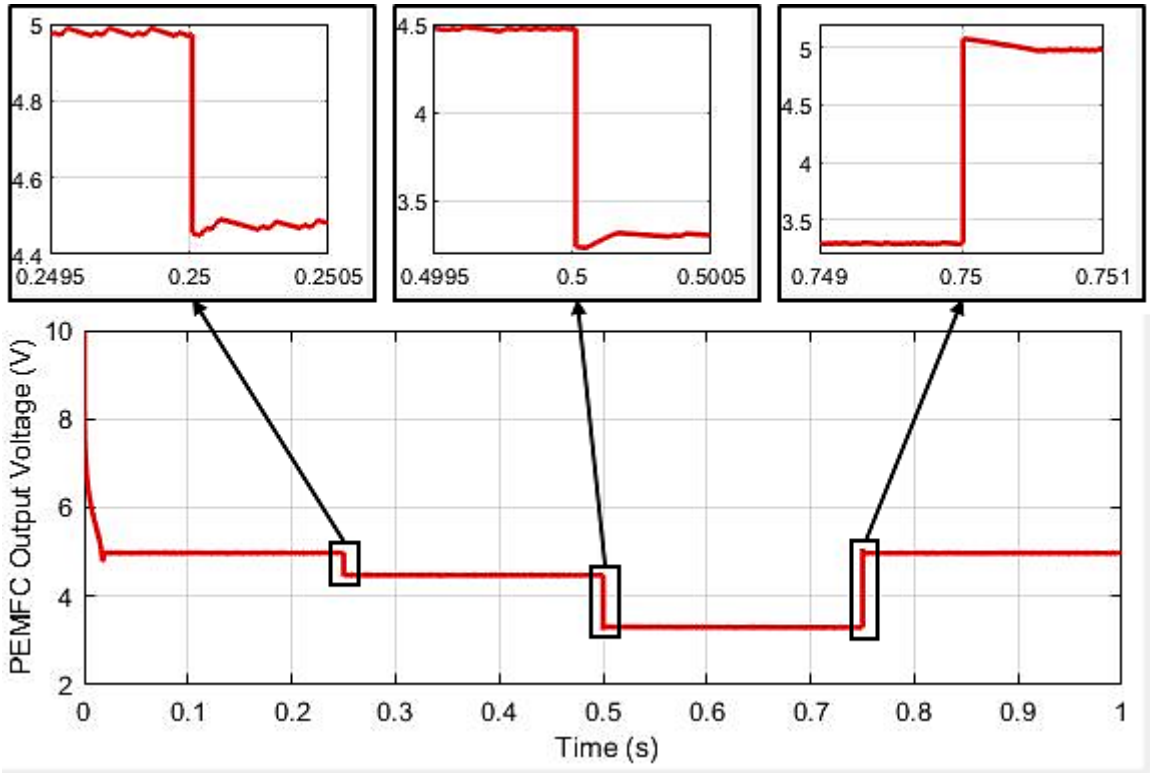


Figure 4.38: Simulation Results of PEMFC Output Voltage for Predictive Duty Cycle MPPT under Variable PEMFC Parameters

Figure 4.38 shows that the simulation result of PEMFC output voltage for the duty cycle method had the same pattern as the switching state method. At $0.25s$, the PEMFC output voltage dropped from $4.976V$ to $4.475V$ with a 0.56% of voltage undershoot within $0.1ms$. During this period, the voltage ripple was 0.56%. Then, it dropped to $3.306V$ at $0.5s$ and experienced a 2.06% voltage undershoot within $0.14ms$. The voltage ripple recorded was 0.49%. At $0.75s$, the PEMFC output voltage returned to $4.971V$ with 2.03% of voltage overshoot within $0.5ms$.

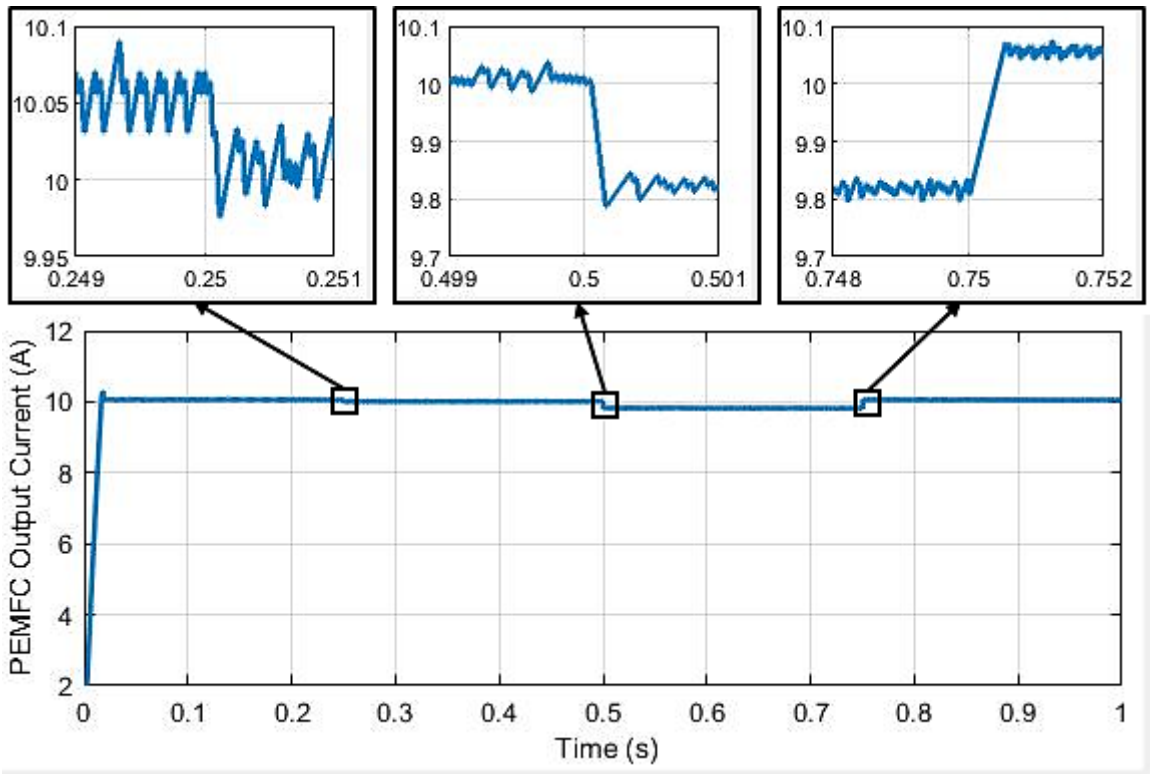


Figure 4.39: Simulation Results of PEMFC Output Current for Predictive Duty Cycle MPPT under Variable PEMFC Parameters

The PEMFC output current dropped from $10.06A$ to $10.01A$ at $0.25s$ with a current undershoot of 0.34% within $0.1ms$. The current ripple recorded at this period is 0.53%. At $0.5s$, it dropped to $9.83A$ with a 0.46% current undershoot within $0.14ms$. During this period, the current ripple recorded is 0.49%. Lastly, the PEMFC output current returned to $10.06A$ at $0.75s$ without current overshoot.

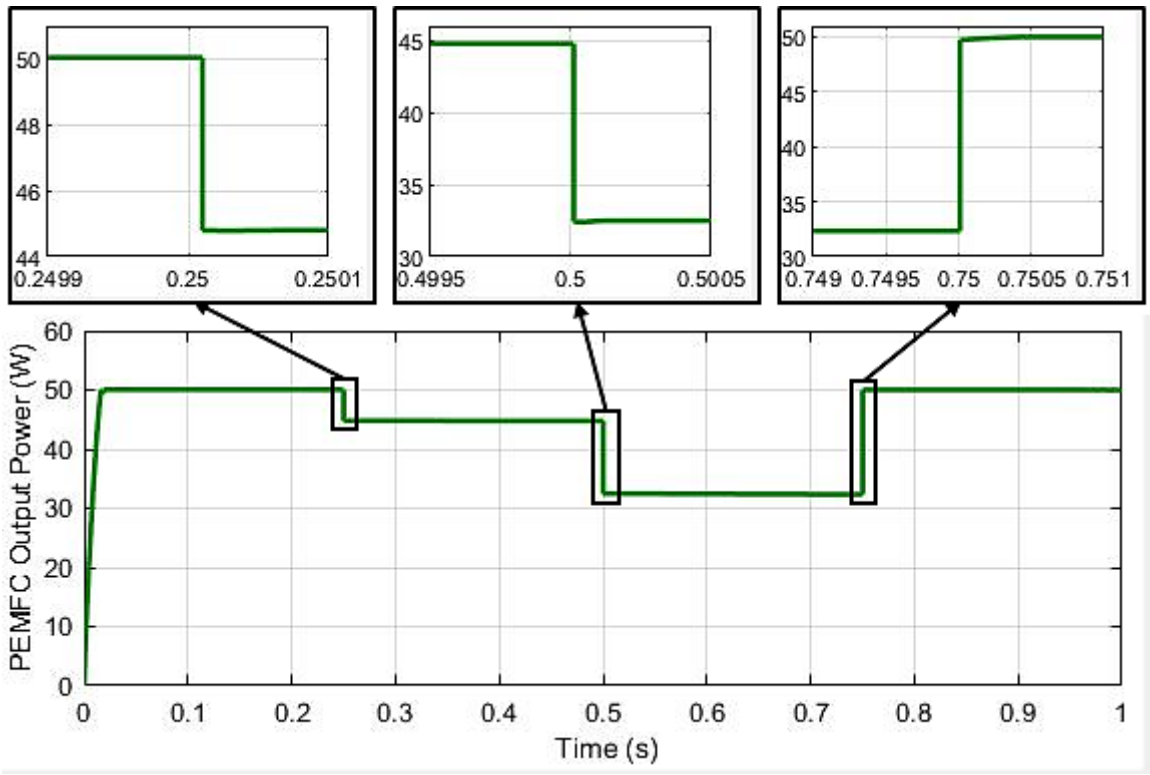


Figure 4.40: Simulation Results of PEMFC Output Power for Predictive Duty Cycle MPPT under Variable PEMFC Parameters

From Figure 4.40, the PEMFC output power dropped to $44.8W$ with a 0.029% of power undershoot within $0.1ms$ when the input flow rates of hydrogen and oxygen were reduced from 100% to 50%. During the fast variation of hydrogen and oxygen input flow rates from 50% to 10%, the PEMFC output power dropped to $32.49W$ with 0.29% of power undershoot within $0.14ms$. Lastly, the PEMFC output power returned to $50W$ without any power undershoot when the input flow rate returned to the original value. When the input flow rates of hydrogen and oxygen were 50% and 10%, the power ripple recorded were 0.0087% and 0.0043% respectively.

This predictive MPPT by duty cycle technique determined the duty cycle of the switch within 0.25 and 1. At $0.25s$ and $0.5s$, the hydrogen and oxygen input flow rates were

reduced from 100% to 50% and 50% to 10% respectively. From the figure, the duty cycle dropped to 0 instantaneously at $0.25s$ and $0.5s$. The purpose of selecting zero as the duty cycle was to reduce the PEMFC output current approaching the MPP current. Figure 4.41 shows the duty cycle determined by the predictive MPPT controller under variable PEMFC parameters.

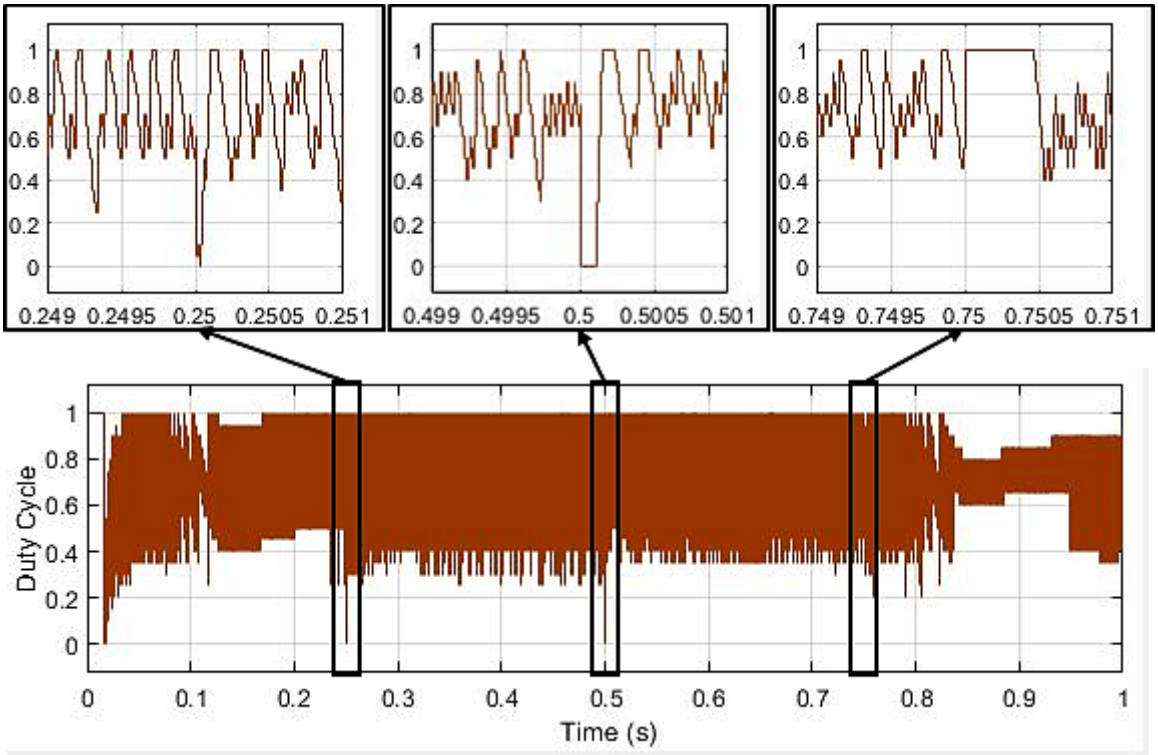


Figure 4.41: Simulation Results of Duty Cycle for Predictive Duty Cycle MPPT under Variable PEMFC Parameters

The switching state was controlled by the duty shown in Figure 4.41. At $0.25s$ and $0.5s$, the switching state became unstable due to the drop in hydrogen and oxygen input flow rate. At the same time, the predictive MPPT controller regulated the PEMFC output current to the MPP current within a short period. After that, the switching state became stable again. When the input flow rates were increased from 10% to 100%, the switch was always ON

for a few switching cycles. This was to increase the PEMFC output current to MPP current. Figure 4.42 depicts the switching state controlled by the predictive MPPT controller.

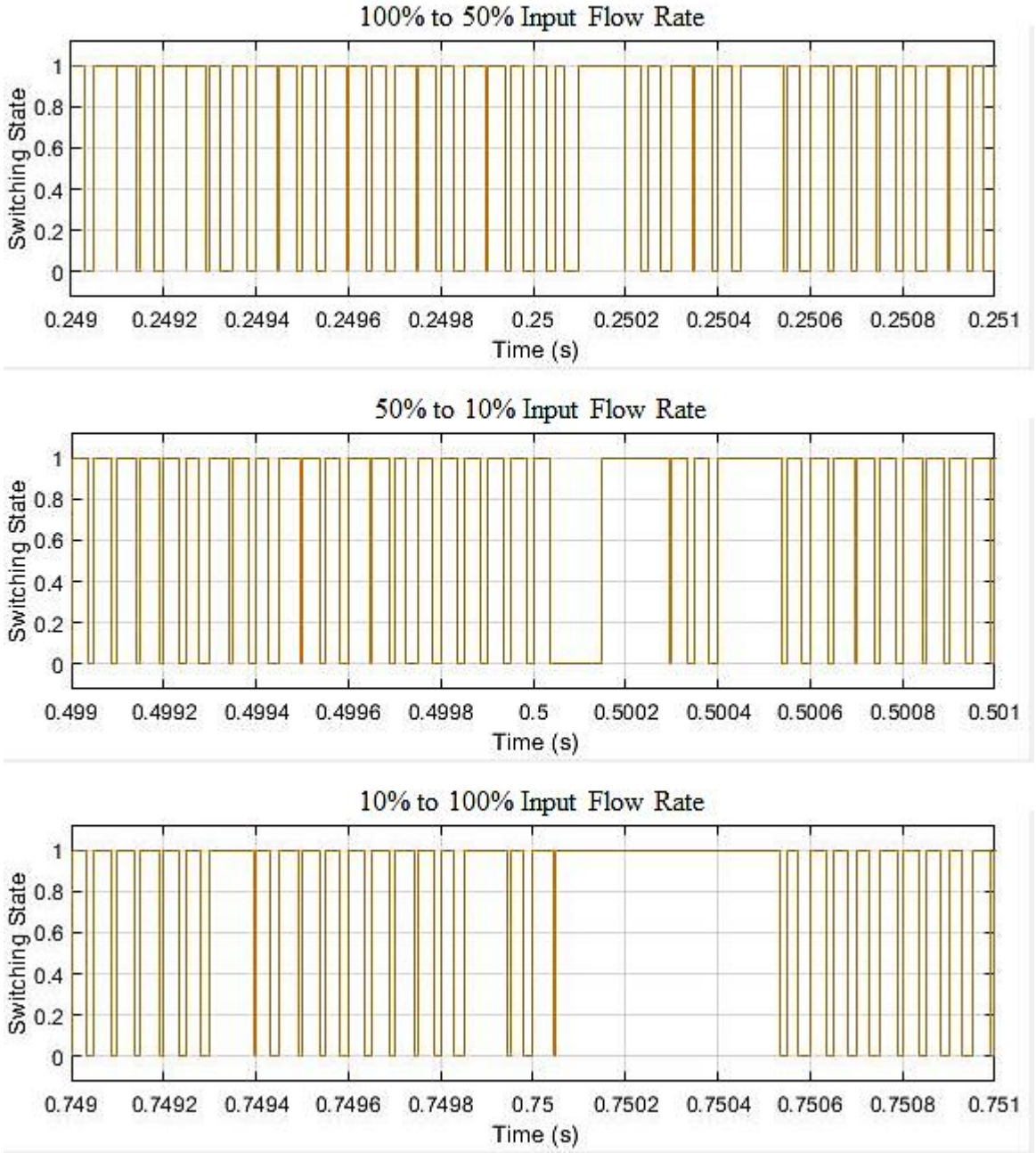


Figure 4.42: Simulation Results of Switching State for Predictive Duty Cycle MPPT under Variable PEMFC Parameters

For the load, the simulation results were also similar to the predictive MPPT by switching state technique. Figure 4.43, Figure 4.44, and Figure 4.45 illustrate the load voltage, current, and power under fast variations of hydrogen and oxygen input flow rates.

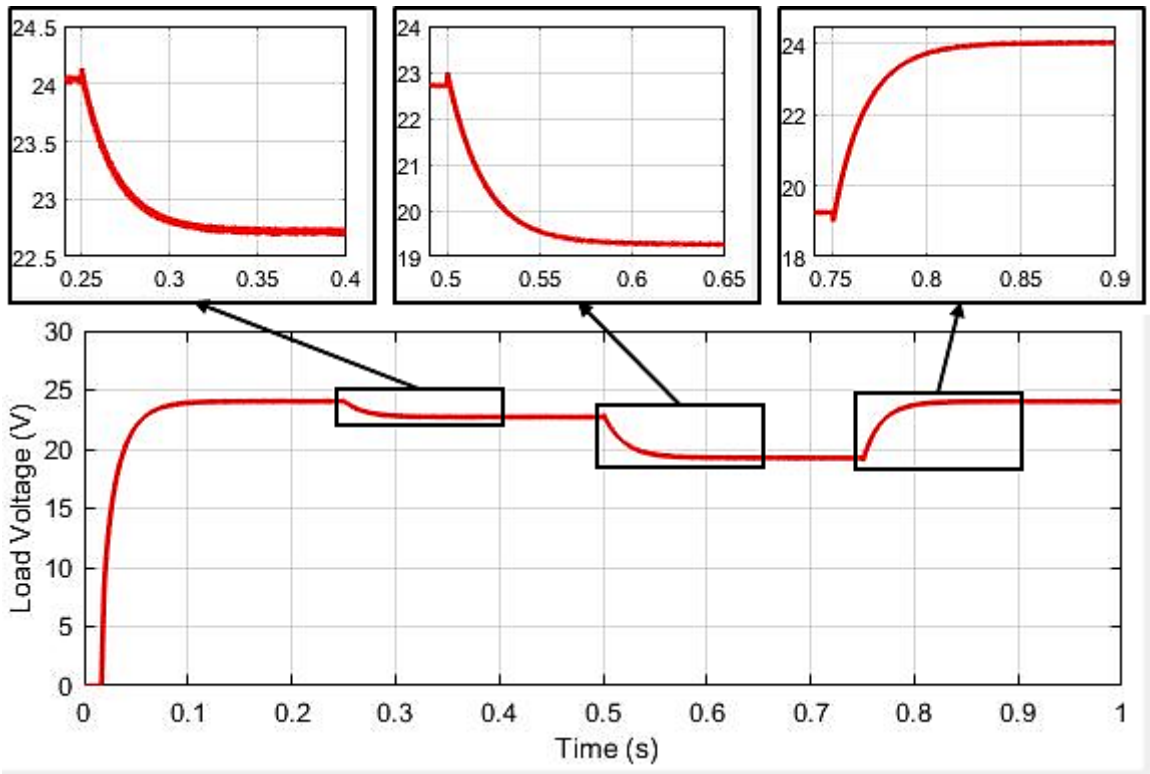


Figure 4.43: Simulation Results of Load Voltage for Predictive Duty Cycle MPPT under Variable PEMFC Parameters

At $0.25s$, the load experienced a 0.44% voltage overshoot, and the voltage started to decrease from $24.03V$ to $22.71V$. After that, the load experienced another voltage overshoot with 1.23% and then started to decrease until $19.24V$. Lastly, the load experienced a 1.3% voltage undershoot and then returned to $24.03V$. The voltage ripple recorded was between 0.34% and 0.38%.

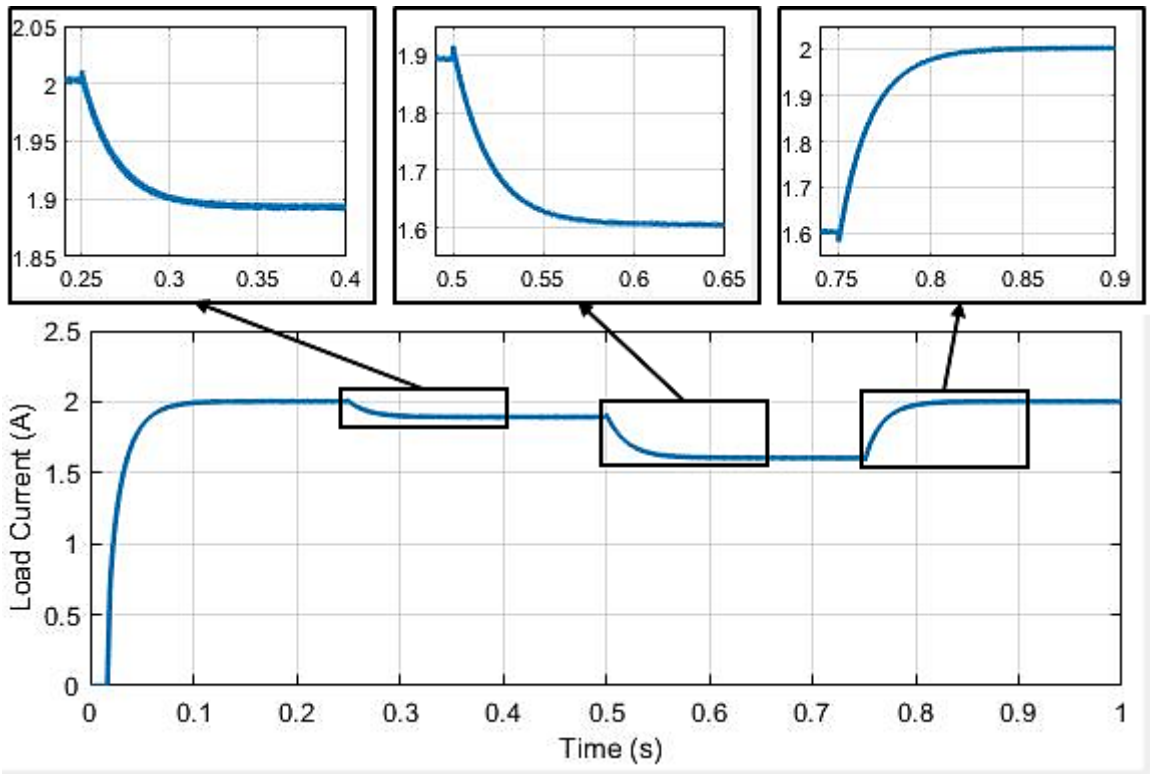


Figure 4.44: Simulation Results of Load Current for Predictive Duty Cycle MPPT under Variable PEMFC Parameters

The load experienced a 0.41% of current overshoot, and the current started to decrease from $2.003A$ to $1.893A$ at $0.25s$. At $0.5s$, the load current experienced another 1.22% of current overshoot and decreased to $1.604A$. The current ripple recorded before $0.5s$ and $0.75s$ was 0.33% and 0.36% respectively. Lastly, the load experienced a 1.37% current undershoot, and then the current returned to $2.002A$.

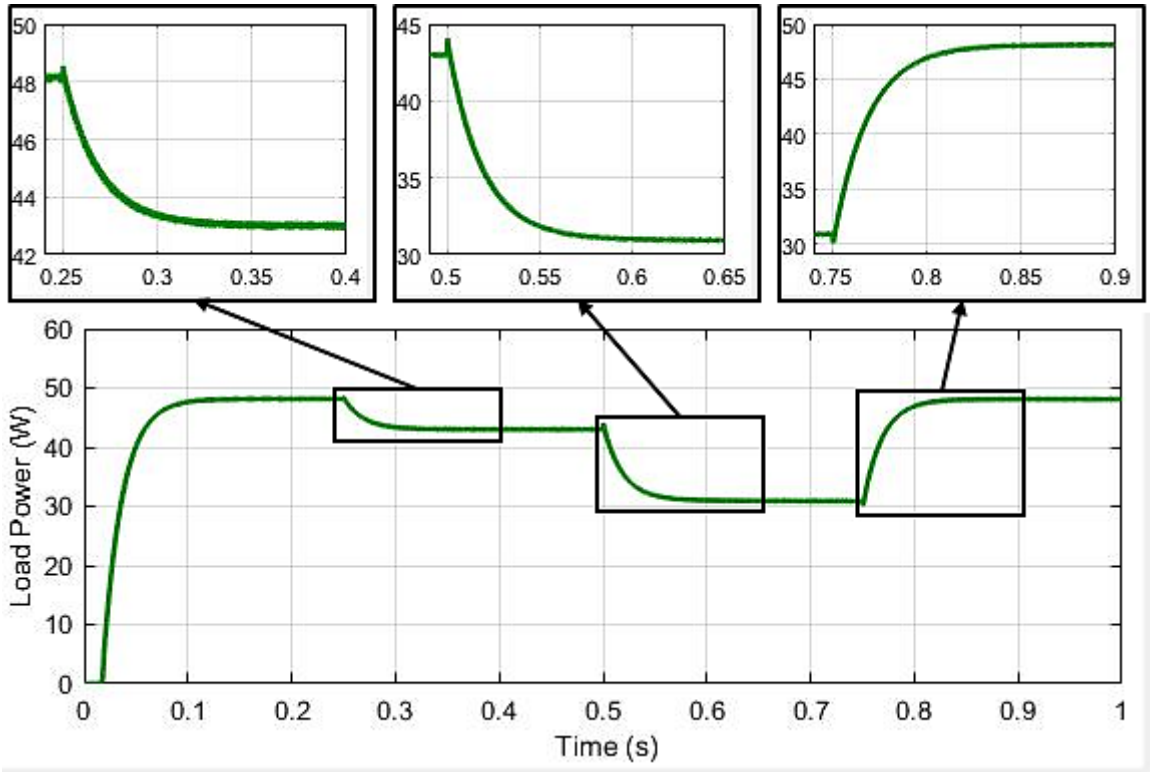


Figure 4.45: Simulation Results of Load Power for Predictive Duty Cycle MPPT under Variable PEMFC Parameters

In Figure 4.45, the load power was decreased from $48.1W$ to $43.0W$ with 0.66% of ripple after 0.85% of power overshoot at $0.25s$. Then, the load experienced 2.49% power overshoot and started to decrease until $30.9W$ with 0.76% of ripple at $0.5s$. At $0.75s$, the load experienced a 2.66% power undershoot, and the load power returned to $48.1W$.

4.4.3 Simulation with Variable PEMFC Parameters by Predictive Switching State MPPT with Frequency Reduction Technique

The simulation results in section 4.3.3 show that the predictive switching state MPPT with a 0.3 weighting factor of frequency reduction had the best performance among the predictive MPPT with switching frequency reduction techniques. Therefore, the 0.3 weighting factor of switching frequency reduction was chosen for the simulation in this

section. The simulation was done, and the output for PEMFC is shown in Figure 4.46, Figure 4.47, and Figure 4.48.

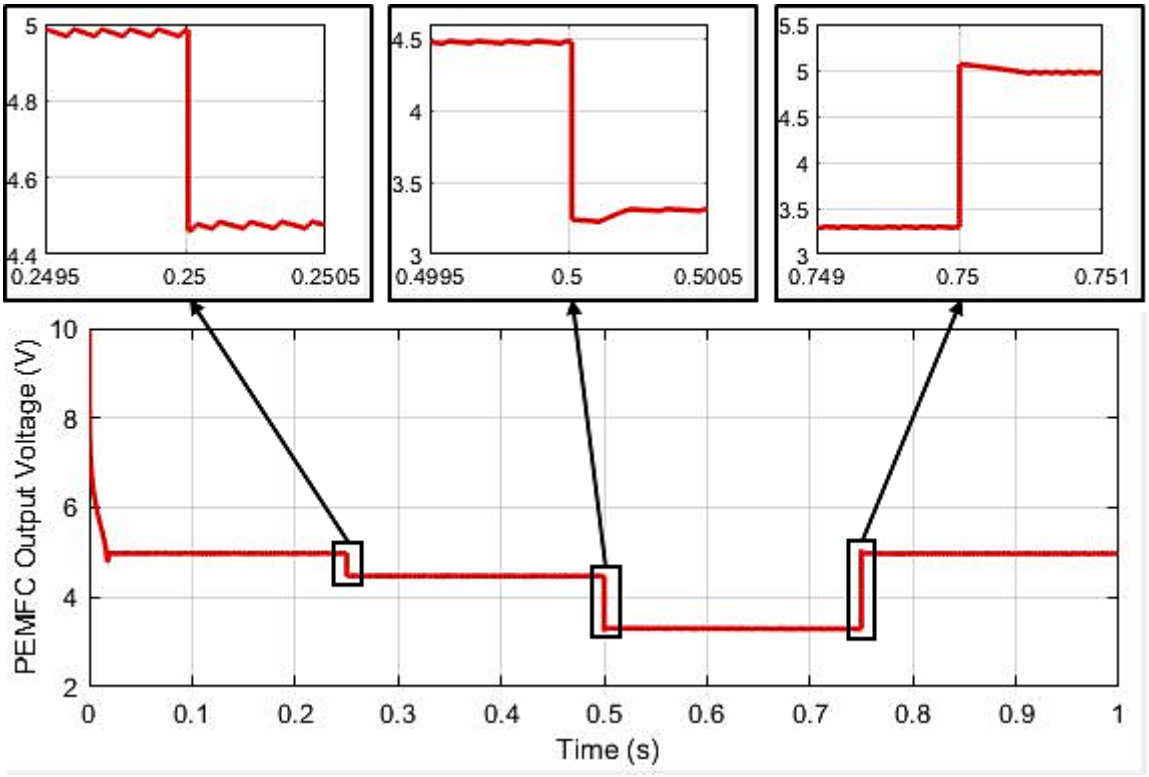


Figure 4.46: Simulation Results of PEMFC Output Voltage for Predictive Switching State MPPT with Frequency Reduction under Variable PEMFC Parameters

Figure 4.46 shows that the predictive switching state MPPT with frequency reduction method also regulated the PEMFC output voltage to the maximum power voltage. When the hydrogen and oxygen input flow rate dropped from 100% to 50%, the PEMFC output voltage dropped from $4.976V$ to $4.475V$ with a 0.34% of voltage undershoot within $0.05ms$. At $0.5s$, it dropped to $3.306V$ and experienced a 2.36% voltage undershoot within $0.2ms$. At $0.75s$, the PEMFC output voltage returned to $4.971V$ with 1.87% of voltage overshoot within $0.5ms$. There were voltage ripple recorded between 0.33% to 0.37%.

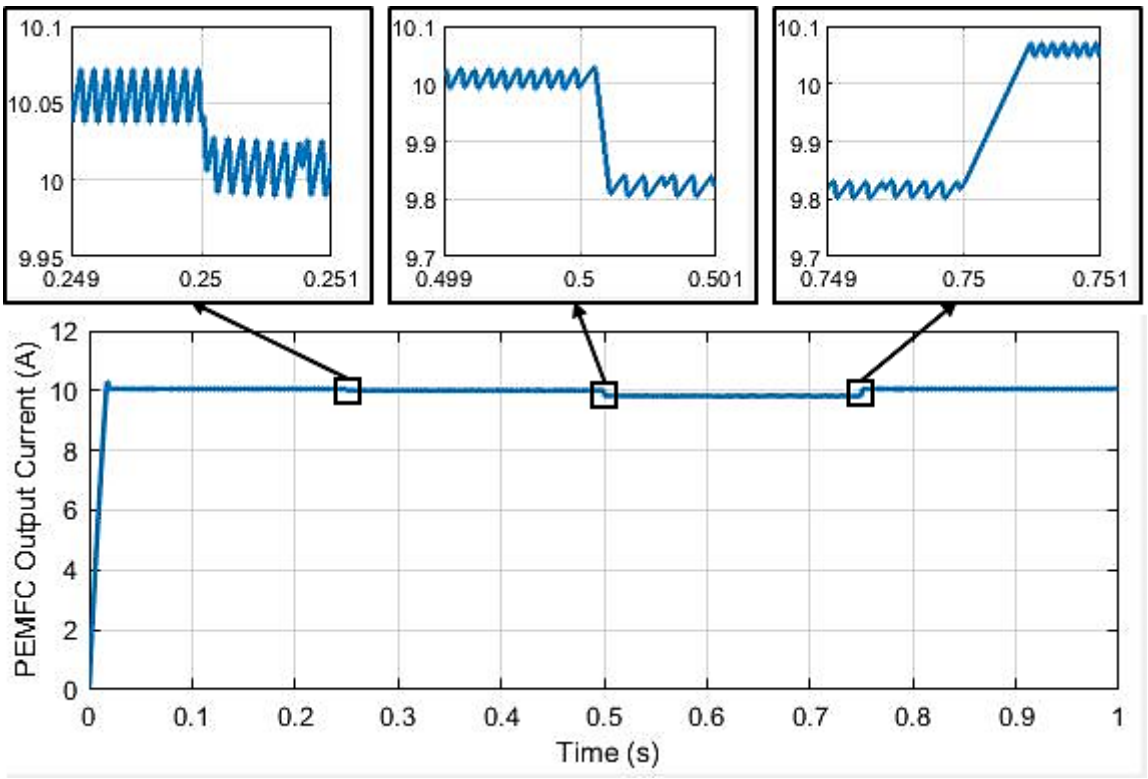


Figure 4.47: Simulation Results of PEMFC Output Current for Predictive Switching State MPPT with Frequency Reduction under Variable PEMFC Parameters

At $0.25s$ and $0.5s$, the PEMFC output current dropped from $10.06A$ to $10.01A$ and then to $9.83A$ without any current undershoot. At $0.75s$, the PEMFC output current returned to $10.06A$ at $0.75s$ without current overshoot. For this simulation, the current ripple recorded was between 0.34% to 0.38%.

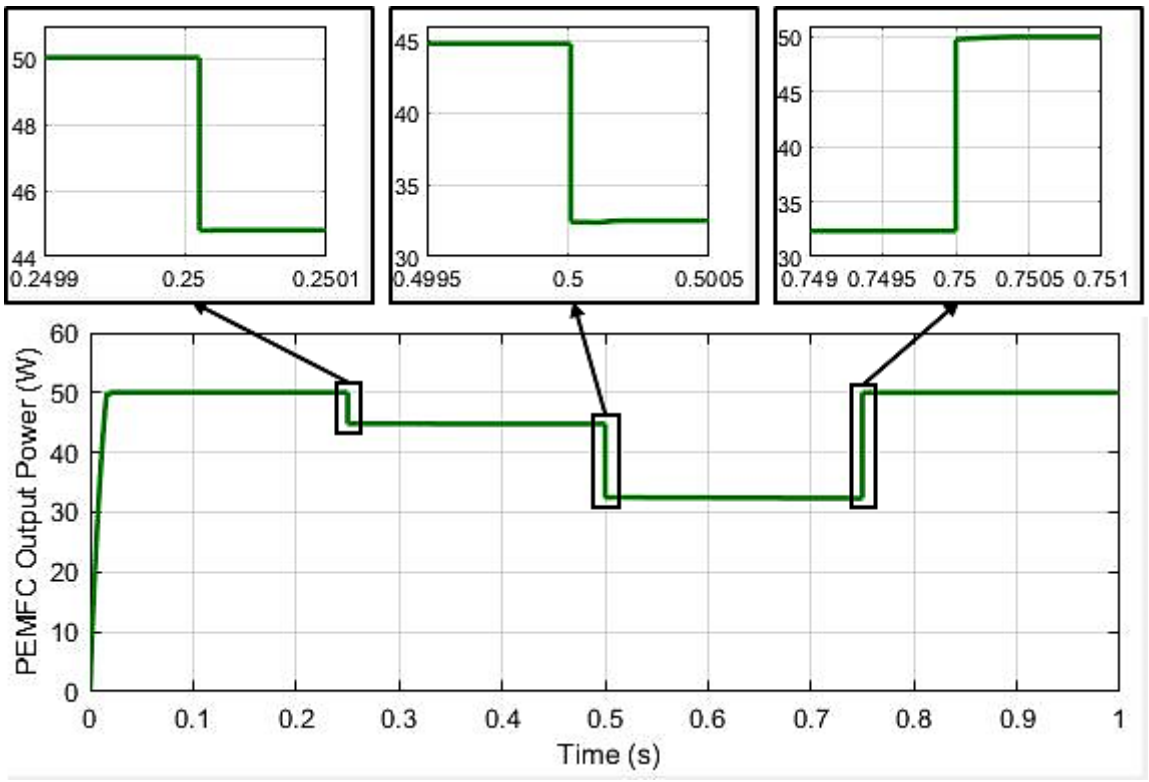


Figure 4.48: Simulation Results of PEMFC Output Power for Predictive Switching State MPPT with Frequency Reduction under Variable PEMFC Parameters

At $0.25s$, the PEMFC output power dropped from $50W$ to $44.8W$ with a 0.007% power undershoot within $0.05ms$. At $0.5s$, it dropped to $32.49W$ with 0.38% of power undershoot within $0.2ms$. Lastly, the PEMFC output power returned to $50W$ without any power undershoot at $0.75s$. When the input flow rates of hydrogen and oxygen were 100%, 50%, and 10%, the power ripple recorded was 0.006%, 0.0056%, and 0.0028% respectively.

Since the predictive switching state MPPT with frequency reduction method can reduce the switching frequency, its switching frequency should be lower than that of the pure predictive switching state MPPT. Figure 4.49 shows the switching state of the DC-DC boost

converter when the predictive switching state MPPT with frequency reduction method was applied.

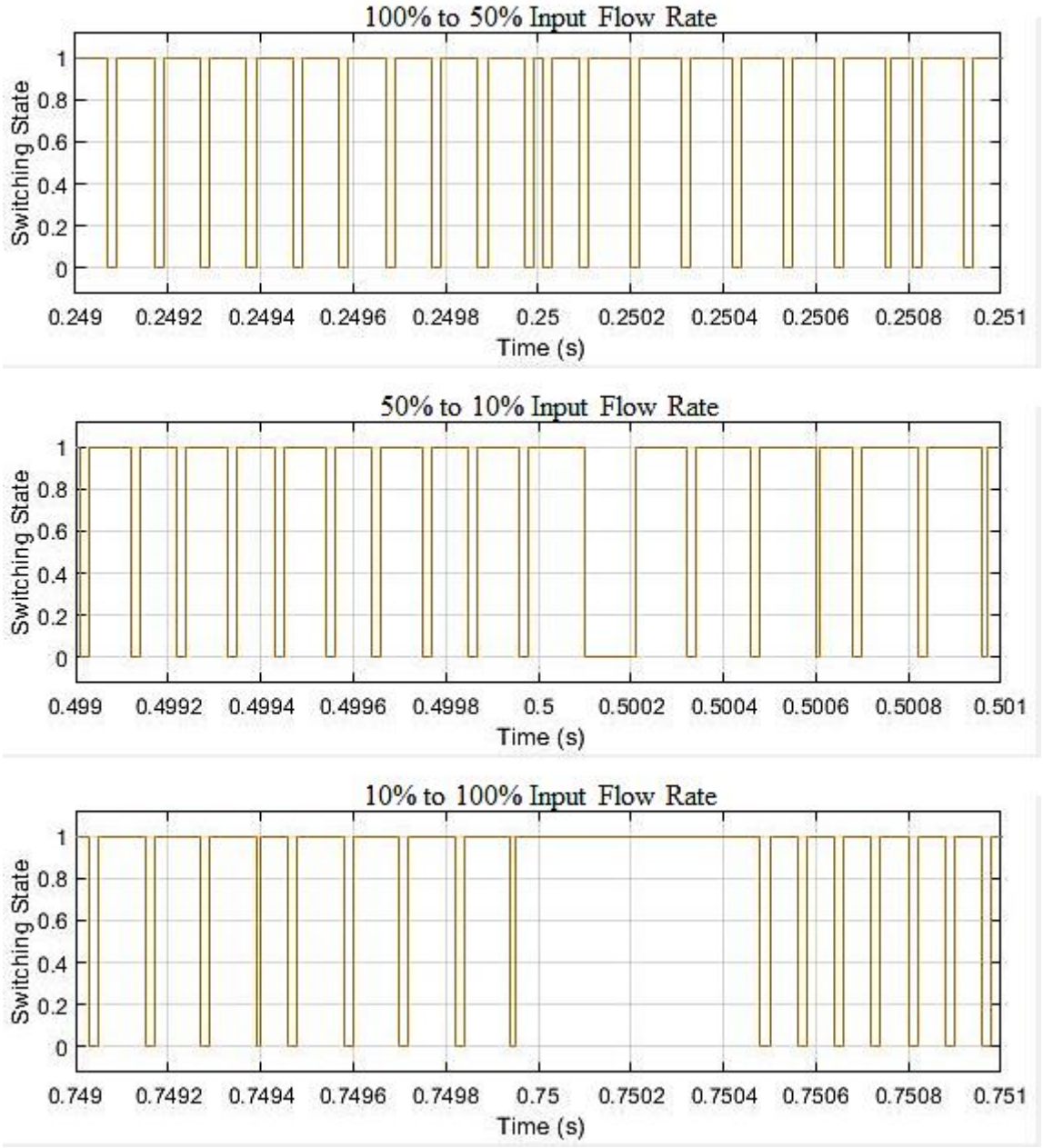


Figure 4.49: Simulation Results of Switching State for Predictive Switching State MPPT with Frequency Reduction under Variable PEMFC Parameters

Figure 4.49 shows that the predictive switching state MPPT with the frequency reduction method had a lower switching frequency than the pure predictive switching state MPPT. From the simulation results, approximately $10kHz$ switching frequency was recorded when the input flow rate of hydrogen and oxygen was 100% and 50%. After the input flow rate of hydrogen and oxygen dropped to 10%, the switching frequency was decreased to $9kHz$.

For the load, the simulation results were almost the same as the results obtained in sections 4.4.1 and 4.4.2. The simulation results of load voltage, current, and power under fast variations of hydrogen and oxygen input flow rates were illustrated in Figure 4.50, Figure 4.51, and Figure 4.52, respectively.

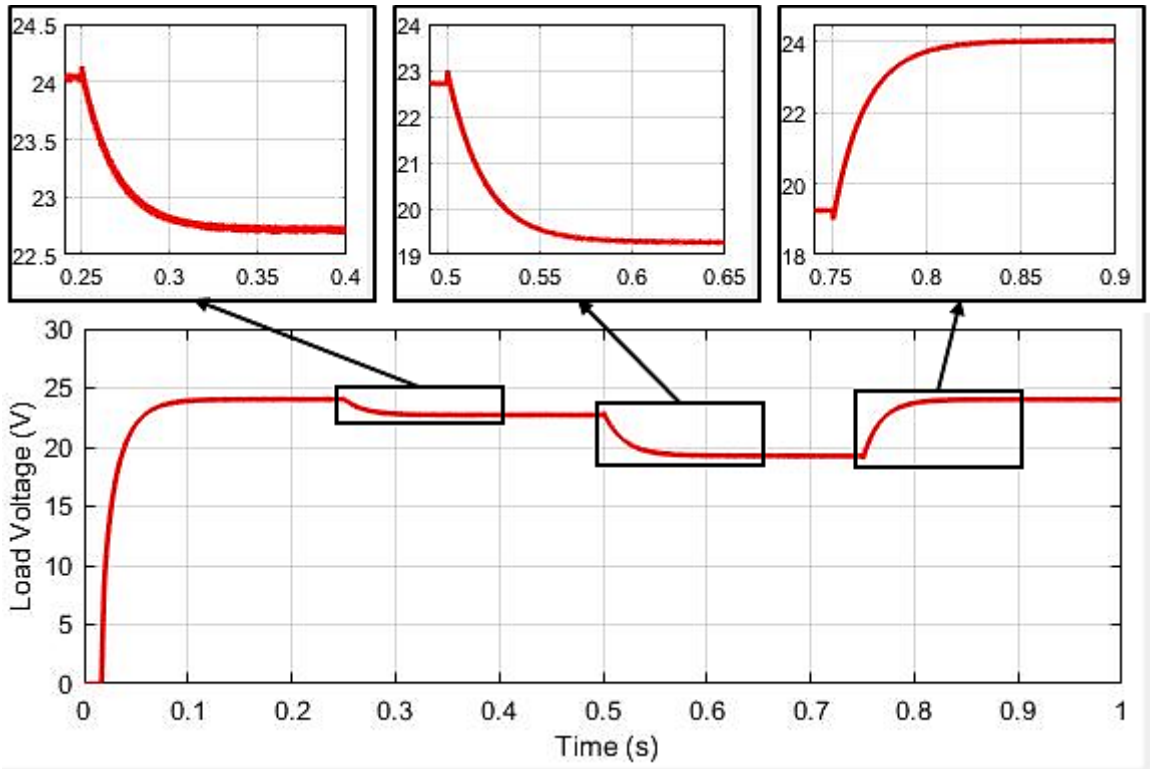


Figure 4.50: Simulation Results of Load Voltage for Predictive Switching State MPPT with Frequency Reduction under Variable PEMFC Parameters

The load voltage achieved the maximum power voltage at $24.03V$ before $0.25s$. When the input flow rate of hydrogen and oxygen was decreased from 100% to 50%, there was 0.32% voltage overshoot, and then the load voltage was decreased to $22.71V$ with 0.23% ripple. At $0.5s$, there was another voltage overshoot with 1.06% and then the load voltage decreased to $19.24V$. During this period, the voltage ripple recorded was 0.28%. Lastly, the load experienced a 1.4% voltage undershoot and then returned to $24.03V$.

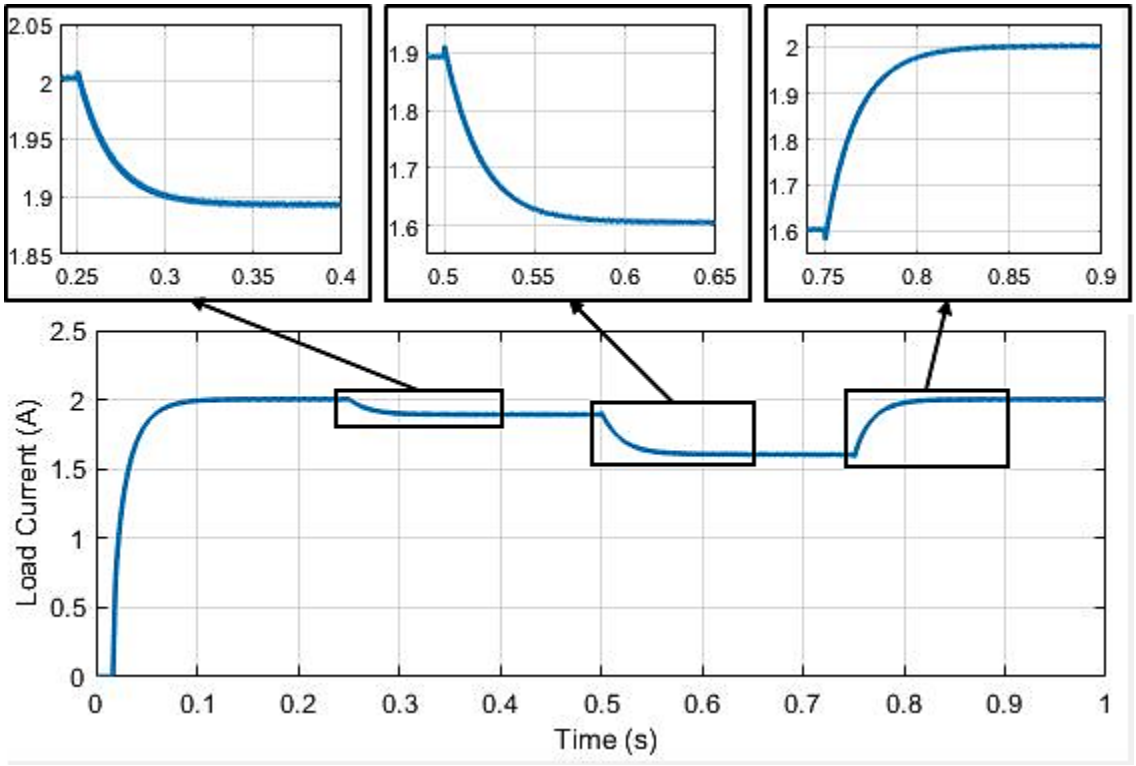


Figure 4.51: Simulation Results of Load Current for Predictive Switching State MPPT with Frequency Reduction under Variable PEMFC Parameters

At $0.25s$, the load experienced a 0.32% current overshoot, and the load current started to decrease from $2.003A$ to $1.893A$. Then, the load current experienced another 1.03% current overshoot and decreased to $1.604A$ at $0.5s$. At $0.75s$, the load experienced a

1.43% current undershoot, and then the current returned to $2.002A$. The load current ripple had almost the same percentage as the load voltage ripple.

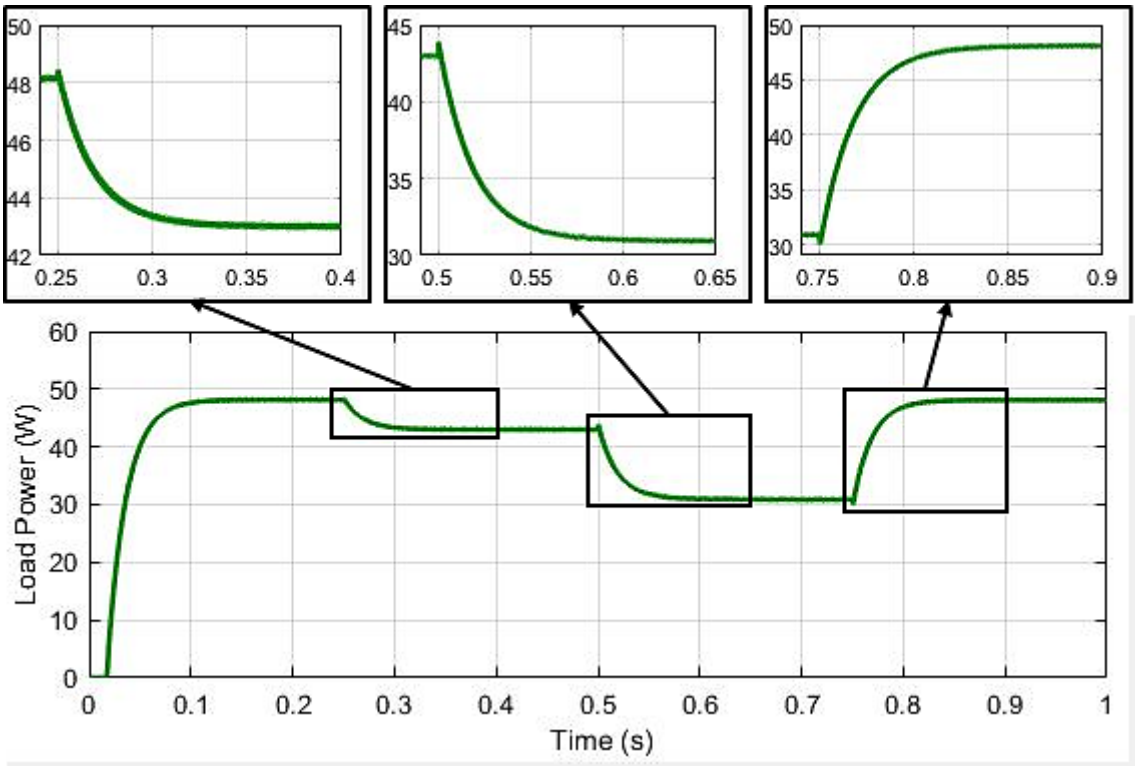


Figure 4.52: Simulation Results of Load Power for Predictive Switching State MPPT with Frequency Reduction under Variable PEMFC Parameters

At $0.25s$ and $0.5s$, the load power was decreased from $48.1W$ to $43.0W$ and then to $30.9W$ with the power overshoot of 0.62% and 2.09% respectively. Then, the load experienced 2.79% power undershoot and returned to $48.1W$. The power ripple recorded was between 0.39% and 0.55%.

4.4.4 Summary of Simulation Results with Variable PEMFC Parameters

The simulation results for PEMFC indicate that a change in the PEMFC parameters will change its output voltage, current, and power. As discussed in section 4.4, the MPP was moved to another point when the PEMFC parameters were changed. This also caused the

change of MPP voltage and MPP current. The PEMFC output power in the simulation was $50W$, $44.81W$ and $32.49W$ when the input flow rates of hydrogen and oxygen were 100%, 50%, and 10% respectively. When these values are compared with the theoretical values in section 4.4, it is found that the accuracy of the predictive MPPT technique is between 98.66% and 99.88%.

This section compares the performance of predictive MPPT by switching state and duty cycle methods under fast variation of PEMFC parameters. From the simulation results of PEMFC, the data can be analyzed and shown in Table 4.5.

Table 4.5: Comparison of Proposed Predictive MPPT Techniques under Variable PEMFC Parameters

Comparison	Hydrogen and Oxygen Input Flow Rate	Predictive Switching State MPPT	Predictive Duty Cycle MPPT	Predictive Switching State MPPT with Frequency Reduction
Accuracy	100%	99.88%	99.88%	99.88%
	50%	99.87%	99.87%	99.87%
	10%	98.66%	98.66%	98.66%
MPP Tracking Time	100% to 50%	$0.05ms$	$0.10ms$	$0.05ms$
	50% to 10%	$0.10ms$	$0.14ms$	$0.20ms$
	10% to 100%	$0.50ms$	$0.50ms$	$0.50ms$
Switching Frequency	100%	$\approx 20kHz$	$20kHz$	$\approx 10kHz$
	50%	$\approx 19kHz$	$20kHz$	$\approx 10kHz$
	10%	$\approx 16kHz$	$20kHz$	$\approx 9kHz$

Table 4.5 continued

PEMFC Voltage Undershoot	100% to 50%	0.51%	0.56%	0.34%
	50% to 10%	2.15%	2.06%	2.36%
PEMFC Voltage Overshoot	10% to 100%	1.93%	2.03%	1.87%
PEMFC Current Overshoot	100% to 50%	0%	0.34%	0%
	50% to 10%	0%	0.46%	0%
PEMFC Current Undershoot	10% to 100%	0%	0%	0%
PEMFC Power Undershoot	100% to 50%	0.022%	0.029%	0.007%
	50% to 10%	0.310%	0.290%	0.380%
PEMFC Power Overshoot	10% to 100%	0%	0%	0%
PEMFC Voltage Ripple	100%	0.15%	0.34%	0.34%
	50%	0.18%	0.56%	0.37%
	10%	0.17%	0.49%	0.33%
PEMFC Current Ripple	100%	0.22%	0.35%	0.35%
	50%	0.18%	0.53%	0.38%
	10%	0.16%	0.49%	0.34%
PEMFC Power Ripple	100%	0.0015%	0.0126%	0.0060%
	50%	0.0013%	0.0087%	0.0056%
	10%	0.0006%	0.0043%	0.0028%

The results illustrated in Table 4.5 show that all the proposed predictive MPPT methods have the same performance in MPPT accuracy. They have a similar range of power undershoot and the same settling time within $0.50ms$. These results show that the predictive MPPT methods have an excellent performance with extremely low power undershoot and

short settling time. It is found that such an approach produces good quality results in terms of accuracy and robustness. However, the power ripple of the predictive duty cycle MPPT method is seven to eight times higher than that of the predictive switching state MPPT method. Although they had almost the same switching frequency, the predictive switching state MPPT method was able to generate the PEMFC output power with a lower power ripple. This means that the predictive switching state MPPT method has better performance in power quality and stability control. For predictive switching state MPPT with frequency reduction method, it cuts the switching frequency to around half, but its power ripple is four to five times higher than the pure predictive switching state MPPT method. However, its performance outstands the predictive duty cycle MPPT method with lower switching frequency and lower power ripple. Its advantage is that the switching frequency can be reduced from originally around $20kHz$ to $10kHz$ while the power ripple is still maintained at a low percentage within 0.006%.

For the load, the power quality for all the proposed predictive MPPT methods are compared. The results are presented in Table 4.6.

Table 4.6: Comparison of Load Power Quality under Variable PEMFC Parameters

Comparison	**Hydrogen and Oxygen Input Flow Rate**	**Predictive Switching State MPPT**	**Predictive Duty Cycle MPPT**	**Predictive Switching State MPPT with Frequency Reduction**
Load Power	100%	$48.1W$	$48.1W$	$48.1W$
	50%	$43.0W$	$43.0W$	$43.0W$
	10%	$30.9W$	$30.9W$	$30.9W$

Table 4.6 continued

Settling Time	100% to 50%	$0.14s$	$0.14s$	$0.14s$
	50% to 10%	$0.14s$	$0.14s$	$0.14s$
	10% to 100%	$0.13s$	$0.13s$	$0.13s$
Load Voltage Overshoot	100% to 50%	0.33%	0.44%	0.32%
	50% to 10%	1.10%	1.23%	1.06%
Load Voltage Undershoot	10% to 100%	1.30%	1.30%	1.40%
Load Current Overshoot	100% to 50%	0.32%	0.41%	0.32%
	50% to 10%	1.11%	1.22%	1.03%
Load Current Undershoot	10% to 100%	1.34%	1.37%	1.43%
Load Power Overshoot	100% to 50%	0.62%	0.85%	0.62%
	50% to 10%	2.21%	2.49%	2.09%
Load Power Undershoot	10% to 100%	2.62%	2.66%	2.79%
Load Voltage Ripple	100%	0.08%	0.34%	0.20%
	50%	0.12%	0.37%	0.23%
	10%	0.14%	0.38%	0.28%
Load Current Ripple	100%	0.08%	0.33%	0.19%
	50%	0.11%	0.36%	0.23%
	10%	0.14%	0.38%	0.28%
Load Power Ripple	100%	0.17%	0.66%	0.39%
	50%	0.23%	0.72%	0.47%
	10%	0.27%	0.76%	0.55%

The results in Table 4.6 show that all the proposed predictive MPPT methods generate the same electrical power for the load. The only difference between the performances of these MPPT techniques is the power quality. The predictive switching state MPPT method provided the best power quality to the load, while the predictive duty cycle MPPT method produced the worst power quality. However, the power ripple is within 0.76% which is acceptable.

Figure 4.37, Figure 4.45, and Figure 4.52 show that the load consumption was $48.1W$, $43.0W$, and $30.9W$ when the input flow rates of hydrogen were 100%, 50%, and 10% respectively. It means that the percentage of load power consumption from the PEMFC was 96.20%, 95.96%, and 95.11% respectively. This was because the PEMFC output power was decreased when the input flow rates of the reactant gases were reduced. Figure 4.35, Figure 4.36, Figure 4.43, Figure 4.44, Figure 4.50, and Figure 4.51 also illustrate the fact that the load power affected the load voltage and current. According to Ohm's Law, the decrease in load power caused the load voltage and current to drop due to the constant load resistance.

Since the capacitor inside the DC-DC boost converter opposed the abrupt voltage changes, it required 0.15s to regulate the load voltage to a stable level by releasing the electrical energy. When the PEMFC output power was decreased, the capacitor was discharged to a lower voltage. On the contrary, the capacitor was charged to a higher voltage when the PEMFC output power was increased. The time required for the capacitor to charge or discharge 63.2% of its voltage was $0.019s$. Therefore, the time constant, τ of the capacitor was $0.019s$. The capacitor charging and discharging formulas are defined as Equation 4.6 and Equation 4.7, respectively.

$$V_c(t) = V_s\left(1 - e^{-\frac{t}{\tau}}\right)$$ Equation 4.6

$$V_c(t) = V_s e^{-\frac{t}{\tau}}$$ Equation 4.7

where V_c is the capacitor voltage, V_s is the charging voltage and τ is the time constant of the capacitor.

Based on the comparison in Table 4.6, the performances of both predictive MPPT techniques are almost the same. They have similar load power consumption, settling time, load power overshoot, and undershoot issues. The load consumed the same amount of electrical power with the same settling time. From the viewpoint of load power quality, the predictive MPPT by switching state is slightly better than the duty cycle technique due to low power ripple. It is interesting to note that this approach works well in fast variations of PEMFC parameter change.

4.5 Simulation with Constant PEMFC Parameters and Variable Load Resistance

In this simulation, the simulation was run through constant PEMFC parameters with a fast variation of the load resistance. This simulation aims to investigate the robustness of the proposed MPPT technique to changes in load. The initial load resistance was 12Ω, and it was decreased to 6Ω, 4Ω, and 3Ω every $0.25s$. Figure 4.53 shows the time variations of load resistance in this simulation.

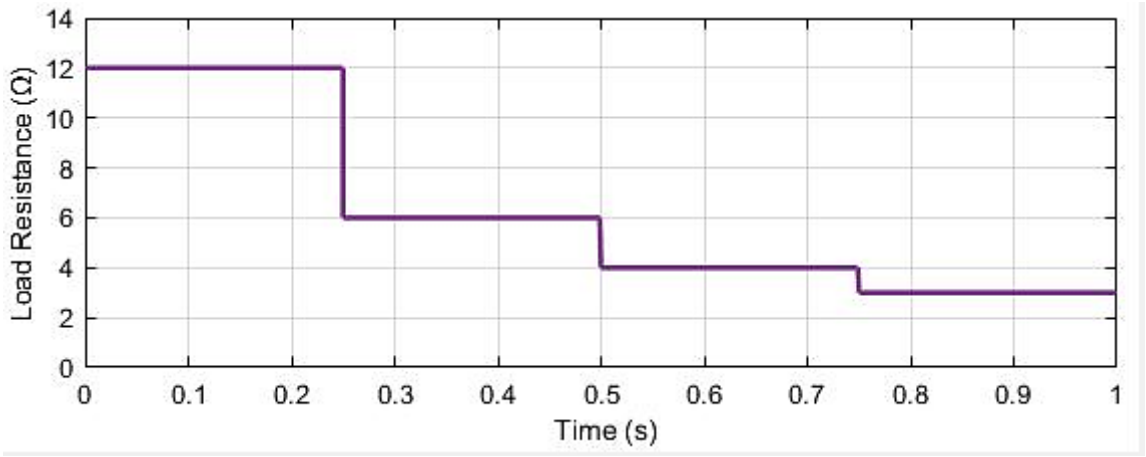


Figure 4.53: Variations of Load Resistance

4.5.1 Simulation with Variable Load by Predictive Switching State MPPT Technique

This section provides the simulation results with the predictive switching state MPPT method. Figure 4.54, Figure 4.55, and Figure 4.56 present the simulation results of the PEMFC output voltage, current, and power under constant PEMFC parameters and variable load.

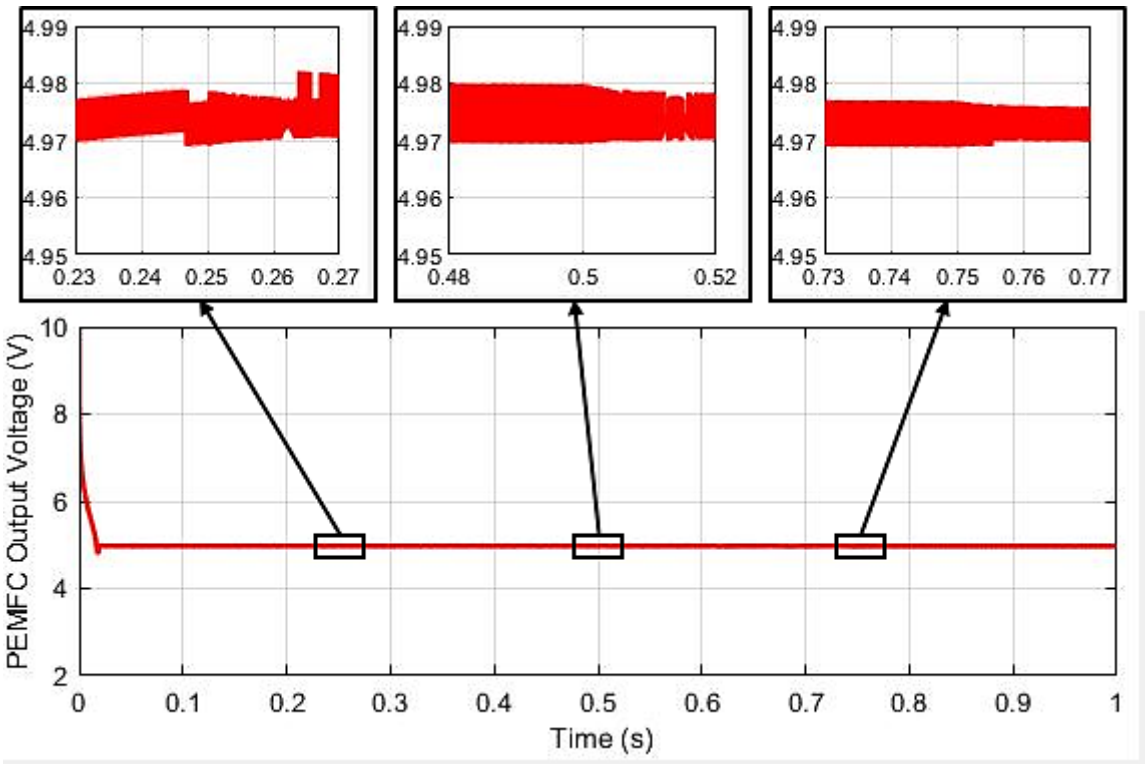


Figure 4.54: Simulation Results of PEMFC Output Voltage for Predictive Switching State MPPT under Variable Load Resistance

In Figure 4.54, the PEMFC output voltage was kept at $4.97V$ from the beginning until the end of the simulation. However, there was a minor effect of load variation on the voltage ripple. The PEMFC voltage ripple recorded was 0.23%, 0.16%, and 0.12% when the load resistance was 6Ω, 4Ω and 3Ω respectively.

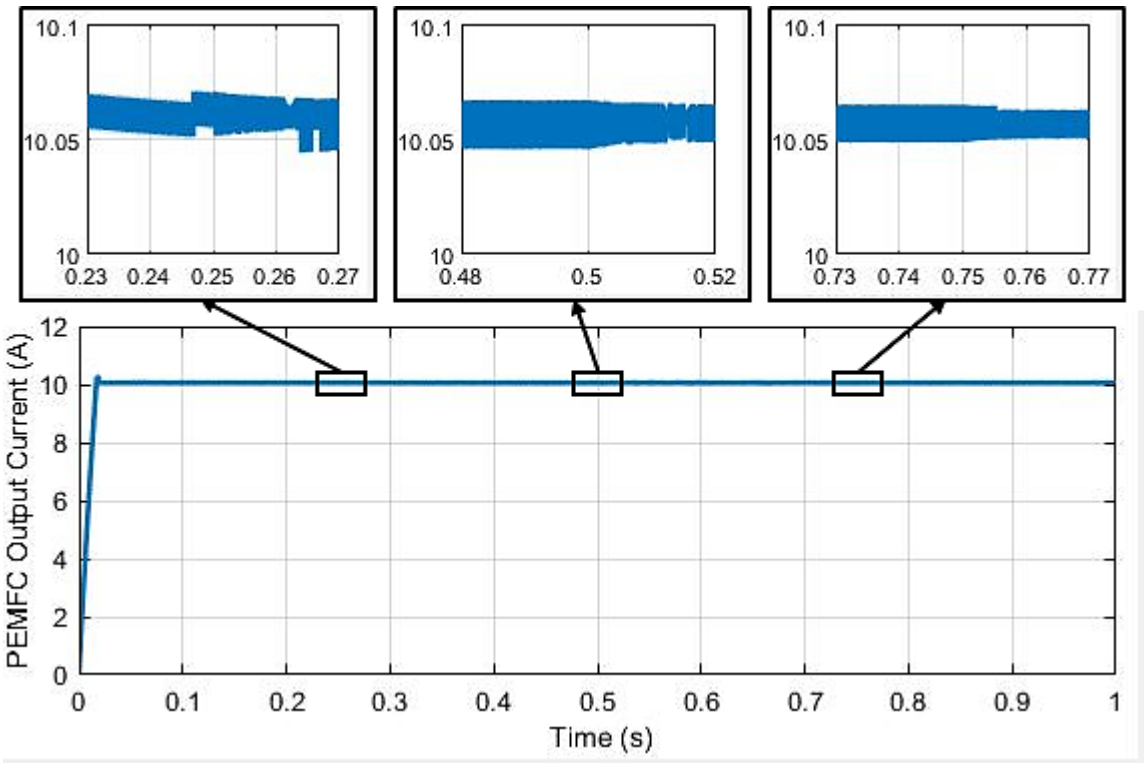


Figure 4.55: Simulation Results of PEMFC Output Current for Predictive Switching State MPPT under Variable Load Resistance

The PEMFC output current was kept at $10.06A$ throughout the simulation. The current ripple was also affected by the variation of the load. The current ripple recorded was between 0.13% and 0.21%.

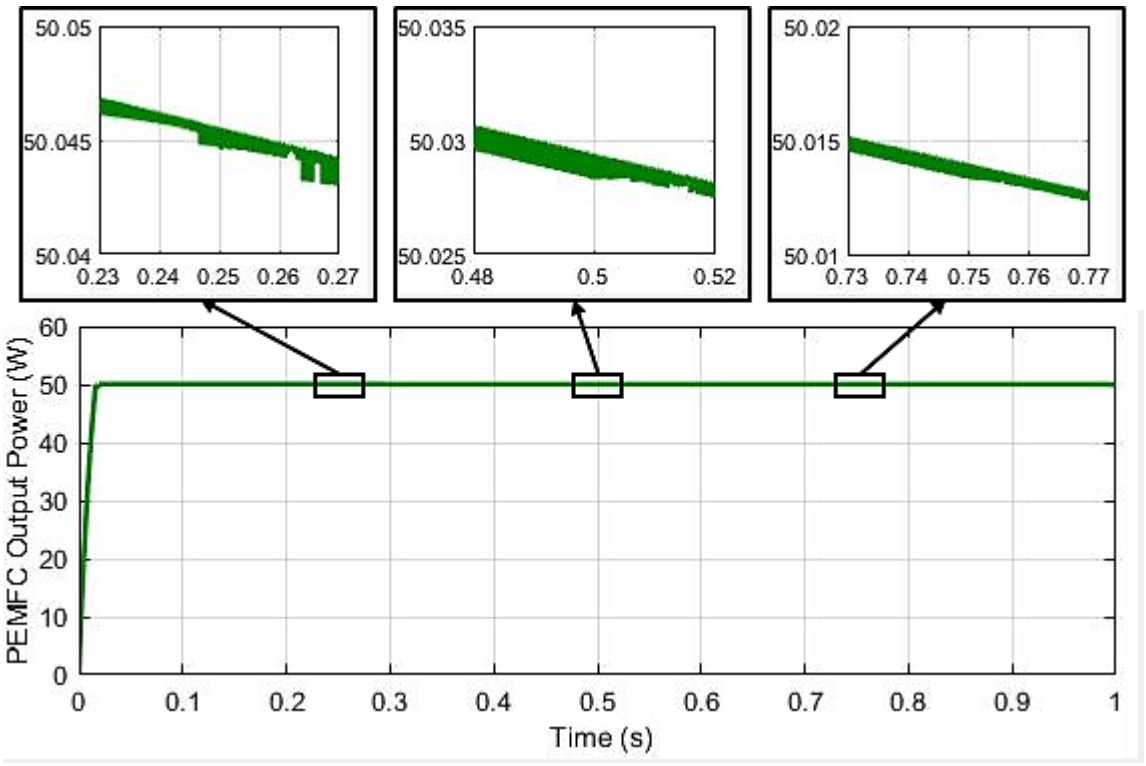


Figure 4.56: Simulation Results of PEMFC Output Power for Predictive Switching State MPPT under Variable Load Resistance

For PEMFC output power, it achieved $50W$ and kept the maximum power throughout the simulation. The power ripple recorded was between 0.0008% and 0.0022%.

The switching frequency of the predictive switching state MPPT method varied between $17kHz$ and $24kHz$. Figure 4.57 illustrates the switching state during the change in load resistance.

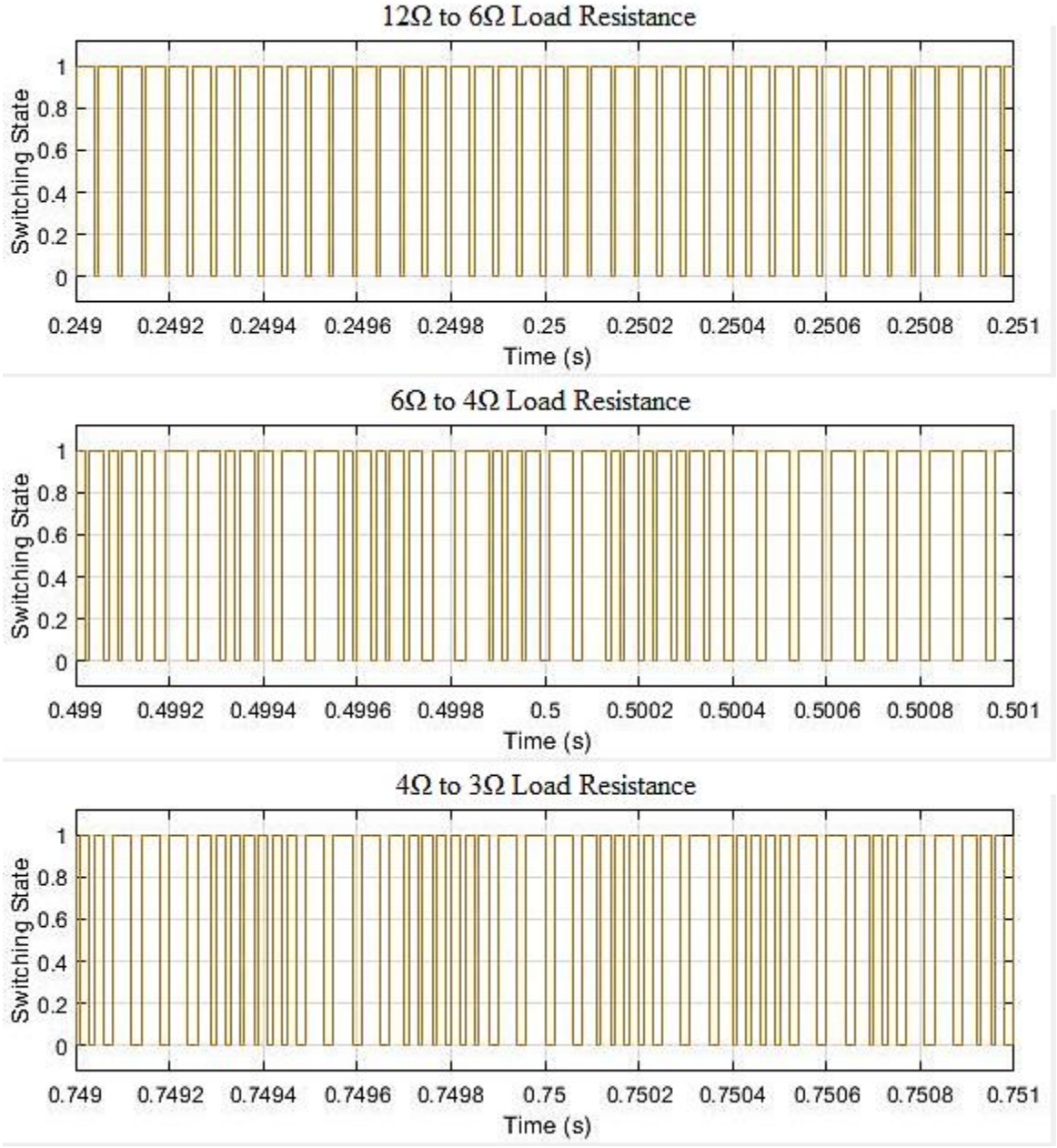


Figure 4.57: Simulation Results of Switching State for Predictive Switching State MPPT under Variable Load Resistance

Figure 4.57 shows that the switching frequency was $20kHz$ before $0.25s$. When the load resistance was changed to 6Ω, the switching frequency varied between $20kHz$ and $22kHz$. Then, the switching frequency varied between $17kHz$ and $24kHz$ when the load

resistance is 4Ω. When the load resistance was dropped to 3Ω, the switching frequency recorded was between $21kHz$ and $24kHz$.

On the load side, the load power consumption was always $48.15W$. However, there were power transients when there was a change in load resistance. The simulation results of load voltage, current, and power are presented in Figure 4.58, Figure 4.59, and Figure 4.60, respectively.

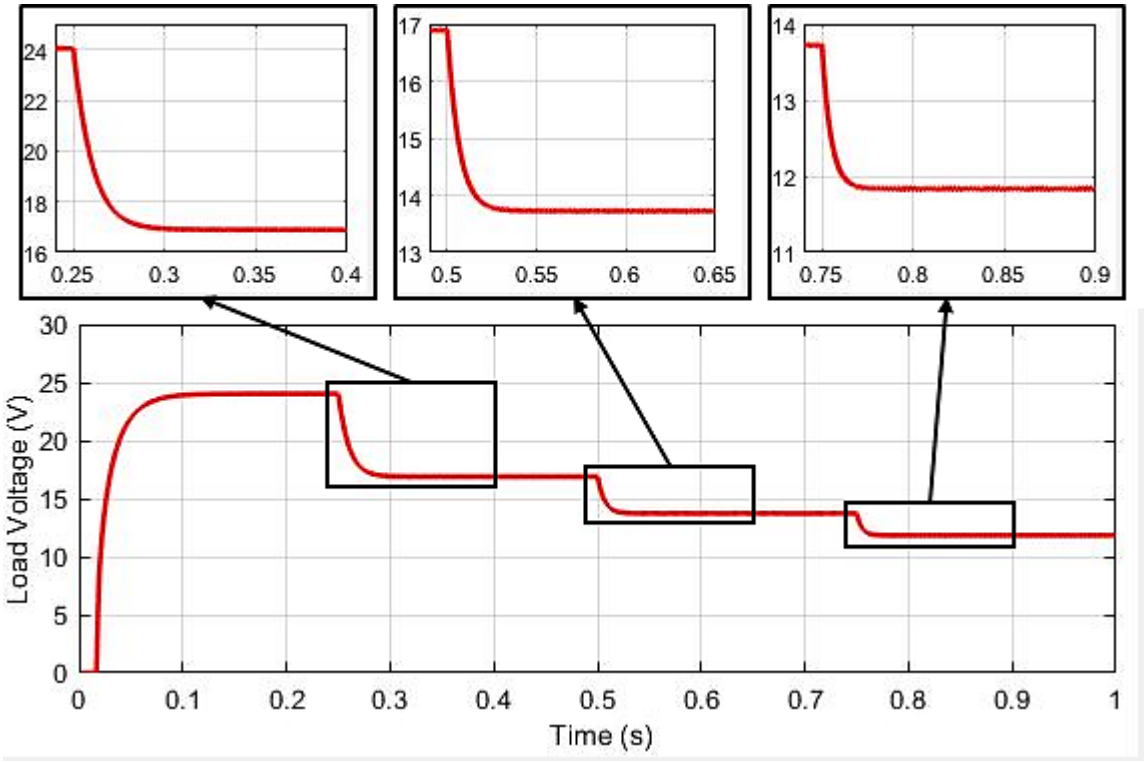


Figure 4.58: Simulation Results of Load Voltage for Predictive Switching State MPPT under Variable Load Resistance

At the beginning of the simulation, the load voltage was raised to $24.03V$. Then, it started to decrease until $16.9V$ with a 0.24% ripple when the load resistance was changed to 6Ω. At $0.5s$, it started to decrease until $13.72V$ with 0.28% of ripple. Lastly, the load voltage was decreased to $11.83V$ with 0.27% of ripple.

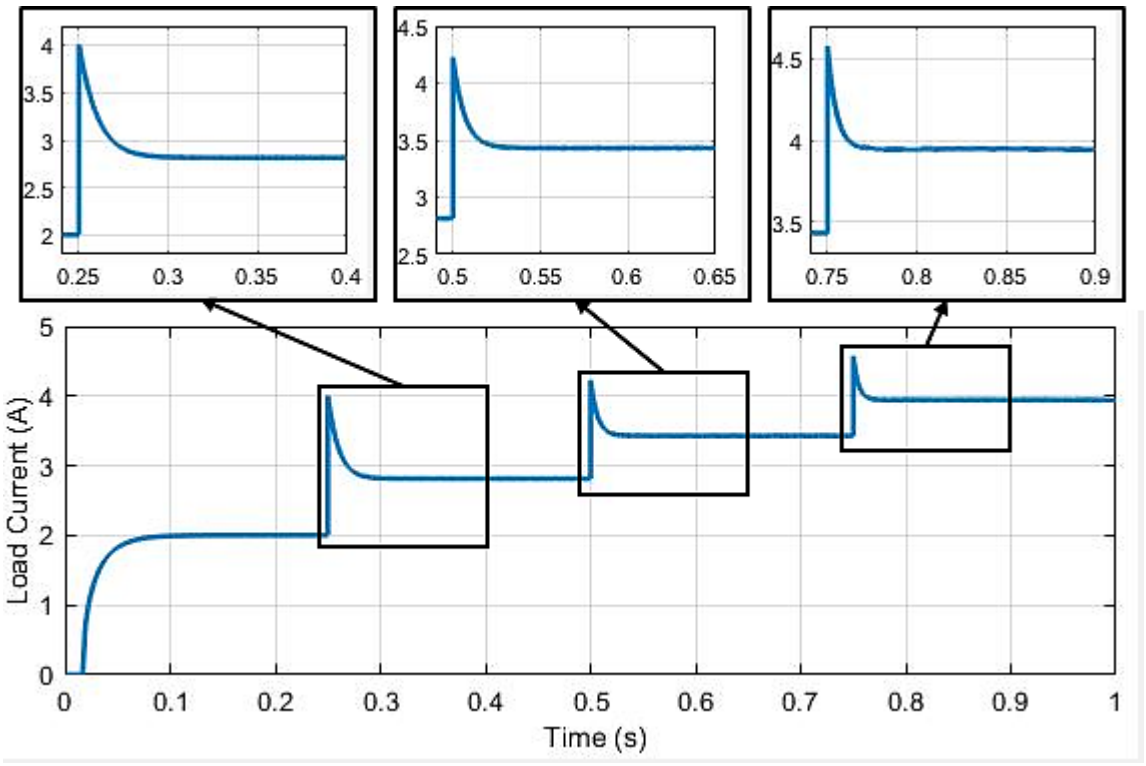


Figure 4.59: Simulation Results of Load Current for Predictive Switching State MPPT under Variable Load Resistance

The simulation result of the behavior load current was different from the load voltage. The load current was increased instead of decreased when the load resistance was decreased. First, the load current was increased to $2.003A$ since the load resistance was 12Ω. Then, it experienced a 42.27% current overshoot and then slowly decreased to $2.816A$ when the load resistance was changed to 6Ω. At $0.5s$, the load experienced another current overshoot with 22.99% and the current dropped to $3.431A$. Lastly, the load experienced a 15.91% current overshoot, and then the current was increased to $3.944A$. The current ripple recorded was between 0.11% and 0.28%.

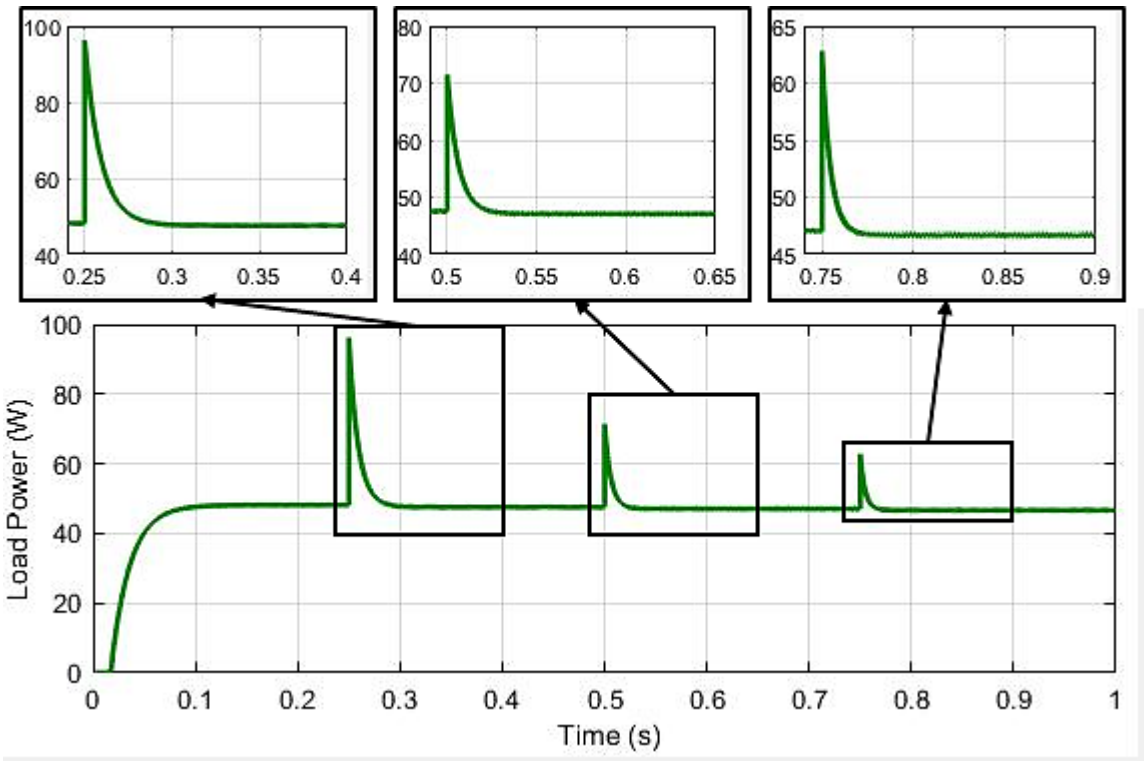


Figure 4.60: Simulation Results of Load Power for Predictive Switching State MPPT under Variable Load Resistance

At the beginning of the simulation, the load power increased from $0W$ to $48.15W$ within $0.14s$. When the load resistance dropped from 6Ω, 4Ω, and 3Ω, the load power dropped to $47.55W$, $47.1W$, and $46.7W$ with power transients within $60ms$. At $0.25s$, there was a 102.49% power overshoot. At $0.5s$, the load experienced 51.31% of power overshoot. At $0.75s$, the load experienced another 34.33% power overshoot. The power ripple recorded was 0.47%, 0.56%, and 0.55% when the load resistance was 6Ω, 4Ω, and 3Ω, respectively.

4.5.2 Simulation with Variable Load by Predictive Duty Cycle MPPT Technique

This section presents the simulation results of PEMFC applied with the predictive duty cycle MPPT method with $20kHz$ frequency under variable load. The simulation results

of the PEMFC output voltage, current, and power are shown in Figure 4.61, Figure 4.62, and Figure 4.63, respectively.

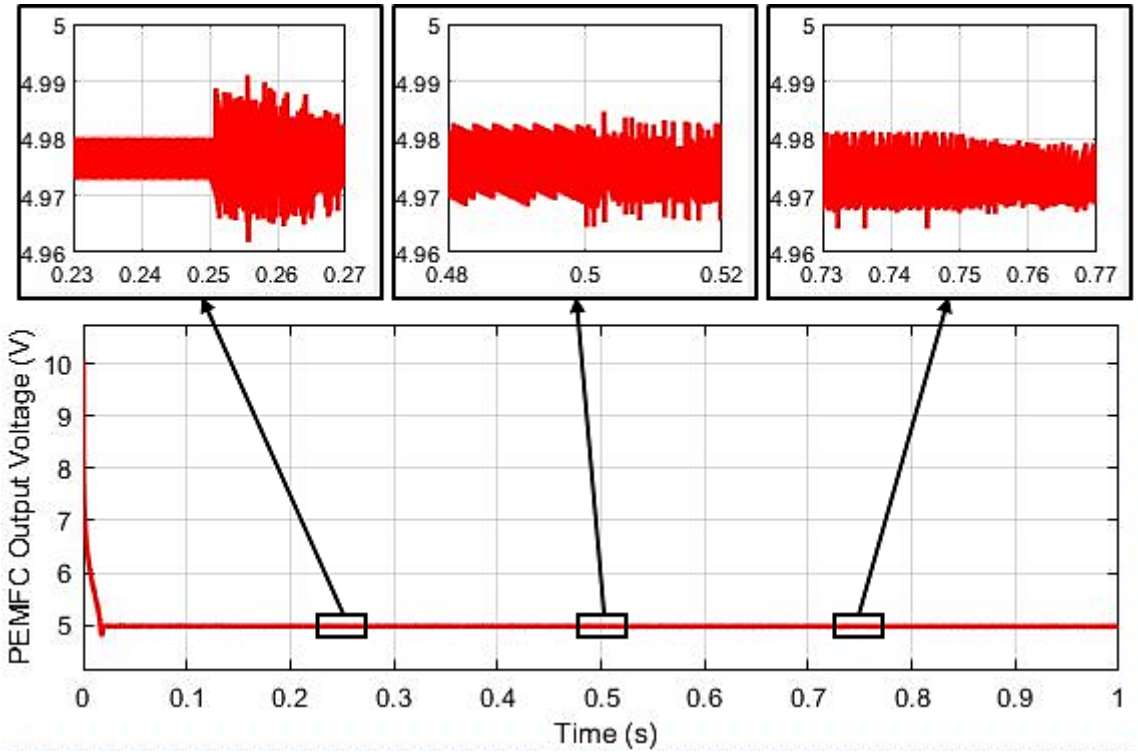


Figure 4.61: Simulation Results of PEMFC Output Voltage for Predictive Duty Cycle MPPT under Variable Load Resistance

The simulation results of the PEMFC output voltage by the predictive duty cycle MPPT method kept at $4.97V$, which was similar to the predictive switching state MPPT method. However, the PEMFC voltage ripple was slightly higher than that of the predictive switching state MPPT method. The ripple was recorded as 0.37%, 0.34%, and 0.24% when the load resistance was 6Ω, 4Ω, and 3Ω, respectively.

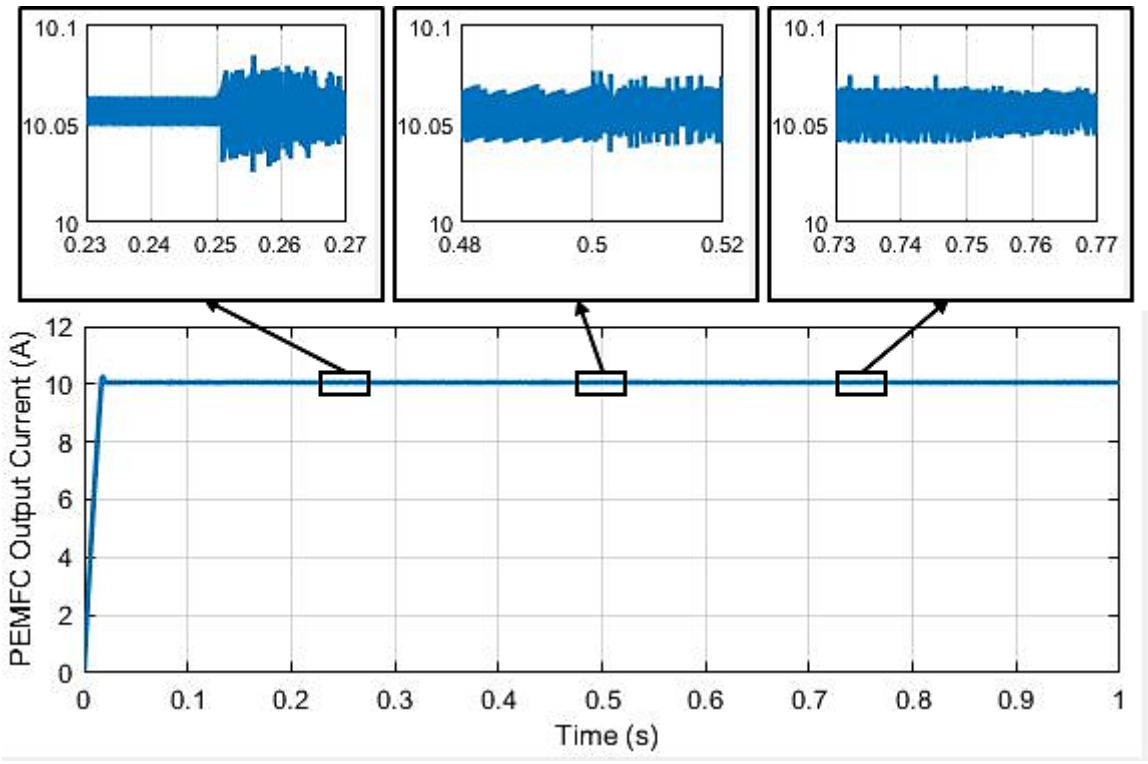


Figure 4.62: Simulation Results of PEMFC Output Current for Predictive Duty Cycle MPPT under Variable Load Resistance

The PEMFC output current was kept at MPP current throughout the simulation. The percentage of current ripple recorded was almost the same as the percentage of voltage ripple.

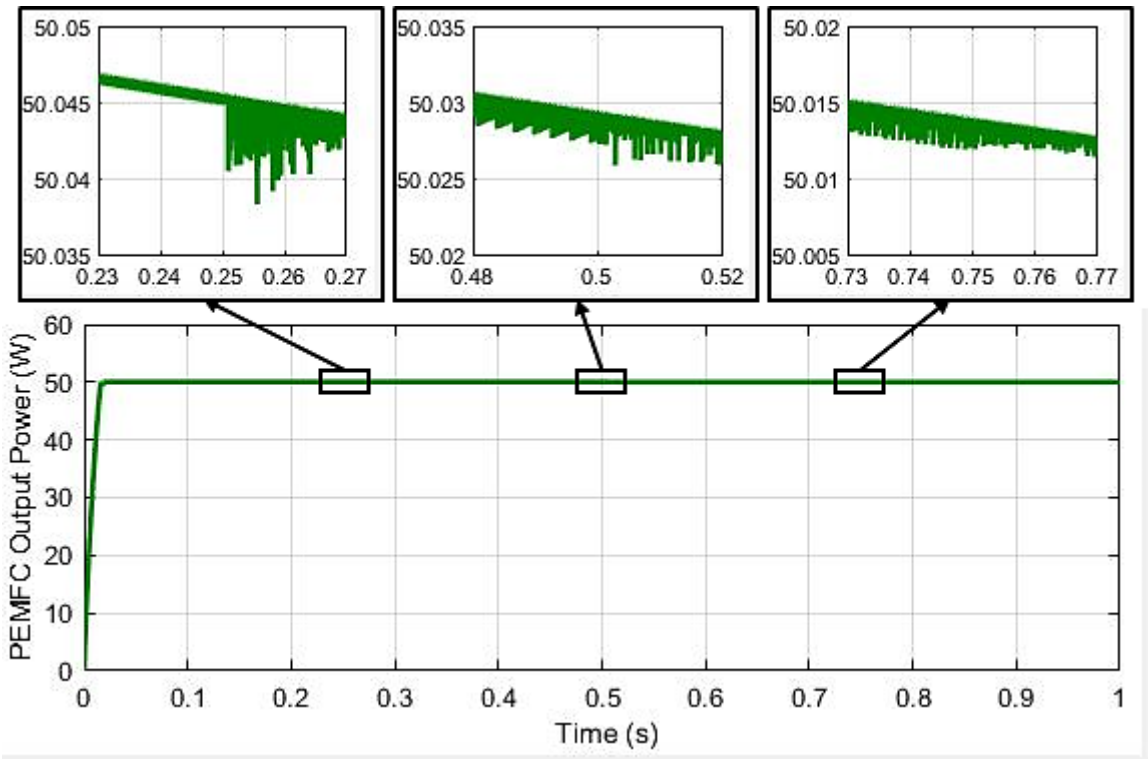


Figure 4.63: Simulation Results of PEMFC Output Power for Predictive Duty Cycle MPPT under Variable Load Resistance

The PEMFC output power kept the power at $50W$ throughout the simulation. The power ripple recorded was 0.0043%, 0.0044%, and 0.0028% when the load resistance was 6Ω, 4Ω, and 3Ω, respectively.

Next, Figure 4.64 illustrates the duty cycle selected by the predictive duty cycle MPPT controller in each sampling step under variable load resistance.

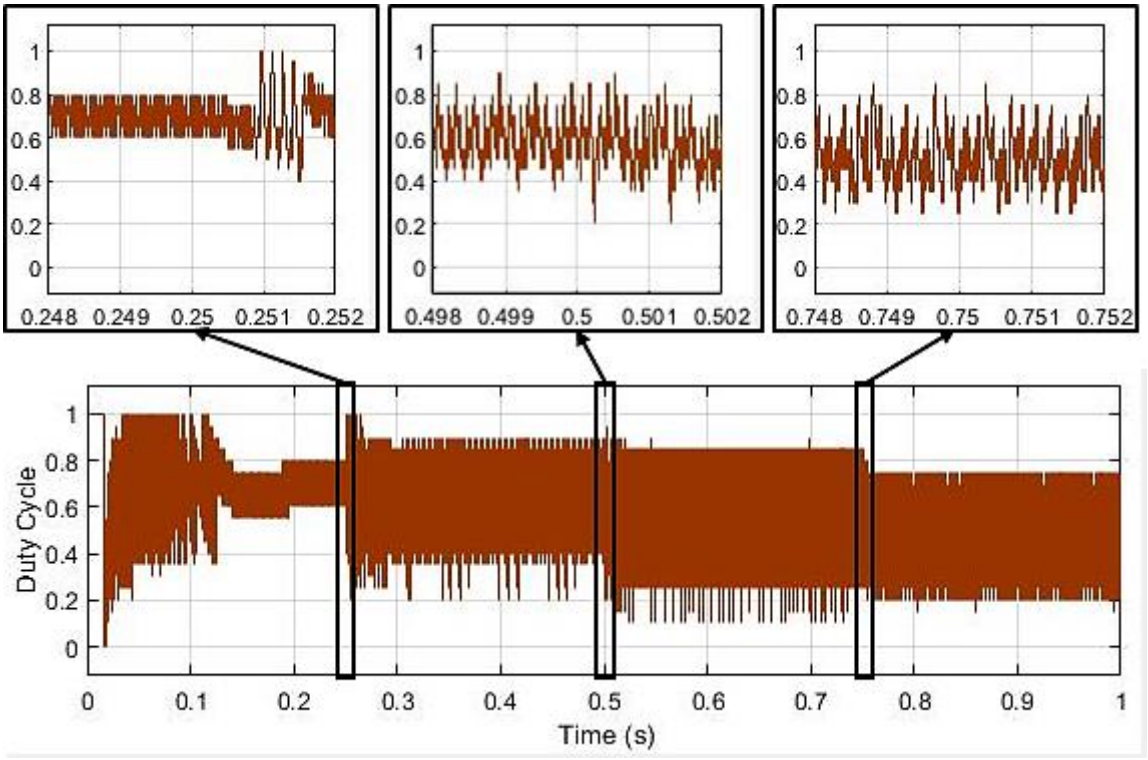


Figure 4.64: Simulation Results of Duty Cycle for Predictive Duty Cycle MPPT under Variable Load Resistance

The simulation result shows that the predictive controller determined the duty cycle based on the changes in load. When the total load resistance was varied from 12Ω to 6Ω, the duty cycle selected was between 0.4 and 1. Then, the predictive controller selected the duty cycle between 0.2 and 0.9 when the load resistance was 6Ω. When the load resistance dropped to 4Ω, the duty cycle was changed to a range between 0.1 and 0.85. Lastly, the duty cycle from 0.2 to 0.75 was selected when the load resistance was 3Ω. The switching state during the change of load resistance is illustrated in Figure 4.65. The results show that the switching frequency was always $20kHz$ throughout the simulation.

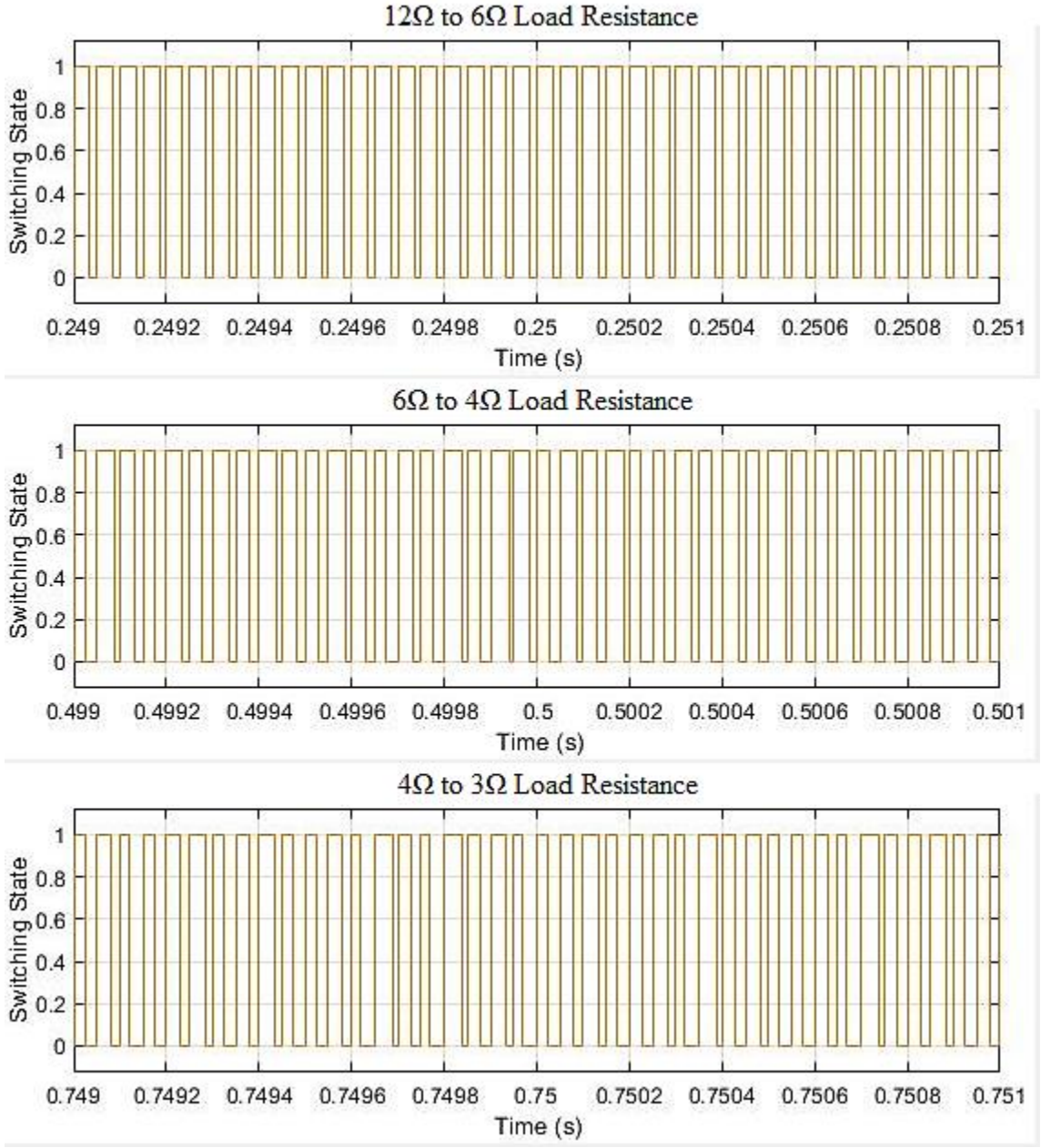


Figure 4.65: Simulation Results of Switching State for Predictive Duty Cycle MPPT under Variable Load Resistance

For the predictive duty cycle MPPT technique, the load had similar simulation results as the predictive switching state MPPT method. However, its power ripple was slightly higher than that of the predictive switching state MPPT method. The simulation results of

load voltage, current, and power are shown in Figure 4.66, Figure 4.67, and Figure 4.68, respectively.

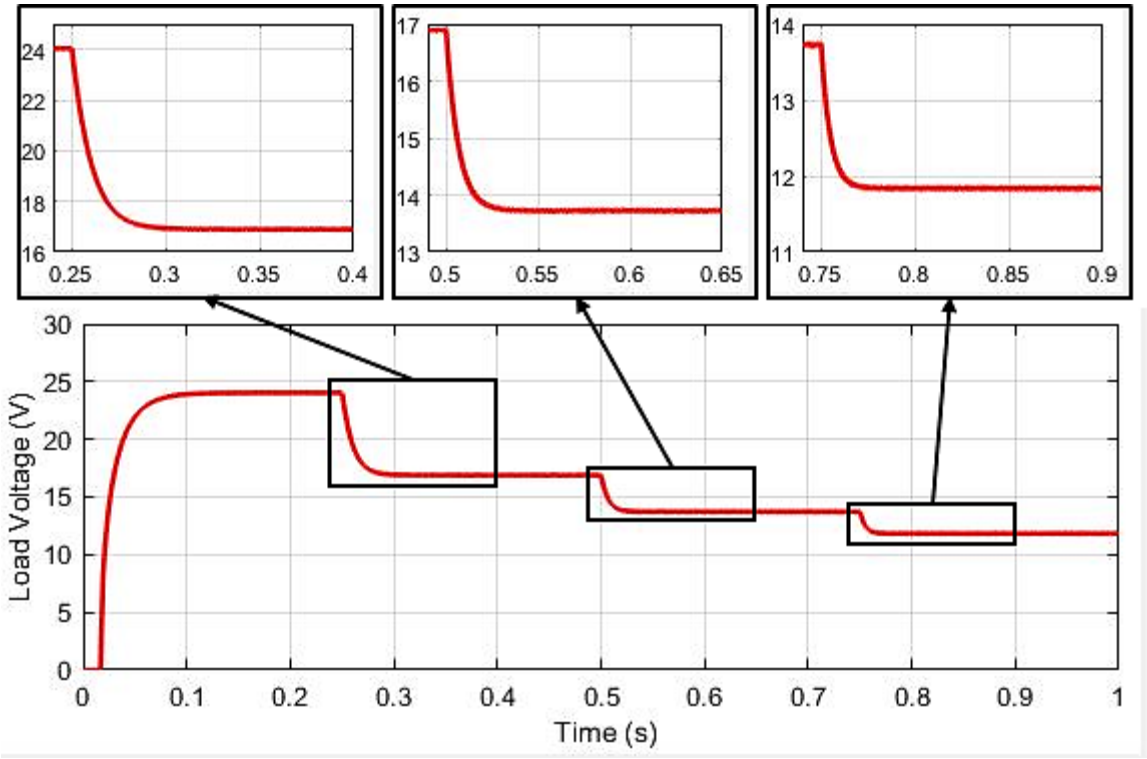


Figure 4.66: Simulation Results of Load Voltage for Predictive Duty Cycle MPPT under Variable Load Resistance

Same as the previous simulation, the load voltage was raised to $24.03V$ at the beginning of the simulation. It decreased to $16.9V$, $13.72V$, and $11.83V$ when the load resistance dropped to 6Ω, 4Ω, and 3Ω. The voltage ripple recorded was 0.4%, 0.58%, and 0.53% respectively.

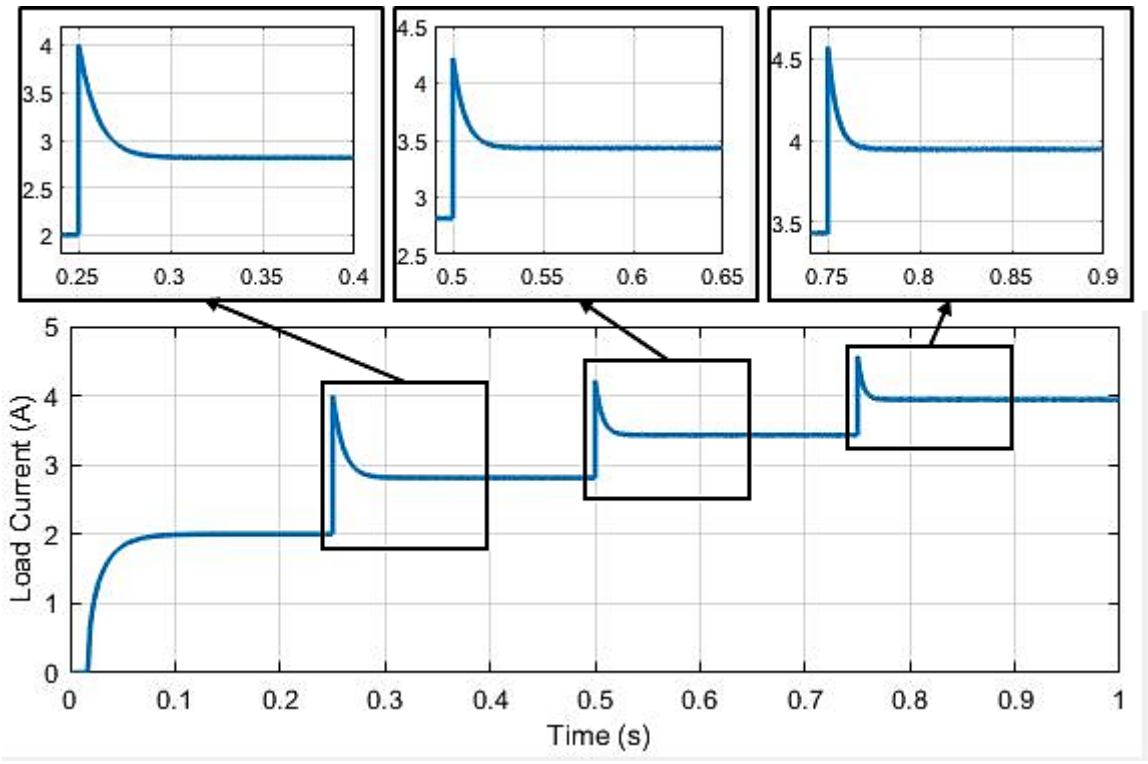


Figure 4.67: Simulation Results of Load Current for Predictive Duty Cycle MPPT under Variable Load Resistance

The simulation result shows that the load current was $2.003A$ when the load resistance was 12Ω. When the load resistance was changed to 6Ω, the current increased to $2.816A$ after a 42.25% current overshoot. At $0.5s$, the load experienced another current overshoot with 23.02% and the current dropped to $3.431A$. When the load resistance was changed from 4Ω to 3Ω, the load experienced a 15.91% current overshoot, and then the current returned to $3.944A$. The current ripple recorded was 0.39%, 0.58%, and 0.55% when the load resistance was 6Ω, 4Ω, and 3Ω, respectively.

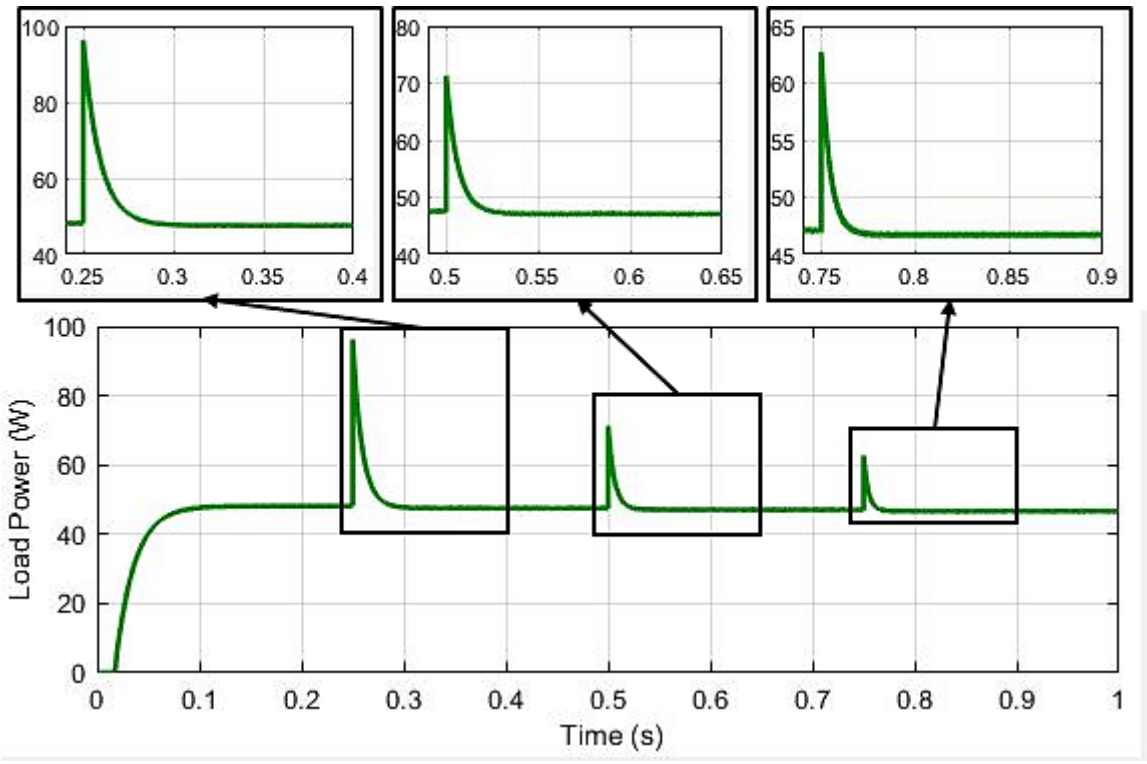


Figure 4.68: Simulation Results of Load Power for Predictive Duty Cycle MPPT under Variable Load Resistance

For load power, the simulation result shows that it consumed $48.15W$, $47.55W$, $47.1W$, and $46.7W$ of electrical power when the load resistance dropped from 12Ω to 6Ω, 4Ω, and 3Ω, respectively. When the load resistance was 12Ω, 6Ω, 4Ω and 3Ω, the power ripple recorded was 0.82%, 1.17%, and 1.10% respectively. During the changing of load resistance, the load experienced 102.45%, 50.38%, and 34.33% at $0.25s$, $0.5s$, and $0.75s$, respectively.

4.5.3 Simulation with Variable Load by Predictive Switching State MPPT with Frequency Reduction Technique

This section includes the 0.3 weighting factor of the switching frequency technique in the predictive switching state MPPT method. The simulation results were presented and

discussed. Figure 4.69, Figure 4.70, and Figure 4.71 illustrate the behavior of the PEMFC output voltage, current, and power under variable load resistance.

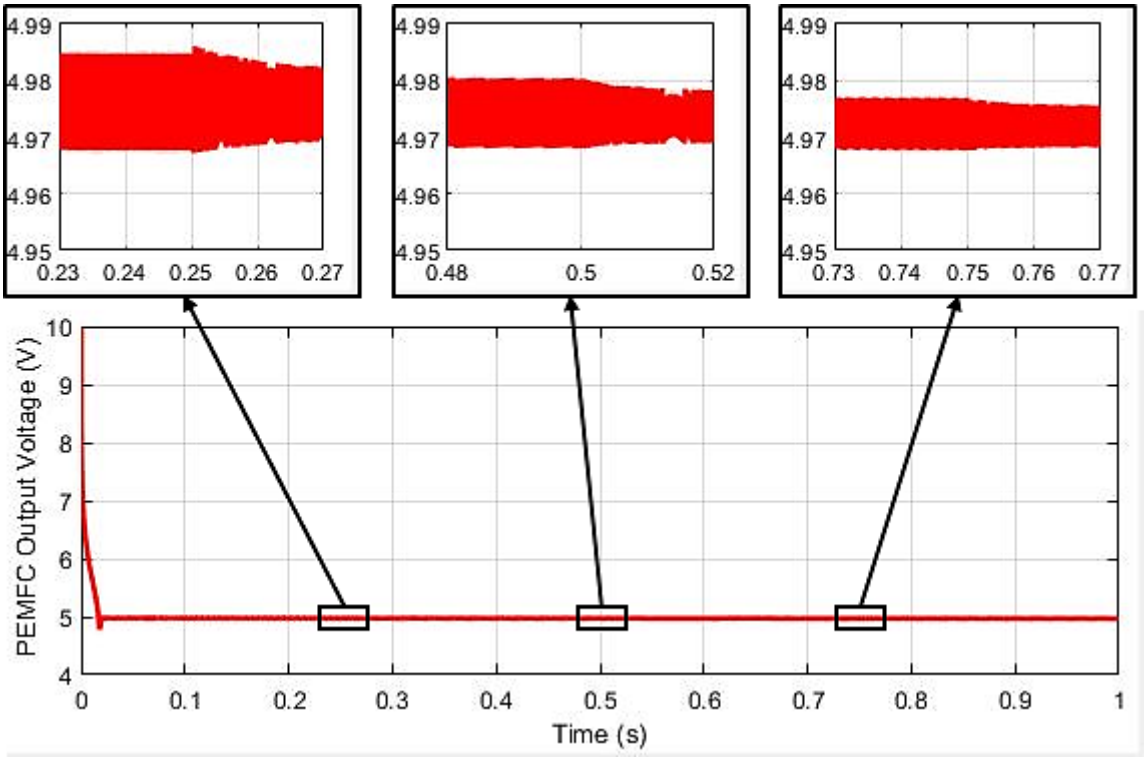


Figure 4.69: Simulation Results of PEMFC Output Voltage for Predictive Switching State MPPT with Frequency Reduction under Variable Load Resistance

From the simulation result, the PEMFC output voltage was kept at $4.97V$ from the beginning until the end of the simulation. During the fast variation of the load resistance, there was a minor change in the voltage ripple. When the load resistance was 6Ω, 4Ω, and 3Ω, the voltage ripple recorded was 0.27%, 0.18%, and 0.13% respectively.

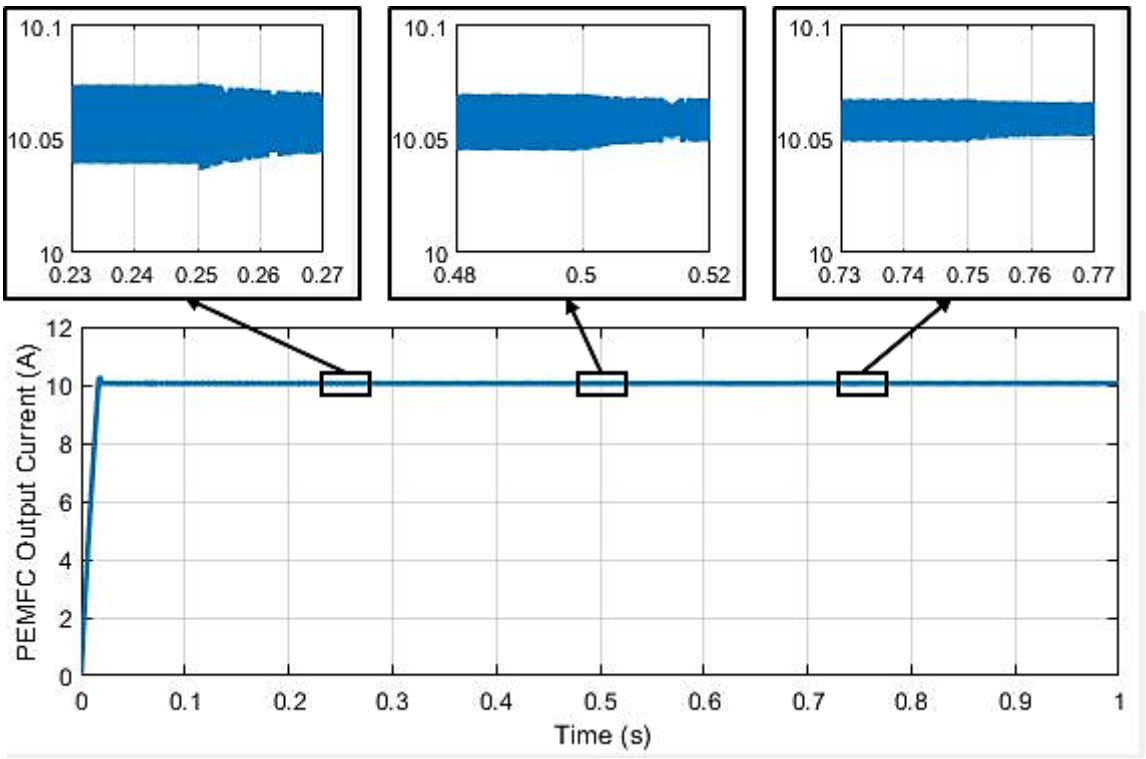


Figure 4.70: Simulation Results of PEMFC Output Current for Predictive Switching State MPPT with Frequency Reduction under Variable Load Resistance

The PEMFC output current was kept at MPP, which was $10.06A$ throughout the simulation. When the load resistance was 6Ω, 4Ω, and 3Ω, the current ripple was 0.25%, 0.19%, and 0.15% respectively.

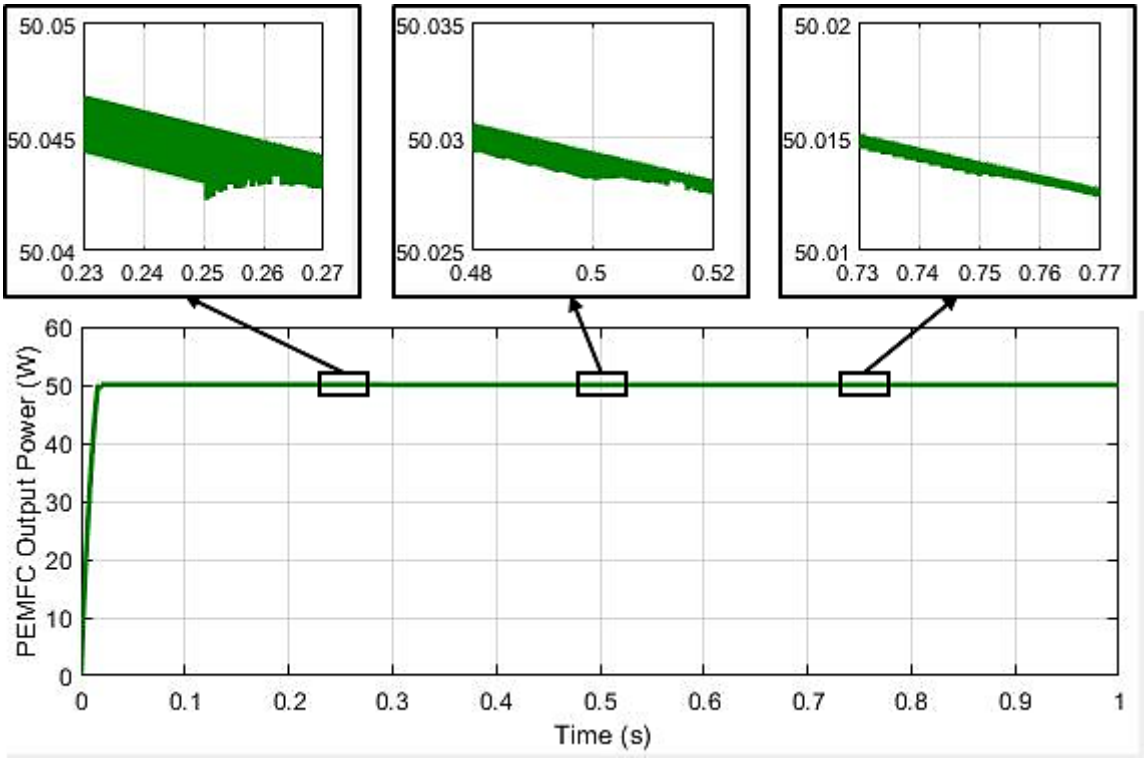


Figure 4.71: Simulation Results of PEMFC Output Power for Predictive Switching State MPPT with Frequency Reduction under Variable Load Resistance

Similar to the simulation in sections 4.5.1 and 4.5.2, the PEMFC output power was kept at $50W$ throughout the simulation. The power ripple recorded was 0.0026%, 0.0012%, and 0.0007% when the load resistance was 6Ω, 4Ω, and 3Ω respectively.

The switching frequency of the predictive switching state MPPT with frequency reduction method varied between $10kHz$ and $19kHz$. Figure 4.72 shows the switching state during the fast variation of load resistance.

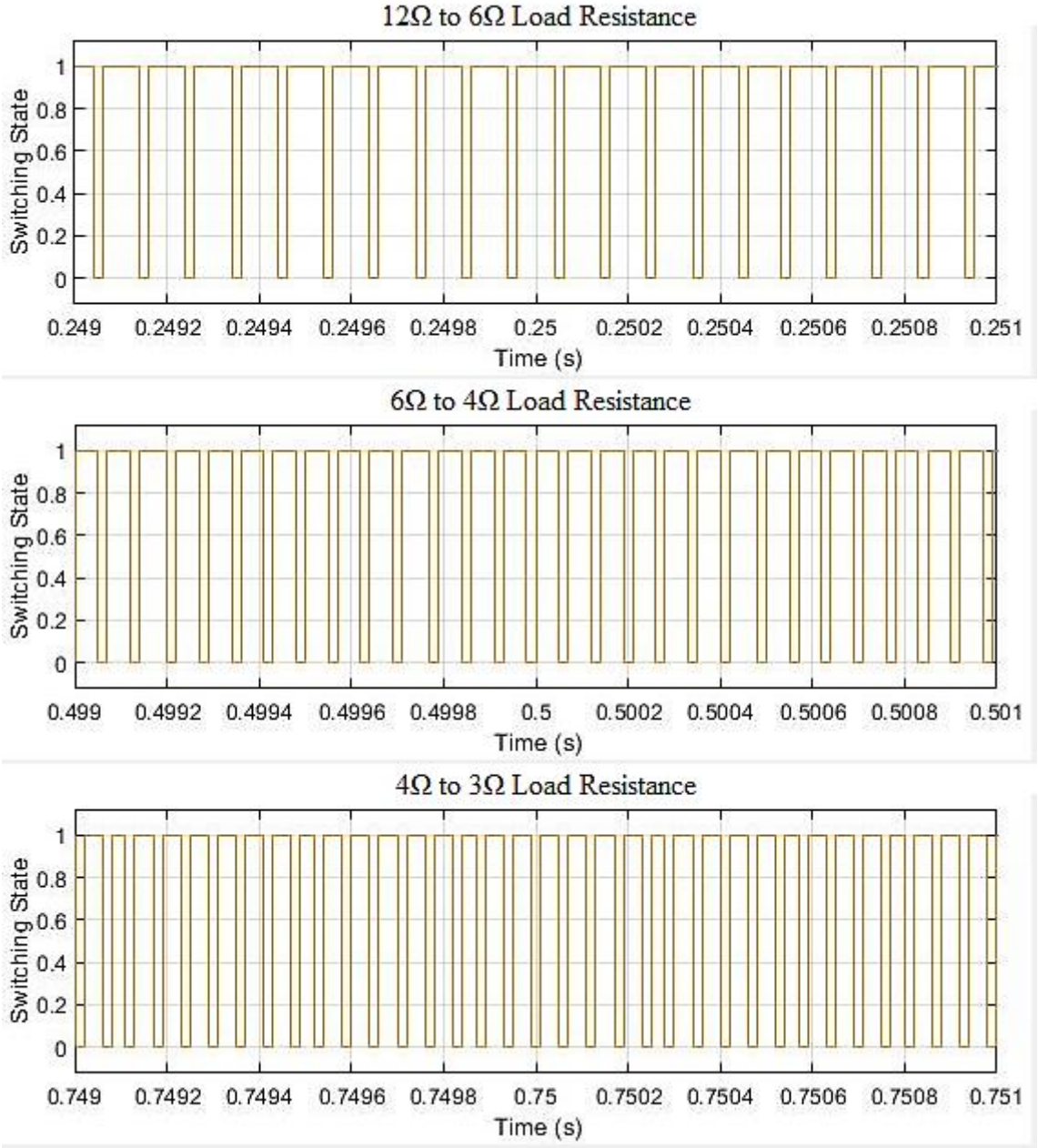


Figure 4.72: Simulation Results of Switching State for Predictive Switching State MPPT with Frequency Reduction under Variable Load Resistance

Before $0.25s$, the switching frequency was around $10kHz$. When the load resistance was changed to 6Ω, the switching frequency was increased, and it reached $14kHz$ before $0.5s$. Between $0.5s$ and $0.75s$, the switching frequency recorded was between $14kHz$ and

$18kHz$. After the load resistance was dropped to 3Ω, the highest switching frequency recorded $19kHz$.

The load power consumption $48.15W$ of electrical power throughout the simulation. Power transients occurred during the fast variation of load resistance. Figure 4.73, Figure 4.74, and Figure 4.75 show the simulation results of load voltage, current, and power.

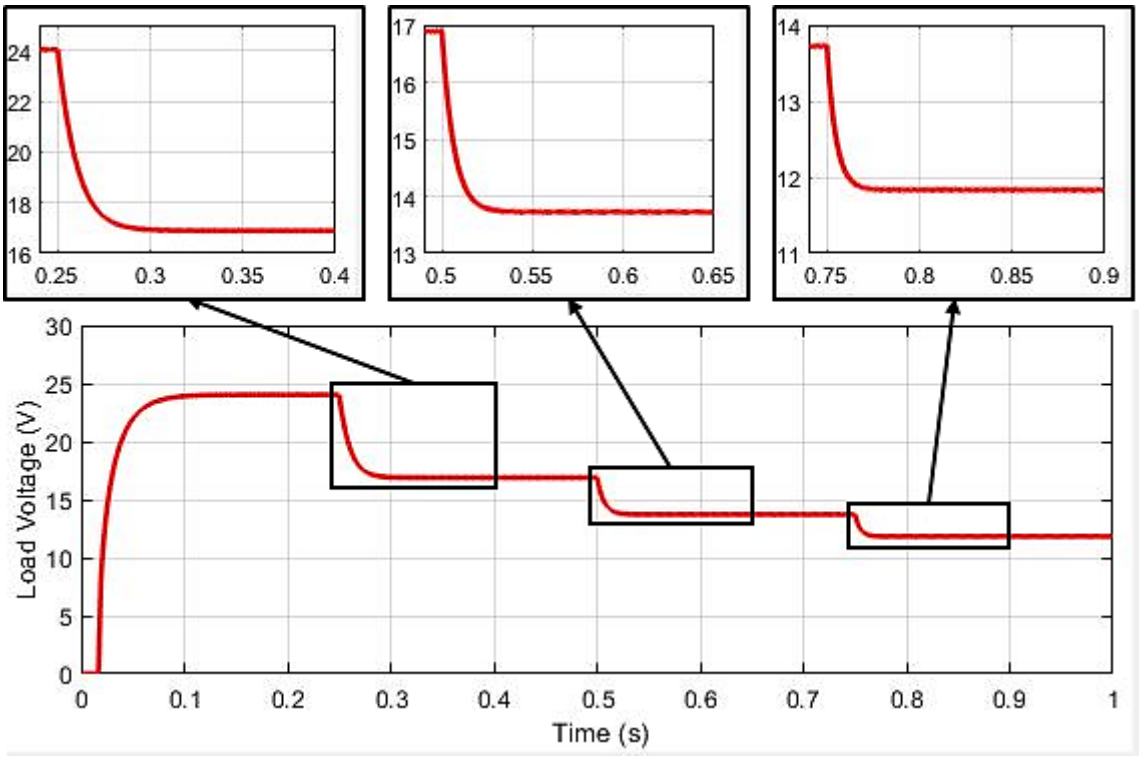


Figure 4.73: Simulation Results of Load Voltage for Predictive Switching State MPPT with Frequency Reduction under Variable Load Resistance

The simulation result of load voltage shows the same pattern as in sections 4.5.1 and 4.5.2. The voltage ripple recorded was between 0.24% and 0.34%.

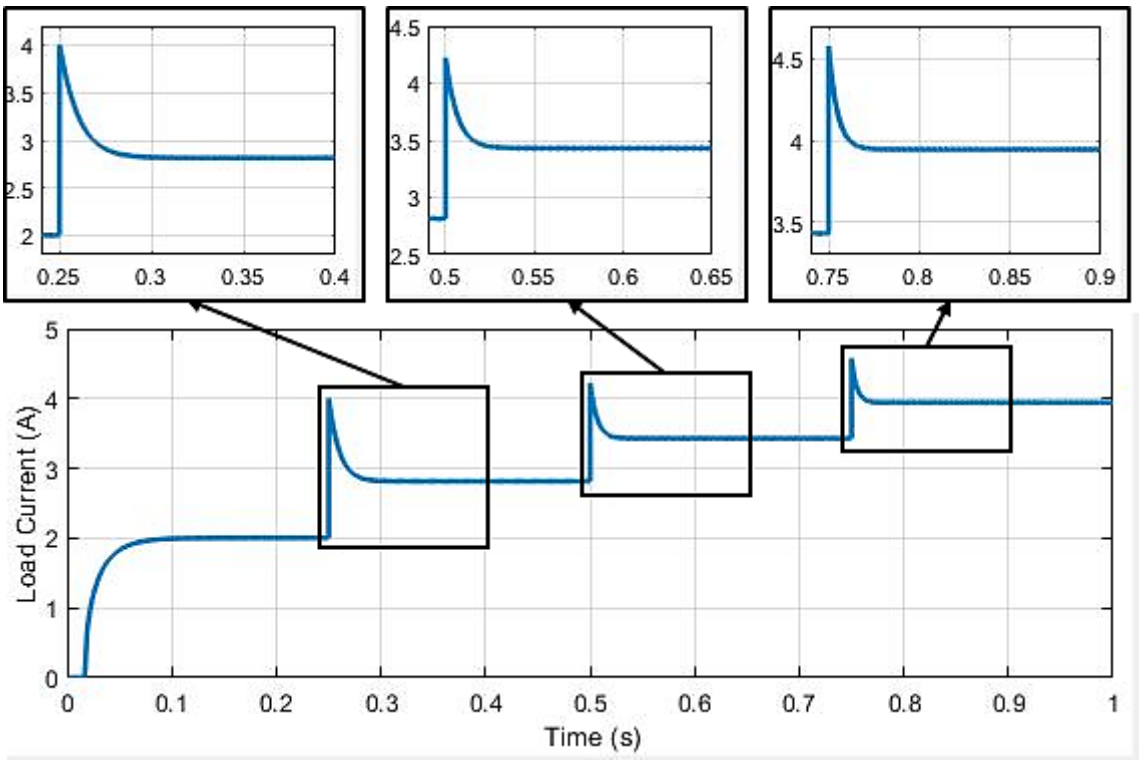


Figure 4.74: Simulation Results of Load Current for Predictive Switching State MPPT with Frequency Reduction under Variable Load Resistance

The simulation result of the behavior load current was different from the load voltage. The load current was increased instead of decreased when the load resistance was decreased. At $0.25s$, the load experienced a 42.17% current overshoot, and the current started to increase to $2.816A$. Then, the current increased to $3.431A$ with a 23.08% of current overshoot at $0.5s$. At $0.75s$, the load experienced another current overshoot of 16.05%, and the current was increased to $3.944A$. When the load resistance was 6Ω, 4Ω, and 3Ω, the current ripple recorded was 0.29%, 0.32%, and 0.37%, respectively.

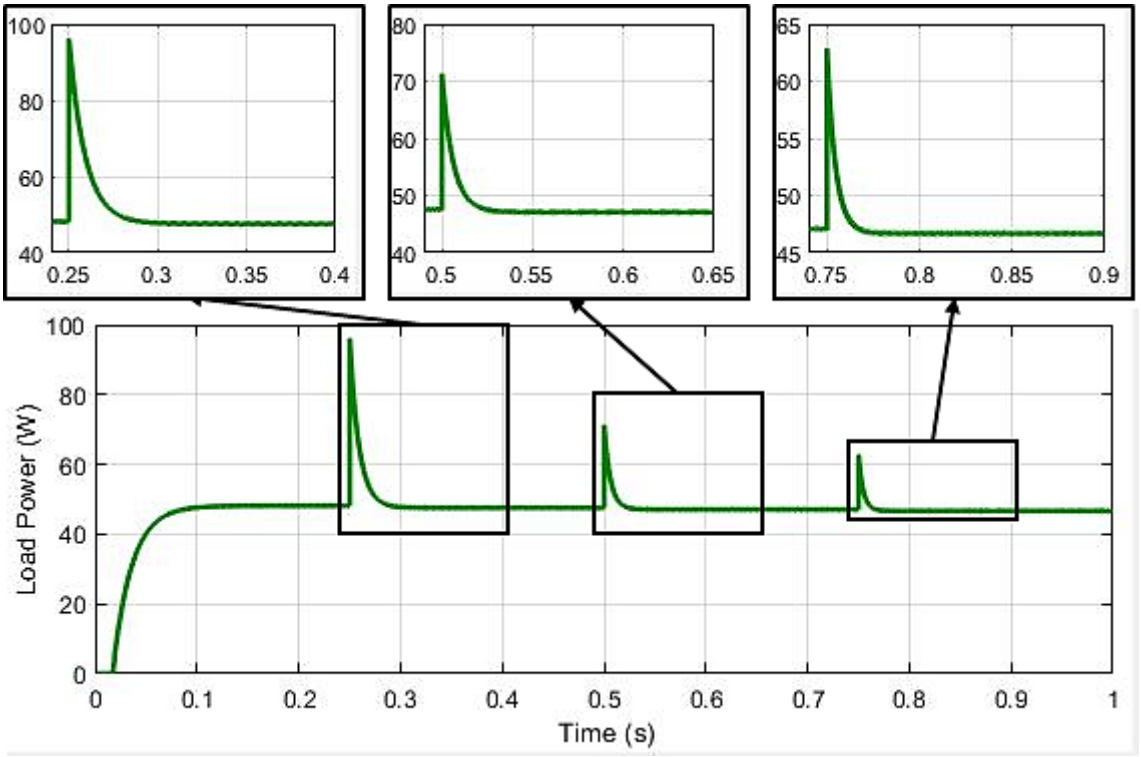


Figure 4.75: Simulation Results of Load Power for Predictive Switching State MPPT with Frequency Reduction under Variable Load Resistance

At $0.25s$, the load experienced 102.22% power overshoot, and the load power was decreased from $48.15W$ to $47.55W$. When the load resistance dropped from 6Ω to 4Ω, the load experienced another 51.54% power overshoot, and the load power dropped to $47.1W$. At $0.75s$, there was a fast variation of load resistance from 4Ω to 3Ω, causing 34.65% of power overshoot. Then, the load power was decreased to $46.7W$. Throughout the simulation, the power ripple recorded was between 0.39% and 0.69%.

4.5.4 Summary of Simulation Results with Variable Load Resistance

The simulation results in Figure 4.56 and Figure 4.63 show that the PEMFC was always generating $50W$ of electrical power even though the load resistance was varied. This was because the PEMFC parameters were constant throughout the simulation. Therefore, the

MPP was not moving to the other point. This means that the change in the load should not affect the PEMFC output power. From the results, all the predictive MPPT methods for PEMFC were able to produce the maximum power with constant PEMFC parameters under variation of load resistance. The results also show that there was no power transient at the PEMFC output power when there was a fast variation of load. The outcome so far has been satisfactory. The performances of all the proposed predictive MPPT techniques are tabulated in Table 4.7.

Table 4.7: Comparison of Proposed Predictive MPPT Techniques under Variable Load Resistance

Comparison	Load Resistance	Predictive Switching State MPPT	Predictive Duty Cycle MPPT	Predictive Switching State MPPT with Frequency Reduction
Accuracy	12Ω	99.88%	99.88%	99.88%
	6Ω	99.88%	99.88%	99.88%
	4Ω	99.88%	99.88%	99.88%
	3Ω	99.88%	99.88%	99.88%
Switching Frequency	12Ω	$\approx 20kHz$	$20kHz$	$\approx 10kHz$
	6Ω	$20kHz$ to $22kHz$	$20kHz$	$10kHz$ to $14kHz$
	4Ω	$17kHz$ to $22kHz$	$20kHz$	$14kHz$ to $18kHz$
	3Ω	$21kHz$ to $24kHz$	$20kHz$	$17kHz$ to $19kHz$
PEMFC Voltage Ripple	12Ω	0.20%	0.15%	0.34%
	6Ω	0.23%	0.37%	0.27%
	4Ω	0.16%	0.34%	0.18%
	3Ω	0.12%	0.24%	0.13%

Table 4.7 continued

PEMFC Current Ripple	12Ω	0.19%	0.15%	0.35%
	6Ω	0.21%	0.37%	0.25%
	4Ω	0.16%	0.35%	0.19%
	3Ω	0.13%	0.24%	0.15%
PEMFC Power Ripple	12Ω	0.0019%	0.0014%	0.0050%
	6Ω	0.0022%	0.0043%	0.0026%
	4Ω	0.0012%	0.0044%	0.0012%
	3Ω	0.0008%	0.0028%	0.0007%

The comparison in Table 4.7 shows that the accuracies of all the predictive MPPT techniques were the same. For power quality, the predictive duty cycle MPPT method performed the best when the load was 12Ω. It has the lowest power ripple within 0.0014% among the other predictive MPPT techniques. However, its power quality was the worst when the total load resistance was below 6Ω. Generally, the predictive switching state MPPT method had the best power quality for the load with ripple below 0.0022%. The predictive switching state MPPT with frequency reduction method is slightly worse than the predictive switching state MPPT method, but its switching frequency is slightly lower than that of the predictive switching state MPPT method. Although the power quality of all the predictive MPPT methods had different performances, the power ripples were extremely low.

When there was a fast variation of load, the electrical power extracted from the PEMFC remained at MPP. This was because the PEMFC parameters were constant. Therefore, the PEMFC should generate the same amount of electrical power. The PEMFC

output power was transmitted to the load through a DC-DC boost converter. Since the PEMFC output power remained at $50W$, the electrical power absorbed by the load should also be maintained at $50W$. This phenomenon is illustrated in Figure 4.60, Figure 4.68, and Figure 4.75. Based on the formula of power shown in Equation 4.4, the load voltage should be reduced when the total load resistance is decreased. Theoretically, the load voltage for 12Ω, 6Ω, 4Ω and 3Ω loads are $24.49V$, $17.32V$, $14.14V$ and $12.25V$ respectively. For load current, it should be $2.04A$, $2.89A$, $3.54A$ and $4.08A$ respectively. This phenomenon also fulfils the Ohm's Law. The simulation results in Figure 4.58, Figure 4.59, Figure 4.66, Figure 4.67, Figure 4.73, and Figure 4.74 also show the scenarios explained.

Based on Equation 3.27, the DC-DC boost converter regulates the output voltage with a reciprocal function of the duty cycle. As discussed, for a constant power electrical system, the load voltage will be reduced when the total load resistance is decreased. Due to the constant PEMFC output voltage, the decreasing load voltage will minimize the ratio between the input and output voltage of the boost converter. Therefore, the duty cycle will be decreased when the total load resistance is decreased. This phenomenon can also be observed in the simulation results in Figure 4.64.

For the load power quality, the performances for both predictive MPPT by switching state and duty cycle are compared in Table 4.8.

Table 4.8: Comparison of Load Power Quality under Variable Load Resistance

Comparison	Total Load Resistance	Predictive Switching State MPPT	Predictive Duty Cycle MPPT	Predictive Switching State MPPT with Frequency Reduction
Load Power	12Ω	$48.15W$	$48.15W$	$48.15W$
	6Ω	$47.55W$	$47.55W$	$47.55W$
	4Ω	$47.10W$	$47.10W$	$47.10W$
	3Ω	$46.70W$	$46.70W$	$46.70W$
Settling Time	12Ω to 6Ω	$0.06s$	$0.06s$	$0.06s$
	6Ω to 4Ω	$0.04s$	$0.04s$	$0.04s$
	4Ω to 3Ω	$0.35s$	$0.35s$	$0.35s$
Load Current Overshoot	12Ω to 6Ω	42.27%	42.25%	42.17%
	6Ω to 4Ω	22.99%	23.02%	23.08%
	4Ω to 3Ω	15.91%	15.91%	16.05%
Load Power Overshoot	12Ω to 6Ω	102.49%	102.45%	102.22%
	6Ω to 4Ω	51.31%	50.38%	51.54%
	4Ω to 3Ω	34.33%	34.33%	34.65%
Load Voltage Ripple	12Ω	0.11%	0.08%	0.2%
	6Ω	0.24%	0.40%	0.28%
	4Ω	0.28%	0.58%	0.32%
	3Ω	0.27%	0.53%	0.34%

Table 4.8 continued

Load Current Ripple	12Ω	0.11%	0.08%	0.19%
	6Ω	0.24%	0.39%	0.29%
	4Ω	0.28%	0.58%	0.32%
	3Ω	0.27%	0.55%	0.37%
Load Power Ripple	12Ω	0.23%	0.17%	0.39%
	6Ω	0.47%	0.82%	0.55%
	4Ω	0.56%	1.17%	0.64%
	3Ω	0.55%	1.10%	0.69%

Table 4.8 shows that all the proposed predictive MPPT techniques had the same load power consumption, settling time, load current, and power overshoot issues. However, the comparison of the load voltage, current, and power ripple in Table 4.8 shows that the predictive duty cycle MPPT method was around two times higher than the predictive switching state MPPT method. However, its power quality for the load with 12Ω resistance was the best. For predictive switching state MPPT with frequency reduction method, the power ripple is slightly higher than that of the predictive switching state MPPT method. In summary, all the proposed predictive MPPT methods are robust to the load resistance changes. The predictive switching state MPPT method has the best performance with lower power ripple, but it requires a higher switching frequency.

The table also shows that the load consumption was $48.1W$, $47.6W$, $47.1W$, and $46.7W$ when the load resistance was 12Ω, 6Ω, 4Ω, and 3Ω, respectively. It means that the load consumed 96.2%, 95.2%, 94.2%, and 93.4% of the electrical power, respectively,

from the PEMFC. Based on available data, it can be proposed that the lower the load resistance, the higher the electrical power loss to the DC-DC boost converter.

During the change in load resistance, there were load current and power overshoots found. When the load resistance dropped instantly, the load voltage did not drop rapidly. This was because the capacitor inside the DC-DC boost converter opposes the voltage changes. The same scenario is explained in section 4.4.4. According to Ohm's Law, when the resistance is decreased with an unchanged voltage, the current should increase. Since the total load resistance was suddenly decreased while the voltage was still maintained at a high level, the changes must be falling on the load current. This caused the load current overshoot and power transient to occur.

By carefully examining the data, it is found that the output current will overshoot if the total load resistance is changed from high to low. The current raised can be estimated from the ratio of resistance changes. At $0.25s$, the load resistance was changed from 12Ω to 6Ω. The initial resistance was two times greater than the resistance after 0.25s. It is found that the current overshot is two times higher than the initial current. The same phenomenon also occurred at $0.5s$ and $0.75s$.

From Table 4.8, the time required to regulate the load voltage was $0.6s$, $0.4s$, and $0.35s$ at the first, second, and third resistance changes. The discharging of the capacitor is explained in Section 4.4.4, and its behavior follows the formula shown in Equation 4.7. Based on Figure 4.58, Figure 4.66, and Figure 4.73, the estimated capacitor time constants at $0.25s$, $0.5s$, and $0.75s$ were $0.0102s$, $0.0065s$, and $0.0049s$. From these results, it can be deduced that the capacitor time constant decreased when the load resistance was decreased. This is because the capacitor time constant is equal to the product of the resistance

value and the capacitance value. So, a lower resistance value will result in a lower capacitor time constant and cause the time required for the voltage to achieve the steady state to become faster.

4.6 Simulation with Variable AC Load

In the previous section, all the simulations were done by extracting the maximum power from the PEMFC to the load without the voltage control technique. The load absorbed the DC electrical power directly after the power regulation by the DC-DC boost converter. This section provides the simulation results of tracking the MPP of the PEMFC, and it involves the voltage control technique at the load side. The purpose of including the predictive voltage control technique is to invert the DC power from the PEMFC to become a stable AC power. It supplies and maintains an AC voltage with constant rms voltage and frequency to the load. In this simulation, the AC voltage was set to $12V_{rms}$ with $50Hz$ of frequency. To validate the robustness of the predictive voltage control technique, the changes of load resistance in Section 4.5 was duplicated.

Since the load voltage is constant, the power consumed by the load should follow Equation 4.4, and it depends on the load resistance. However, the electrical energy produced by the PEMFC must be consumed. To solve this problem, the fuel control algorithm is explained in Section 3.9.3. For the simulation in this section, the reference voltage setting for the capacitor is $80V$. The purpose of this algorithm to supply a suitable amount of fuel to the PEMFC for generating sufficient power to the load. As discussed in Sections 4.4 and 4.5, all the proposed predictive MPPT can track the MPP for any changes in the input flow rate of the fuel and the total load resistance. In this section, the input flow rate of hydrogen

and oxygen gases was adjusted to match the power consumption of the load. Then, the predictive MPPT methods kept tracking the MPP for all variations of the fuel.

4.6.1 Simulation by Predictive Switching State MPPT with Voltage Control Method

Since the PEMFC output power was controlled by the input flow rate of the fuel, the input flow rate of hydrogen and oxygen gases, and the PEMFC output power are presented in Figure 4.76.

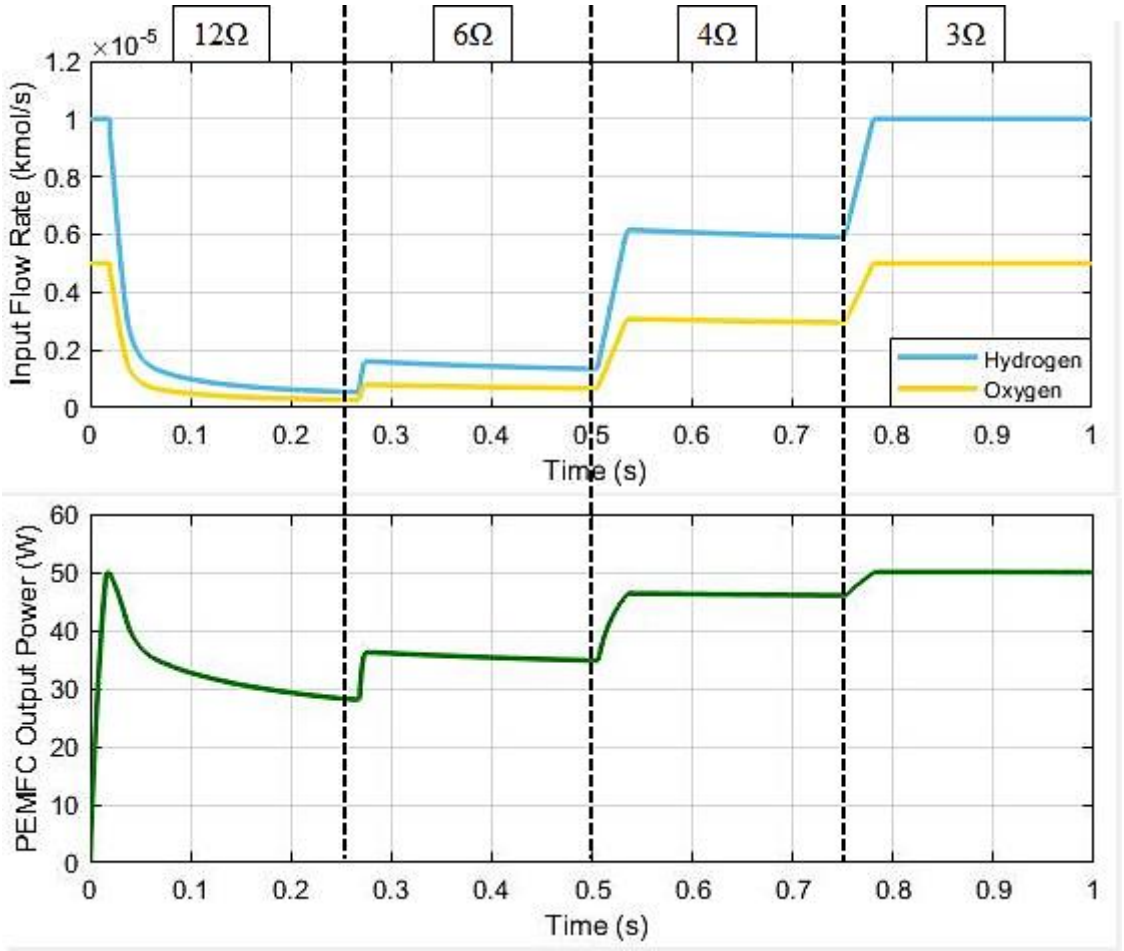


Figure 4.76: Simulation Results of PEMFC for Predictive Switching State MPPT with Voltage Control Technique

At first, the input flow rate of hydrogen gas was $10^{-5}\ kmol\ s^{-1}$ and it dropped to below $10^{-6}\ kmol\ s^{-1}$ after $0.1s$. The PEMFC output power dropped to below $30W$ before $0.25s$. This is because the total power consumption of the load was low. The fuel control algorithm regulated the flow rate of the hydrogen and oxygen gases to decrease the output power of the PEMFC. When the total load resistance was decreased to 6Ω, 4Ω, and 3Ω, the hydrogen input flow rate was raised to $1.5 \times 10^{-6}\ kmol\ s^{-1}$, $6 \times 10^{-6}\ kmol\ s^{-1}$ and $10^{-5}\ kmol\ s^{-1}$ respectively. At the same time, the PEMFC output power was increased to $35W$, $46W$, and $50W$, respectively. The power ripple recorded was between 0.0053% and 0.014%.

Before the electrical power was consumed by the load, the DC voltage was boosted through the DC-DC boost converter. Therefore, the boosted voltage can be measured from the potential difference of the capacitor inside the DC-DC boost converter. Since the reference voltage setting for the capacitor voltage was $80V$, the capacitor voltage should approach $80V$. Figure 4.77 illustrates the voltage, current, and power of the capacitor.

From the simulation results, the rate of change of capacitor voltage was different every $0.25s$. This was because the changing of the PEMFC output power and the load resistance affected the energy flow of the capacitor. Before $0.75s$, the capacitor voltage was approaching $80V$. However, the capacitor voltage dropped after $0.75s$. This means that the input power was greater than the load power consumption before $0.75s$, but it was insufficient for the load consumption after $0.75s$. The capacitor current was varying between $-7.2A$ and $17A$. In addition, the capacitor power varied between $-470W$ and $1090W$. The positive current indicates the capacitor was charging, while the negative current indicates the discharging of the capacitor. Similarly, the capacitor absorbed the electrical energy when

the capacitor power was positive. It released energy when the capacitor power was negative. These simulation results show that the capacitor was charged and discharged rapidly.

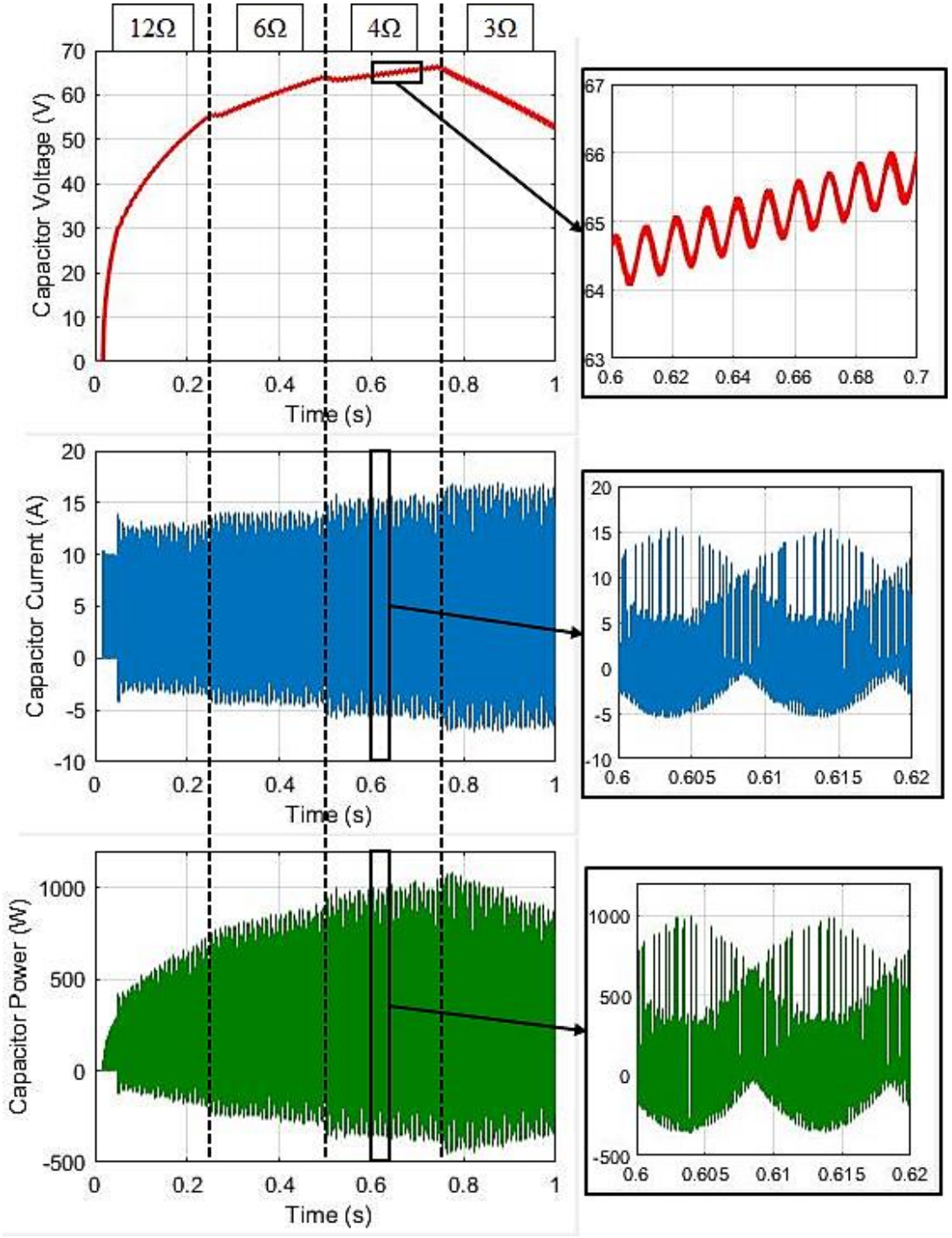


Figure 4.77: Simulation Results of Capacitor Behaviour for Predictive Switching State MPPT with Voltage Control Technique

After the DC voltage was boosted, the predictive voltage control technique inverted the DC voltage to an AC voltage. A stable AC voltage with a constant rms value and frequency was supplied to the load. Figure 4.78 presents the load voltage, current, and power.

From Figure 4.78, the load absorbed the electrical power with a constant AC voltage supply. The load voltage simulation results show that the predictive voltage control inverted the capacitor voltage to a sinusoidal AC voltage with $50Hz$ frequency. The voltage amplitude was maintained at $17V$ which gives a rms value of $12V$. It is exactly the value as the setting value mentioned in section 4.6. The amplitude of the load voltage was unchanged even though the load resistance was dropped from high to low. When the total load resistance was reduced, the load current and power were increased. The rms load current recorded was $1A$, $2A$, $3A$, and $4A$ when the load resistance was 12Ω, 6Ω, 4Ω, and 3Ω respectively. For load power, the average power recorded was $12W$, $24W$, $36W$, and $48W$ respectively. The highest THD recorded was 1.6% between $0.05s$ and $0.075s$. After that, the THD was dropped to below 0.6%.

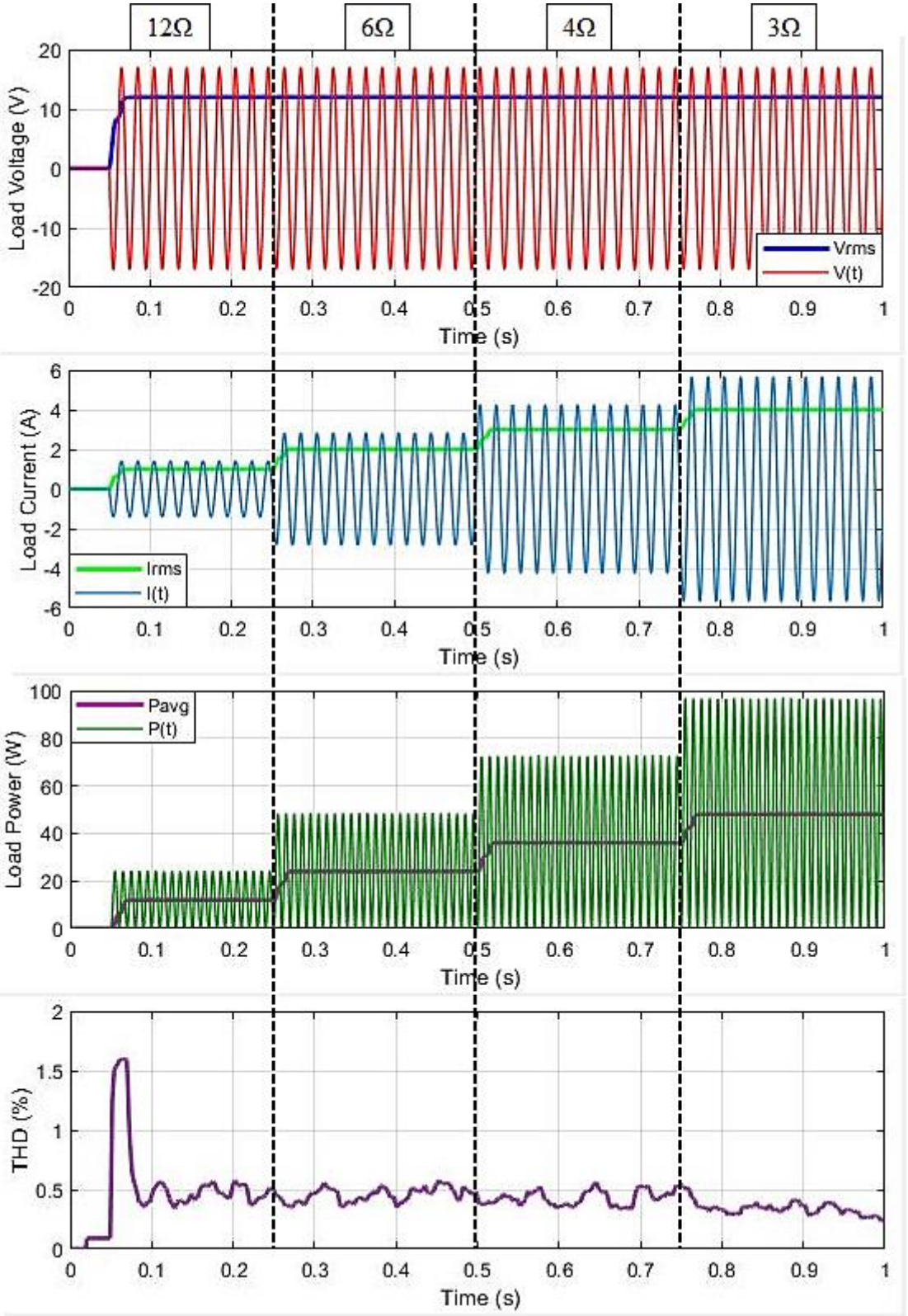


Figure 4.78: Simulation Results of Load for Predictive Switching State MPPT with Voltage Control Technique

4.6.2 Simulation by Predictive Duty Cycle MPPT with Voltage Control Method

In this section, the simulation in the previous section was repeated by replacing the predictive switching state MPPT method with the predictive duty cycle MPPT method. In this simulation, the predictive duty cycle MPPT with $20kHz$ switching frequency was merged with the voltage control technique. The simulation results of the PEMFC are shown in Figure 4.79.

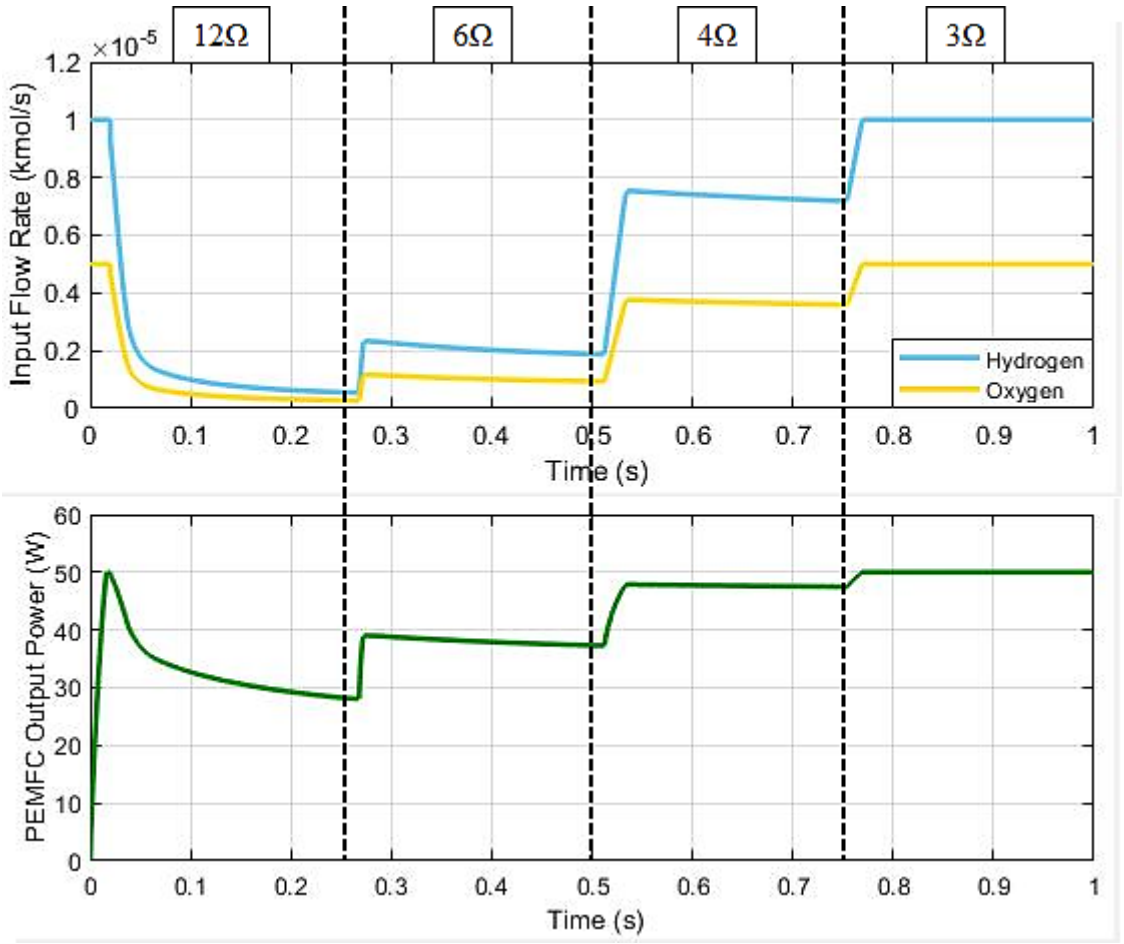


Figure 4.79: Simulation Results of PEMFC for Predictive Duty Cycle MPPT with Voltage Control Technique

Same as the previous simulation, the PEMFC output power depended on the load power consumption. When the load power consumption was low, the fuel control algorithm

limited the flow rate of the fuel to reduce the PEMFC output power. On the contrary, the input flow rate of the fuel was maximized when the load power consumption was high. When the total load resistance was 6Ω and 4Ω, the PEMFC output power was slightly higher than that of the predictive switching state MPPT technique. The power ripple recorded was between 0.0153% and 0.0509%.

Next, Figure 4.80 shows the simulation results of the capacitor voltage, current, and power of the DC-DC boost converter. The capacitor voltage was always increasing before $0.75s$ because the PEMFC output power was greater than the load power consumption. For the predictive duty cycle MPPT method, the capacitor voltage during the period between $0.25s$ and $0.75s$ is slightly higher than the predictive switching state MPPT method. This was due to the higher PEMFC output power generation when the load resistance was 6Ω. The capacitor current was alternated between $-7.3A$ and $17.3A$ while the power fluctuated between $-510W$ and $1180W$.

Figure 4.81 recorded similar simulation results to Figure 4.78. The predictive voltage control inverted the capacitor voltage to a sinusoidal AC voltage. The AC voltage with rms $12V$ and $50Hz$ frequency was transmitted to the load. The load absorbed an average power of $12W$, $24W$, $36W$, and $48W$ when the load resistance was 12Ω, 6Ω, 4Ω, and 3Ω respectively. The THD were mostly lower than 0.8% and the highest THD recorded was 1.6% between $0.05s$ and $0.075s$.

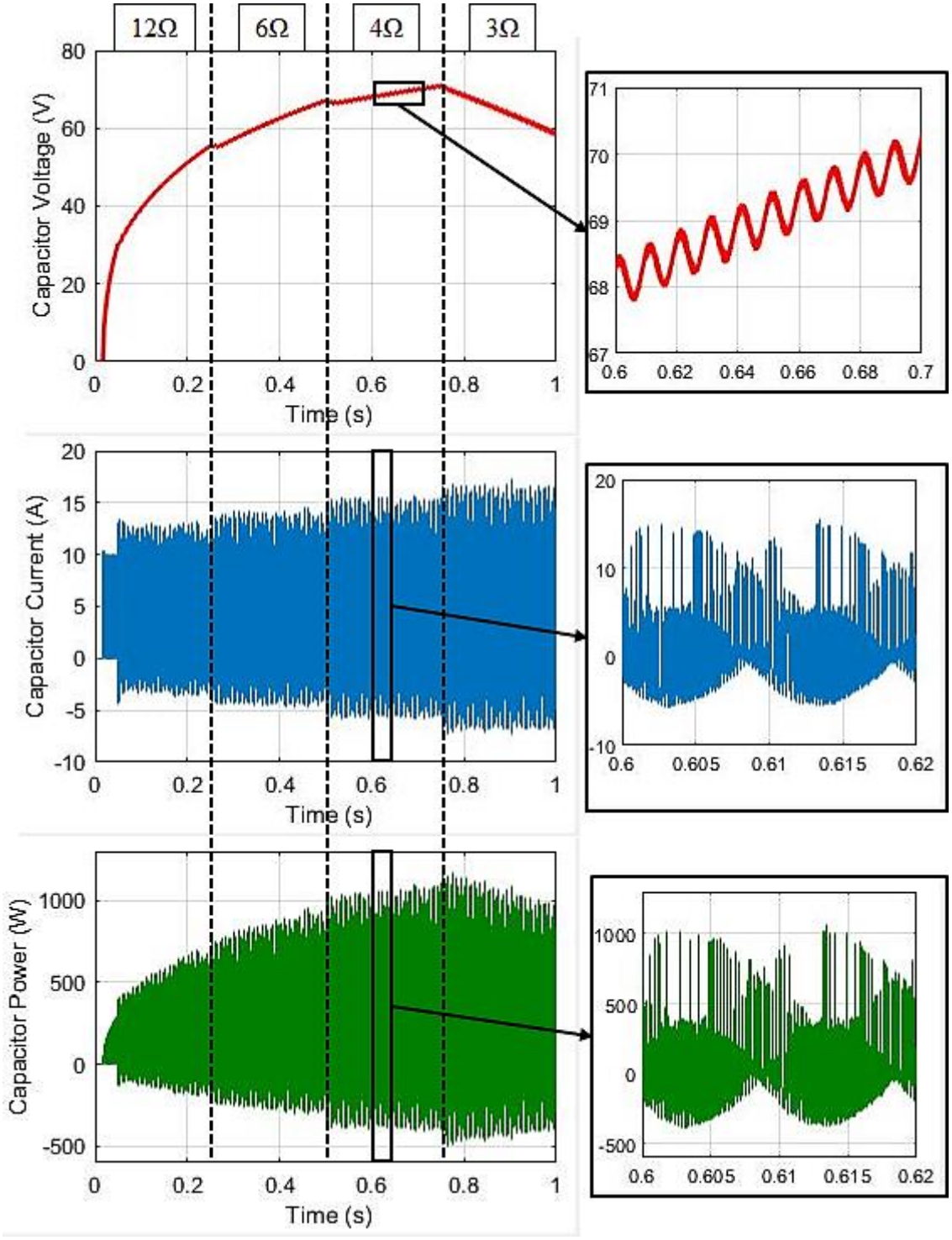


Figure 4.80: Simulation Results of Capacitor Behaviour for Predictive Duty Cycle MPPT with Voltage Control Technique

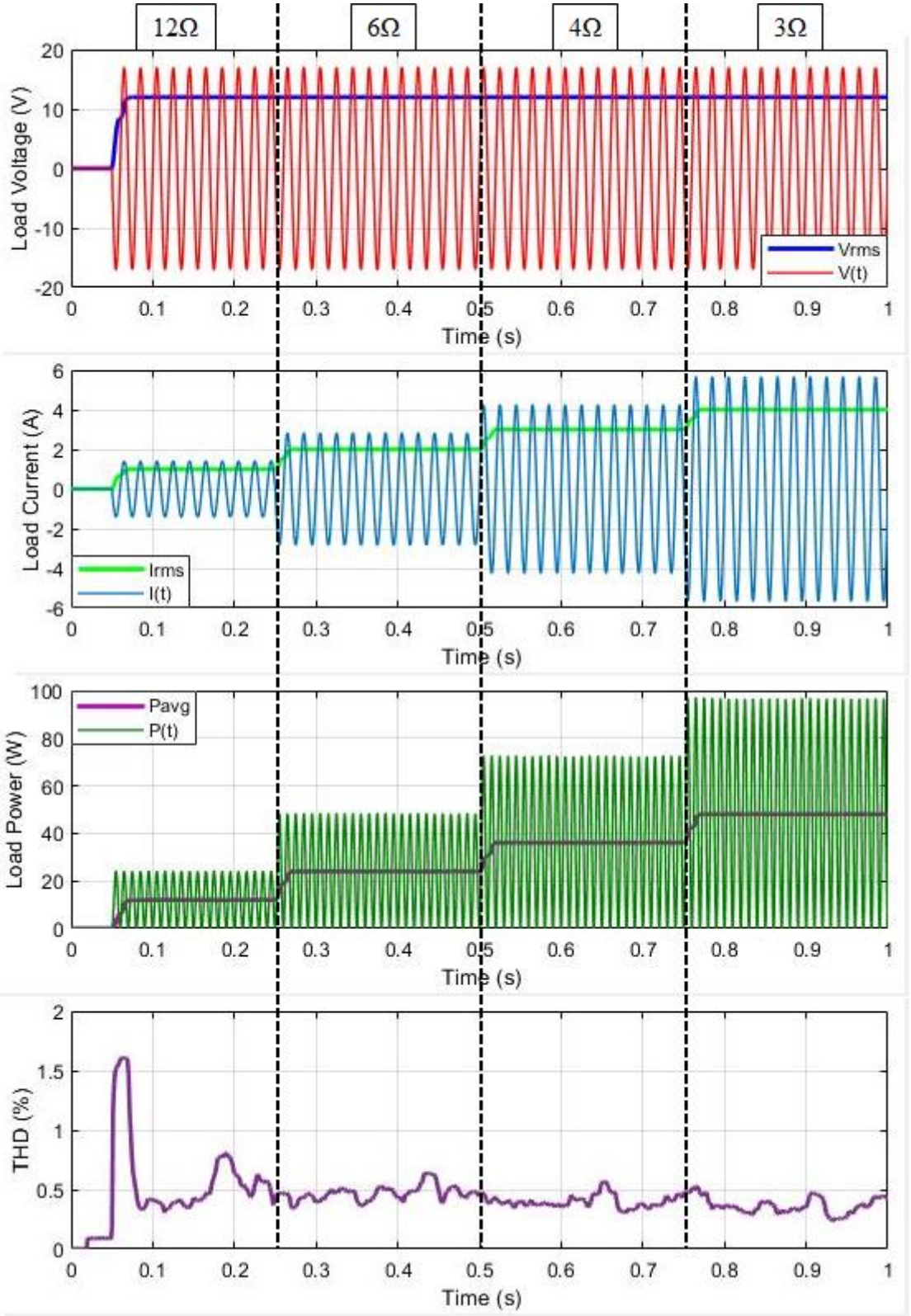


Figure 4.81: Simulation Results of Load for Predictive Duty Cycle MPPT with Voltage Control Technique

4.6.3 Simulation by Predictive Switching State MPPT with Frequency Reduction and Voltage Control Method

This section also repeats the simulation in section 4.6.1 with an additional 0.3 weighting factor of the switching frequency reduction technique. The simulation results of PEMFC are presented in Figure 4.82.

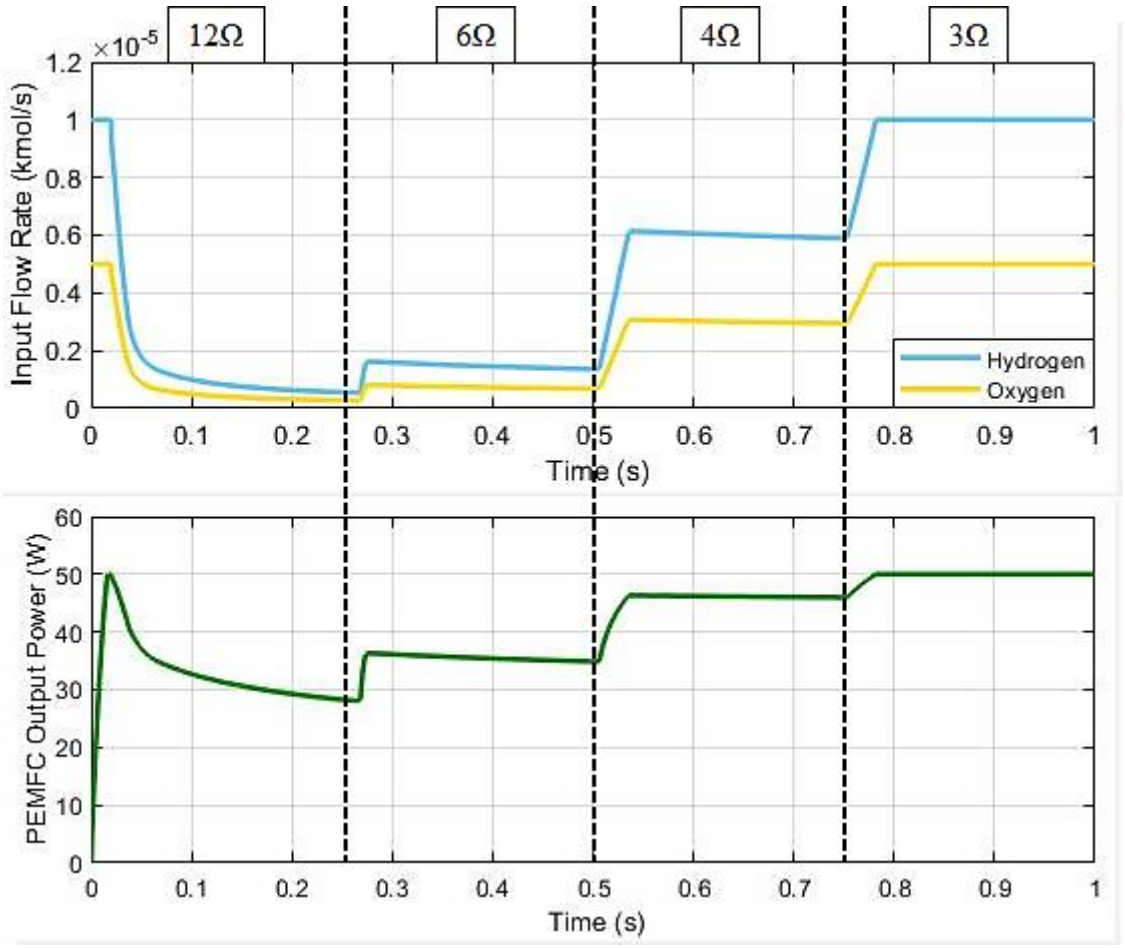


Figure 4.82: Simulation Results of PEMFC for Predictive Switching State MPPT with Frequency Reduction and Voltage Control Technique

For the predictive switching state MPPT with frequency reduction method, the simulation results were almost the same as those of the predictive switching state MPPT

method. However, its power ripple was slightly higher than that of the predictive switching state MPPT method. The power ripple recorded was between 0.0082% and 0.024%.

For the simulation results of the capacitor, the capacitor voltage had the same behavior as the simulation results in Figure 4.77. The minimum and maximum capacitor currents were $-7.1A$ and $17A$ respectively. The capacitor power fluctuated between $-470W$ and $1190W$. The simulation results of the capacitor voltage, current, and power of the DC-DC boost converter are presented in Figure 4.83.

The AC voltage supplied to the load was a sinusoidal waveform and always at rms value of $12V$ with $50Hz$ frequency. The rms load current increased when the load resistance was increased. This caused the average power to be increased. The simulation results were also the same as the results of applying the predictive switching state MPPT method and the predictive duty cycle MPPT method. The THD recorded was almost the same as the predictive duty cycle MPPT method. Figure 4.84 shows the simulation results of the load.

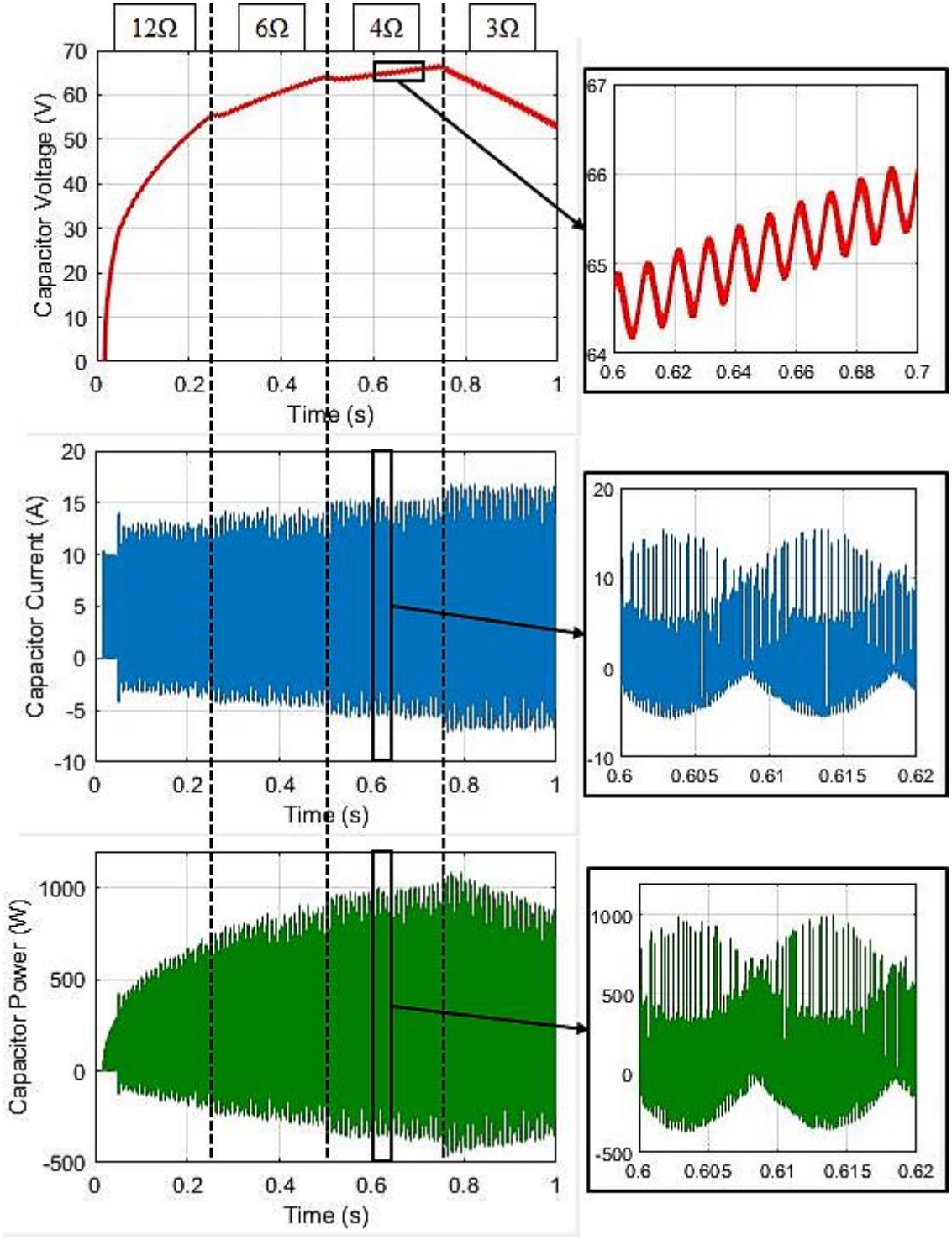


Figure 4.83: Simulation Results of Capacitor Behaviour for Predictive Switching State MPPT with Frequency Reduction and Voltage Control Technique

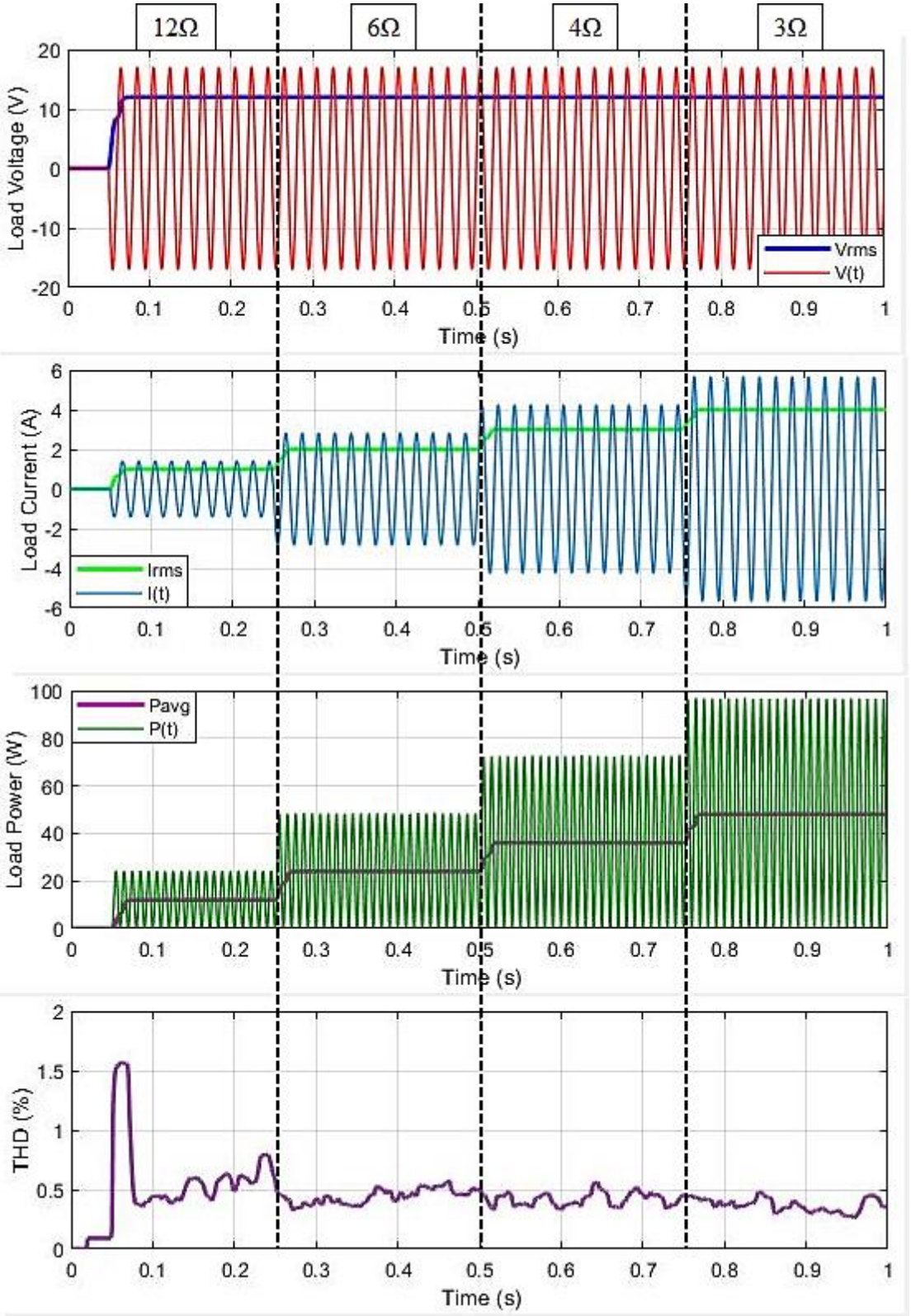


Figure 4.84: Simulation Results of Load for Predictive Switching State MPPT with Frequency Reduction and Voltage Control Technique

4.6.4 Summary of Simulation by Predictive MPPT and Voltage Control Techniques

Figure 4.76, Figure 4.79, and Figure 4.82 show that the input flow rate of the hydrogen was $10^{-5} kmol\ s^{-1}$ at the beginning of the simulation. This was because the initial flow rate of the hydrogen was set as $10^{-5} kmol\ s^{-1}$. In addition, the initial capacitor voltage was $0V$. Therefore, the PEMFC generate the maximum power to charge the capacitor. Then, the input flow rate of the fuel was decreased when the capacitor started to be charged. The PEMFC output power dropped to the lowest value when the total load resistance was the highest. This finding arises from the fact that the high load resistance required low power consumption. Therefore, the fuel control algorithm limited the fuel to lower the PEMFC output power so that the power matched the power consumption while charging the capacitor. When the total load resistance was decreased, the fuel controller supplied more fuel to the PEMFC so that more power could be generated from the PEMFC. The purpose of increasing the PEMFC output power was to provide sufficient power to the load while charging the capacitor.

Figure 4.77, Figure 4.80, and Figure 4.83 show that the capacitor voltage seems like a sinusoidal waveform with a frequency of $100Hz$. This was because the predictive voltage controller inverted the DC power from the capacitor to become an AC power. At the load side, the load power graphs shown in Figure 4.78, Figure 4.81, and Figure 4.84 also have the same frequency waveform. It can be deduced that the increase in the load power will decrease the capacitor voltage due to the power transfer from the capacitor to the load.

The capacitor experienced rapid charge and discharge during the power conversion. The minimum and maximum capacitor power recorded were $-510W$ and $1190W$, respectively. It seems like the energy absorbed by the capacitor was much higher than the

PEMFC output power. However, the energy absorption and energy release are instantaneous. The peak power of the capacitor was caused by the sum of the power distributed from the PEMFC and the reverse power transmitted from the AC power converter. The simulation result of the power distributed to the capacitor and AC power inverter is shown in Figure 4.85.

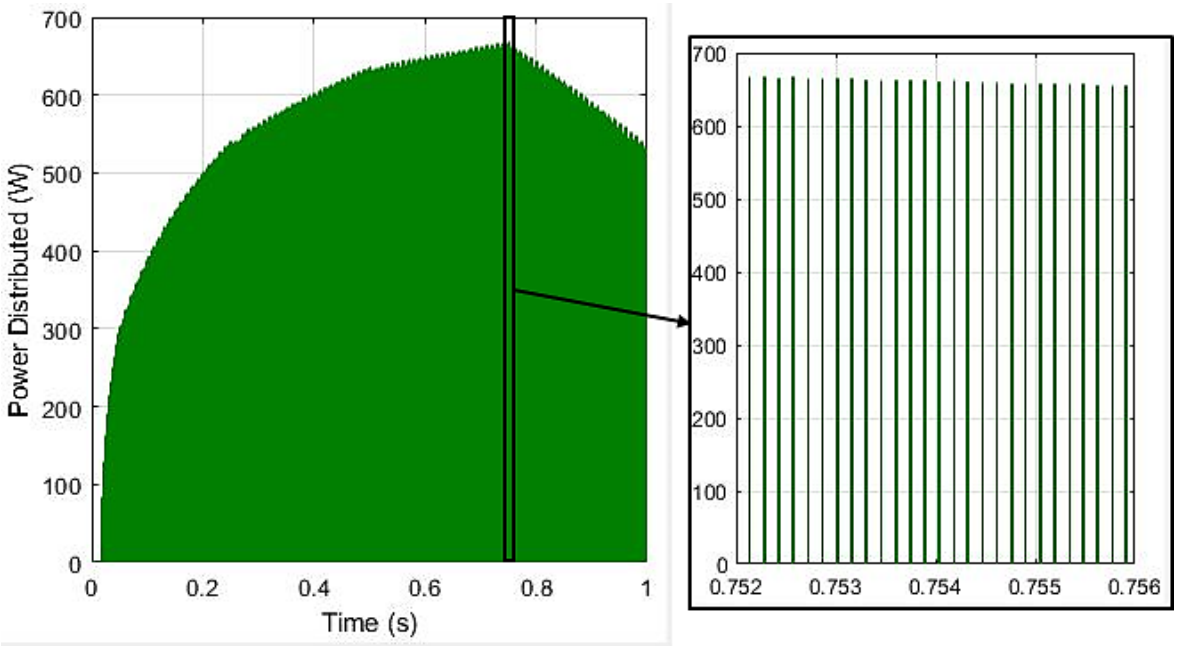


Figure 4.85: Simulation Results of Electrical Power Distributed to Capacitor and AC Power Converter

As discussed in Section 4.3.4, the power distributed from the PEMFC was divided into multiple portions of energy, which is shown in Figure 4.28. In this section, the same phenomenon occurred due to the switching cycle of the switch controlled by the predictive MPPT controller. The power distribution was not stable because the PEMFC output power was regulated to maintain the capacitor voltage at the set value. However, the area under the graph was always approximately the same as the energy that was continuously supplied $50W$ of power. Based on Equation 4.3, when the power was increased, the time for the

switch to OFF must be reduced to supply the same amount of energy. On the other side, the AC power converter may not always receive the electrical energy from the DC-DC boost converter, but sometimes it returns a smaller portion of energy to the DC-DC boost converter. The simulation result of the DC-DC boost converter output power is displayed in Figure 4.86.

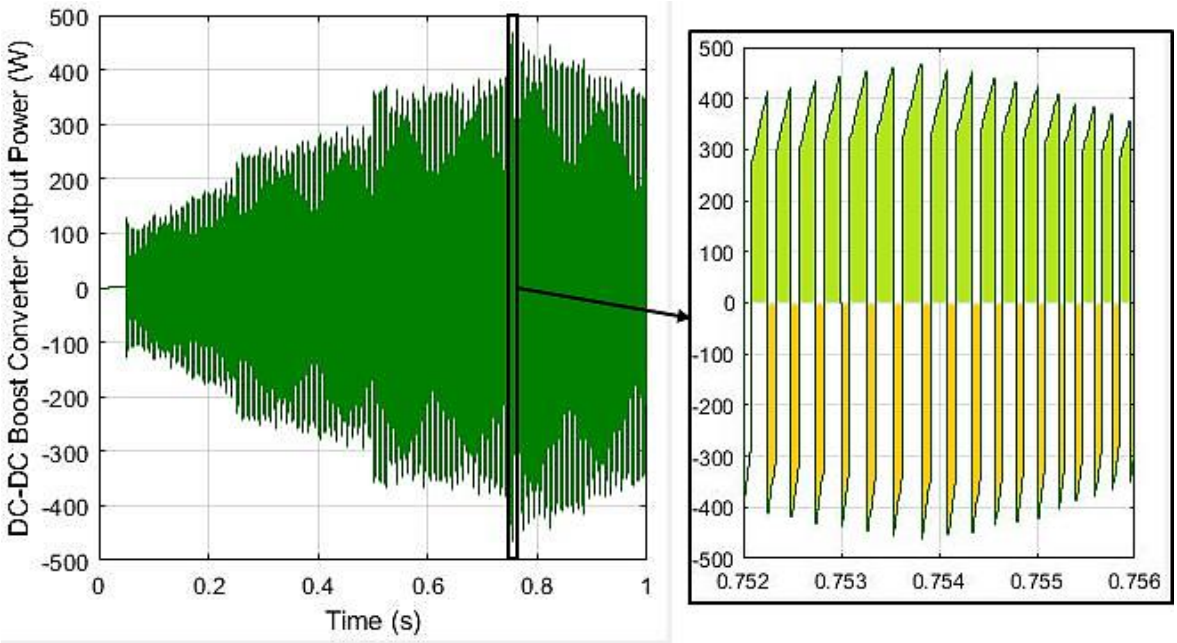


Figure 4.86: Simulation Results of DC-DC Boost Converter Output Power

In Figure 4.86, the positive value indicates the power transmitted to the H-bridge inverter, while the negative value indicates the returned power from the AC power converter. The simulation result clearly shows that the electrical power was supplied and returned alternately. This was because the secondary filter in the H-bridge inverter required some regulation in controlling a stable AC voltage. If the capacitor voltage of the secondary filter is higher than expected, the energy must be released to lower the capacitor voltage. The electrical energy can be determined by estimating the area under the graph to the Time-axis.

By carefully observing the graph, the output power of the DC-DC boost converter had a larger positive area than the negative area under the graph. It means that the DC-DC boost converter was supplying more energy than it was receiving. This phenomenon is expected because the load was consuming the electrical energy through the AC power converter.

From Figure 4.85 and Figure 4.86, the peak power of the capacitor occurred when the energy was returned to the DC-DC boost converter, and the switch of the DC-DC boost converter was OFF. At this moment, the total capacitor current was the sum of both incoming currents, resulting in an instantaneous peak current. The current flow inside the DC-DC boost converter is depicted in Figure 4.87.

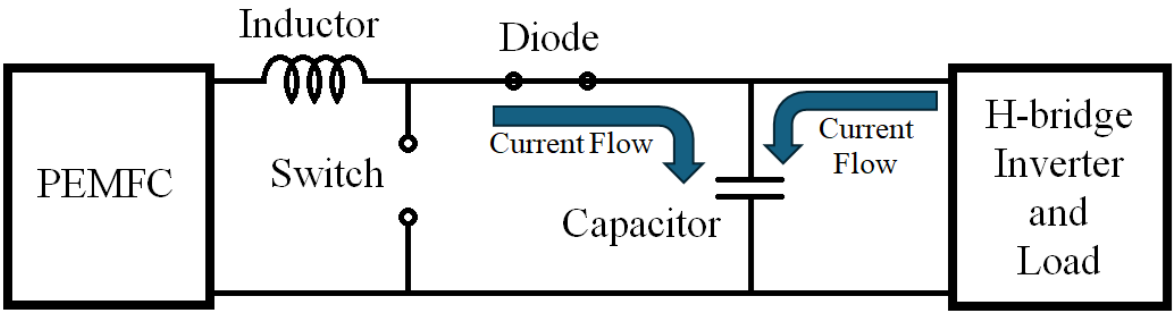


Figure 4.87: Current Flow in DC-DC Boost Converter when Peak Capacitor Current Occurs

When the capacitor voltage and current were high, the peak capacitor power occurred instantaneously. However, the capacitor charged and discharged rapidly. Averagely, the capacitor power was $17W$, $6.7W$, $2.5W$, and $-9.5W$ when the total load resistance was 12Ω, 6Ω, 4Ω, and 3Ω respectively. Figure 4.88 illustrates the PEMFC output power, load power consumption, and the average capacitor power. The power consumption by the load was inverted to a negative value to show a clearer comparison.

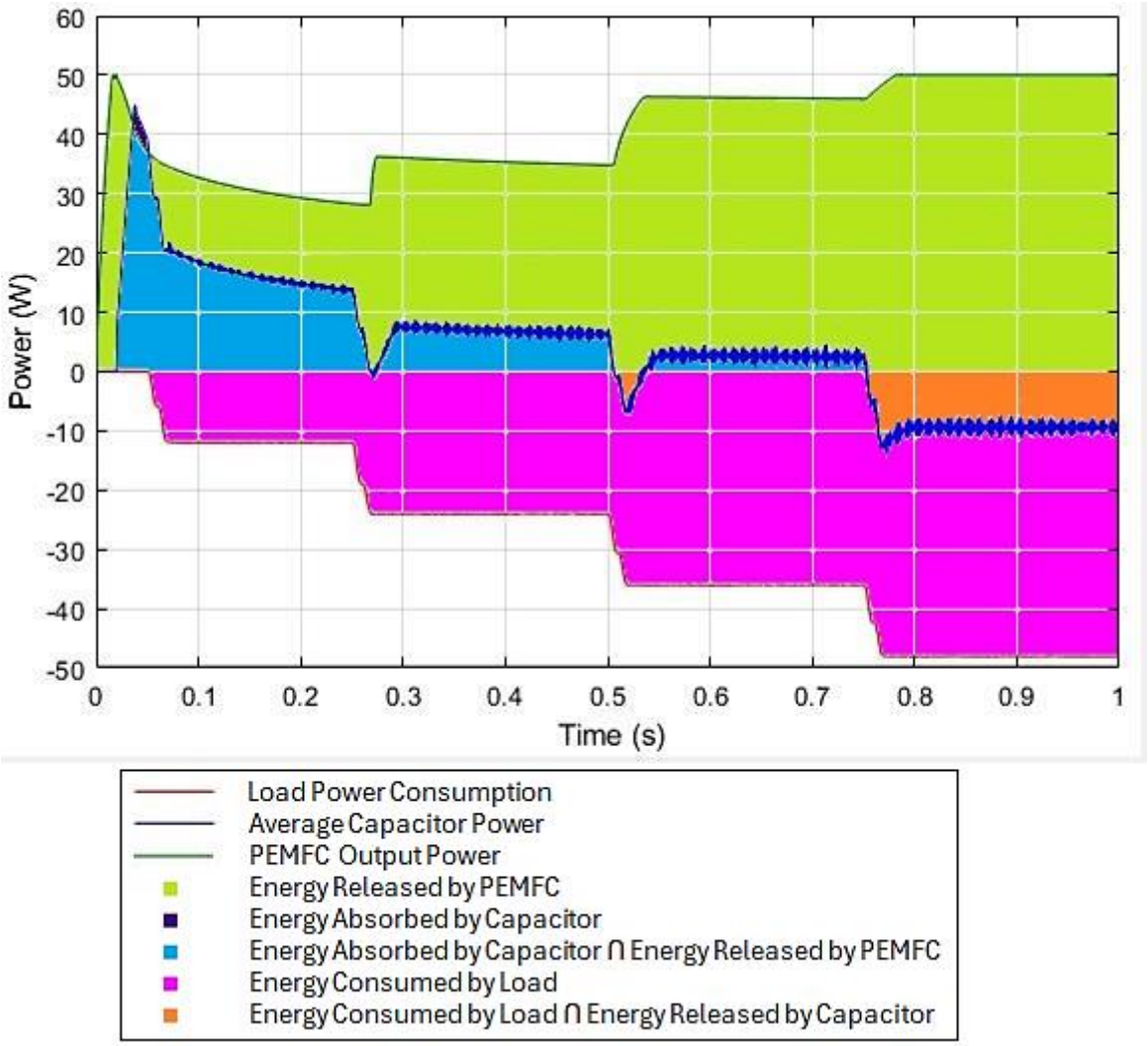


Figure 4.88: Simulation Results of PEMFC Output Power, Load Power Consumption, and Average Capacitor Power

Before $0.75s$, the PEMFC output power was higher than the load power consumption. Therefore, the capacitor could absorb the electrical power from the PEMFC. After $0.75s$, the total resistance dropped to 3Ω. Although the simulation results show the PEMFC output power was sufficient for the load consumption, it required more power for the secondary filter at the H-bridge inverter due to a higher load current. This situation led to the total power consumption being greater than the PEMFC output power. In this case, the capacitor released electrical energy to supply the stable AC power to the load.

Figure 4.77, Figure 4.80, and Figure 4.83 also illustrate that the capacitor voltage was increasing before $0.75s$. It means that the capacitor was charged, and it was absorbing power more than releasing power. At this period, the capacitor voltage was approaching the reference voltage at $80V$. If there was no changing for the total load resistance, the capacitor voltage will keep approaching to the reference voltage. Figure 4.89 shows a three-second simulation result for the fuel control to the effect of capacitor behavior when the constant load resistance of 12Ω was set.

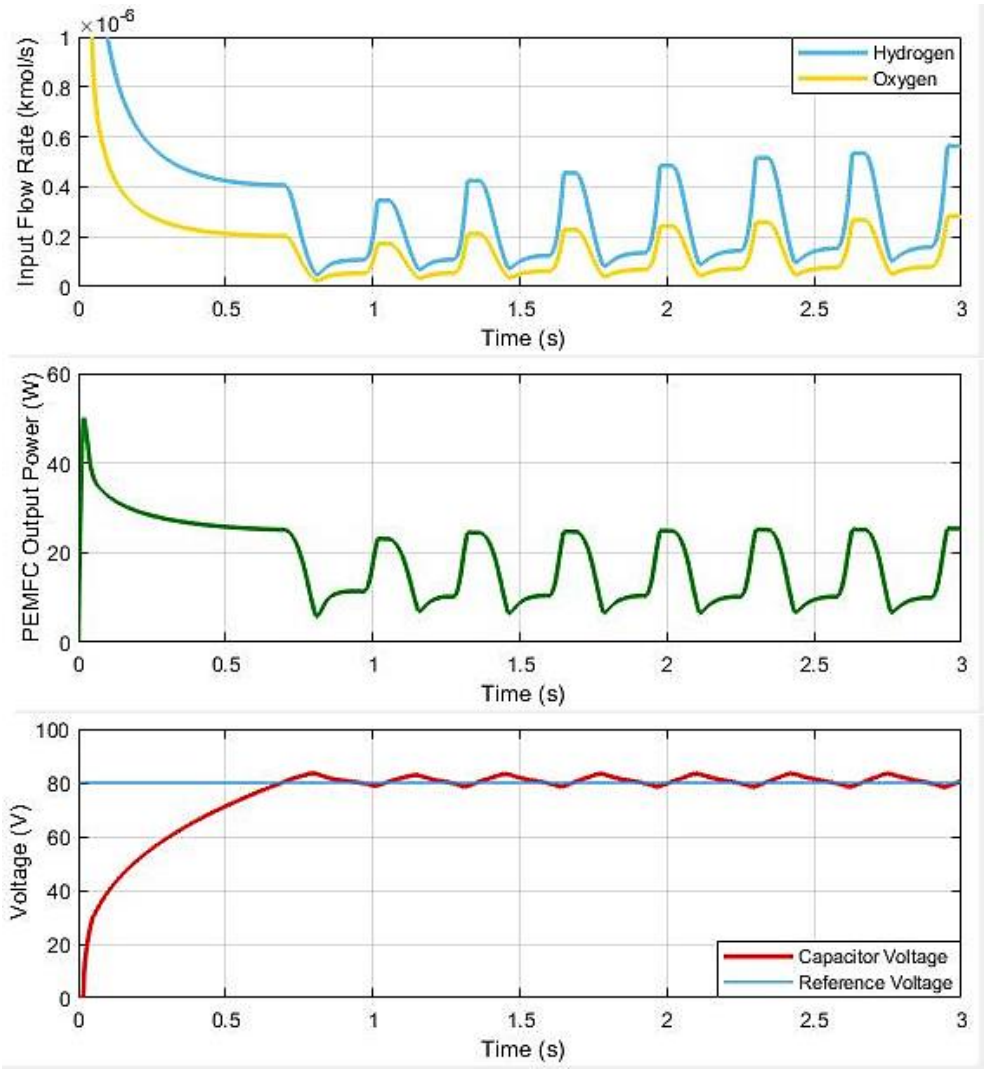


Figure 4.89: Simulation Results of Input Flow Rate of Fuel, PEMFC Output Power, and Capacitor Voltage for 3 Seconds Simulation

When the total load resistance was dropped to 3Ω, the fuel controller maximized the input flow rate of the fuel so that the PEMFC could generate the maximum rated output power. However, the capacitor voltage dropped although it was away from the reference voltage. This was because the PEMFC output power was insufficient for the load power consumption. Therefore, the capacitor was releasing the energy to the load. If the capacitor voltage was dropped to $20V$, the voltage would be insufficient to be converted to $12V_{rms}$ of AC voltage. The behavior of the PEMFC and capacitor in the DC-DC boost converter in each simulation is summarized in Table 4.9.

Table 4.9: Comparison of PEMFC Behaviour by Predictive MPPT with Voltage Control Techniques

Comparison	**Period**	**Predictive Switching State MPPT**	**Predictive Duty Cycle MPPT**	**Predictive Switching State MPPT with Frequency Reduction Technique**
Hydrogen Input Flow Rate ($kmol\ s^{-1}$)	Before $0.25s$	5.50×10^{-7}	5.50×10^{-7}	5.50×10^{-7}
	Before $0.5s$	1.35×10^{-6}	1.88×10^{-6}	1.37×10^{-6}
	Before $0.75s$	5.90×10^{-6}	7.19×10^{-6}	5.90×10^{-6}
	Before $1s$	1.00×10^{-5}	1.00×10^{-5}	1.00×10^{-5}
PEMFC Output Power	Before $0.25s$	$28.1W$	$28.1W$	$28.1W$
	Before $0.5s$	$34.8W$	$37.3W$	$34.9W$
	Before $0.75s$	$46.0W$	$47.5W$	$46.0W$
	Before $1s$	$50.0W$	$50.0W$	$50.0W$

Table 4.9 continued

PEMFC Power Ripple	Before $0.25s$	0.0053%	0.0153%	0.0082%
	Before $0.5s$	0.0083%	0.0354%	0.0143%
	Before $0.75s$	0.0133%	0.0491%	0.0239%
	Before $1s$	0.0092%	0.0332%	0.0160%
Capacitor Voltage	Before $0.25s$	$55.3V$	$55.3V$	$55.4V$
	Before $0.5s$	$64.1V$	$67.1V$	$64.1V$
	Before $0.75s$	$66.2V$	$70.8V$	$66.3V$
	Before $1s$	$53.0V$	$58.8V$	$53.1V$

For this simulation, the total load resistance was decreased from 12Ω to 3Ω with a timestamp $0.25s$. Since the load voltage has a constant amplitude, it required more electrical power when the total load resistance was reduced. Therefore, the PEMFC output power was increased from $28.1W$ to $50.0W$. However, the input flow rate of the hydrogen gas was slightly higher during the change of total load resistance when the predictive duty cycle MPPT method was applied. This caused a higher output power generation from the PEMFC and led to a higher capacitor voltage. Nevertheless, the predictive duty cycle MPPT method had the highest PEMFC output power ripple and switching frequency. The predictive switching state MPPT method had the same switching frequency as the predictive switching state MPPT method with frequency reduction technique, but it had the lowest power ripple. A diagram of the comparison of the switching state between $0.2s$ and $0.202s$ for all the predictive MPPT techniques is illustrated in Figure 4.90.

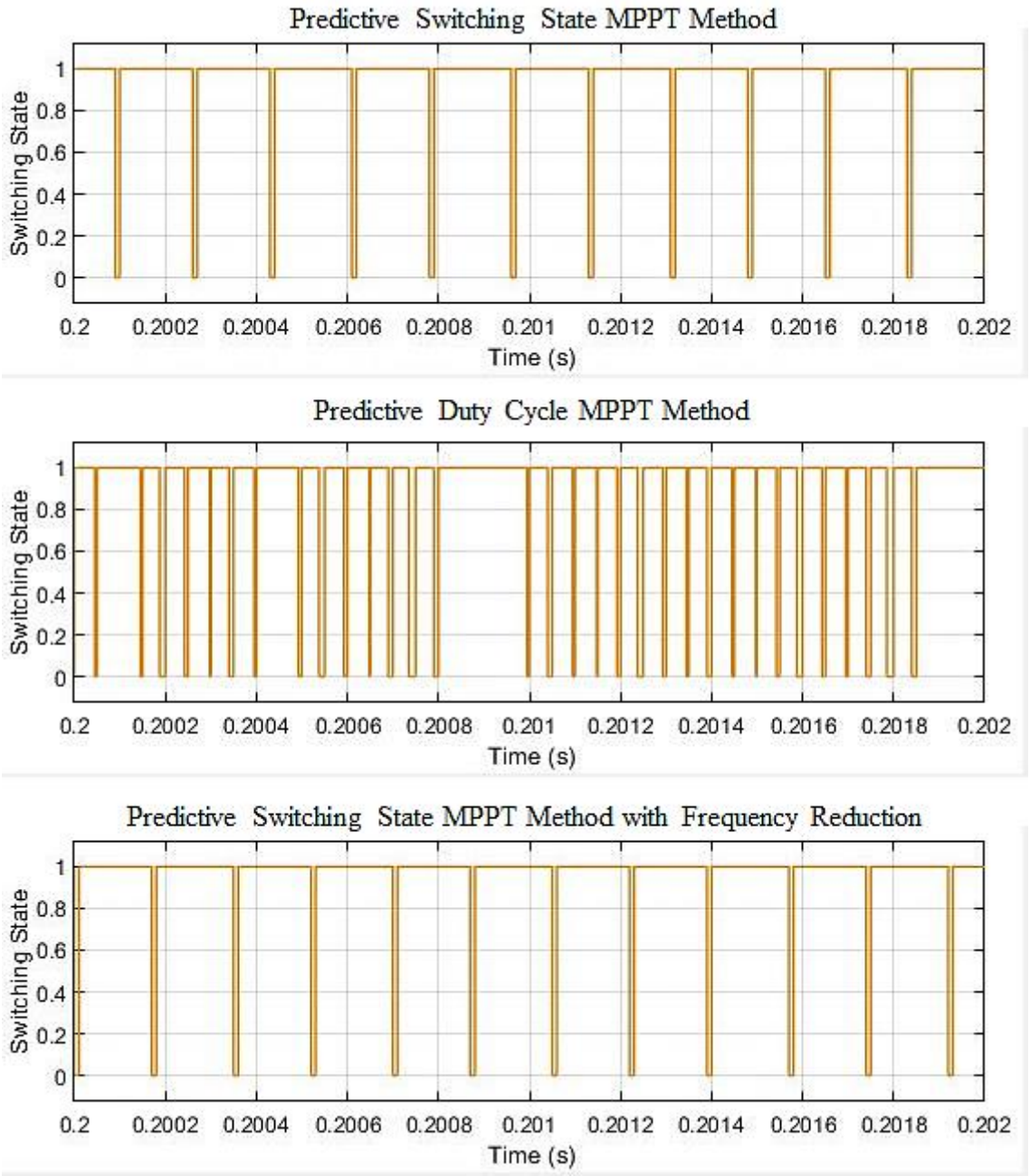


Figure 4.90: Simulation Results of Switching State for All Predictive MPPT with Voltage Control Technique

Figure 4.90 shows that the predictive duty cycle method had the highest switching frequency. In conclusion, the predictive switching state had the best performance with lower switching frequency while providing a better power quality.

At the load side, the simulation results in Figure 4.78, Figure 4.81, and Figure 4.84 show that the load voltage displayed was a sinusoidal waveform with an amplitude of $17V$ throughout the simulation. It proved that the predictive voltage control technique could invert the DC power to become AC power supply. It kept the rms voltage at $12V$ with a frequency of $50Hz$ even though there were fast variations of the load resistance. The results demonstrate the adequacy of the method for inverting DC to AC power with high robustness in load changes. The load voltage and current waveforms for a pure sinusoidal waveform are shown in Equation 4.8 and Equation 4.9, respectively.

$$V(t) = V_{peak} \sin(2\pi f t) \qquad \text{Equation 4.8}$$

$$I(t) = I_{peak} \sin(2\pi f t) \qquad \text{Equation 4.9}$$

where V_{peak} is the voltage amplitude, I_{peak} is the current amplitude, f is the AC frequency, and t is the time. For AC power, the rms value is used to measure the amount of AC power that has the same heating effect as DC power. The rms voltage and current can be defined as Equation 4.10 and Equation 4.11, respectively.

$$V_{rms} = \frac{V_{peak}}{\sqrt{2}} \qquad \text{Equation 4.10}$$

$$I_{rms} = \frac{I_{peak}}{\sqrt{2}} \qquad \text{Equation 4.11}$$

When the load resistance was decreased, the load current amplitude was increased due to Ohm's Law. Since the load used in the simulation was a pure resistive load, the load voltage and current were in phase. There was no phase angle between the load voltage and load current. All the electrical power transmitted to the load was the active power. From the simulation results in Figure 4.78, Figure 4.81, and Figure 4.84, the waveform of the load

power has a double frequency when compared with the voltage waveform. The power is computed by the product of voltage and current, which is the multiplication of Equation 4.8 and Equation 4.9. Therefore, the equation of the AC power can be defined as Equation 4.12.

$$P(t) = \frac{P_{peak}}{2}[1 - \cos(4\pi ft)] \qquad \text{Equation 4.12}$$

where P_{peak} is the power amplitude. By comparing Equation 4.12 with Equation 4.8 and Equation 4.9, the frequency of power $(4\pi ft)$ is the double frequency of voltage and current $(2\pi ft)$. Based on Equation 4.12, the average load power is ${P_{peak}}/{2}$. These calculations have been done and presented in Table 4.10.

Table 4.10: Comparison of Load Power Quality by Predictive Voltage Control Technique

Comparison	Total Load Resistance	Predictive Switching State MPPT	Predictive Duty Cycle MPPT	Predictive Switching State MPPT with Frequency Reduction Technique
Load rms Voltage	12Ω	$12.00V$	$12.00V$	$12.00V$
	6Ω	$12.00V$	$12.00V$	$12.00V$
	4Ω	$12.01V$	$12.01V$	$12.01V$
	3Ω	$12.01V$	$12.01V$	$12.01V$
Load rms Current	12Ω	$1.000A$	$1.000A$	$1.000A$
	6Ω	$2.001A$	$2.001A$	$2.001A$
	4Ω	$3.001A$	$3.002A$	$3.001A$
	3Ω	$4.002A$	$4.002A$	$4.002A$

Table 4.10 continued

Load Average Power	12Ω	$12.00W$	$12.00W$	$12.00W$
	6Ω	$24.01W$	$24.01W$	$24.01W$
	4Ω	$36.03W$	$36.04W$	$36.03W$
	3Ω	$48.05W$	$48.06W$	$48.04W$
Load THD	12Ω	0.47%	0.50%	0.53%
	6Ω	0.46%	0.47%	0.45%
	4Ω	0.44%	0.41%	0.42%
	3Ω	0.33%	0.37%	0.37%

From the comparison in Table 4.10, superior results are seen for all the simulations. All the predictive MPPT methods that merged with the predictive voltage control techniques give similar results in the load power quality. It can be deduced that the predictive MPPT methods do not affect much on the predictive voltage control techniques.

As mentioned in Table 3.7, there was a 0.539Ω resistor used for the secondary filter at the H-bridge inverter. Therefore, there was a power loss to the resistor. Based on the formula of electrical power mentioned in Equation 4.4, the power loss is dependent on the current flow through the resistor. Theoretically, the power loss was $0.539W$, $2.156W$, $4.851W$, and $8.624W$ when the total load resistance was 12Ω, 6Ω, 4Ω, and 3Ω respectively. To charge the capacitor, the PEMFC output power must be greater than the sum of the power loss and the load power consumption. Based on Table 4.9 and Table 4.10, the PEMFC output power before 0.75s was greater than the sum of the power loss and the load power consumption. Therefore, the energy was stored in the capacitor, and it caused the

capacitor voltage to increase. After $0.75s$, the PEMFC output power was not enough to supply the power to the load due to the high power loss at the filter. At this period, the capacitor was releasing power and the capacitor voltage had dropped. For a $50W$ PEMFC with a $12V_{rms}$ power conversion system, the total load resistance must be higher than 3.54Ω so that the PEMFC output power is sufficient for the load power consumption.

To test the robustness of the predictive voltage control technique, the simulation was done by increasing the frequency of the reference AC voltage. Due to the presence of the inductor and capacitor at the secondary filter of the H-bridge inverter, the increment of the frequency will increase the reactance of the components. After the testing by simulation, the $50W$ PEMFC is not sufficient to power up a 12Ω resistor with a stable $12V_{rms}$ AC voltage when the frequency is $175Hz$. If the frequency is $174Hz$, it can supply a stable $12V_{rms}$ AC voltage to the load with the resistance higher than 4.9Ω. For AC voltage amplitude, it depends on the capacitor voltage. The capacitor voltage must be higher so that it can reach the amplitude of the AC voltage.

4.7 Chapter Summary

This chapter reports the simulation results of the proposed predictive MPPT technique applied to the PEMFC. Before the predictive MPPT technique was implemented on the PEMFC, the characteristics of the PEMFC were studied. In section 4.2, the mathematical model of PEMFC was simulated to obtain the V-I and P-I curves. This step is important to observe the MPP and verify the MPPT method.

After the behavior of PEMFC was determined, the predictive MPPT method was implemented to achieve the maximum power. In section 4.3, the results obtained by using predictive MPPT methods are presented. The comparison of all the predictive MPPT

methods shows that the predictive switching state MPPT method had the best performance in power quality, with lower power ripple. In addition, the predictive switching state MPPT with a 0.3 weighting factor of the switching frequency reduction technique performs the best in reducing the switching frequency while maintaining a better power quality. For the predictive duty cycle MPPT method, the $20kHz$ switching frequency had the best performance, but it did not surpass the other two predictive MPPT methods. However, all the proposed MPPT techniques had an excellent performance in accuracy and fast-tracking. Based on Table 4.3, the proposed MPPT method had extremely short tracking speed and excellent accuracy when compared with other MPPT methods.

Besides, the robustness of the proposed MPPT method was validated by changing the parameters of the PEMFC. In section 4.4, the input flow rate of hydrogen and oxygen had fast variations to test the response of the predictive MPPT controllers. The purpose of this simulation is to imitate the sudden changes in the setting of the electronic gas flow controller. The simulation results show that the predictive MPPT methods tracked the MPP for the changes in PEMFC parameters. In addition, the fast variations of load resistance in section 4.5 also demonstrated that the changes in load will not affect the power extraction of the PEMFC. Although the load resistance had fast variations, the predictive MPPT methods could keep the PEMFC output power at MPP. All the simulations prove that the predictive MPPT techniques have high robustness for PEMFC operating parameters and load resistance.

In section 4.6, the simulation included the predictive voltage control technique to provide the AC voltage to the load. For this simulation, fuel control was also included. This was because the predictive voltage control technique provided a stable AC voltage with

constant amplitude. For any changes in total load resistance, the power consumption will be different. The employment of the fuel controller was to adjust the maximum output power of the PEMFC to match the load power consumption and protect the capacitor from overcharging. All the simulation results show that the predictive MPPT with the voltage control technique could convert the DC power from the PEMFC to the AC load. During the operation, the fuel controller was robust to the changes in the load.

CHAPTER 5

CONCLUSIONS AND RECOMMENDATIONS

5.1 Research Outcomes

This research investigates the predictive MPPT techniques for the PEMFC. Before the predictive MPPT techniques were designed, the algorithm was examined through simulation to ensure its performance achieved outstanding results. During the simulation, the fully functional mathematical model of PEMFC was computed to imitate its actual behavior. The mathematical model of PEMFC was studied, and its equations were computed in MATLAB/Simulink. The V-I and P-I characteristics curves of the PEMFC were plotted through the software. Therefore, the MPP of the PEMFC can be determined for any PEMFC parameter change. The first objective was accomplished.

Since this research is investigating the predictive MPPT technique, the predictive MPPT algorithm for the power converters was developed and simulated. In section 4.3, the proposed predictive MPPT methods demonstrated their performance. It had a high accuracy of 99.88% and fast tracking speed within $0.0192s$ in managing a $50W$ PEMFC. Even if it is implemented in a high-power PEMFC, its performance surpasses all the other MPPT methods listed in Table 4.3. Besides, the predictive switching state methods performed the best to supply an outstanding power quality with the lower power ripple below 0.015% for all simulations. When the switching frequency reduction technique was applied, it was found that a few kHz of switching frequency can be reduce with a slight increase of power ripple. In section 4.6, a single-phase DC-AC power inverter using a predictive voltage control method was also developed. The simulation results of the predictive voltage control inverter are presented in Section 4.6. It had excellent performance for inverting the DC voltage to

become an AC supply. This can be observed from the simulation results of the load voltage. The DC voltage was inverted to an AC voltage in a pure sinusoidal waveform. The AC power had a constant rms voltage of $12V$ and a constant frequency of $50Hz$. In addition, the THD of the AC voltage was always below 2%. Therefore, the second objective was also attained completed.

After the predictive MPPT and voltage control techniques were developed, the configuration of the whole PEMFC system was designed. With the consideration of varying load resistance, the algorithm for adjusting the input flow rate of hydrogen and oxygen was computed. In section 4.6, the simulation results show that the PEMFC system can supply the electrical power to the AC load through the AC power converter. The predictive MPPT controller always maximized the PEMFC output power throughout the simulation. In addition, the fuel control algorithm regulated the PEMFC output power to match the load power consumption while protecting the capacitor from overvoltage. Besides, the fuel control algorithm also contributes to the saving of fuel. Thus, the third objective was attained.

The robustness of the newly designed algorithm was examined by varying the PEMFC parameters and the load resistance. In section 4.4, the predictive MPPT methods were able to control the output power of the PEMFC to achieve the MPP for the input flow rate of reactant gases that changes from 10% to 100%. The tracking speed to a new MPP was as short as $0.5ms$. Section 4.5 and 4.6 tested the robustness of the predictive MPPT and voltage control techniques by changing the total load resistance. In section 4.5, the predictive MPPT methods could regulate the output power of the PEMFC at MPP for the load resistance changes between 12Ω to 3Ω. In section 4.6, the simulation results proved that the

predictive voltage control inverter could maintain the rms voltage and frequency. These examinations validated the robustness of the proposed MPPT and voltage control techniques. Hence, the fourth objective was also achieved.

5.2 Research Contributions

There are several contributions to the knowledge of the research by addressing the critical need for efficient MPPT in PEMFC. Through a series of meticulous studies and designs, this research achieves its objectives and leads to the development and validation of the predictive MPPT technique.

The first major contribution of this research is the development of a comprehensive mathematical model of PEMFC. This mathematical model captures the fundamental dynamics and characteristics of PEMFC operation. The model serves as an essential tool for testing and optimizing the suggested MPPT approaches since it accurately simulates the behavior of the PEMFC under different settings. By providing a realistic representation of PEMFC performance, this foundational study guarantees that the following advances are based on reliable and applicable research findings.

This research introduces the predictive MPPT technique with predictive voltage control. The predictive MPPT techniques anticipate the future output current based on present operating conditions and PEMFC parameters. Due to the ability to forecast, it can lead to the output current approaching the MPP. The research demonstrates that the predictive MPPT maintains optimal performance under a variety of operating conditions. Simultaneously, the predictive voltage control inverts the DC voltage to AC voltage within desired limits with constant frequency, even if there are fluctuations in load resistance. It also investigates the MPC application in the electronics field.

This dual approach aims to optimize the power output of PEMFC while ensuring stable voltage regulation for electrical appliances. This development may promote the application of the PEMFC in the AC field, including the grid-connected system. In addition, the idea of fuel control may improve the sustainability of the energy by saving fuel. This dual-control strategy represents a significant advancement in PEMFC management, offering both efficiency and stability. It shows a significant contribution to the development of the PEMFC technology.

The research verifies the accuracy and effectiveness of the predictive MPPT and voltage control strategies through a series of simulations. Since the simulation results show good performance of the proposed MPPT and voltage control method, it confirms the reliability of the mathematical model and the efficacy of the control techniques. This validation demonstrates the feasibility of implementing the proposed solutions in PEMFC systems.

5.3 Future Recommendation

This research investigates the predictive MPPT and voltage control technique for PEMFC. The outcomes prove that the methods perform with sufficient reliability when used in real-time. However, this research has its limitations that must be acknowledged. The study relies heavily on simulations conducted using MATLAB software to validate the proposed methods. Although simulations are effective in analyzing system behaviours under controlled conditions, they may not fully replicate the complexities and uncertainties of real-world environments. While this research primarily relied on simulations, future studies should implement the proposed techniques in laboratory testing of the PEMFC systems. This

would guarantee the performance and reliability of the predictive MPPT and voltage control methods in practical scenarios.

After the predictive MPPT methods are validated, the scalability of the proposed methods should be explored further. Although the algorithms were tested on small-scale PEMFC systems, their integration into larger or multi-cell systems should be investigated. For the algorithm, the MPC may combine with other algorithms such as RBFN or FLC. It may keep the advantages of fast-tracking speed with high stability while addressing the uncertainty of the mathematical computation of PEMFC. In addition, FLC can be merged with the TOPSIS algorithm to improve the switching frequency reduction technique.

The power electronics used in this research are the conventional DC-DC boost converter and the fundamental single-phase DC-AC inverter. Future work may consider interleaved boost converters or reconfigured quadratic boost converters to improve PEMFC stability (Niu et al., 2023; K. J. Reddy & Sudhakar, 2017; Srinivasan et al., 2021). The performance of power quality may be improved if the DC-DC power converter is enhanced. Besides, the single-phase DC-AC inverter can only regulate the DC input voltage to three levels. A single-phase five-level inverter from a previous study can be further investigated to improve power quality (X. Li et al., 2017). Moreover, a three-phase five-level inverter can also be tested for three-phase power distribution in PEMFC systems (Liu et al., 2020). This enhancement requires the new MPC algorithm, which is specified for the power converter applied.

REFERENCES

Abbassi, R., Saidi, S., Abbassi, A., Jerbi, H., Kchaou, M., & Alhasnawi, B. N. (2023). Accurate key parameters estimation of PEMFCs' models based on Dandelion optimization algorithm. *Mathematics*, *11*(6), 1298. https://doi.org/10.3390/math11061298

Abdel-Basset, M., Mohamed, R., & Chang, V. (2021). An efficient parameter estimation algorithm for proton exchange membrane fuel cells. *Energies*, *14*(21), 7115. https://doi.org/10.3390/en14217115

Abdi, S., Afshar, K., Bigdeli, N., & Ahmadi, S. (2012). A novel approach for robust maximum power point tracking of PEM fuel cell generator using sliding mode control approach. *International Journal of Electrochemical Science*, *7*(5), 4192–4209. https://doi.org/10.1016/S1452-3981(23)19531-9

Afsharinejad, A., Asemani, M. H., & Dehghani, M., 2020. Optimal linear parameter varying controller design for proton exchange membrane fuel cell using LMI techniques. In: IEEE (Ed.), *2020 28th Iranian Conference on Electrical Engineering, ICEE 2020*, Tabriz, Iran, 04 – 06 August 2020. IEEE. https://doi.org/10.1109/ICEE50131.2020.9260820

Agwa, A. M., Alanazi, T. I., Kraiem, H., Touti, E., Alanazi, A., & Alanazi, D. K. (2023). MPPT of PEM fuel cell using PI-PD controller based on golden jackal optimization algorithm. *Biomimetics*, *8*(5), 426. https://doi.org/10.3390/biomimetics8050426

Ahmad, S., Nawaz, T., Ullah, A., Ahmed, M., Khan, M. O., Saher, S., Qamar, A., & Sikandar, M. A. (2020). Thermal optimization of manganese dioxide nanorods with enhanced ORR activity for alkaline membrane fuel cell. *Electrochemical Science*

Advances, *1*(3), e2000032. https://doi.org/10.1002/elsa.202000032

Ahmadi, S., Abdi, S., & Kakavand, M. (2017). Maximum power point tracking of a proton exchange membrane fuel cell system using PSO-PID controller. *International Journal of Hydrogen Energy*, *42*(32), 20430–20443. https://doi.org/10.1016/j.ijhydene.2017.06.208

Ahmed, H., Adebayo, P., Ahmed, M., & Arbab, A. I. (2023). Hydrogen Fuel Cell Technology: Benefits, Challenges, and Future Potential. *Journal of Energy Technologies and Policy*, *13*(1), 48–56. https://doi.org/10.7176/jetp/13-1-06

Albira, M. E., Alzahrani, A., & Zohdy, M., 2020. Model predictive control of DC-DC buck-boost converter with various resistive load values. In: IEEE (Ed.), *Proceedings of 2020 Global Mosharaka Congress on Electrical Engineering, GC-ElecEng 2020*, Valencia, Spain, 04 – 06 September 2020. IEEE. https://doi.org/10.23919/GC-ElecEng48342.2020.9285986

Aly, M., Mohamed, E. A., Rezk, H., Nassef, A. M., Elhosseini, M. A., & Shawky, A. (2023). An improved optimally designed fuzzy logic-based MPPT method for maximizing energy extraction of PEMFC in green buildings. *Energies*, *16*(3), 1197. https://doi.org/10.3390/en16031197

Amphlett, J. C., Baumert, R. M., Mann, R. F., Peppley, B. A., Roberge, P. R., & Harris, T. J. (1995). Performance modeling of the ballard mark IV solid polymer electrolyte fuel cell: I. mechanistic model development. *Journal of The Electrochemical Society*, *142*(1), 1–8. https://doi.org/10.1149/1.2043959

Andrew, L. D., & David, A. J. R. (2018). *Fuel cell systems explained,* 3rd ed., Hoboken: John Wiley & Sons.

Ashraf, N., Abbas, G., Abbassi, R., & Jerbi, H. (2021). Power quality analysis of the output

voltage of AC voltage and frequency controllers realized with various voltage control techniques. *Applied Sciences*, *11*(2), 538. https://doi.org/10.3390/app11020538

Austin, L. G. (1976). *Fuel cells,* Washignton: National Aeronautics and Space Administration.

Bacon, F. T. (1969). Fuel cells, past, present and future. *Electrochimica Acta*, *14*(7), 569–585. https://doi.org/10.1016/0013-4686(69)87042-8

Barhoumi, E. M., Chukwuleke Okonkwo, P., Belgacem, I. Ben, & Zghaibeh, M., 2020. MPPT control of an interleaved boost converter for a polymer electrolyte membrane fuel cell applications. In: IEEE (Ed.), *2020 International Conference on Electrical and Information Technologies (ICEIT)*, Rabat, Morocco, 04 – 07 March 2020. IEEE. https://doi.org/10.1109/ICEIT48248.2020.9113228

Başarır, E., Özkan, G., & Özkan, G. (2021). Synthesis of nickel boride and investigation of availability as an additive in the molten carbonate fuel cell anode material. *International Journal of Energy Research*, *46*(8), 10088–10098. https://doi.org/10.1002/er.6626

Basri, H. M., & Mekhilef, S. (2022). Predictive current control for three-level four-leg indirect matrix converter under unbalanced input voltage. *IEEE Journal of Emerging and Selected Topics in Power Electronics*, *11*(4), 3738–3750. https://doi.org/10.1109/JESTPE.2022.3179286

Borreggine, S., Monopoli, V. G., Rizzello, G., Naso, D., Cupertino, F., & Consoletti, R., 2019. A review on model predictive control and its applications in power electronics. In: IEEE (Ed.), *2019 AEIT International Conference of Electrical and Electronic Technologies for Automotive (AEIT AUTOMOTIVE)*, Turin, Italy, 02 – 04 July 2019. IEEE. https://doi.org/10.23919/EETA.2019.8804594

Bououden, S., Hazil, O., Filali, S., & Chadli, M., 2014. Modelling and model predictive

control of a DC-DC boost converter. In: IEEE (Ed.), *2014 15th International Conference on Sciences and Techniques of Automatic Control and Computer Engineering (STA)*, Hammamet, Tunisia, 21 – 23 December 2014. IEEE. https://doi.org/10.1109/STA.2014.7086663

Celikel, R., Aydogmus, O., & Yilmaz, M. (2025). A modified perturb and observe MPPT algorithm for PEMFC with rapid convergence and low power oscillation. *Scientific Reports*, *15*, 27848. https://doi.org/10.1038/s41598-025-09947-3

Cheng, L., Acuna, P., Aguilera, R. P., Ciobotaru, M., & Jiang, J., 2016. Model predictive control for DC-DC boost converters with constant switching frequency. In: IEEE (Ed.), *2016 IEEE 2nd Annual Southern Power Electronics Conference (SPEC)*, Auckland, New Zealand, 05 – 08 December 2016. IEEE. https://doi.org/10.1109/SPEC.2016.7846189

Cheng, L., Acuna, P., Aguilera, R. P., Jiang, J., Wei, S., Fletcher, J. E., & Lu, D. D. C. (2017). Model predictive control for DC-DC boost converters with reduced-prediction horizon and constant switching frequency. *IEEE Transactions on Power Electronics*, *33*(10), 9064–9075. https://doi.org/10.1109/TPEL.2017.2785255

Chowdhury, M. S. A., Mamun, K. A. Al, & Rahman, A. M., 2016. Modelling and simulation of power system of battery, solar and fuel cell powered hybrid electric vehicle. In: IEEE (Ed.), *2016 3rd International Conference on Electrical Engineering and Information Communication Technology (ICEEICT)*, Dhaka, Bangladesh, 22 – 24 September 2016. IEEE. https://doi.org/10.1109/CEEICT.2016.7873126

Daming, Z. (2018). *Modeling and multi-dimensional analysis of a proton exchange membrane fuel cell,* PhD thesis, Université Bourgogne Franche-Comté.

Derbeli, M., Barambones, O., Farhat, M., Ramos-Hernanz, J. A., & Sbita, L. (2020). Robust

high order sliding mode control for performance improvement of PEM fuel cell power systems. *International Journal of Hydrogen Energy*, *45*(53), 29222–29234. https://doi.org/10.1016/j.ijhydene.2020.07.172

Derbeli, M., Barambones, O., Farhat, M., & Sbita, L., 2019. Efficiency boosting for proton exchange membrane fuel cell power system using new MPPT method. In: IEEE (Ed.), *2019 10th International Renewable Energy Congress (IREC)*, Sousse, Tunisia,26 – 28 March 2019. IEEE. https://doi.org/10.1109/IREC.2019.8754587

Derbeli, M., Barambones, O., & Sbita, L. (2018). A robust maximum power point tracking control method for a PEM fuel cell power system. *Applied Sciences*, *8*(12), 2449. https://doi.org/10.3390/app8122449

Derbeli, M., Charaabi, A., Barambones, O., & Napole, C. (2021). High-performance tracking for proton exchange membrane fuel cell system pemfc using model predictive control. *Mathematics*, *9*(11), 1158. https://doi.org/10.3390/math9111158

Ebrahimi, M., Kujawski, W., Fatyeyeva, K., & Kujawa, J. (2021). A review on ionic liquids-based membranes for middle and high temperature polymer electrolyte membrane fuel cells (Pem fcs). *International Journal of Molecular Sciences*, *22*(11), 5430. https://doi.org/10.3390/ijms22115430

Elmore, G. V., & Tanner, H. A. (1961). Intermediate temperature fuel cells. *Journal of The Electrochemical Society*, *108*(7), 669–671. https://doi.org/10.1149/1.2428186

Estrada, L., Vazquez, N., Vaquero, J., Hernandez, C., Arau, J., & Huerta, H. (2021). Finite control set-model predictive control based on sliding mode for bidirectional power inverter. *IEEE Transactions on Energy Conversion*, *36*(4), 2814–2824. https://doi.org/10.1109/TEC.2021.3063601

Fan, L., & Ma, X. (2022). Maximum power point tracking of PEMFC based on hybrid

artificial bee colony algorithm with fuzzy control. *Scientific Reports*, *12*, 4316. https://doi.org/10.1038/s41598-022-08327-5

Fang, F., Tian, H., & Li, Y. (2021). Finite control set model predictive control for AC-DC matrix converter with virtual space vectors. *IEEE Journal of Emerging and Selected Topics in Power Electronics*, *9*(1), 616–628. https://doi.org/10.1109/JESTPE.2019.2937330

Fathy, A., Abdelkareem, M. A., Olabi, A. G., & Rezk, H. (2021). A novel strategy based on salp swarm algorithm for extracting the maximum power of proton exchange membrane fuel cell. *International Journal of Hydrogen Energy*, *46*(8), 6087–6099. https://doi.org/10.1016/j.ijhydene.2020.02.165

Fathy, A., & Rezk, H. (2018). Multi-verse optimizer for identifying the optimal parameters of PEMFC model. *Energy*, *143*, 634–644. https://doi.org/10.1016/j.energy.2017.11.014

Fathy, A., Rezk, H., & Alanazi, T. M. (2021). Recent approach of Forensic-based investigation algorithm for optimizing fractional order PID-based MPPT with proton exchange membrane fuel cell. *IEEE Access*, *9*, 18974–18992. https://doi.org/10.1109/ACCESS.2021.3054552

Fayyaz, M. M., Syed, I. M., Meng, Y., & Aman, M. N. (2023). Comprehensive predictive control model for a three-phase four-legged inverter. *Energies*, *16*(6), 2650. https://doi.org/10.3390/en16062650

Gaouzi, K., El Fadil, H., Rachid, A., Belhaj, F. Z., & Giri, F., 2017. Constrained model predictive control for DC-DC buck power converters. In: IEEE (Ed.), *2017 International Conference on Electrical and Information Technologies (ICEIT)*, Rabat, Morocco, 15 – 18 November 2017. IEEE. https://doi.org/10.1109/EITech.2017.8255245

Ghamari, S. M., Khavari, F., Molaee, H., & Wheeler, P. (2022). Generalised model predictive controller design for A DC–DC non-inverting buck–boost converter optimised with a novel identification technique. *IET Power Electronics*, *15*(13), 1350–1364. https://doi.org/10.1049/pel2.12309

Ghenai, C., Al-Ani, I., Khalifeh, F., Alamaari, T., & Hamid, A. K., 2019. Design of solar PV/fuel cell/diesel generator energy system for Dubai ferry. In: IEEE (Ed.), *2019 Advances in Science and Engineering Technology International Conferences (ASET)*. Dubai, United Arab Emirates, 26 March 2019 – 10 April 2019. IEEE. https://doi.org/10.1109/ICASET.2019.8714292

Grove, W. R. (1839). XXIV. On voltaic series and the combination of gases by platinum. *Philosophical Magazine Series 3*, *14*(86), 127–130. https://doi.org/10.1080/14786443908649684

Grubb, W. T., & Niedrach, L. W. (1960). Batteries with solid ion-exchange membrane electrolytes. *Journal of The Electrochemical Society*, *107*(2), 131–135.

Guo, H., Chen, L., Ismail, S. A., Jiang, L., Guo, S., Gu, J., Zhang, X., Li, Y., Zhu, Y., Zhang, Z., & Han, D. (2022). Gas Diffusion Layer for Proton Exchange Membrane Fuel Cells: A Review. *Materials*, *15*(24), 8800. https://doi.org/10.3390/ma15248800

Gupta, J., Nijhawan, P., & Ganguli, S. (2021). Optimal parameter estimation of PEM fuel cell using slime mould algorithm. *International Journal of Energy Research*, *45*(10), 14732–14744. https://doi.org/10.1002/er.6750

Hamedani, E. A., Alenabi, S. A., & Talebi, S. (2024). Hydrogen as an energy source: A review of production technologies and challenges of fuel cell vehicles. *Energy Reports*, *12*, 3778–3794. https://doi.org/10.1016/j.egyr.2024.09.030

Harrag, A., & Messalti, S. (2018). How fuzzy logic can improve PEM fuel cell MPPT

performances? *International Journal of Hydrogen Energy*, *43*(1), 537–550. https://doi.org/10.1016/j.ijhydene.2017.04.093

Hassani, H., Rekioua, D., Aissou, S., Bacha, S., & Zaouche, F., 2018. Hybrid stand-alone photovoltaic/batteries/fuel cells system for green cities. In: IEEE (Ed.), *2018 6th International Renewable and Sustainable Energy Conference (IRSEC)*, Rabat, Morocco, 05 – 08 December 2018. IEEE. https://doi.org/10.1109/IRSEC.2018.8702278

Hossain, K. K., & Jamal, T., 2015. Solar PV- Hydrogen Fuel cell system for electrification of a remote village in Bangladesh. In: IEEE (Ed.), *2015 International Conference on Advances in Electrical Engineering (ICAEE)*, Dhaka, Bangladesh, 17 – 19 December 2015. IEEE. https://doi.org/10.1109/ICAEE.2015.7506787

Huang, Z., Zhou, J., & Cui, Y., 2020. Performance simulation of proton exchange membrane fuel cell system based on fuzzy logic. In: IEEE (Ed.), *2020 IEEE Conference on Telecommunications, Optics and Computer Science (TOCS)*, Shenyang, China, 11 – 13 December 2020. IEEE. https://doi.org/10.1109/TOCS50858.2020.9339730

Jawad, N. H., Yahya, A. A., Al-Shathr, A. R., Salih, H. G., Rashid, K. T., Al-Saadi, S., Abdulrazak, A. A., Salih, I. K., Zrelli, A., & Alsalhy, Q. F. (2022). Fuel cell types, properties of membrane, and operating conditions: A review. *Sustainability*, *14*(21), 14653. https://doi.org/10.3390/su142114653

Jiao, J., & Cui, X. (2013). Adaptive control of MPPT for fuel cell power system. *Journal of Convergence Information Technology*, *8*(4), 362–371. https://doi.org/10.4156/jcit.vol8.issue4.43

Jun, E. S., Nguyen, M. H., & Kwak, S. (2020). Model predictive control method based on deterministic reference voltage for single-phase three-level NPC converters. *Applied*

Sciences, *10*(24), 8840. https://doi.org/10.3390/app10248840

Justin, L. (2017). *The analysis of solar - Fuel cell hybrid systems,* Master thesis, Arizona State University.

Kanouni, B., Badoud, A. E., Mekhilef, S., Elsanabary, A., Bajaj, M., & Zaitsev, I. (2024). A fuzzy-predictive current control with real-time hardware for PEM fuel cell systems. *Scientific Reports*, *14*, 27166. https://doi.org/10.1038/s41598-024-78030-0

Karamanakos, P., Liegmann, E., Geyer, T., & Kennel, R. (2020). Model predictive control of power electronic systems: Methods, results, and challenges. *IEEE Open Journal of Industry Applications*, *1*, 95–114. https://doi.org/10.1109/OJIA.2020.3020184

Karami, N., Khoury, L. El, Khoury, G., & Moubayed, N., 2014. Comparative study between P&O and incremental conductance for fuel cell MPPT. In: IEEE (Ed.), *International Conference on Renewable Energies for Developing Countries 2014*, Beirut, Lebanon, 26 – 27 November 2014. IEEE. https://doi.org/10.1109/REDEC.2014.7038524

Karthikeyan, V., Das P, V., & Blaabjerg, F., 2018. Implementation of MPPT control in fuel cell fed high step up ratio DC-DC converter. In: IEEE (Ed.), *2018 2nd IEEE International Conference on Power Electronics, Intelligent Control and Energy Systems (ICPEICES)*, Delhi, India, 22 – 24 October 2018. IEEE. https://doi.org/10.1109/ICPEICES.2018.8897443

Khalilzadeh, M., Vaez-Zadeh, S., Rodriguez, J., & Heydari, R. (2021). Model-free predictive control of motor drives and power converters: A review. *IEEE Access*, *9*, 105733–105747. https://doi.org/10.1109/ACCESS.2021.3098946

Kheirandish, A. (2016). *Dynamic modelling of proton exchange membrane fuel cell system for electric bicycle,* PhD thesis, University of Malaya.

Li, C., & Hu, Y., 2020. On-line degradation estimation of proton exchange membrane fuel

cell based on IMM-EKF. In: IEEE (Ed.), *2020 Chinese Automation Congress (CAC)*, Shanghai, China, 06 – 08 November 2020. IEEE. https://doi.org/10.1109/CAC51589.2020.9327440

Li, X., Zhang, H., Shadmand, M. B., & Balog, R. S. (2017). Model predictive control of a voltage-source inverter with seamless transition between islanded and grid-connected operations. *IEEE Transactions on Industrial Electronics*, *64*(10), 7906–7918. https://doi.org/10.1109/TIE.2017.2696459

Li, Y., Ma, Z., Zheng, M., Li, D., Lu, Z., & Xu, B. (2021). Performance analysis and optimization of a high-temperature pemfc vehicle based on particle swarm optimization algorithm. *Membranes*, *11*(9), 691. https://doi.org/10.3390/membranes11090691

Liu, Z., Xia, Z., Li, D., Wang, Y., & Li, F. (2020). An optimal model predictive control method for five-level active NPC inverter. *IEEE Access*, *8*, 221414–221423. https://doi.org/10.1109/ACCESS.2020.3043604

Loo, K. H., Zhu, G. R., Lai, Y. M., & Tse, C. K.. 2011. Development of a maximum-power-point tracking algorithm for direct methanol fuel cell and its realization in a fuel cell/supercapacitor hybrid energy system. In: IEEE (Ed.), *8th International Conference on Power Electronics - ECCE Asia*. Jeju, Korea (South), 30 May 2011 – 03 June 2011. IEEE. https://doi.org/10.1109/ICPE.2011.5944478

Luta, D. N., & Raji, A. K. (2019a). Comparing fuzzy rule-based and fractional open circuit voltage MPPT techniques in a fuel cell stack. *Energy Procedia*, *8*(4), 402–411. https://doi.org/https://doi.org/10.14419/ijet.v8i4.29343

Luta, D. N., & Raji, A. K. (2019b). Fuzzy rule-based and particle swarm optimisation MPPT techniques for a fuel cell stack. *Energies*, *12*(5), 936. https://doi.org/10.3390/en12050936

Mann, R. F., Amphlett, J. C., Hooper, M. A. I., Jensen, H. M., Peppley, B. A., & Roberge, P. R. (2000). Development and application of a generalized steady-state electrochemical model for a PEM fuel cell. *Journal of Power Sources*, *86*(1), 173–180. https://doi.org/10.1016/S0378-7753(99)00484-X

Menesy, A. S., Sultan, H. M., Korashy, A., Banakhr, F. A., Ashmawy, M. G., & Kamel, S. (2020). Effective parameter extraction of different polymer electrolyte membrane fuel cell stack models using a modified artificial ecosystem optimization algorithm. *IEEE Access*, *8*, 31892–31909. https://doi.org/10.1109/ACCESS.2020.2973351

Najjar, M., Shahparasti, M., Heydari, R., & Nymand, M. (2021). Model predictive controllers with capacitor voltage balancing for a single-phase five-level SiC/Si based ANPC inverter. *IEEE Open Journal of Power Electronics*, *2*, 202–211. https://doi.org/10.1109/OJPEL.2021.3066924

Naseri, N., El Hani, S., Aghmadi, A., El Harouri, K., Heyine, M. S., & Mediouni, H., 2018. Proton exchange membrane fuel cell modelling and power control by P&O algorithm. In: IEEE (Ed.), *2018 6th International Renewable and Sustainable Energy Conference (IRSEC)*, Rabat, Morocco, 05 – 08 December 2018. IEEE. https://doi.org/10.1109/IRSEC.2018.8703002

Niu, R., Zhang, H., & Song, J. (2023). Model predictive control of DC–DC boost converter based on generalized proportional integral observer. *Energies*, *16*(3), 1245. https://doi.org/10.3390/en16031245

Obaid, W., Hamid, A. K., & Ghenai, C., 2018. Hybrid PEM fuel-cell-diesel-solar power system design with fuzzy battery management system and weather forecasting for electric boats. In: IEEE (Ed.), *2018 6th International Renewable and Sustainable Energy Conference (IRSEC)*, Rabat, Morocco, 05 – 08 December 2018. IEEE.

https://doi.org/10.1109/IRSEC.2018.8702862

Obaid, W., Hamid, A. K., & Ghenai, C., 2019. Wind-fuel-cell-solar hybrid electric boat power design with MPPT system. In: IEEE (Ed.), *2019 8th International Conference on Modeling Simulation and Applied Optimization (ICMSAO)*, Manama, Bahrain, 15 – 17 April 2019. IEEE. https://doi.org/10.1109/ICMSAO.2019.8880330

Pathan, J. (2020). Model predictive control of DC-DC buck converter and its comparison with PID controller. *International Journal of Advanced Research in Engineering and Technology*, *11*(9), 362–367. https://doi.org/10.34218/IJARET.11.9.2020.037

Rana, K. P. S., Kumar, V., Sehgal, N., & George, S. (2019). A novel dP/dI feedback based control scheme using GWO tuned PID controller for efficient MPPT of PEM fuel cell. *ISA Transactions*, *93*, 312–324. https://doi.org/10.1016/j.isatra.2019.02.038

Reddy, K. A., Srinivas, K., & Ayyappan, G. S., 2015. Simulation of power management circuit in a standalone solar photovoltaic-fuel cell-battery hybrid power system. In: IEEE (Ed.), *2015 IEEE IAS Joint Industrial and Commercial Power Systems / Petroleum and Chemical Industry Conference (ICPSPCIC)*, Hyderabad, India, 19 – 21 November 2015. IEEE. https://doi.org/10.1109/CICPS.2015.7974070

Reddy, K. J., & Sudhakar, N. (2017). High voltage gain interleaved boost converter with neural network based mppt controller for fuel cell based electric vehicle applications. *IEEE Access*, *6*, 3899–3908. https://doi.org/10.1109/ACCESS.2017.2785832

Ren, Z., Huangfu, Y., Xie, R., & Ma, R., 2020. Modeling of proton exchange membrane fuel cell based on LSTM neural network. In: IEEE (Ed.), *2020 Chinese Automation Congress (CAC)*, Shanghai, China, 06 – 08 November 2020. IEEE. https://doi.org/10.1109/CAC51589.2020.9326514

Rezk, H., 2016. Performance of incremental resistance MPPT based proton exchange

membrane fuel cell power system. In: IEEE (Ed.), *2016 Eighteenth International Middle East Power Systems Conference (MEPCON)*, Cairo, Egypt, 27 – 29 December 2016. IEEE. https://doi.org/10.1109/MEPCON.2016.7836891

Rezk, H., Aly, M., & Ghoniem, R. M. (2023). Robust fuzzy logic MPPT using gradient-based optimization for PEMFC power system. *Sustainability (Switzerland)*, *15*(18), 13368. https://doi.org/10.3390/su151813368

Rezk, H., & Fathy, A. (2020). Performance improvement of PEM fuel cell using variable step-size incremental resistance MPPT technique. *Sustainability*, *12*(14), 5601. https://doi.org/10.3390/su12145601

Rezk, H., Fathy, A., & Abdelaziz, A. Y. (2017). A comparison of different global MPPT techniques based on meta-heuristic algorithms for photovoltaic system subjected to partial shading conditions. *Renewable and Sustainable Energy Reviews*, *74*, 377–386. https://doi.org/10.1016/j.rser.2017.02.051

Rodriguez, J., & Cortes, P. (2012). *Predictive control of power converters and electrical drives,* West Sussex: John Wiley & Sons. https://doi.org/10.1002/9781119941446

Rodriguez, J., Heydari, R., Rafiee, Z., Young, H. A., Flores-Bahamonde, F., & Shahparasti, M. (2020). Model-free predictive current control of a voltage source inverter. *IEEE Access*, *8*, 211104–211114. https://doi.org/10.1109/ACCESS.2020.3039050

Ryan, O., Suk-Won, C., Whitney, G. C., & Fritz, B. P. (2016). *Fuel cell fundamentals,* 3rd ed., New Jersey: John Wiley & Sons.

Saavedra, J. L., Baier, C. R., Marciel, E. I., Rivera, M., Carreno, A., Hernandez, J. C., & Melín, P. E. (2023). Comparison of FCS-MPC strategies in a grid-connected single-phase quasi-Z source inverter. *Electronics*, *12*(9), 1–17.

Sadeghi, S., & Baniasad Askari, I. (2020). Performance and economic investigation of a

combined phosphoric acid fuel cell/organic Rankine cycle/electrolyzer system for sulfuric acid production; Energy-based organic fluid selection. *International Journal of Energy Research*, *44*(4), 2704–2725. https://doi.org/10.1002/er.5073

Saeed, E. W., & Warkozek, E. G. (2015). Modeling and analysis of renewable PEM fuel cell system. *Energy Procedia*, *74*, 87–101. https://doi.org/10.1016/j.egypro.2015.07.527

Samal, S., Ramana, M., & Barik, P. K., 2018. Modeling and simulation of interleaved boost converter with MPPT for fuel cell application. In: IEEE (Ed.), *2018 Technologies for Smart-City Energy Security and Power (ICSESP)*, Bhubaneswar, India, 28 – 30 March 2018. IEEE. https://doi.org/10.1109/ICSESP.2018.8376704

Sarvi, M., & Barati, M. M., 2010. Voltage and current based MPPT of fuel cells under variable temperature conditions. In: IEEE (Ed.), *45th International Universities Power Engineering Conference UPEC2010*. Cardiff, UK, 31 August 2010 – 03 September 2010. IEEE.

Schwenzer, M., Ay, M., Bergs, T., & Abel, D. (2021). Review on model predictive control: an engineering perspective. *International Journal of Advanced Manufacturing Technology*, *117*, 1327–1349. https://doi.org/10.1007/s00170-021-07682-3

Shan, Y., Hu, J., & Guerrero, J. M. (2019). A model predictive power control method for PV and energy storage systems with voltage support capability. *IEEE Transactions on Smart Grid*, *11*(2), 1018–1029. https://doi.org/10.1109/TSG.2019.2929751

Shi, X., Zhu, J., Lu, D., & Li, L. (2019). Multi-functional model predictive control with mutual influence elimination for three-phase AC/DC converters in energy conversion. *Energies*, *12*(9), 1616. https://doi.org/10.3390/en12091616

Singla, M. K., Gupta, J., Singh, B., Nijhawan, P., Abdelaziz, A. Y., & El-Shahat, A. (2023). Parameter estimation of fuel cells using a hybrid optimization algorithm. *Sustainability*,

15(8), 6676. https://doi.org/10.3390/su15086676

Smolinka, T., Bergmann, H., Garche, J., & Kusnezoff, M. (2022). *Electrochemical Power Sources: Fundamentals, Systems, and Applications,* Burlington: Elsevier Science. https://doi.org/https://doi.org/10.1016/B978-0-12-819424-9.00010-0

Soltani, I., Sarvi, M., & Marefatjou, H. (2013). An intelligent, fast and robust maximum power point tracking for proton exchange membrane fuel cell. *World Applied Programming*, *3*(7), 264–281.

Spiegel, C. (2008). *PEM fuel cell modeling and simulation using MATLAB,* Burlington: Elsevier Science. https://doi.org/10.1016/B978-0-12-374259-9.X5001-0

Springer, T. E., Zawodzinski, T. A., & Gottesfeld, S. (1991). Polymer electrolyte fuel cell model. *Journal of The Electrochemical Society*, *138*(8), 2334–2342. https://doi.org/10.1149/1.2085971

Srinivasan, S., Tiwari, R., Krishnamoorthy, M., Lalitha, M. P., & Raj, K. K. (2021). Neural network based MPPT control with reconfigured quadratic boost converter for fuel cell application. *International Journal of Hydrogen Energy*, *46*(9), 6709–6719. https://doi.org/10.1016/j.ijhydene.2020.11.121

Sultan, H. M., Menesy, A. S., Kamel, S., Hasanien, H. M., & Al-Durra, A., 2020. Identifying optimal parameters of proton exchange membrane fuel cell using water cycle algorithm. In: IEEE (Ed.), *2020 2nd International Conference on Smart Power & Internet Energy Systems (SPIES)*, Bangkok, Thailand, 15 – 18 September 2020. IEEE. https://doi.org/10.1109/SPIES48661.2020.9242973

Sultan, H. M., Menesy, A. S., Kamel, S., Tostado-Veliz, M., & Jurado, F., 2020. Parameter identification of proton exchange membrane fuel cell stacks using Bonobo optimizer. In: IEEE (Ed.), *2020 IEEE International Conference on Environment and Electrical*

Engineering and 2020 IEEE Industrial and Commercial Power Systems Europe (EEEIC / I&CPS Europe), Madrid, Spain, 09 – 12 June 2020. IEEE. https://doi.org/10.1109/EEEIC/ICPSEurope49358.2020.9160597

Toledo, S., Caballero, D., Maqueda, E., Cáceres, J. J., Rivera, M., Gregor, R., & Wheeler, P. (2022). Predictive control applied to matrix converters: A systematic literature review. *Energies*, *15*(20), 7801. https://doi.org/10.3390/en15207801

Vijayagopal, M., Zanchetta, P., Empringham, L., De Lillo, L., Tarisciotti, L., & Wheeler, P. (2017). Control of a direct matrix converter with modulated model-predictive control. *IEEE Transactions on Industry Applications*, *53*(3), 2342–2349. https://doi.org/10.1109/TIA.2017.2674602

Wang, Z., Yan, Y., Yang, J., Li, S., & Li, Q. (2019). Robust voltage regulation of a DC-AC inverter with load variations via a HDOBC approach. *IEEE Transactions on Circuits and Systems II: Express Briefs*, *66*(7), 1172–1176. https://doi.org/10.1109/TCSII.2018.2872330

Wei, M., Ge, H., Shuang, J., Liu, Y., Chen, X., & Zhong, S. (2022). Highly conductive hematite electrolyte for low-temperature solid oxide fuel cell. *International Journal of Energy Research*, *46*(2), 1126–1136. https://doi.org/10.1002/er.7233

Wu, H., Zhang, L., Yang, J., & Li, S., 2017. Model predictive control for DC-DC buck power converter-DC motor system with uncertainties using a GPI observer. In: IEEE (Ed.), *2017 36th Chinese Control Conference (CCC)*, Dalian, China, 26 – 28 July 2017. IEEE. https://doi.org/10.23919/ChiCC.2017.8028129

Yang, X., Fang, Y., Fu, Y., Mi, Y., Li, H., & Wang, Y. (2020). Low-complexity model predictive control of AC/DC converter with constant switching frequency. *IEEE Access*, *8*, 137975–137985. https://doi.org/10.1109/ACCESS.2020.3012163

Yaqoob, L., Noor, T., & Iqbal, N. (2021). Recent progress in development of efficient electrocatalyst for methanol oxidation reaction in direct methanol fuel cell. *International Journal of Energy Research*, *45*(5), 6550–6583. https://doi.org/10.1002/er.6316

Young, J. M., Mondal, A., Barckholtz, T. A., Kiss, G., Koziol, L., & Panagiotopoulos, A. Z. (2021). Predicting chemical reaction equilibria in molten carbonate fuel cells via molecular simulations. *AIChE Journal*, *67*(3), e16988. https://doi.org/10.1002/aic.16988

Zadeh, L., & Whalen, B. (1962). On optimal control and linear programming. *IRE Transactions on Automatic Control*, *7*(4), 45–46. https://doi.org/10.1109/tac.1962.1105469

Zhang, J., Norambuena, M., Li, L., Dorrell, D., & Rodriguez, J. (2019). Sequential model predictive control of three-phase direct matrix converter. *Energies*, *12*(2), 214. https://doi.org/10.3390/en12020214

Zhi, Y., Weiqing, W., Haiyun, W., & Razmjooy, N. (2021). New approaches for regulation of solid oxide fuel cell using dynamic condition approximation and STATCOM. *International Transactions on Electrical Energy Systems*, *31*(2), e12756. https://doi.org/10.1002/2050-7038.12756

Zhong, Z., Huo, H., Zhu, X., Cao, G., & Ren, Y. (2008). Adaptive maximum power point tracking control of fuel cell power plants. *Journal of Power Sources*, *176*(1), 259–269. https://doi.org/10.1016/j.jpowsour.2007.10.080

APPENDICES

Appendix A: Journal Publications

1. **Fam, J. Y.,** Basri, H. M., Wong, S. Y., Lias, K., Mekhilef, S., & Abdullah, M. O. (2025). Predictive maximum power point tracking with Newton Raphson technique for proton exchange membrane fuel cell. Journal of Advanced Research in Fluid Mechanics and Thermal Sciences, 133(1), 37–58. https://doi.org/10.37934/arfmts.133.1.3758.
2. **Fam, J. Y.,** Wong, S. Y., Basri, H. M., Lias, K., & Abdullah, M. O. (2024). An enhanced maximum power point tracking and voltage control for proton exchange membrane fuel cell using predictive model control techniques. *Energy Reports*, *12*, 2958–2970. https://doi.org/10.1016/j.egyr.2024.08.055.
3. **Fam, J. Y.,** Wong, S. Y., Abdullah, M. O., Lias, K., Mekhilef, S., & Basri, H. M. (2023). Predictive-TOPSIS-based MPPT for PEMFC featuring switching frequency reduction. *Indonesian Journal of Electrical Engineering and Informatics*, *11*(3), 656–672. https://doi.org/10.52549/ijeei.v11i3.4350.
4. **Fam, J. Y.,** Wong, S. Y., Basri, H. M., Abdullah, M. O., Lias, K., & Mekhilef, S. (2021). Predictive maximum power point tracking for proton exchange membrane fuel cell system. *IEEE Access*, *9*, 157384–157397. https://doi.org/10.1109/ACCESS.2021.3129849.

Appendix B: Mathematical Equations

This section shows all the details of mathematical working steps for first and second derivatives of PEMFC mathematical equations to be used in Newton–Raphson Method required in Section 3.3.

1. First Derivative of Reversible Thermodynamic Power

$$\frac{dI_{FC}E_{nerst}}{dI_{FC}} = \frac{dI_{FC}\left[1.229 - 8.5\times10^{-4}(T-298.15) + 4.308\times10^{-5}T\ln P_{H_2}P_{O_2}^{0.5}\right]}{dI_{FC}}$$

$$\frac{dI_{FC}E_{nerst}}{dI_{FC}} = \frac{d\left[1.229I_{FC} - 8.5\times10^{-4}I_{FC}(T-298.15) + 4.308\times10^{-5}TI_{FC}\ln P_{H_2}P_{O_2}^{0.5}\right]}{dI_{FC}}$$

$$Let\ a_1 = \frac{d\left(4.308\times10^{-5}\times T\times I_{FC}\times\ln P_{H_2}\right)}{dI_{FC}}$$

$$Let\ b_1 = \frac{d\left(4.308\times10^{-5}\times T\times I_{FC}\times\ln P_{O_2}^{0.5}\right)}{dI_{FC}}$$

By substituting Equation 2.5 and Equation 2.6 into a_1 and b_1 respectively,

$$a_1 = 4.308\times10^{-5}T\left[\frac{-2k_rI_{FC}\left(1-e^{\left(-\frac{t}{\tau_{H_2}}\right)}\right)}{q_{H_2}^{in}-2k_rI_{FC}\left(1-e^{\left(-\frac{t}{\tau_{H_2}}\right)}\right)} + \ln\frac{q_{H_2}^{in}-2k_rI_{FC}\left(1-e^{\left(-\frac{t}{\tau_{H_2}}\right)}\right)}{k_{H_2}}\right]$$

$$b_1 = 2.154\times10^{-5}T\left[\frac{-k_rI_{FC}\left(1-e^{\left(-\frac{t}{\tau_{O_2}}\right)}\right)}{q_{O_2}^{in}-k_rI_{FC}\left(1-e^{\left(-\frac{t}{\tau_{O_2}}\right)}\right)} + \ln\frac{q_{O_2}^{in}-k_rI_{FC}\left(1-e^{\left(-\frac{t}{\tau_{O_2}}\right)}\right)}{k_{O_2}}\right]$$

Final equation of first derivative of reversible thermodynamic power,

$$\boldsymbol{\frac{dI_{FC}E_{nerst}}{dI_{FC}} = 1.229 - 8.5\times10^{-4}(T-298.15) + a_1 + b_1}$$

2. Second Derivative of Reversible Thermodynamic Power

$$\frac{d^2 I_{FC} E_{nerst}}{dI_{FC}{}^2} = \frac{d[1.229 - 8.5 \times 10^{-4}(T - 298.15) + a_1 + b_1]}{dI_{FC}}$$

$$\frac{d^2 I_{FC} E_{nerst}}{dI_{FC}{}^2} = \frac{d[1.229 - 8.5 \times 10^{-4}(T - 298.15)]}{dI_{FC}} + \frac{da_1}{dI_{FC}} + \frac{db_1}{dI_{FC}}$$

$$\frac{d[1.229 - 8.5 \times 10^{-4}(T - 298.15)]}{dI_{FC}} = 0$$

Derive $^{da_1}/_{dI_{FC}}$,

$$\frac{da_1}{dI_{FC}} = \frac{d\left[4.308 \times 10^{-5} T \left(\frac{-2k_r I_{FC}\left(1 - e^{\left(-\frac{t}{\tau_{H_2}}\right)}\right)}{q_{H_2}^{in} - 2k_r I_{FC}\left(1 - e^{\left(-\frac{t}{\tau_{H_2}}\right)}\right)} + \ln \frac{q_{H_2}^{in} - 2k_r I_{FC}\left(1 - e^{\left(-\frac{t}{\tau_{H_2}}\right)}\right)}{k_{H_2}}\right)\right]}{dI_{FC}}$$

$$Let\ a_4 = -2k_r I_{FC}\left(1 - e^{\left(-\frac{t}{\tau_{H_2}}\right)}\right)$$

$$\frac{da_4}{dI_{FC}} = -2k_r\left(1 - e^{\left(-\frac{t}{\tau_{H_2}}\right)}\right)$$

$$Let\ b_4 = q_{H_2}^{in} - 2k_r I_{FC}\left(1 - e^{\left(-\frac{t}{\tau_{H_2}}\right)}\right)$$

$$\frac{db_4}{dI_{FC}} = -2k_r\left(1 - e^{\left(-\frac{t}{\tau_{H_2}}\right)}\right)$$

$$Let\ c_4 = \ln \frac{q_{H_2}^{in} - 2k_r I_{FC}\left(1 - e^{\left(-\frac{t}{\tau_{H_2}}\right)}\right)}{k_{H_2}}$$

$$\frac{dc_4}{dI_{FC}} = -\frac{2k_r\left(1 - e^{\left(-\frac{t}{\tau_{H_2}}\right)}\right)}{q_{H_2}^{in} - 2k_r I_{FC}\left(1 - e^{\left(-\frac{t}{\tau_{H_2}}\right)}\right)}$$

$$\frac{da_1}{dI_{FC}} = 4.308 \times 10^{-5} T\left(\frac{b_4 \frac{da_4}{dI_{FC}} - a_4 \frac{db_4}{dI_{FC}}}{b_4^2} + \frac{dc_4}{dI_{FC}}\right)$$

$$\frac{da_1}{dI_{FC}} = 4.308\times10^{-5}T\left(\frac{q_{H_2}^{in} - 2k_rI_{FC}\left(1-e^{\left(-\frac{t}{\tau_{H_2}}\right)}\right)\left[-2k_r\left(1-e^{\left(-\frac{t}{\tau_{H_2}}\right)}\right)\right] - \left[-2k_rI_{FC}\left(1-e^{\left(-\frac{t}{\tau_{H_2}}\right)}\right)\right]\left[-2k_r\left(1-e^{\left(-\frac{t}{\tau_{H_2}}\right)}\right)\right]}{\left[q_{H_2}^{in} - 2k_rI_{FC}\left(1-e^{\left(-\frac{t}{\tau_{H_2}}\right)}\right)\right]^2}\right.$$

$$\left. + \left[-\frac{2k_r\left(1-e^{\left(-\frac{t}{\tau_{H_2}}\right)}\right)}{q_{H_2}^{in} - 2k_rI_{FC}\left(1-e^{\left(-\frac{t}{\tau_{H_2}}\right)}\right)}\right]\right)$$

$$\frac{da_1}{dI_{FC}} = 4.308\times10^{-5}T\left(\frac{I_{FC}\left[2k_r\left(1-e^{\left(-\frac{t}{\tau_{H_2}}\right)}\right)\right]^2 - 2q_{H_2}^{in}k_r\left(1-e^{\left(-\frac{t}{\tau_{H_2}}\right)}\right) - I_{FC}\left[2k_r\left(1-e^{\left(-\frac{t}{\tau_{H_2}}\right)}\right)\right]^2}{\left[q_{H_2}^{in} - 2k_rI_{FC}\left(1-e^{\left(-\frac{t}{\tau_{H_2}}\right)}\right)\right]^2}\right.$$

$$\left. + \left[-\frac{2k_r\left(1-e^{\left(-\frac{t}{\tau_{H_2}}\right)}\right)}{q_{H_2}^{in} - 2k_rI_{FC}\left(1-e^{\left(-\frac{t}{\tau_{H_2}}\right)}\right)}\right]\right)$$

$$\frac{da_1}{dI_{FC}} = 4.308\times10^{-5}T\left(\frac{-2q_{H_2}^{in}k_r\left(1-e^{\left(-\frac{t}{\tau_{H_2}}\right)}\right)}{\left[q_{H_2}^{in} - 2k_rI_{FC}\left(1-e^{\left(-\frac{t}{\tau_{H_2}}\right)}\right)\right]^2} - \frac{2k_r\left(1-e^{\left(-\frac{t}{\tau_{H_2}}\right)}\right)}{q_{H_2}^{in} - 2k_rI_{FC}\left(1-e^{\left(-\frac{t}{\tau_{H_2}}\right)}\right)}\right)$$

$$\frac{da_1}{dI_{FC}} = 4.308\times10^{-5}T\left(\frac{-2q_{H_2}^{in}k_r\left(1-e^{\left(-\frac{t}{\tau_{H_2}}\right)}\right)}{\left[q_{H_2}^{in} - 2k_rI_{FC}\left(1-e^{\left(-\frac{t}{\tau_{H_2}}\right)}\right)\right]^2} - \frac{2k_r\left(1-e^{\left(-\frac{t}{\tau_{H_2}}\right)}\right)\left[q_{H_2}^{in} - 2k_rI_{FC}\left(1-e^{\left(-\frac{t}{\tau_{H_2}}\right)}\right)\right]}{\left[q_{H_2}^{in} - 2k_rI_{FC}\left(1-e^{\left(-\frac{t}{\tau_{H_2}}\right)}\right)\right]^2}\right)$$

$$\frac{da_1}{dI_{FC}} = 4.308\times10^{-5}T\left(\frac{-2q_{H_2}^{in}k_r\left(1-e^{\left(-\frac{t}{\tau_{H_2}}\right)}\right)}{\left[q_{H_2}^{in} - 2k_rI_{FC}\left(1-e^{\left(-\frac{t}{\tau_{H_2}}\right)}\right)\right]^2} - \frac{2q_{H_2}^{in}k_r\left(1-e^{\left(-\frac{t}{\tau_{H_2}}\right)}\right) - I_{FC}\left[2k_r\left(1-e^{\left(-\frac{t}{\tau_{H_2}}\right)}\right)\right]^2}{\left[q_{H_2}^{in} - 2k_rI_{FC}\left(1-e^{\left(-\frac{t}{\tau_{H_2}}\right)}\right)\right]^2}\right)$$

$$\frac{da_1}{dI_{FC}} = 4.308\times10^{-5}T\left(\frac{I_{FC}\left[2k_r\left(1-e^{\left(-\frac{t}{\tau_{H_2}}\right)}\right)\right]^2 - 4q_{H_2}^{in}k_r\left(1-e^{\left(-\frac{t}{\tau_{H_2}}\right)}\right)}{\left[q_{H_2}^{in} - 2k_rI_{FC}\left(1-e^{\left(-\frac{t}{\tau_{H_2}}\right)}\right)\right]^2}\right)$$

Derive $^{db_1}/_{dI_{FC}}$,

$$\frac{db_1}{dI_{FC}} = \frac{d\left[2.154\times10^{-5}T\left(\frac{-k_rI_{FC}\left(1-e^{\left(-\frac{t}{\tau_{O_2}}\right)}\right)}{q_{O_2}^{in} - k_rI_{FC}\left(1-e^{\left(-\frac{t}{\tau_{O_2}}\right)}\right)} + \ln\frac{q_{O_2}^{in} - k_rI_{FC}\left(1-e^{\left(-\frac{t}{\tau_{O_2}}\right)}\right)}{k_{O_2}}\right)\right]}{dI_{FC}}$$

$$Let\ a_5 = -k_r I_{FC}\left(1 - e^{\left(-\frac{t}{\tau_{O_2}}\right)}\right)$$

$$\frac{da_5}{dI_{FC}} = -k_r\left(1 - e^{\left(-\frac{t}{\tau_{O_2}}\right)}\right)$$

$$Let\ b_5 = q_{O_2}^{in} - k_r I_{FC}\left(1 - e^{\left(-\frac{t}{\tau_{O_2}}\right)}\right)$$

$$\frac{db_5}{dI_{FC}} = -k_r\left(1 - e^{\left(-\frac{t}{\tau_{O_2}}\right)}\right)$$

$$Let\ c_5 = \ln\frac{q_{O_2}^{in} - k_r I_{FC}\left(1 - e^{\left(-\frac{t}{\tau_{O_2}}\right)}\right)}{k_{O_2}}$$

$$\frac{dc_5}{dI_{FC}} = -\frac{k_r\left(1 - e^{\left(-\frac{t}{\tau_{O_2}}\right)}\right)}{q_{O_2}^{in} - k_r I_{FC}\left(1 - e^{\left(-\frac{t}{\tau_{O_2}}\right)}\right)}$$

$$\frac{db_1}{dI_{FC}} = 2.154 \times 10^{-5} T\left(\frac{b_5\frac{da_5}{dI_{FC}} - a_5\frac{db_5}{dI_{FC}}}{b_5^2} + \frac{dc_5}{dI_{FC}}\right)$$

$$\frac{db_1}{dI_{FC}} = 2.154 \times 10^{-5} T\left(\frac{q_{O_2}^{in} - k_r I_{FC}\left(1 - e^{\left(-\frac{t}{\tau_{O_2}}\right)}\right)\left[-k_r\left(1 - e^{\left(-\frac{t}{\tau_{O_2}}\right)}\right)\right] - \left[-k_r I_{FC}\left(1 - e^{\left(-\frac{t}{\tau_{O_2}}\right)}\right)\right]\left[-k_r\left(1 - e^{\left(-\frac{t}{\tau_{O_2}}\right)}\right)\right]}{\left[q_{O_2}^{in} - k_r I_{FC}\left(1 - e^{\left(-\frac{t}{\tau_{O_2}}\right)}\right)\right]^2}\right.$$

$$\left. + \left[-\frac{k_r\left(1 - e^{\left(-\frac{t}{\tau_{O_2}}\right)}\right)}{q_{O_2}^{in} - k_r I_{FC}\left(1 - e^{\left(-\frac{t}{\tau_{O_2}}\right)}\right)}\right]\right)$$

$$\frac{db_1}{dI_{FC}} = 2.154 \times 10^{-5} T\left(\frac{I_{FC}\left[k_r\left(1 - e^{\left(-\frac{t}{\tau_{O_2}}\right)}\right)\right]^2 - q_{O_2}^{in} k_r\left(1 - e^{\left(-\frac{t}{\tau_{O_2}}\right)}\right) - I_{FC}\left[k_r\left(1 - e^{\left(-\frac{t}{\tau_{O_2}}\right)}\right)\right]^2}{\left[q_{O_2}^{in} - k_r I_{FC}\left(1 - e^{\left(-\frac{t}{\tau_{O_2}}\right)}\right)\right]^2}\right.$$

$$\left. - \frac{k_r\left(1 - e^{\left(-\frac{t}{\tau_{O_2}}\right)}\right)}{q_{O_2}^{in} - k_r I_{FC}\left(1 - e^{\left(-\frac{t}{\tau_{O_2}}\right)}\right)}\right)$$

$$\frac{db_1}{dI_{FC}} = 2.154 \times 10^{-5} T \left(\frac{-q_{O_2}^{in} k_r \left(1 - e^{\left(-\frac{t}{\tau_{O_2}}\right)}\right)}{\left[q_{O_2}^{in} - k_r I_{FC}\left(1 - e^{\left(-\frac{t}{\tau_{O_2}}\right)}\right)\right]^2} - \frac{k_r \left(1 - e^{\left(-\frac{t}{\tau_{O_2}}\right)}\right)}{q_{O_2}^{in} - k_r I_{FC}\left(1 - e^{\left(-\frac{t}{\tau_{O_2}}\right)}\right)} \right)$$

$$\frac{db_1}{dI_{FC}} = 2.154 \times 10^{-5} T \left(\frac{-q_{O_2}^{in} k_r \left(1 - e^{\left(-\frac{t}{\tau_{O_2}}\right)}\right)}{\left[q_{O_2}^{in} - k_r I_{FC}\left(1 - e^{\left(-\frac{t}{\tau_{O_2}}\right)}\right)\right]^2} - \frac{k_r \left(1 - e^{\left(-\frac{t}{\tau_{O_2}}\right)}\right)\left[q_{O_2}^{in} - k_r I_{FC}\left(1 - e^{\left(-\frac{t}{\tau_{O_2}}\right)}\right)\right]}{\left[q_{O_2}^{in} - k_r I_{FC}\left(1 - e^{\left(-\frac{t}{\tau_{O_2}}\right)}\right)\right]^2} \right)$$

$$\frac{db_1}{dI_{FC}} = 2.154 \times 10^{-5} T \left(\frac{-q_{O_2}^{in} k_r \left(1 - e^{\left(-\frac{t}{\tau_{O_2}}\right)}\right)}{\left[q_{O_2}^{in} - k_r I_{FC}\left(1 - e^{\left(-\frac{t}{\tau_{O_2}}\right)}\right)\right]^2} - \frac{q_{O_2}^{in} k_r \left(1 - e^{\left(-\frac{t}{\tau_{O_2}}\right)}\right) - I_{FC}\left[k_r \left(1 - e^{\left(-\frac{t}{\tau_{O_2}}\right)}\right)\right]^2}{\left[q_{O_2}^{in} - k_r I_{FC}\left(1 - e^{\left(-\frac{t}{\tau_{O_2}}\right)}\right)\right]^2} \right)$$

$$\frac{db_1}{dI_{FC}} = 2.154 \times 10^{-5} T \left(\frac{I_{FC}\left[k_r \left(1 - e^{\left(-\frac{t}{\tau_{O_2}}\right)}\right)\right]^2 - 2q_{O_2}^{in} k_r \left(1 - e^{\left(-\frac{t}{\tau_{O_2}}\right)}\right)}{\left[q_{O_2}^{in} - k_r I_{FC}\left(1 - e^{\left(-\frac{t}{\tau_{O_2}}\right)}\right)\right]^2} \right)$$

Final equation of second derivative of reversible thermodynamic power loss,

$$\boldsymbol{\frac{d^2 I_{FC} E_{nerst}}{dI_{FC}^{\,2}} = \frac{da_1}{dI_{FC}} + \frac{db_1}{dI_{FC}}}$$

3. First Derivative of Activation Power Loss

$$\frac{dI_{FC} V_{act}}{dI_{FC}} = \frac{dI_{FC}\left(\xi_1 + \xi_2 T + \xi_3 T \ln C_{O_2} + \xi_4 T \ln I_{FC}\right)}{dI_{FC}}$$

$$\frac{dI_{FC} V_{act}}{dI_{FC}} = \frac{d\left(\xi_1 I_{FC} + \xi_2 T I_{FC} + \xi_3 T I_{FC} \ln C_{O_2} + \xi_4 T I_{FC} \ln I_{FC}\right)}{dI_{FC}}$$

By substituting Equation 2.9 into the equation,

$$\frac{dI_{FC} V_{act}}{dI_{FC}} = \frac{d\left(\xi_1 I_{FC} + \xi_2 T I_{FC} + \xi_3 T I_{FC} \ln \frac{P_{O_2}}{(5.08 \times 10^6) e^{\frac{-498}{T}}} + \xi_4 T I_{FC} \ln I_{FC}\right)}{dI_{FC}}$$

$$Let\ a_2 = \frac{d\left(\xi_3 T I_{FC} \ln \frac{P_{O_2}}{(5.08 \times 10^6) e^{\frac{-498}{T}}}\right)}{dI_{FC}}$$

$$a_2 = \frac{d\left[\xi_3 T I_{FC}\left(\ln P_{O_2} - \ln(5.08 \times 10^6) e^{\frac{-498}{T}}\right)\right]}{dI_{FC}}$$

By substituting Equation 2.6 into a_2,

$$a_2 = \xi_3 T \left[\frac{-k_r I_{FC}\left(1 - e^{\left(-\frac{t}{\tau_{O_2}}\right)}\right)}{q_{O_2}^{in} - k_r I_{FC}\left(1 - e^{\left(-\frac{t}{\tau_{O_2}}\right)}\right)} + \ln \frac{q_{O_2}^{in} - k_r I_{FC}\left(1 - e^{\left(-\frac{t}{\tau_{O_2}}\right)}\right)}{k_{O_2}(5.08 \times 10^6) e^{\frac{-498}{T}}}\right]$$

Final equation of first derivative of activation power loss,

$$\boldsymbol{\frac{dI_{FC}V_{act}}{dI_{FC}} = \xi_1 + \xi_2 T + a_2 + \xi_4 T(1 + \ln I_{FC})}$$

4. Second Derivative of Activation Power Loss

$$\frac{d^2 I_{FC} V_{act}}{dI_{FC}^{\ 2}} = \frac{d[\xi_1 + \xi_2 T + a_2 + \xi_4 T(1 + \ln I_{FC})]}{dI_{FC}}$$

$$\frac{d[\xi_1 + \xi_2 T + \xi_4 T(1 + \ln I_{FC})]}{dI_{FC}} = \frac{\xi_4 T}{I_{FC}}$$

Derive da_2/dI_{FC},

$$\frac{da_2}{dI_{FC}} = \frac{d\left[\xi_3 T\left(\frac{-k_r I_{FC}\left(1 - e^{\left(-\frac{t}{\tau_{O_2}}\right)}\right)}{q_{O_2}^{in} - k_r I_{FC}\left(1 - e^{\left(-\frac{t}{\tau_{O_2}}\right)}\right)} + \ln \frac{q_{O_2}^{in} - k_r I_{FC}\left(1 - e^{\left(-\frac{t}{\tau_{O_2}}\right)}\right)}{k_{O_2}(5.08 \times 10^6) e^{\frac{-498}{T}}}\right)\right]}{dI_{FC}}$$

$$Let\ a_6 = -k_r I_{FC}\left(1 - e^{\left(-\frac{t}{\tau_{O_2}}\right)}\right)$$

$$\frac{da_6}{dI_{FC}} = -k_r\left(1 - e^{\left(-\frac{t}{\tau_{O_2}}\right)}\right)$$

$$Let\ b_6 = q_{O_2}^{in} - k_r I_{FC}\left(1 - e^{\left(-\frac{t}{\tau_{O_2}}\right)}\right)$$

$$\frac{db_6}{dI_{FC}} = -k_r\left(1 - e^{\left(-\frac{t}{\tau_{O_2}}\right)}\right)$$

$$Let\ c_6 = \ln\frac{q_{O_2}^{in} - k_r I_{FC}\left(1 - e^{\left(-\frac{t}{\tau_{O_2}}\right)}\right)}{k_{O_2}(5.08 \times 10^6)e^{\frac{-498}{T}}}$$

$$\frac{dc_6}{dI_{FC}} = -\frac{k_r\left(1 - e^{\left(-\frac{t}{\tau_{O_2}}\right)}\right)}{q_{O_2}^{in} - k_r I_{FC}\left(1 - e^{\left(-\frac{t}{\tau_{O_2}}\right)}\right)}$$

$$\frac{da_2}{dI_{FC}} = \xi_3 T\left(\frac{b_6\frac{da_6}{dI_{FC}} - a_6\frac{db_6}{dI_{FC}}}{b_6^2} + \frac{dc_6}{dI_{FC}}\right)$$

$$\frac{da_2}{dI_{FC}} = \xi_3 T\left(\frac{q_{O_2}^{in} - k_r I_{FC}\left(1 - e^{\left(-\frac{t}{\tau_{O_2}}\right)}\right)\left[-k_r\left(1 - e^{\left(-\frac{t}{\tau_{O_2}}\right)}\right)\right] - \left[-k_r I_{FC}\left(1 - e^{\left(-\frac{t}{\tau_{O_2}}\right)}\right)\right]\left[-k_r\left(1 - e^{\left(-\frac{t}{\tau_{O_2}}\right)}\right)\right]}{\left[q_{O_2}^{in} - k_r I_{FC}\left(1 - e^{\left(-\frac{t}{\tau_{O_2}}\right)}\right)\right]^2}\right.$$

$$\left. + \left[-\frac{k_r\left(1 - e^{\left(-\frac{t}{\tau_{O_2}}\right)}\right)}{q_{O_2}^{in} - k_r I_{FC}\left(1 - e^{\left(-\frac{t}{\tau_{O_2}}\right)}\right)}\right]\right)$$

$$\frac{da_2}{dI_{FC}} = \xi_3 T\left(\frac{I_{FC}\left[k_r\left(1 - e^{\left(-\frac{t}{\tau_{O_2}}\right)}\right)\right]^2 - q_{O_2}^{in}k_r\left(1 - e^{\left(-\frac{t}{\tau_{O_2}}\right)}\right) - I_{FC}\left[k_r\left(1 - e^{\left(-\frac{t}{\tau_{O_2}}\right)}\right)\right]^2}{\left[q_{O_2}^{in} - k_r I_{FC}\left(1 - e^{\left(-\frac{t}{\tau_{O_2}}\right)}\right)\right]^2}\right.$$

$$\left. - \frac{k_r\left(1 - e^{\left(-\frac{t}{\tau_{O_2}}\right)}\right)}{q_{O_2}^{in} - k_r I_{FC}\left(1 - e^{\left(-\frac{t}{\tau_{O_2}}\right)}\right)}\right)$$

$$\frac{da_2}{dI_{FC}} = \xi_3 T \left(\frac{-q_{O_2}^{in} k_r \left(1 - e^{\left(-\frac{t}{\tau_{O_2}}\right)}\right)}{\left[q_{O_2}^{in} - k_r I_{FC}\left(1 - e^{\left(-\frac{t}{\tau_{O_2}}\right)}\right)\right]^2} - \frac{k_r \left(1 - e^{\left(-\frac{t}{\tau_{O_2}}\right)}\right)}{q_{O_2}^{in} - k_r I_{FC}\left(1 - e^{\left(-\frac{t}{\tau_{O_2}}\right)}\right)} \right)$$

$$\frac{da_2}{dI_{FC}} = \xi_3 T \left(\frac{-q_{O_2}^{in} k_r \left(1 - e^{\left(-\frac{t}{\tau_{O_2}}\right)}\right)}{\left[q_{O_2}^{in} - k_r I_{FC}\left(1 - e^{\left(-\frac{t}{\tau_{O_2}}\right)}\right)\right]^2} - \frac{k_r \left(1 - e^{\left(-\frac{t}{\tau_{O_2}}\right)}\right)\left[q_{O_2}^{in} - k_r I_{FC}\left(1 - e^{\left(-\frac{t}{\tau_{O_2}}\right)}\right)\right]}{\left[q_{O_2}^{in} - k_r I_{FC}\left(1 - e^{\left(-\frac{t}{\tau_{O_2}}\right)}\right)\right]^2} \right)$$

$$\frac{da_2}{dI_{FC}} = \xi_3 T \left(\frac{-q_{O_2}^{in} k_r \left(1 - e^{\left(-\frac{t}{\tau_{O_2}}\right)}\right)}{\left[q_{O_2}^{in} - k_r I_{FC}\left(1 - e^{\left(-\frac{t}{\tau_{O_2}}\right)}\right)\right]^2} - \frac{q_{O_2}^{in} k_r \left(1 - e^{\left(-\frac{t}{\tau_{O_2}}\right)}\right) - I_{FC}\left[k_r \left(1 - e^{\left(-\frac{t}{\tau_{O_2}}\right)}\right)\right]^2}{\left[q_{O_2}^{in} - k_r I_{FC}\left(1 - e^{\left(-\frac{t}{\tau_{O_2}}\right)}\right)\right]^2} \right)$$

$$\frac{da_2}{dI_{FC}} = \xi_3 T \left(\frac{I_{FC}\left[k_r \left(1 - e^{\left(-\frac{t}{\tau_{O_2}}\right)}\right)\right]^2 - 2q_{O_2}^{in} k_r \left(1 - e^{\left(-\frac{t}{\tau_{O_2}}\right)}\right)}{\left[q_{O_2}^{in} - k_r I_{FC}\left(1 - e^{\left(-\frac{t}{\tau_{O_2}}\right)}\right)\right]^2} \right)$$

Final equation of second derivative of activation power loss,

$$\boldsymbol{\frac{d^2 I_{FC} V_{act}}{dI_{FC}^{\,2}} = \frac{da_2}{dI_{FC}} + \frac{\xi_4 T}{I_{FC}}}$$

5. First Derivative of Ohmic Power Loss

$$\frac{dI_{FC}V_{ohm}}{dI_{FC}} = \frac{d\left[I_{FC}^2 \times \frac{t_m}{A} \times 181.6 \times \frac{1 + 0.03\left(\frac{I_{FC}}{A}\right) + 0.062\left(\frac{T}{303}\right)^2\left(\frac{I_{FC}}{A}\right)^{2.5}}{\left[\lambda_m - 0.634 - 3\left(\frac{I_{FC}}{A}\right)\right] e^{4.18\left(\frac{T-303}{T}\right)}}\right]}{dI_{FC}}$$

$$\frac{dI_{FC}V_{ohm}}{dI_{FC}} = \frac{d\left[\frac{181.6 t_m \left[I_{FC}^2 + 0.03\left(\frac{I_{FC}^3}{A}\right) + 0.062\left(\frac{T}{303}\right)^2\left(\frac{I_{FC}^{4.5}}{A^{2.5}}\right)\right]}{(\lambda_m A - 0.634A - 3I_{FC}) e^{4.18\left(\frac{T-303}{T}\right)}}\right]}{dI_{FC}}$$

$$Let\ a_3 = 181.6 t_m \left[I_{FC}^2 + 0.03\left(\frac{I_{FC}^3}{A}\right) + 0.062\left(\frac{T}{303}\right)^2\left(\frac{I_{FC}^{4.5}}{A^{2.5}}\right)\right]$$

$$\frac{da_3}{dI_{FC}} = 363.2t_m I_{FC} + 16.344t_m\left(\frac{I_{FC}^2}{A}\right) + 5.51867\times10^{-4}t_m T^2\left(\frac{I_{FC}^{3.5}}{A^{2.5}}\right)$$

$$Let\ b_3 = (\lambda_m A - 0.634A - 3I_{FC})e^{4.18\left(\frac{T-303}{T}\right)}$$

$$\frac{db_3}{dI_{FC}} = -3e^{4.18\left(\frac{T-303}{T}\right)}$$

Final equation of first derivative of ohmic power loss,

$$\boldsymbol{\frac{dI_{FC}V_{ohm}}{dI_{FC}} = \frac{b_3\frac{da_3}{dI_{FC}} - a_3\frac{db_3}{dI_{FC}}}{b_3^2}}$$

6. Second Derivative of Ohmic Power Loss

$$\frac{d^2I_{FC}V_{ohm}}{dI_{FC}^{\ 2}} = \frac{d\left[\dfrac{b_3\frac{da_3}{dI_{FC}} - a_3\frac{db_3}{dI_{FC}}}{b_3^2}\right]}{dI_{FC}}$$

$$\frac{d^2I_{FC}V_{ohm}}{dI_{FC}^{\ 2}} = \frac{b_3^2\left[b_3\frac{d^2a_3}{dI_{FC}^{\ 2}} + \frac{da_3}{dI_{FC}}\frac{db_3}{dI_{FC}} - \left(a_3\frac{d^2b_3}{dI_{FC}^{\ 2}} + \frac{db_3}{dI_{FC}}\frac{da_3}{dI_{FC}}\right)\right] - \frac{db_3^2}{dI_{FC}}\left(b_3\frac{da_3}{dI_{FC}} - a_3\frac{db_3}{dI_{FC}}\right)}{b_3^4}$$

$$\frac{d^2I_{FC}V_{ohm}}{dI_{FC}^{\ 2}} = \frac{b_3^2\left[b_3\frac{d^2a_3}{dI_{FC}^{\ 2}} - a_3\frac{d^2b_3}{dI_{FC}^{\ 2}}\right] - \frac{db_3^2}{dI_{FC}}\left(b_3\frac{da_3}{dI_{FC}} - a_3\frac{db_3}{dI_{FC}}\right)}{b_3^4}$$

Derive $d^2a_3/dI_{FC}^{\ 2}$,

$$\frac{d^2a_3}{dI_{FC}^{\ 2}} = \frac{d\left[363.2t_m I_{FC} + 16.344t_m\left(\frac{I_{FC}^2}{A}\right) + 5.51867\times10^{-4}t_m T^2\left(\frac{I_{FC}^{3.5}}{A^{2.5}}\right)\right]}{dI_{FC}}$$

$$\frac{d^2a_3}{dI_{FC}^{\ 2}} = 363.2t_m + 32.688t_m\left(\frac{I_{FC}}{A}\right) + 1.93153\times10^{-3}t_m T^2\left(\frac{I_{FC}^{2.5}}{A^{2.5}}\right)$$

Derive $d^2b_3/dI_{FC}^{\ 2}$,

$$\frac{d^2 b_3}{dI_{FC}{}^2} = \frac{d\left[-3e^{4.18\left(\frac{T-303}{T}\right)}\right]}{dI_{FC}}$$

$$\frac{d^2 b_3}{dI_{FC}{}^2} = 0$$

Derive $db_3^2 \Big/ dI_{FC}$,

$$\frac{db_3^2}{dI_{FC}} = \frac{d\left[(\lambda_m A - 0.634A - 3I_{FC})e^{4.18\left(\frac{T-303}{T}\right)}\right]^2}{dI_{FC}}$$

$$\frac{db_3^2}{dI_{FC}} = \frac{d[(\lambda_m A)^2 - 1.268\lambda_m A^2 - 6\lambda_m A I_{FC} + 0.402A^2 + 3.804AI_{FC} + 9I_{FC}^2]\left[e^{4.18\left(\frac{T-303}{T}\right)}\right]^2}{dI_{FC}}$$

$$\frac{db_3^2}{dI_{FC}} = (18I_{FC} + 3.804A - 6\lambda_m A)\left[e^{4.18\left(\frac{T-303}{T}\right)}\right]^2$$

Since $d^2 b_3 \Big/ dI_{FC}{}^2 = 0$, the second derivative of $I_{FC}V_{ohm}$ can be simplified as:

$$\boldsymbol{\frac{d^2 I_{FC} V_{ohm}}{dI_{FC}{}^2} = \frac{b_3^2\left(b_3 \frac{d^2 a_3}{dI_{FC}{}^2}\right) - \frac{db_3^2}{dI_{FC}}\left(b_3 \frac{da_3}{dI_{FC}} - a_3 \frac{db_3}{dI_{FC}}\right)}{b_3^4}}$$

7. First Derivative of Concentration Power Loss

$$\frac{dI_{FC}V_{conc}}{dI_{FC}} = \frac{dI_{FC}\left[-\frac{RT}{nF}\ln\left(1 - \frac{I_{FC}}{i_L A}\right)\right]}{dI_{FC}}$$

$$\frac{dI_{FC}V_{conc}}{dI_{FC}} = \frac{dI_{FC}\left[-\frac{RT}{nF}\ln\left(\frac{i_L A - I_{FC}}{i_L A}\right)\right]}{dI_{FC}}$$

$$\frac{dI_{FC}V_{conc}}{dI_{FC}} = -\frac{RT}{nF}\frac{dI_{FC}[\ln(i_L A - I_{FC}) - \ln(i_L A)]}{dI_{FC}}$$

$$\frac{dI_{FC}V_{conc}}{dI_{FC}} = -\frac{RT}{nF}\left(\ln(i_L A - I_{FC}) - \ln(i_L A) - \frac{I_{FC}}{i_L A - I_{FC}}\right)$$

$$\frac{dI_{FC}V_{conc}}{dI_{FC}} = -\frac{RT}{nF}\left[\ln\left(1-\frac{I_{FC}}{i_L A}\right) - \frac{I_{FC}}{i_L A - I_{FC}}\right]$$

$$\boldsymbol{\frac{dI_{FC}V_{conc}}{dI_{FC}} = \frac{RT}{nF}\left[\frac{I_{FC}}{i_L A - I_{FC}} - \ln\left(1-\frac{I_{FC}}{i_L A}\right)\right]}$$

8. Second Derivative of Concentration Power Loss

$$\frac{d^2 I_{FC}V_{conc}}{dI_{FC}{}^2} = \frac{d\left[\frac{RT}{nF}\left[\frac{I_{FC}}{i_L A - I_{FC}} - \ln\left(1-\frac{I_{FC}}{i_L A}\right)\right]\right]}{dI_{FC}}$$

$$\frac{d^2 I_{FC}V_{conc}}{dI_{FC}{}^2} = \frac{RT}{nF}\left[\frac{i_L A - I_{FC} + I_{FC}}{(i_L A - I_{FC})^2} - \frac{i_L A}{i_L A - I_{FC}} \times \left(-\frac{1}{i_L A}\right)\right]$$

$$\frac{d^2 I_{FC}V_{conc}}{dI_{FC}{}^2} = \frac{RT}{nF}\left[\frac{i_L A}{(i_L A - I_{FC})^2} + \frac{1}{i_L A - I_{FC}}\right]$$

$$\boldsymbol{\frac{d^2 I_{FC}V_{conc}}{dI_{FC}{}^2} = \frac{RT}{nF}\left[\frac{2i_L A - I_{FC}}{(i_L A - I_{FC})^2}\right]}$$